ISSN 1349-0087

SPring-8 Research Frontiers

2004

CONTENTS
2004

Editor's Note

SPring-8 Research Frontiers describes the remarkable scientific achievements made at SPring-8 as well as developments in the accelerator and beamlines and the status of the facility. This seventh issue "2004" covers advances made during the two consecutive research terms, the second half of 2003 and the first half of 2004.

In the previous issue "2003" the editing plan was changed considerably. This time, minor changes were made as follows. First, one of the categorized research fields, "Life Science," was divided into two parts, Life Science: Structural Biology and Life Science: Medical Biology. As a result, the number of categories in research fields has become ten. Next, a new heading "New Apparatus and Upgrades" was made in the Facility Status section. Here the apparatus newly installed in the beamlines and experimental stations are introduced together with their performance. Upgrades of existing apparatus are also described. Finally, the principal publication(s) concerning the article are indicated with all authors' names in italics in the list of references.

We invited nine specialists from the Proposal Review Committee to serve as the Editing Coordinators for their respective researc hfields:

Life Science: Structural Biology - *Prof. Keiichi Fukuyama* (Osaka University)
Life Science: Medical Biogy - *Prof. Fumihiko Kajiya* (Okayama University)
Materials Science: Structure - *Prof. Makoto Sakata* (Nagoya University)
Materials Science: Electronics & Magnetism - *Assoc. Prof. Toyohiko Kinoshita* (The University of Tokyo)
Chemical Science - *Assoc. Prof. Tsunehiro Tsunehiro Tanaka* (Kyoto University)
Earth & Planetary Science - *Prof. Tetsuo Irifune* (Ehime University)
Environmental Science - *Dr. Momoko Takemura* (Toshiba Co., Ltd.)
Industrial Application - *Prof. Tokuhiko Okamoto* (Ritsumeikan University)
Instrumentation & Methodology - *Prof. Masaharu Nomura* (High Energy Accelerator Research Organization)

We would like to express our most sincere appreciation to Editing Coordinators for their efforts in preparing the introductory overview and providing comments on each research field. We would also like to express our gratitude to the users and staff members of SPring-8 for contributing their reports to SPring-8 Research Frontiers.

SPring-8 Research Frontiers will be sent on request. Its full text is also available on the SPring-8 Website: http://www.spring8.or.jp/

Preface

This volume covers the highlight of the achievement attained at SPring-8 in its 7th year of operation. The results demonstrate that utilization and application of SPring-8 are closing to a peak under the present conditions. By the present conditions, I would like to mean that SPring-8 is not yet complete because the sites for 14 beamlines are still vacant. No plans for new beamlines have been approved by the Government since 2002, owing to the poor economics of the country. The latest and second-latest constructed are all contract beamlines: the one by Hyogo prefecture (2005) and the other by Pharmaceutical Consortium (2002).

The big topic in facilities was the start of the top-up operations, of which details are described in this issue. The users seem to accept the top-up operation favorably. I hope that the advantageous effects of top-up operation will appear in reports of next issue of the Research Frontiers.

Promotion of industrial application is still the largest concern of the Japanese Government. The Government starts a new program to promote industrial application at some large public facilities for common use in 2005 fiscal year, in which SPring-8 was included. This program will probably lead to a new system of governmental support to the public research facilities.

In a policy of the medical application at SPring-8, emphasis was shifted from clinical utilization to basic medical-bio applications after arguments over 5 years. I hope that the release from the limitation based on the clinical use would activate useful applications that finally contribute to clinical medicine.

Since its opening, JASRI has operated SPring-8 entrusted by JAERI and RIKEN, the owners of the facilities. However, as a result of the innovation of governmental organizations, JAERI is to withdraw from the administration of SPring-8 after September 2005, but will remain as a major user who owns 4 contract beamlines. RIKEN will take over the facilities JAERI owned. This scheme may change again in near future if the above-mentioned new system for large public facilities starts.

Akira Kira
Director General
SPring-8 / JASRI

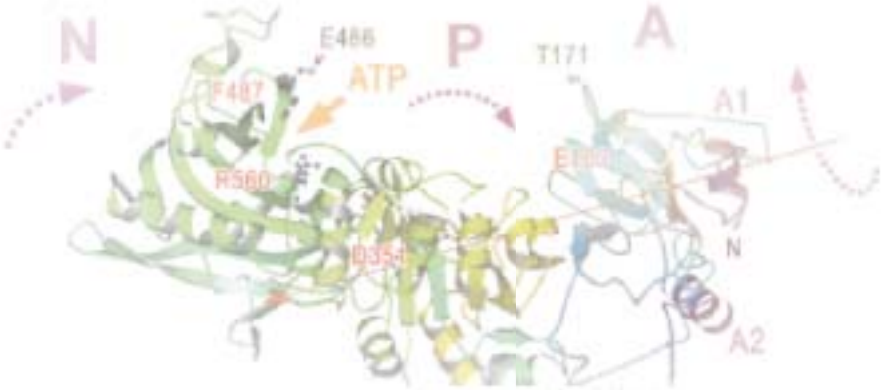

Scientific Frontiers

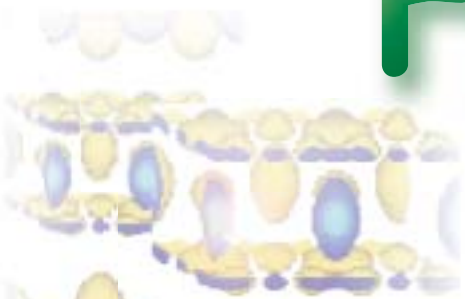

Life Science
Structural Biology

Biological macromolecules (proteins, nucleic acids, and carbohydrates) play leading roles in the processes of living cells and attract much of the attention of scientists. In particular, successes in structural biology research on proteins and protein-nucleic acid complexes are notable, providing their remarkable structures as the basis of fine-tuned complicated functions. In addition, many genome analyses, including the Human Genome Project, have provided much genetic information, including the amino acid sequences of proteins. Thus, structural biology research becomes increasingly important for elucidating the three-dimensional structures and functions, and Structural Genomics projects as postgenomic research are progressing worldwide.

Synchrotron radiation (SR), particularly the third generation SR, is now indispensable for structural biology and structural genomics research. At SPring-8, five undulator and seven bending magnet beamlines have been contributing in the field of macromolecular crystallography, small angle X-ray scattering (SAXS) and fiber diffraction studies. A large format CCD detector (ADSC Quantum 315), which enables high-throughput data collection with a higher resolution than previous detectors, was installed at BL41XU. Moreover, a standardized user-friendly beamline control system (BSS) was installed for a more efficient data collection in many beamlines.

Many new structures of biologically important macromolecules were determined by crystallography last year. The structural determination of all four principal states in the calcium pump has been completed, elucidating the gating mechanism that underlies release of the calcium ions into the lumen. The structure of the MexAB-OprM pump assembly, which crosses the inner and outer membranes, gave insight into the mechanism of multidrug efflux. The precise structural analysis of cytochrome *c* oxidase revealed a redox-coupled conformational change, on the basis of which the mechanism of the proton-pumping process was proposed. The structure of the clock oscillator protein KaiA led to the identification of the crucial residue for circadian rhythms, the daily activity cycles. The structures of the human DNA recombinase Dmc1 and elongation factor P from *Thermus thermophilus* HB8 brought breakthroughs in the studies of cell division and genetic translation process. The conversion of iron-sulfur clusters was shown by aerobic and anaerobic structures of ferredoxin.

SAXS and fiber diffraction were applied to the study of nanoscale molecular structures. The dynamical study of apo-myoglobin folding provided insight into protein-folding trajectory, and wide-angle X-ray scattering study led to the construction of the hierarchical map of unfolding-refolding transition of proteins. The fiber diffraction study of prion Sup35 amyloid fibers revealed the β-helix backbone as the core structure.

Keiichi Fukuyama

Crystal Structure of the Calcium Pump with a Bound ATP Analogue

Nature uses ion gradients across cell membranes very efficiently. When cell membrane excites, ions come into cytoplasm rapidly following the ion gradients. To restore the original resting state, the ions must be pumped back. P-type ATPase is a family of ion transporting ATPases that are responsible for establishing such ion gradients. They include Na^+K^+-ATPase, Ca^{2+}-ATPase and gastric H^+K^+-ATPase among others. The transport is thought to be achieved by changing the binding sites from high affinity and facing cytoplasm (E1 form) to low affinity and facing the extracellular side (E2 form). One important feature of the pumping process is that, before being released, bound cations are occluded; that is, become inaccessible from either side of the membrane. Binding in itself does not lock the cytoplasmic gate, and bound cations can be exchanged with those in the cytoplasm.

Of the P-type ATPase superfamily, the Ca^{2+}-ATPase of fast skeletal muscle sarcoplasmic reticulum (SR) is structurally and functionally the best studied member. It is an integral membrane protein of 110 kD, consisting of 3 (A (actuator), N (nucleotide binding) and P (phosphorylation)) cytoplasmic domains and 10 (M1-M10) transmembrane helices (Fig. 1). We already published the structures in a Ca^{2+}-bound state (E1·2Ca^{2+}; PDB accession code 1SU4) [1] and a Ca^{2+}-unbound state (E2(TG)) [2], stabilized by a potent inhibitor, thapsigargin (PDB accession code 1IWO), and have now succeeded in determining the structure of the ATPase with a non-hydrolysable analogue, AMPPCP, a Mg^{2+} and two Ca^{2+} ions bound at their respective binding sites (PDB accession code 1VFP) [3]. This structure (abbreviated as E1·AMPPCP) explains how the γ-phosphate and Mg^{2+} binding to the P-domain results in the occlusion of the bound Ca^{2+} at some 50 Å away.

The binding of AMPPCP and a Mg^{2+} ion to the P-domain causes large and global changes in the structure (Fig. 1). The most prominent difference is that the 3 cytoplasmic domains, widely separated in E1·2Ca^{2+}, now form a compact headpiece, with the N- and P-domains cross-linked by AMPPCP. This causes a nearly 90° inclination of the N-domain, which now makes contacts with the A-domain. To achieve this, the γ-phosphate bends the P-domain to gain an extra ~30° of inclination. At the same time, ATP induces the binding of Mg^{2+}, which bends the P-domain in nearly orthogonal direction so that the M2 side is brought higher up. As a combined result of

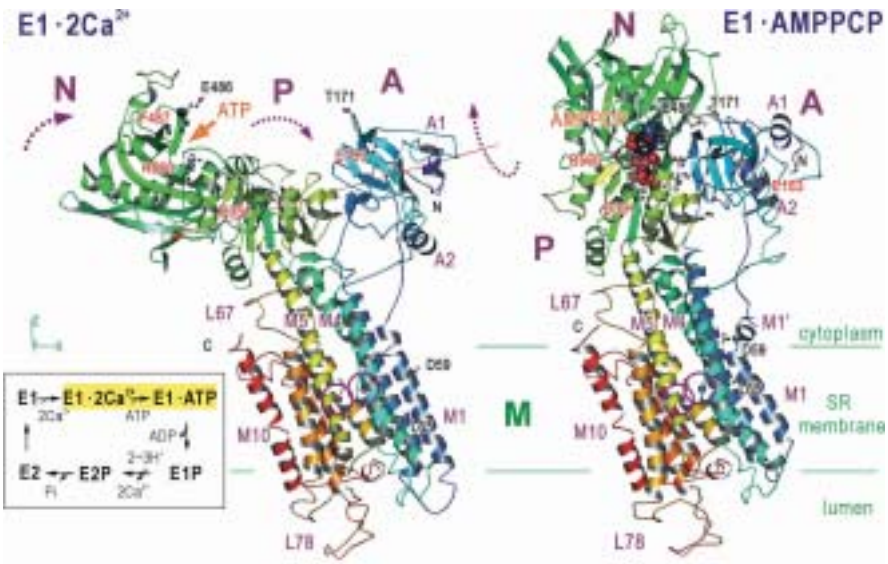

Fig. 1. Structures of Ca^{2+}-ATPase of sarcoplasmic reticulum in the presence of Ca^{2+} with (E1·AMPPCP) and without (E1·2Ca^{2+}) AMPPCP, a non-hydrolysable ATP analogue. Color changes gradually from the N terminus (blue) to the C terminus (red). Two purple spheres (circled) in the membrane domain represent bound Ca^{2+} ions. AMPPCP is shown in space fill. Large arrows in E1·2Ca^{2+} indicate the directions of movements of the cytoplasmic domains (A, N and P) in E1·2Ca^{2+} →E1·AMPPCP; the axis of tilting of the A-domain is also specified (thin red line). Inset is a simplified reaction scheme; the two states compared here are shown with a yellow background.

these, the A-domain tilts by ~30° to pull up the M1-M2 helices (Fig. 1) and to strain the loop connecting to M3. This strain appears to be the driving force for another A-domain rotation to open the lumenal gate.

The M1 helix is pulled up and largely bent at the membrane surface. The functional meaning of this movement is evident. In E1·2Ca^{2+}, which represents the state after the binding of both Ca^{2+}, Glu309, the gating residue, caps the Ca^{2+} in site II (Fig. 2(a)). But a large empty space around it will allow Glu309 to adopt other side chain conformations and the site II Ca^{2+} to escape. In E1·AMPPCP, this space is occupied by M1 and Leu65 makes van der Waals contacts with the Glu309 side chain (Fig. 2(b)). As a result, the conformation of Glu309 is locked and bound Ca^{2+} cannot escape.

Thus, Ca^{2+}-ATPase changes the orientation of the A-domain to regulate the cytoplasmic gate of Ca^{2+}-binding pathway by moving, primarily, the M1 helix. This means that the interfaces between the A-domain and two other cytoplasmic domains are critically important and adjusted during the reaction cycle. ATP works as the principal modifier of the interfaces together with Mg^{2+}.

The data were obtained at beamline **BL41XU.**

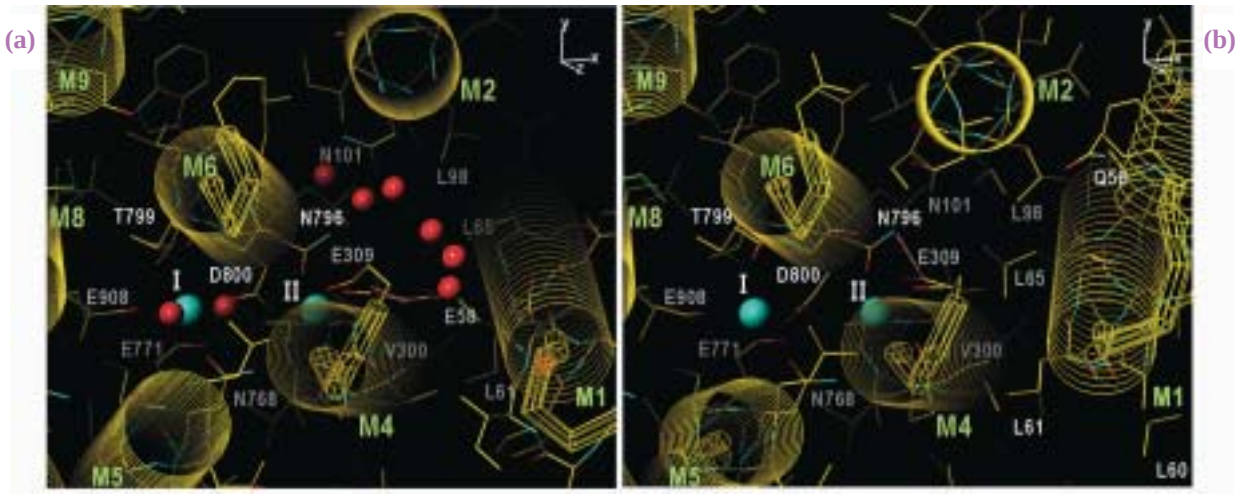

Fig. 2. Transmembrane Ca^{2+}-binding sites (I and II) in E1·2Ca^{2+} **(a)** and E1·AMPPCP **(b)**, viewed from the cytoplasmic side. Cyan spheres represent bound Ca^{2+}; red spheres in **(a)** indicate water molecules in the crystals.

Chikashi Toyoshima* and Tatsuaki Mizutani

Institute of Molecular and Cellular Biosciences,
The University of Tokyo

*E-mail: ct@iam.u-tokyo.ac.jp

References

[1] C. Toyoshima, M. Nakasako, H. Nomura and H. Ogawa: Nature **405** (2000) 647.
[2] C. Toyoshima and H. Nomura: Nature **418** (2002) 605.
[3] *C. Toyoshima and T. Mizutani: Nature **430** (2004) 529.*

Crystal Structure and Function of MexAB-OprM Antibiotic Efflux Pump Subunits of *Pseudomonas aeruginosa*

Emergence of bacteria resistance to many different antibiotics and of drug-resistant cancer cells is a great concern in human health. An important factor contributing to the multidrug resistance would be the drug efflux pump, which lowers the intracellular drug concentration by exporting incoming chemotherapeutic agents across the membranes. *Pseudomonas aeruginosa* often infects hospitalized patients whose immune activity is lowered by some reasons, and such an infection is often life-threatening. The multi-antibiotic resistance of this organism is largely attributable to the production of multidrug efflux pumps.

The MexAB-OprM efflux pump of *P. aeruginosa* consists of three membrane-bound subunits, MexA, MexB and OprM, anchored to the inner and outer membranes, respectively. The MexB subunit crosses the cytoplasmic membrane 12 times, selects and transports the antibiotics [1]. The crystal structure of an MexB homologue, AcrB of *Escherichia coli*, showed that the protein consists mainly of three domains: the membrane-spanning domain, the pore domain and the TolC-docking domain [2]. The OprM subunit is the outer membrane-anchored lipoprotein that is assumed to form the antibiotic discharge duct across the outer membrane. The MexA subunit anchors to an inner membrane via N-terminal fatty acids [3]. Removal of fatty acids liberates a protein from the membrane and the protein becomes freely soluble in aqueous solutions. Therefore, MexA is assumed to link MexB and OprM, helping the assembly of the functional pump unit. For better understanding of the role of the antibiotic efflux pump subunits, we analyzed the X-ray crystal structures of OprM and MexA (**BL44XU**).

[OprM structure] We studied the X-ray crystallographic structure of OprM at 2.56 Å resolution [4]. The overall structure exhibited a trimeric assembly of the OprM monomer that consisted mainly of two domains: the membrane-anchoring β-barrel and the cavity-forming α-barrel (Fig. 1). OprM anchored to the outer membrane via two modes of membrane insertions. One was via covalently attached N-terminal fatty acids and the another via the β-barrel structure consensus on intrinsic outer membrane proteins. The β-barrel had a pore with a diameter of about 6 to 8 Å, which is not sufficiently large to accommodate the exit of any antibiotics (Fig. 1). The α-barrel was about 100 Å long formed mainly by a bundle of α-helices that formed a solvent-filled cavity of about 25,000 $Å^3$. The proximal end of the cavity was tightly sealed, thereby not permitting the entry of any molecule. This structure showed that the resting state of OprM had a small outer membrane pore and a

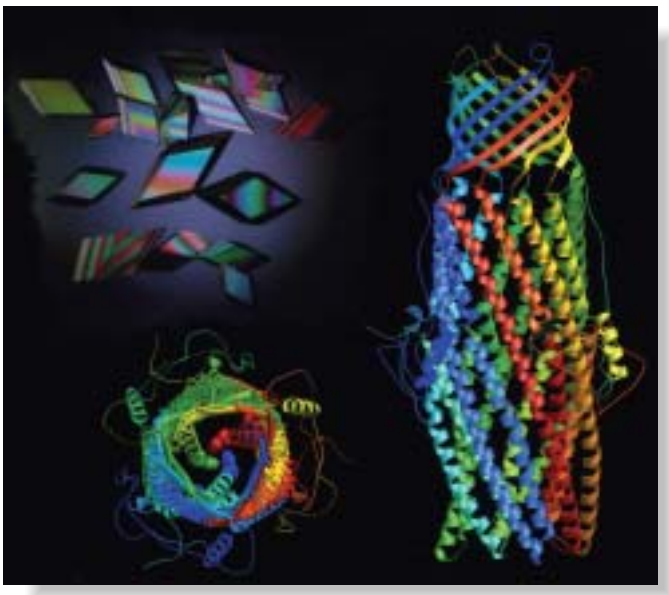

Fig. 1. Structure of OprM. Right figure illustrates a side view of the OprM trimer. The monomer is colored in a gradient from yellow to red. Left-lower image illustrates the top view of the trimer featuring an open top and a tightly sealed bottom.

tightly closed periplasmic end, which sounds plausible because the protein should not allow free access of antibiotics.

[MexA structure] We showed the X-ray crystallographic structure of MexA at a resolution of 2.40 Å [5]. The global MexA structure showed unexpected new features with a spiral assembly of six and seven monomers that were joined together at one end by a pseudo two-fold image (Fig. 2). The monomer showed a new protein structure with a tandem arrangement consisting of at least three domains and presumably one more. (i) The rod domain had a long hairpin of twisted coiled-coil that extended to one end. (ii) The second domain adjacent to the rod α-helical domain was globular and constructed by a cluster of eight short β-sheets. (iii) The third domain located distal to the α-helical rod was globular and composed of seven short β-sheets and one short α-helix. The structure suggests that MexA functions as a molecular clump connecting MexB and OprM.

On the basis of these results, we constructed a model of the MexAB-OprM pump assembly (Fig. 3). The pump assembly cross bridge the inner and outer membranes. The substrates taken up by MexB may be injected into the OprM cavity by the energy of proton motive force across the inner membrane. MexA clumps the MexB and OprM. OprM forms the antibiotic-ejecting duct.

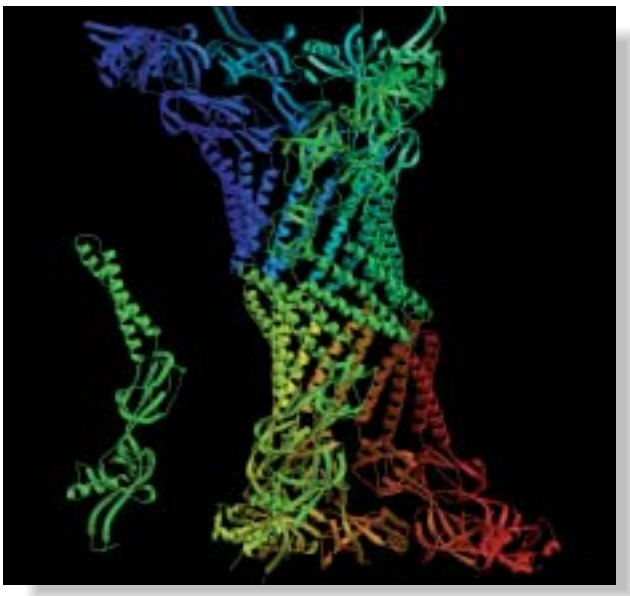

Fig. 2. Crystal structure of MexA. Right figure illustrates a tridecamer of MexA and left figure is a monomeric form.

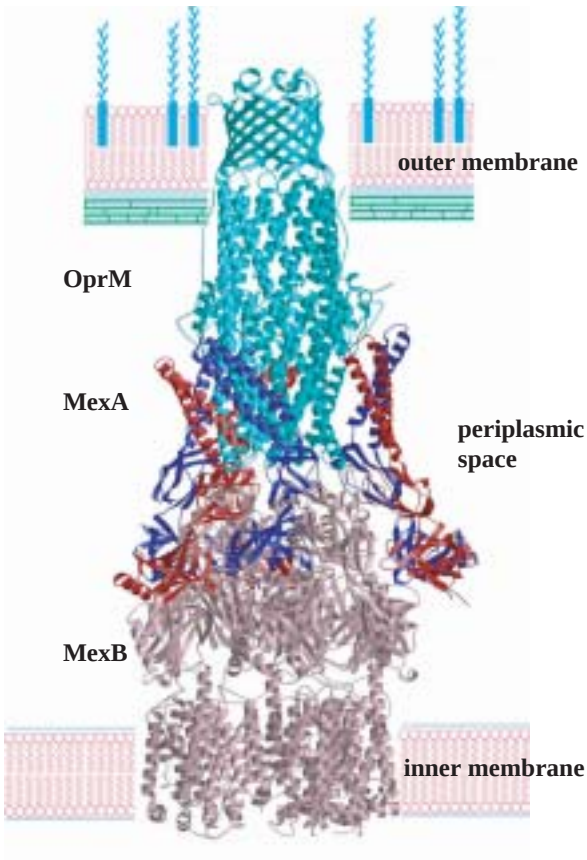

Fig. 3. Proposed assembly model of MexAB-OprM antibiotic efflux pump.

Taiji Nakae [a,b]

(a) Tokai University School of Medicine
(b) The Kitasato Institute

E-mail: nakae@is.icc.u-tokai.ac.jp

References

[1] S. Eda *et al.*: J. Biol. Chem. **278** (2003) 2085.
[2] S. Murakami *et al.*: Nature **419** (2002) 587.
[3] H. Yoneyama *et al.*: J. Biol. Chem. **275** (2000) 4628.
[4] *H. Akama, M. Kanemaki, M. Yoshimura, T. Tsukihara, T. Kashiwagi, H. Yoneyama, S. Narita, A. Nakagawa and T. Nakae: J. Biol. Chem.* ***279*** *(2004) 52816.*
[5] *H. Akama, T. Matsuura, S. Kashiwagi, H. Yoneyama, T. Tsukihara, A. Nakagawa and T. Nakae: J. Biol. Chem.* ***279*** *(2004) 25939.*

Low-spin Heme of Cytochrome *c* Oxidase as Driving Element of Proton

Cytochrome *c* oxidase is the terminal enzyme of the respiratory chain, which reduces O_2 to water molecules. The O_2 reduction site of mitochondrial cytochrome *c* oxidase is composed of a high-spin heme (heme a3) and a copper ion (CuB). The protons used for water formation from O_2 are transferred from the inside of the mitochondrial inner membrane (the matrix space) through two hydrogen bond networks known as the K- and D-pathways (Fig. 1). In addition to the transfer of protons to the O_2 reduction site, proton pumping from the matrix space to the intermembrane space through the enzyme results in a proton motive force required to drive ATP synthase.

The X-ray structures of bovine heart cytochrome *c* oxidase in the fully oxidized and reduced states at 2.3 and 2.35 Å resolution, respectively, indicate the movement of Asp51 of subunit I (the largest subunit containing heme *a* and the O_2 reduction site [1]), from the interior of the protein to the intermembrane surface upon the reduction of the enzyme [2]. In the oxidized state, Asp51 makes contact with the matrix space via a hydrogen bond network with a channel in which water molecules in the matrix space are accessible (H-pathway) (Fig. 2). These structures are highly indicative of a proton-pumping event occurring at Asp51 [2].

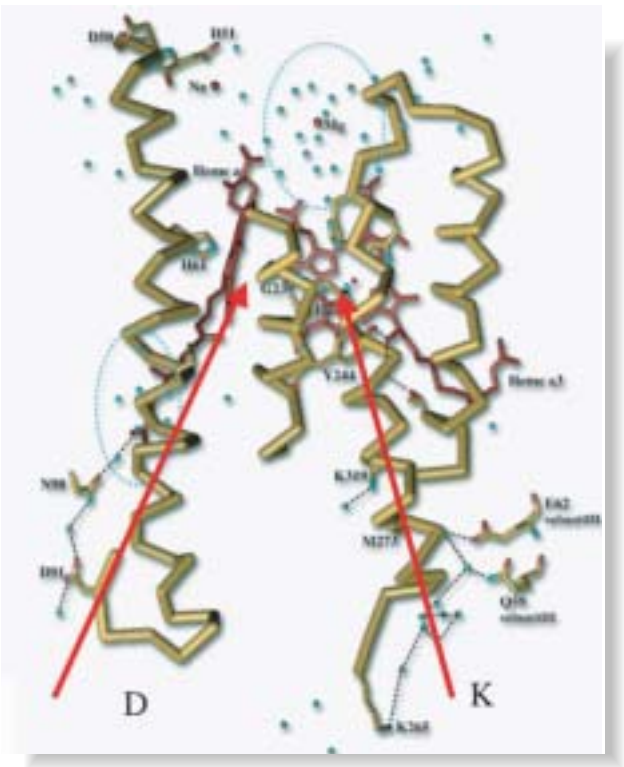

Fig. 1. Protons are transferred to the O_2 reduction site through two hydrogen bond networks known as the K- and D-pathways.

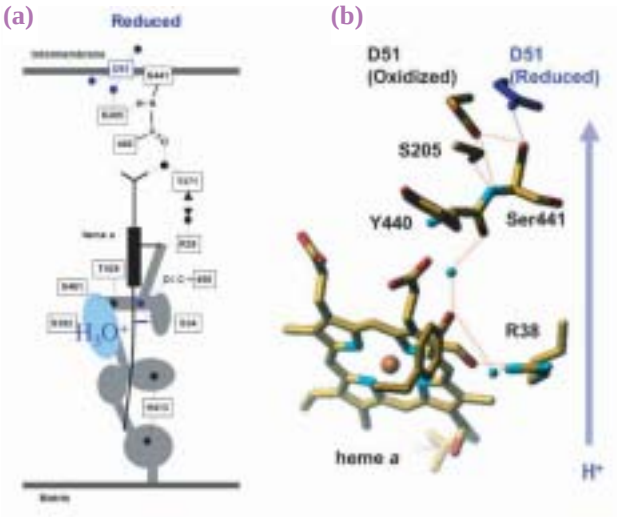

Fig. 2. **(a)** Schematic drawing of H-pathway through which protons are pumped, and **(b)** structure of upper half of H-pathway.

However, the proton-pumping proposal is not yet widely accepted because plant and bacterial enzymes do not have an analogous Asp51 (bovine numbering) residue and because a D-pathway mutation results in a bacterial enzyme as described below. Mutations of amino acid residues within the D-pathway cause a decrease in proton pumping efficiency and O_2 reduction activity [3], observations apparently consistent with a process wherein proton transfer for proton pumping occurs via the proton pathway for water molecule formation. Furthermore, no mechanisms for driving the proton pump at Asp51 have yet been determined. The mutation of Asp51 would provide one of the most direct methods of probing the function of Asp51. However, the site-directed mutagenesis of subunit I, a large transmembrane subunit encoded by a mitochondrial DNA, has not been attempted due to expected technical difficulties [4].

We successfully investigated the role of the H-pathway by X-ray crystallography (**BL44XU**), infrared spectroscopy and site-directed mutagenesis [5]. The X-ray structures of bovine cytochrome *c* oxidase in the oxidized and reduced states at 1.8 and 1.9 Å resolutions, respectively, indicate redox-coupled changes in the conformation of the heme *a* hydroxyfarnesylethyl group (Fig. 3), resulting in an alteration of the capacity of a water channel that connects the matrix surface with the heme a formyl group. A redox-coupled change in the capacity of the water channel of the H-pathway, induced by the hydroxyfarnesylethyl group of the low-spin heme, suggests that the channel functions as an effective proton-collecting region.

The hydrophobicity of the Asp51 environment near the intermembrane surface is also altered. Infrared spectroscopy results indicate that the conformation of Asp51 is controlled only by the oxidation state of the low-spin heme. A hydrogen bond network connects Arg38 with Asp51. Furthermore, an Asp51Asn mutation abolishes the proton-pumping function without impairing O_2 reduction activity. These results indicate that the low-spin heme drives the proton-pumping process via the H-pathway.

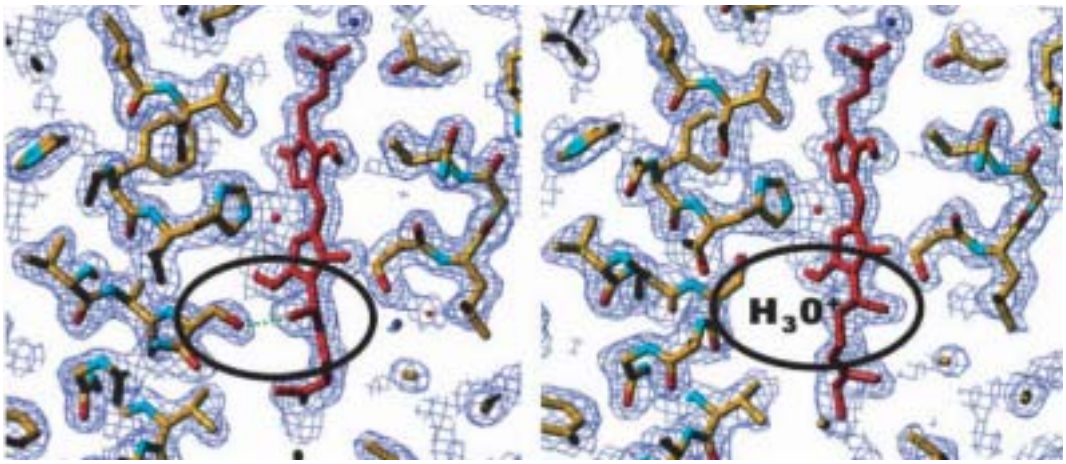

Fig. 3. Structural change of heme *a* hydroxyfarnesylethyl group upon reduction of heme.

Tomitake Tsukihara

Institute for Protein Research, Osaka University

E-mail: tsuki@protein.osaka-u.ac.jp

References

[1] T. Tsukihara *et al.*: Science **272** (1996) 1136.
[2] S. Yoshikawa *et al.*: Science **280** (1998) 1723.
[3. R. B. Gennis: Biochim. Biophys. Acta **1365** (1998) 241.
[4] M.G. Claros *et al.*: Eur. J. Biochem. **228** (1995) 762.
[5] *T. Tsukihara, K. Shimokata, Y. Katayama, H. Shimada, K. Muramoto, H. Aoyama, M. Mochizuki, K. Shinzawa-Itoh, E. Yamashita, M. Yao, Y. Ishimura and S. Yoshikawa: Proc. Natl. Acad. Sci. USA **100** (2003) 15303.*

Crystal Structure of C-terminal Clock-oscillator Domain of KaiA from *Thermosynechococcus elongatus* BP-1

Circadian rhythms, the daily activity cycles exhibited by most organisms, are sustained even in the absence of outside cues. Organisms acquired the rhythms on the genome to match the rotation of the earth by the process of revolution. The biological clock, which is the clock including the body of an organisms, oscillates the circadian rhythms. For example, the oscillation of waking up and sleeping of humans or other organisms is regulated by the biological clock. However, our biological knowledge obtained to date has not yet explained the properties of the biological clock, which are a time constant of ~24 hours and temperature compensation [1].

Cyanobacteria are the most primitive organisms known to exhibit circadian rhythms. The *kaiABC* circadian clock gene cluster in *Synechococcus* sp. strain PCC7942 consists of two operons, *kaiA*, and *kaiBC*. The KaiA protein, which is the *kaiA* product, enhances *kaiBC* promoter activity, and *kaiBC* is repressed by the KaiC protein [2] (Fig. 1(a)). KaiA, KaiB and KaiC proteins, which are necessary to oscillate the rhythms, can directly interact with one another. This interaction has been proposed to be involved in the mechanism underlying circadian rhythms as feedback loop models. Many amino acid substitutions in KaiA, KaiB and KaiC that affect the period length and amplitude of circadian rhythms have been isolated, but the roles of the altered residues have not been elucidated. Therefore, we have started to study the properties and the three-dimensional structure of the KaiA protein.

The limited proteolysis of KaiA from *Themosynechococcus elongatus* BP-1 with trypsin, V8 protease and chymotrypsin showed that KaiA is composed of three regions, which are the N-teminal domain (residue 1-138), central domain (139-173) and C-terminal domain (174-283). In 11 cyanobacteria strains, the C-terminal domain of KaiA shows sequence similarity, whereas the N-terminal and central domains show little similarity, suggesting that the N-terminal and central domains of KaiA may not be fundamental to the clock function. In particular, Anabaena KaiA (110 amino acids) retains only the portion corresponding to the C-terminal domain. Cyanobacteria usually oscillate the circadian rhythms, whereas a *kaiA*-null mutant strain of *Synechococcus kaiA* gene exhibits an arrhythmic phenotype. In order to understand the function of each domain of KaiA, we examined the circadian rhythms when various regions of the *kaiA* gene were transferred into the truncated *Synechococcus kaiA* gene. The C-terminal domain of KaiA showed rhythms although the amplitude of the rhythms was reduced and the period lengthened to about 40 hours. The central and C-terminal domains of KaiA modulated the 24 hours rhythms, suggesting that the central domain has a period-adjuster function. Thus, the C-terminal domain of KaiA has the fundamental clock-oscillator function. The amplitude of the rhythms of full-length KaiA was larger than those of the central and C-terminal domains of KaiA, suggesting that the N-terminal domain has an amplitude-amplifier function (Fig. 1(b)). In addition, the C-terminal domain of KaiA contributes to the dimerization of KaiA, KaiA - KaiC binding, and the enhancement of KaiC phosphorylation [3].

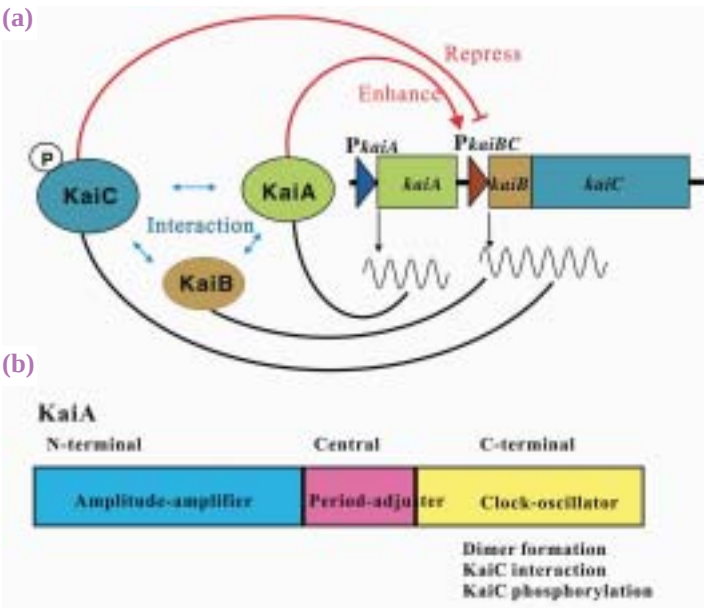

Fig.1. **(a)** Schematic drawing of circadian rhythms of Cyanobacteria. **(b)** Function of KaiA domain.

We attempted to crystallize the full-length KaiA and the C-terminal domain of KaiA from *T. elongates*, and obtained only the C-terminal domain crystals. X-ray diffraction data were collected at the RIKEN Structural Genomics Beamlines **BL26B1** and **BL26B2**. The crystal

structure of the C-terminal clock oscillator domain of KaiA was determined at 1.8 Å resolution by the multiwavelength anomalous dispersion method (MAD) [3]. As shown in Fig. 2(a), the subunit structure forms a right-handed superhelix comprising six helices. The four-helix bundle consists of two sets of antiparallel helices. The KaiA C-terminal domain forms a dimer whose interface mainly consists of the h6 helix. The concave surface formed by the dimer is composed of three helices (h3, h6 and the adjacent h4 of the second subunit). In the 11 strains examined, the 23 conserved residues locate almost in the interior of a subunit or on the dimer interface and are involved in maintaining the stability of the structure.

As shown in Fig. 2, the conserved residue His270 is at the center of the concave dimer surface, extending the side chains outside the concavity. The KaiA (174-283) H270A mutant showed KaiC-binding activity and KaiC phosphorylation enhancement of about 30% of the wild type, and the correct folding of H270A was identified by CD spectrum analysis. In addition, we analyzed the *in vivo* rhythm functions of the residue using a mutated *Synechococcus kaiA* gene and *Synechococcus* host cells. His270 of *T. elongates* KaiA corresponds to His271 of *Synecchococcus* KaiA. As shown in Fig. 3, the H271A KaiA mutant of *Synechococcus* could not oscillate the circadian rhythms. Thus, His271 of *Synechococcus* KaiA (His270 of *T. elongates* KaiA) is crucial for the generation of circadian oscillations. In the present work we identified the residue directly involved in the circadian rhythms for the first time.

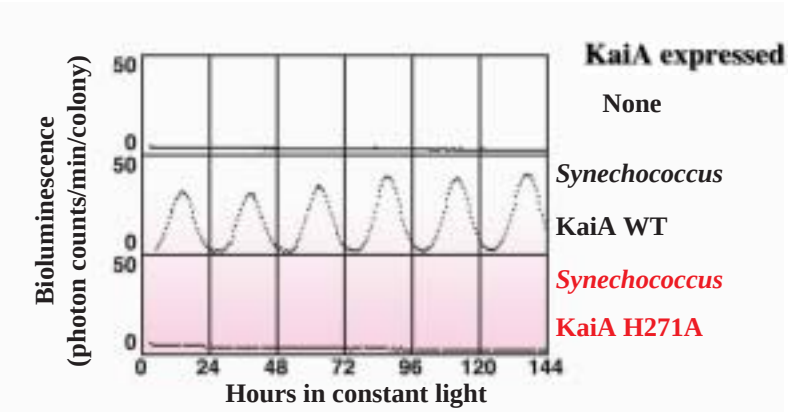

Fig. 3. Bioluminescence rhythms of *Synechococcus* host cells that expressed no KaiA (top), wild-type KaiA (middle) and H271A KaiA mutant (bottom) [3].

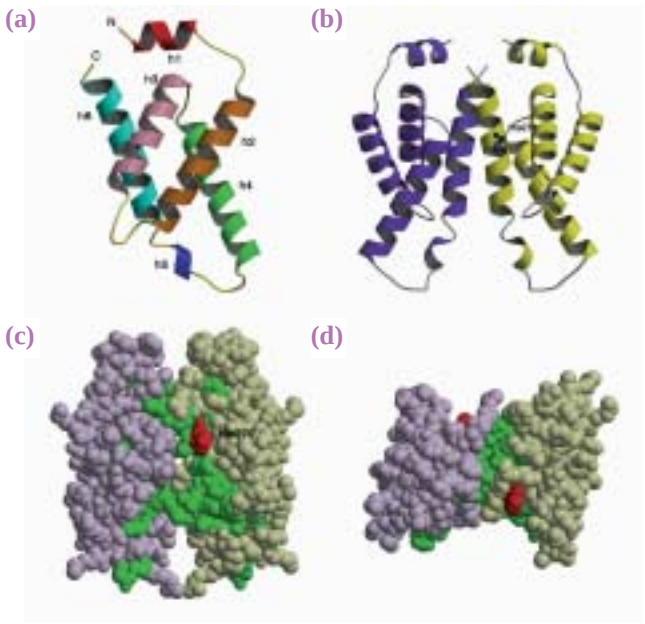

Fig. 2. Crystal structure of KaiA C-terminal domain. Ribbon representation of subunit **(a)** and dimer structure **(b)**. Space filling model of dimer **(c)** and view of **(c)** from different angle **(d)**. The 23 residues conserved in the 11 strains are green, except for His270, which is red [3].

Toru Nakatsu [a,b]

(a) Graduate School of Pharmaceutical Sciences, Kyoto University
(b) SPring-8 / RIKEN

E-mail: nakatsu@pharm.kyoto-u.ac.jp

References

[1] S.S. Golden and S.R. Canales: Nature Reviews Microbiology **1** (2003) 191.
[2] M. Ishiura *et al.*: Science **281** (1998) 1519.
[3] *T. Uzumaki, M. Fujita, T. Nakatsu, F. Hayashi, H. Shibata, N. Itoh, H. Kato and M. Ishura: Nat. Struct. Mol. Biol.* ***11*** *(2004) 623.*

Crystal Structure of Human DNA Recombinase, Dmc1

Meiosis is a cell division process specifically occurring in germ cells (testis and ovary) of eukaryotes. During the cell division, homologous chromosomes pair and parts or all of the genes are shuffled between chromosomes, a process called homologous recombination (Fig. 1) [1]. Eukaryotes obtain genetic variation by this method. Homologous recombination is also essential for the repair of DNA damage, thus, for the cell to function properly, homologous recombination is important. We have focused on the protein that is responsible for the homologous recombination in germ cells, namely Dmc1, and have succeeded in crystallizing the full-length human protein [2]. The crystal was used to determine the three-dimensional structure of Dmc1 at atomic resolution. Based on this structure, we have studied the homologous recombination promoted by Dmc1.

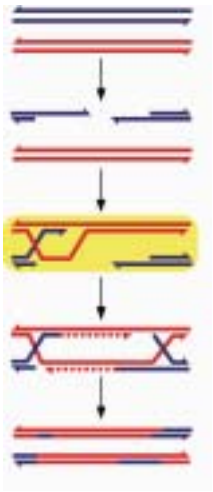

Fig. 1. The model of homologous recombination in meiosis.

The human Dmc1 protein, consisting of 340 amino acids, binds both single-stranded DNA and double-stranded DNA, and promotes the homologous-pairing reaction, a key step of homologous recombination. We overexpressed the Dmc1 protein in *Escherichia coli* and purified the Dmc1 protein using several chromatographic techniques. A single crystal (100 μm × 600 μm × 600 μm) of Dmc1 was obtained, and the crystal structure of Dmc1 was successfully determined using data collected at the synchrotron radiation of the RIKEN Structural Biology II beamline **BL44B2**.

The human Dmc1 protein is a homolog of the *E. coli* RecA protein. Studies have shown that the bacterial RecA protein forms a helical filament structure and promotes homologous pairing. Contrary to the extensive sequence similarity between Dmc1 and RecA, we show that Dmc1 functions as a double-ring structure. The ring consists of eight subunits, and two rings are stacked in a bipolar nature with a diameter of 130 Å and a height of 85 Å (Fig. 2).

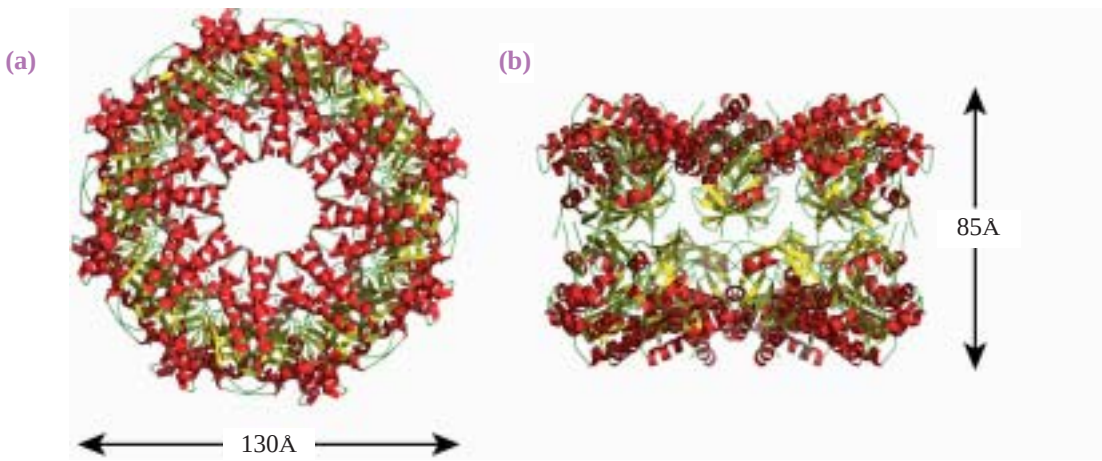

Fig. 2. Crystal structure of Dmc1. Dmc1 double-ring structure viewed from top **(a)** and side **(b)**.

The Dmc1 double-ring structure contains two open-ended passages: one at the center of the ring (about 30 Å in diameter) and the other between the stacked rings (about 15 Å in diameter). On the basis of alanine-scanning mutagenesis studies, the central channel was shown to bind double-stranded DNA, while the passage along the side of the ring that leads to the central channel was shown to bind single-stranded DNA (Fig. 3(a)). These results formed the basis of the model of the ternary complex containing Dmc1, single-stranded DNA, and double-stranded DNA. In this model, homologous pairing occurs at the center of the double ring, and the recombined DNA is spooled out of the passages (Fig. 3(b)). This mechanism contrasts with those proposed for the helical filament forming RecA and Rad51 proteins. Hence, the recent studies suggest that there are at least two recombination mechanisms utilized in germ cells. Such multiple mechanisms may be essential for cells to properly divide during meiosis.

Since homologous recombination is the mechanism underlying gene therapy and genetic engineering, understanding the structural and biochemical properties of eukaryotic recombinases is essential for improving these technologies. The present study may provide a foundation for modifying the activity of Dmc1 recombinase, leading to an increased recombination frequency in eukaryotic cells. Therefore, structural information on Dmc1 recombinase may contribute to the advancement of gene therapeutic and transgenic technologies.

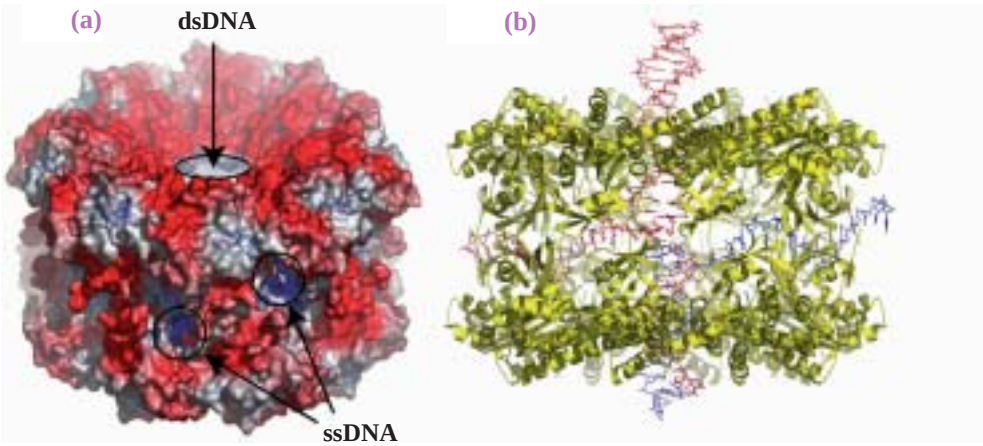

Fig. 3. Model of a homologous pairing intermediate complex of Dmc1, ssDNA, and dsDNA. **(a)** Important region for ssDNA and dsDNA binding on surface of double ring. **(b)** The Dmc1 double ring is a functional unit that could be essential for efficient binding to ssDNA and dsDNA. dsDNA is shown to pass through the central channel, while ssDNA is shown to pass through the channel formed as result of the stacking of two Dmc1 rings. The search and pairing of two homologous sequences could occur at the center of the Dmc1 double ring.

Takashi Kinebuchi[a,*], Hitoshi Kurumizaka[a,b] and Shigeyuki Yokoyama [a,c,d]

(a) GSC / RIKEN
(b) School of Science and Engineering, Waseda University
(c) SPring-8 / RIKEN
(d) Graduate School of Science, The University of Tokyo

*E-mail: kine@gsc.riken.go.jp

References

[1] L.S. Symington: Mol. Biol. Rev. **66** (2003) 630.
[2] *T. Kinebuchi, W. Kagawa, R. Enomoto, K. Tanaka, K. Miyagawa, T. Shibata, H. Kurumizaka and S. Yokoyama: Mol. Cell **14** (2004) 363.*

Crystal Structure of Elongation Factor P from *Thermus thermophilus* HB8

Genetic information encoded in messenger RNA is translated into protein by the ribosome, which is a large ribonucleoprotein complex. It has been clarified that diverse proteins called translation factors and RNAs are involved in genetic translation. Translation elongation factor P (EF-P) is one of the translation factors and stimulates the first peptidyl transferase activity of the ribosome [1]. EF-P is conserved in bacteria, and is essential for their viability. Eukarya and Archaea have an EF-P homologue, eukaryotic initiation factor 5A (eIF-5A).

We succeeded in the determination of the crystal structure of EF-P from *Thermus thermophilus* HB8 at 1.65 Å resolution, using beamline **BL45PX** [2]. The crystallographic asymmetric unit contains two nearly identical EF-P monomers (Fig. 1(a)). EF-P is a β-rich protein containing 16 β-strands, and is composed of three β-barrel domains (domains I, II, and III) (Fig. 1(b)). These domains are arranged in a string with an approximately 95° bending at domain II, to form a unique L-shaped structure of EF-P (Fig. 1(c)).

The most noteworthy finding in the present study is a similarity in the overall shape between EF-P and tRNA molecules (Figs. 1(a,b,c)). In general, overall shapes and sizes of the tRNA molecules are well conserved, as they must bind to the same binding site(s) on the ribosome. The shape and the size of the EF-P molecule are comparable to those of tRNA molecules. Several proteins were found to possess domain(s) similar to a portion of tRNA, by which they interact with the ribosome. The C-terminal domain of elongation factor G (EF-G) has a shape similar to that of the anticodon-stem loop in the elongation factor Tu (EF-Tu)·tRNA·GDPNP ternary complex. Release factor 2 (RF2) and ribosome recycling factor (RRF) were also found to possess a protruding domain, by which they are believed to bind to the ribosome A site [3]. In contrast with these factors, the entire structure of the EF-P mimics the overall shape of the tRNA molecule (Fig. 2). In addition, it is notable that EF-P is an acidic protein and most of its surface is negatively charged. The overall tRNA-like shape of the EF-P molecule and the charge distribution seem to be suitable for this protein to bind to the ribosome by spanning two subunits. Therefore, EF-P may bind to the tRNA-binding site(s) on the ribosome by mimicking the tRNA shape.

It is interesting that domains II and III of EF-P share a remarkable structural similarity to each other; they are superposed on each other with rms of 1.2 Å for 31 Cα atoms (Fig. 3). The crystal structure of the eukaryotic/archaeal EF-P homologue, eIF-5A, was reported. It is shorter than EF-P in its amino-acid sequence; therefore, it consists of only two domains (the N- and C-domains) (Fig. 4). The N-domain of eIF-5A corresponds to EF-P domain I, while the

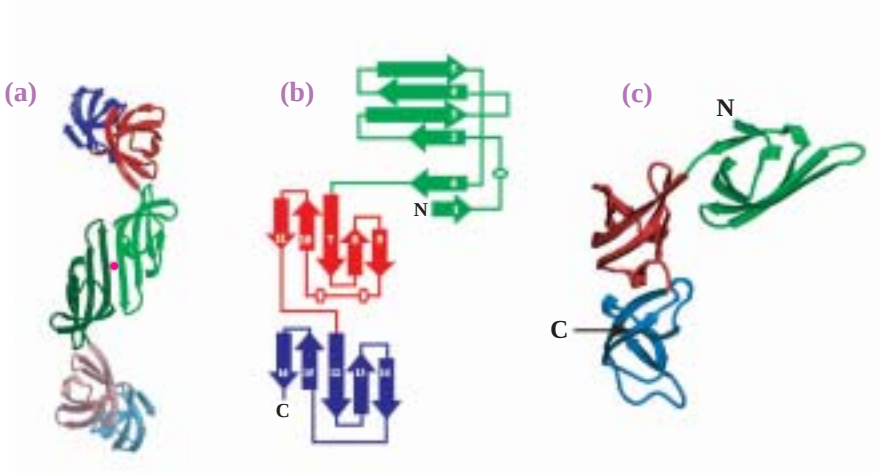

Fig. 1. Structure of *T. thermophilus* EF-P; **(a)** Ribbon diagram showing twofold dimer presents in asymmetric unit. **(b)** Topology diagram of *T. thermophilus* EF-P structure. The arrows represent β sheets and the ellipses 310 helixes. Domains I, II and III are shown in green, red, and blue, respectively. **(c)** Ribbon presentation of *T. thermophilus* EF-P crystal structure.

C-domain is similar to either domain II or III of EF-P. This implies that the two homologous domains II and III of EF-P might be the results of internal domain duplication. On the other hand, it is possible that the C-domain of eIF-5A is formed by a deletion of an EF-P portion (β10 - β14), which is missing in eIF-5A.

Many questions about EF-P still remain. How does EF-P interact with the ribosome? How can it activate the peptidyltransferase of the ribosome? To answer these questions, further functional and structural studies are required.

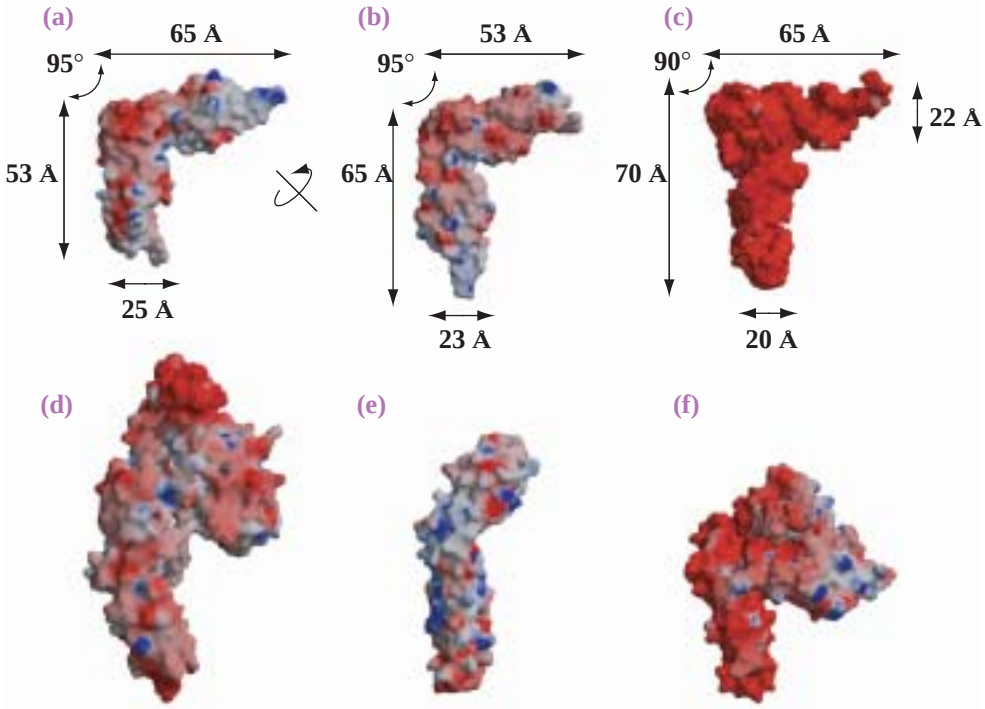

Fig. 2. Structure comparisons of tRNA **(c)** with EF-P (**a** and **b**), EF-G **(d)**, RRF **(e)** and RF2 **(f)**.

Fig. 3. Superimposition of backbone atoms of domains II and III of *T. thermophilus* EF-P. Domain II is in red and domain III in blue.

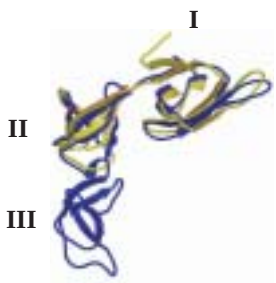

Fig. 4. Structure comparison of EF-P and eIF-5A. *T. thermophilus* EF-P is in blue and *M. jannaschii* eIF-5A in yellow.

Kyoko Hanawa-Suetsugu[a,*], Shun-ichi Sekine[a,b,c], Mikako Shirouzu[a,b] and Shigeyuki Yokoyama[a,b,c]

(a) RIKEN Genomic Sciences Center
(b) SPring-8 / RIKEN
(c) Department of Biophysics and Biochemistry, The University of Tokyo

*E-mail: suetsugu@gsc.riken.go.jp

References

[1] M.C. Ganoza *et al.*: Microbiol. Mol. Biol. Rev. **66** (2002) 460.
[2] *K. Hanawa-Suetsugu, S. Sekine, H. Sakai, C. Hori-Takemoto, T. Terada, S. Unzai, J.R. Tame, S. Kuramitsu, M. Shirouzu and S. Yokoyama: Proc. Natl. Acad. Sci. USA **101** (2004) 9595.*
[3] R.V. de Brodersen: Nature Struct. Biol. **10** (2003) 78.

Anaerobic and Aerobic Structures of Ferredoxin II from *Desulfovibrio Gigas*

Microorganisms such as sulfate-reducing bacteria (SRBs) obtain energy for growth by transferring electrons from an electron donor to an electron acceptor, such as oxygen, nitrate, iron (III), manganese (IV), sulfate and carbon dioxide, during cellular respiration. During this process (electron transport chain), the electron acceptor is reduced and the electron donor is oxidized. Although they are still being considered as strictly anaerobes, when exposed to oxygen, SRBs are capable of surviving as well as taking advantage of the presence of oxygen in terms of energy conservation. In the presence of oxygen, a sulfate reducer, *Desulfovibrio gigas*, starts utilizing internal reserves of polyglucose, which is metabolized via the Embden-Meyerhof-Parnas pathway, thus generating NADH and ATP (Fig. 1) [1].

Ferredoxins (Fds), which are redox proteins containing iron and sulfur atoms, play a role in electron transfer processes related to the phosphoroclastic reaction and the reduction of sulfite by SRBs. These proteins of small molecular weight (~ 6 kDa) have low redox potentials, characteristic electronic spectra, and typical EPR signals. *D. gigas* has two forms of Fd, i.e., Fd I and Fd II. Fd I contains a single [4Fe-4S] cluster while Fd II contains one [3Fe-4S] cluster per molecule [2], and both proteins are composed of the same polypeptide chain of 58 amino acids. Fd I has a redox potential of 450 mV and Fd II exhibits an E_0' of -130 mV.

Most Fds exhibit the biological activity during the stimulation of hydrogen consumption with sulfite as a terminal electron acceptor or during hydrogen production from pyruvate. It has been shown that the tetraheme cytochrome c3 is an intermediate between hydrogenase and ferredoxin. In *D. gigas*, Fd I and Fd II function in different metabolic pathways. Fd I is required in the phosphoroclastic reaction in which hydrogen is evolved from the oxidation of pyruvate. Fd II also stimulates this phosphoroclastic reaction after a long lag phase when it is added to Fd-depleted *D. gigas* crude extract. Pyruvate can induce the conversion of the [3Fe-4S] cluster of *D. gigas* Fd II into the [3Fe-4S] cluster of Fd I in the presence of *D. gigas* crude cell extract. Purified Fd II can also be converted to Fd I following incubation with an excess amount of Fe^{2+} in the presence of dithiothreitol, demonstrating that the polypeptide chain of *D. gigas* Fd can accommodate both [3Fe-4S] and [4Fe-4S] clusters. The [3Fe-4S]/[4Fe-4S] interconversion previously found in *D. gigas* Fds indicated that transition metals, other than iron, could be incorporated into the center of the [3Fe-4S] cluster.

Both aerobic and anaerobic Fd II structures have been independently determined by the Fe-SAD method at beamline **BL12B2** and NSRRC [3]. The aerobic Fd II structure shows that the [3Fe-4S] cluster is bound to the polypeptide chain by three cysteinyl residues: Cys 8, Cys 14, and Cys 50. Residue Cys 11, a potential ligand for the fourth site of the [4Fe-4S] cluster, is twisted away from the cluster. A disulfide bridge between Cys 18 and Cys 42 is located where the second iron-sulfur cluster is found in other 2×[4Fe-4S] Fds. It was observed that this disulfide bridge can be opened during the reduction of Fd II. Furthermore, six additional zinc metal ions are observed at the highly

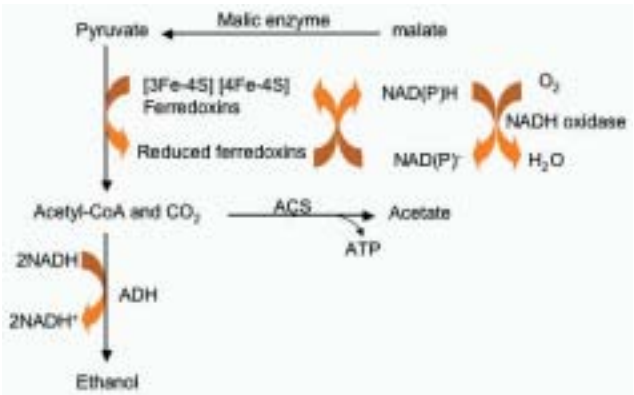

Fig. 1. Scheme of anaerobic metabolic pathways. The ferredoxins in *D. gigas* contain two cluster forms, [3Fe-4S] and [4Fe-4S].

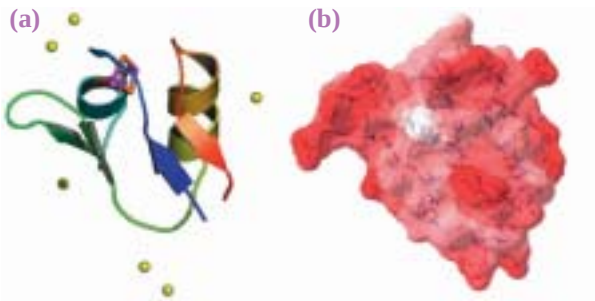

Fig. 2. **(a)** Overall structure of ferredoxin II. Beside the cluster, there are six Zn^{2+} ions bound around the structure. **(b)** The electrostatic potential of ferredoxin II shows negatively charged residues (deep red regions) predominating on the protein surface, which is important for metal binding.

negatively charged surface area ligated with Glu and Asp residues, implying the potential metal-binding sites for iron and other possible heterometal-containing cluster formation and conversion in the reduced state under the metal-abundant environment (Figs. 2(a,b)). In particular, two metal sites with the binding residues Asp6, Asp7, Glu12 and Glu16 are relatively close to the existing [3Fe-4S] cluster. Moreover, an additional [2Zn-2S] cluster bound by residues Glu26, Glu27, Asn35 and Asp37 is found (Fig. 3). Hence, two clusters form the electron transfer pathway with one [3Fe-4S] cluster inside and the other [2Zn-2S] cluster outside the protein.

The superimposition of aerobic and anaerobic Fd II structures shows an overall r.m.s. deviation of 1.01 Å over 58 amino acids with the most significant main-chain structural variations occurring at residues 25-28. The tide disulfide bond (Cys18-Cys42) existing in the aerobic structure shows the double conformations, which can be interpreted as the opening up of the covalent disulfide bond. Moreover, the iron-sulfur cluster geometries in the anaerobic structure are much different from those in the aerobic structure with the maximum increasing and decreasing changes of Fe-S bond distances by 0.15 Å and 0.14 Å, respectively. Hence, the longest and shortest interatomic distances of Fe-S bonds in the cluster are 2.18 Å and 2.36 Å, respectively, which is meaningful for high-resolution data (Figs. 4(a,b)). The influence of these bond variations might play a role in determining the electronic configuration of the reduced cluster. Thus, a comparison between aerobic and anaerobic structures at a high resolution provides valuable insights into different iron-sulfur cluster conversions and disulfide bridge conformations, which may reveal the unique iron storage function and electron transfer mechanism of Fd II from *D. gigas*.

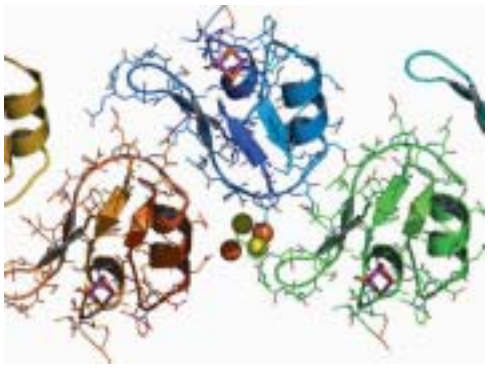

Fig. 3. An additional [2Zn-2S] cluster is bound by residues Glu26, Glu27, Asn35 and Asp37, which may involve the electron transfer pathway with the other existing [3Fe-4S] cluster inside.

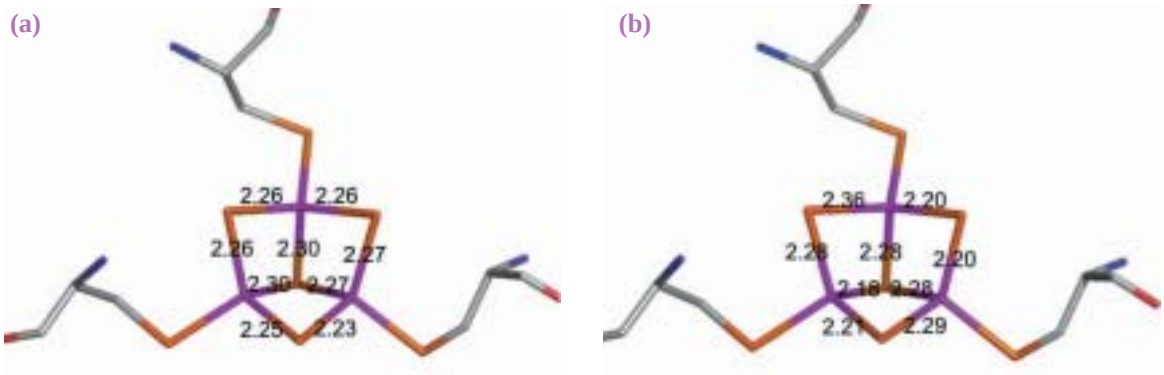

Fig. 4. (a) The iron-sulfur cluster geometries in the aerobic structure show similar Fe-S bond distances with the maximum deviation of 0.7 Å. (b) The anaerobic cluster geometries, however, are much different especially in the longest and shortest distances of 2.18 Å and 2.36 Å, respectively.

Yin-Cheng Hsieh[a,b], Ming-Yih Liu[a] and Chun-Jung Chen[a,c,*]

(a) Biology Group, National Synchrotron Radiation Research Center, Taiwan
(b) Department of Bioinformatics and Structural Biology, National Tsing-Hua University, Taiwan
(c) Department of Physics, National Tsing-Hua University, Taiwan

*E-mail: cjchen@nsrrc.org.tw

References

[1] P. Fareleira *et al.*: J. Bacteriol. **179** (1997) 3972.
[2] C.R. Kissinger *et al.*: J. Mol. Biol. **219** (1991) 693.
[3] *Y.-C. Hsieh, M.-Y. Liu, J. Le Gall and C.-J. Chen: Acta Cryst. D* ***61*** *(2005) 780.*

Collapse and Search Dynamics of Apomyoglobin Folding Revealed by Submillisecond Observations of α-Helical Content and Compactness

Proteins can quickly form their folded structures from randomly unfolded conformations through numerous intraprotein interactions among the mainchains and sidechains. Two important classes of interactions contribute to the stabilization of protein structures. The hydrogen-bonding interactions between the amide groups of mainchains mainly stabilize secondary structures. In contrast, the hydrophobic interactions between sidechains are mainly responsible for the stabilization of tertiary structures. The characterizations of protein-folding dynamics based on kinetic observations of secondary and tertiary structures are important for the understanding of intraprotein interactions that enable the protein-folding phenomena.

In this study [1], we chose apomyoglobin (apoMb) as a representative of α-helical proteins. At neutral pH, apoMb possesses seven helices labeled A~E, G and H, which amount to 55 % of α-helical content (f_H). The helices assemble into a globular shape with a radius of gyration (R_g) of 18.2 Å. The acid-unfolded state of apoMb is observed at pH 2.2, and possesses a small f_H (5 %) and a large R_g (29.7 Å). A simple model of the folding of apoMb assumes that the formation of helices precedes that of tertiary contacts, and implies the importance of local hydrogen bonding in the initial stage of the folding. However, the observation that no peptide fragments of the helix regions of apoMb except for H-helix can maintain helical conformations suggests a collapse of the mainchain before the formation of the secondary and tertiary structures. The difficulty in observing secondary and tertiary structures with a submillisecond resolution precludes us from resolving and analyzing these processes.

We have recently developed an experimental strategy to explore the submillisecond folding dynamics of proteins based on the combined use of a solution mixing device, circular dichroism (CD), and small-angle X-ray scattering (SAXS) [2,3], as shown in Fig. 1 (**BL45XU**). The CD signal monitored at 222 nm gives f_H. The SAXS method is useful for monitoring R_g and shape of proteins. We utilized the developed strategy to induce the folding of apoMb upon a pH jump from pH 2.2 to 6.0, and to observe the folding behavior of apoMb in the time domain from 300 μs to 1 s.

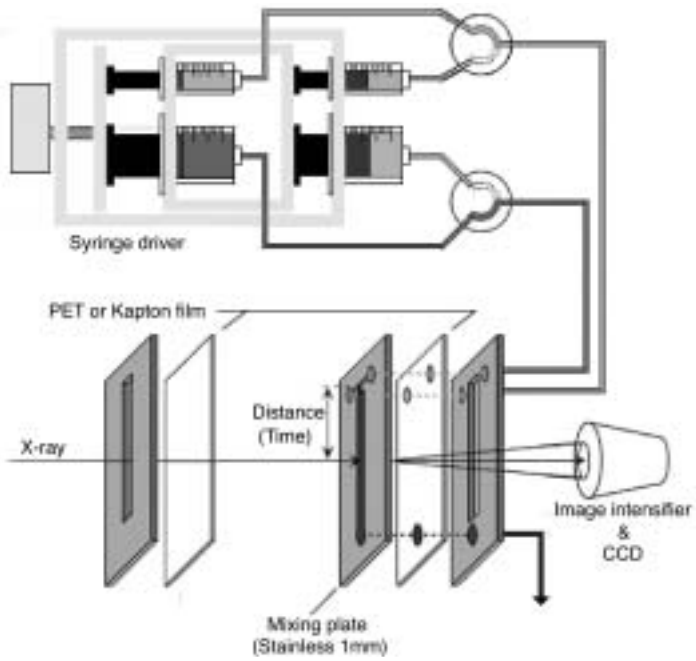

Fig. 1. Developed system for kinetic observations of protein folding by SAXS in submillisecond domain.

The first important finding of this study is the rapid and significant collapse and helix formation that occurs within 300 μs. The amount of collapsed domain estimated from SAXS measurements is more than 80%, indicating that the most of the mainchain is collapsed. The interpretation seems to contradict a previous consensus on the intermediate, i.e., that the collapsed domain is composed of only the A, G and H helices located in the N and C terminal regions [4]. We conclude that the initial collapse involves not only the terminal domain but also the central domain of apoMb. The second important observation of this study is the processes after the initial collapse, which can be described as the stepwise helix formation within the collapsed conformation. Interestingly, several previous reports on the folding of apoMb suggested changes in tertiary contacts in this time domain [5]. The folding after the initial collapse can be interpreted as a stepwise process during which apoMb searches for the correct tertiary contacts within the collapsed conformation to stabilize the helical structures.

We examined the folding trajectories of apoMb and cytochrome *c* (cyt *c*) in the conformational space defined by R_g and f_H as shown in Fig. 2. These are the only proteins without disulfide linkages whose folding dynamics have been characterized in terms of R_g and f_H. Both proteins similarly exhibit cooperative acquisitions of f_H and R_g after the initial collapse, indicating that the secondary and tertiary structures are largely formed together during the protein folding. However, while the folding of apoMb is characterized by a large-scale collapse, corresponding to ~50% of the overall change in R_g from the unfolded state to the native state, the initial collapse of cyt *c* corresponds to only ~ 35 % of the total. Thus, the comparison of the characterized trajectories of these proteins suggests the importance of the initial hydrophobic collapse for the conformational search during protein folding.

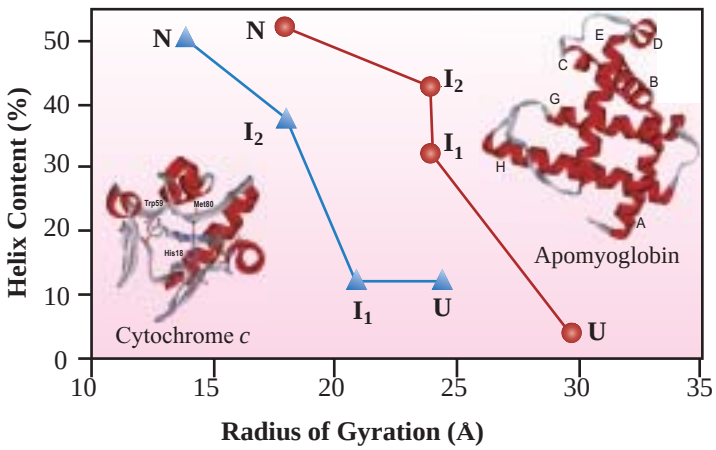

Fig. 2. Folding trajectories of apoMb and cyt *c* in two-dimensional conformational space defined by f_H and R_g.

Satoshi Takahashi[a,*], Takanori Uzawa[b] and Tetsuro Fujisawa[c]

(a) Institute for Protein Research, Osaka University
(b) Department of Molecular Engineering, Kyoto University
(c) SPring-8 / RIKEN

*E-mail: st@protein.osaka-u.ac.jp

References

[1] *T. Uzawa, S. Akiyama, T. Kimura, S. Takahashi, K. Ishimori, I. Morishima, T. Fujisawa: Proc. Natl. Acad. Sci. USA* ***101*** *(2004) 1171.*
[2] S. Akiyama *et al.*: Nature Struct. Biol. **7** (2000) 51.
[3] S. Akiyama *et al.*: Proc. Natl. Acad. Sci. USA **99** (2002) 1329.
[4] P.A. Jennings and P.E. Wright: Science **262** (1993) 892.
[5] M. Jamin and R.L. Baldwin: J. Mol. Biol. **276** (1998) 491.

Wide-angle X-ray Scattering can Reveal Hierarchical Map of Unfolding-refolding Transition of Protein

The X-ray solution scattering technique has a great advantage for studying nanoscale structures of biological materials and those complexes *in situ*. High-brilliant X-ray from a third generation synchrotron radiation (SR) source has been opening a new horizon not only in protein crystallography but also in protein structure analyses in solutions. How proteins fold into their native structures is still one of the main problems in structural biology. Numerous studies on protein folding have become possible because of advances in both experimental methods and theoretical approaches. The experimental resolutions in space and time have been also improving continuously. A time-resolved small-angle X-ray scattering (SAXS) study at a third-generation SR source demonstrates that the collapse process of a protein is now observable in time and spatial resolutions of > 1 ms and > 30 Å, respectively [1]. However, there exists some intrinsic difficulties in folding-kinetics studies for obtaining information on the intramolecular structures of proteins in solutions. Alternatively, the experimental demand for time resolution still competes with that for spatial resolution.

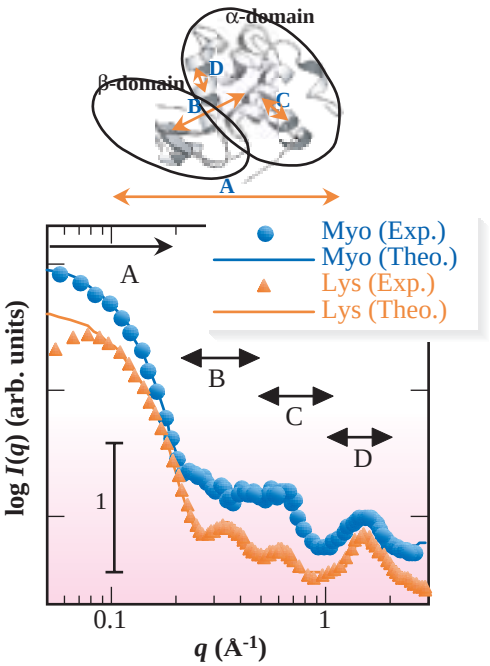

Fig. 1. Experimental and theoretical wide-angle X-ray scattering curves of hen-egg-white lysozyme (HEWL) and horse skeletal muscle myoglobin with schematic image of three-dimensional HEWL structure. The regions of A, B, C and D mostly correspond to the different hierarchical structural levels.

On the other hand, under equilibrium conditions, high-spatial-resolution scattering data of proteins in solutions can be measured using X-ray from a third generation SR source. We have shown that the experimental wide-angle X-ray scattering (WAXS) curves of several typical globular proteins in different structural classes (all α, all β, α+β and α/β) well reflect not only overall structures (molecular size and shape) but also intramolecular structures such as interdomain correlation, intradomain structures, and secondary structures [2]. Figure 1 shows the experimental and theoretical scattering curves of hen-egg-white lysozyme (HEWL) and horse skeletal muscle myoglobin with the schematic image of the three-dimensional HEWL structure. As shown in Fig. 1, the experimental SR-WAXS curves of the proteins are comparable to the theoretical curves in the full q-range calculated from the atomic coordinates of the proteins. The scattering curves in the regions of A, B, C and D mostly correspond to the different hierarchical structural levels of proteins, namely, the quaternary and tertiary structures, the interdomain correlation and intradomain structures, and the secondary structures including closely packed side chains, respectively.

Based on the above results, we have studied the hierarchical features of the thermal unfolding-refolding structural transitions of HEWL in the temperature range from 13 to 84 °C at pH 2.2, 3.1, 3.6, and 4.5 [3] at beamline **BL40B2**. We have successfully obtained high-statistic WAXS data on the reversible unfolding-refolding process in the spatial range from ~2 to ~125 Å, which covers all hierarchical structures of a small globular protein from the tertiary structure to the secondary structure (Fig. 2). We have found that the pH dependence of the thermal structural transition of HEWL is well characterized by the different hierarchical levels and the transition cooperatively among them. In this study we have presented a new hierarchical map depiction of unfolding-refolding transitions, which we call the structural hierarchy (SH) map. According to a method established previously [4], that is, scattering data at wide range of q values allowed us to determine molar fraction α ($\alpha \leq 1$) of the native-like protein structure defined by data at each q range, thus producing a map of the amount of the native-like protein structure as a function of q range, namely, as a function of the hierarchical level or resolution. This map can show the detailed feature of

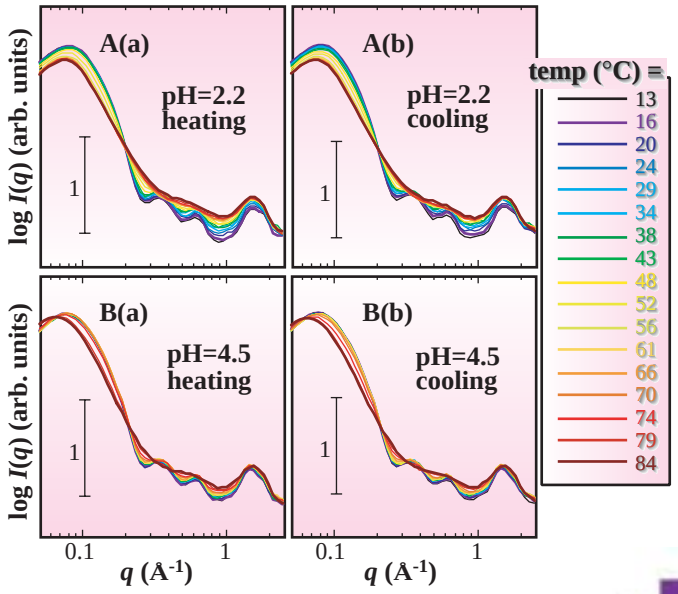

Fig. 2. Temperature dependence of WAXS curve $I(q)$ of HEWL (pH 2.2, A; pH 4.5, B). **(a)** heating (unfolding); **(b)** cooling (refolding).

the unfolding-refolding transition of a protein depending on various structural hierarchical levels. Figure 3 shows the SH maps during heating (unfolding) and cooling (refolding) at pHs 2.2 and 4.5, where we display the α values in rainbow colors and contour lines. In Fig. 3, the contour lines of α = 0.5 in the SH maps at different q values correspond to the transition midpoints for different hierarchical levels. The transition-midpoint temperatures $\boldsymbol{T}_{\mathbf{m}}$ of the α values below q = 0.2 Å^{-1} (tertiary structure) agree well with those determined by calorimetric measurements. Except for structural insensitive regions around q = 1 Å^{-1} and above q = 1.8 Å^{-1}, the density and slope of the contour lines depict the thermal stability and transition feature for each hierarchical level, which would relate to the transition cooperativeness among different hierarchical levels. At pH 4.5, the contour lines for all hierarchical levels are densely packed and parallel around the same transition midpoint temperature, suggesting that the collapse and regeneration of the native-like protein structure proceed concurrently or cooperatively for all hierarchical levels in a two-state transition. The SH map at pH 2.2 shows that the transition midpoints for each hierarchical levels greatly differ from each other, suggesting that the transition proceeds in a multistate manner. SH maps would be related to a hierarchical fine structure of protein-folding energetics such as a "folding funnel" or an "energy landscape."

Thus, SR-WAXS data of proteins obtained using X-ray from a third generation source are sufficiently powerful to clarify detailed transition features for all the hierarchical levels under equilibrium conditions.

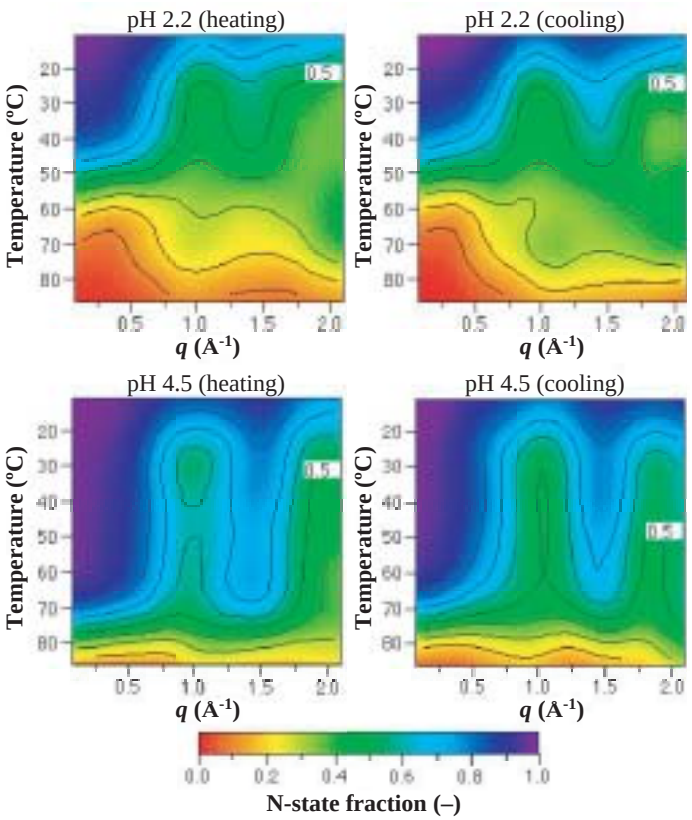

Fig. 3. Hierarchical maps of unfolding-refolding transitions of HEWL given by native molar fraction α at different q values. The α values are displayed in rainbow colors and contour lines. α = 0.5 corresponds to the transition midpoint for each hierarchical level.

Mitsuhiro Hirai* and Masaharu Koizumi

Department of Physics, Gunma University

*E-mail: mhirai@fs.aramaki.gunma-u.ac.jp

References

[1] L. Pollack *et al.*: Phys. Rev. Lett. **86** (2001) 4962.
[2] M. Hirai *et al.*: J. Synchrotron Rad. **9** (2002) 202.
[3] *M. Hirai, M. Koizumi, T. Hayakawa, H. Takahashi, S. Abe, H. Hirai, K. Miura and K. Inoue: Biochemistry* ***43*** *(2004) 9036.*
[4] M. Hirai *et al.*: J. Phys. Chem. B **103** (1999) 549.

β-Helix is a Likely Core Structure of Yeast Prion Sup35 Amyloid Fibers

Prions are infectious proteins that propagate by catalyzing the conformational conversion of the native protein to the prion form [1]. However, the conformational conversion mechanism underlying the propagation of the protein-based genetic information is unknown. Various prion proteins, otherwise unrelated, all assemble into structurally similar β-sheet-rich amyloid fibers [2]. Amyloid fibers have also been implicated in several debilitating neurodegenerative diseases including Alzheimer's, Parkinson's and Huntington's diseases [3]. Knowledge of the fibril structure is essential for understanding the molecular mechanism underlying amyloid formation and could lead to the development of agents that inhibit or reverse the process. The yeast protein Sup35 offers a convenient model for studying both amyloid formation and conformational transmission.

We studied the core structure of the amyloid fibers of the yeast prion protein Sup35 [4]. A prion-inducing fragment of yeast Sup35 consists of two domains: a Gln/Asn-rich N-terminal domain (N); and the highly charged medium domain (M). In order to study the core structure of the amyloid fibers and the involvement of its N and M domains, we prepared three types of fiber from Sup35 fragments: NM (Sup35(1-253)), NMp (Sup35(1-189)), and N (Sup35(1-123)) (Fig. 1). The diameters of the fibers measured by electron microscopy were approximately 120 Å, 80 Å and 60 Å (Fig. 2(a)), respectively .

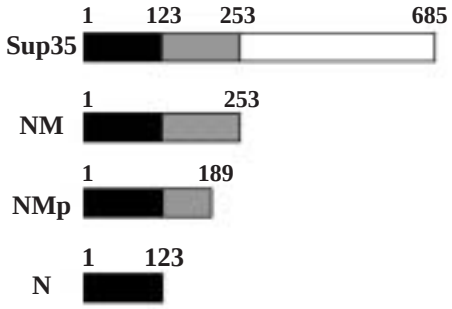

Fig. 1. Domains of Sup35 and Sup35 fragments studied in this work.

We collected X-ray fiber diffraction data at beamline **BL40B2**. X-ray diffraction patterns from dried, oriented fibers (Fig. 2(b)) all show similar set of reflections. The most notable reflection is the sharp

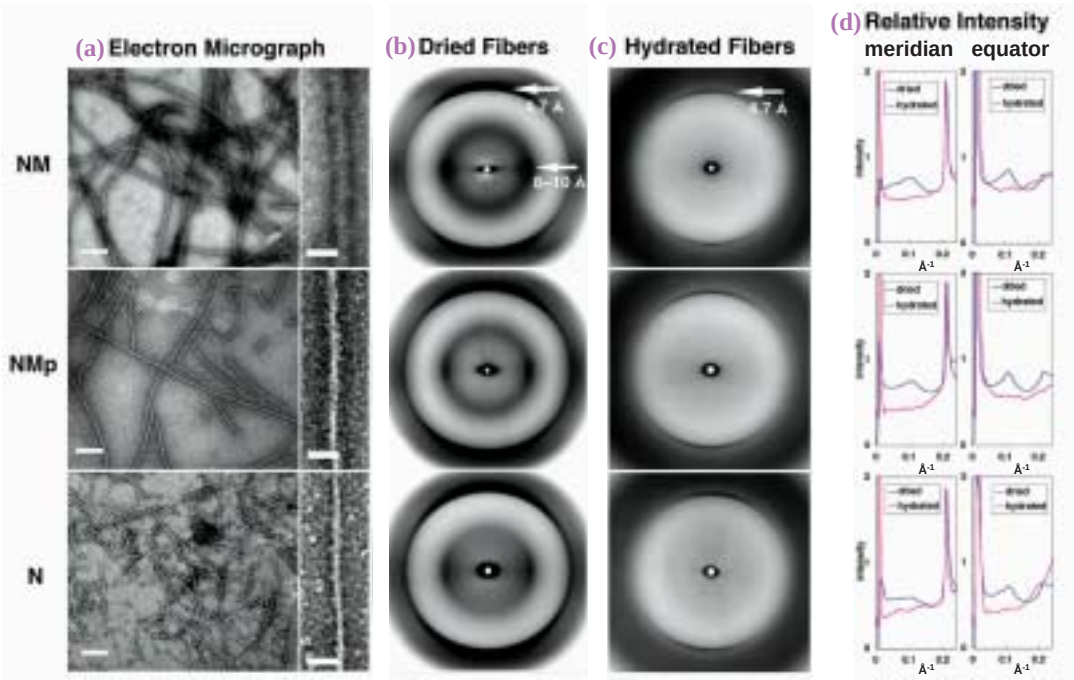

Fig. 2. Structural data obtained from the NM (upper panels), NMp (middle panels) and N fibers (lower panels). **(a)** Electron micrographs. Magnified images of individual fibers are shown in the right panels. Scale bar, 1000 Å (left) and 250 Å (right). **(b)** X-ray fiber diffraction patterns obtained from dried oriented fibers. **(c)** X-ray fiber diffraction patterns from hydrated oriented fibers. **(d)** Comparison of the meridional (left) and equatorial (right) intensity profiles from dried (blue) and hydrated (red) fibers.

meridional one at 4.7 Å due to β-strands running perpendicular to the fiber axis with an interstrand spacing of 4.7 Å. Because the meridional reflection at 9.4 Å, which is expected to arise from antiparallel β-strands, is not observed, it is considered that the fibers are composed of parallel β-strands. Another notable reflection is relatively diffuse in the equatorial region from 10 Å to 8 Å, arising from β-sheets stacked in the direction perpendicular to the fiber axis. The similarity in diffraction pattern indicates the presence of a common core structure. Because the NMp and N fragments were both generated by removing C-terminal regions of the NM fragment, it would be reasonable to assign the N domain to the region that forms the core structure of the fiber. The M domain is, therefore, likely to be located around the fiber core structure.

Interesting observations came from hydrated, oriented fibers, which are shown in Fig. 2(c). The sharp and strong meridional reflection at 4.7 Å is clearly observed, and the absence of the meridional sharp reflection at 9.4 Å is also clear. However, the equatorial diffuse peak at around 9 Å, which was observed in the dried fibers, is missing in the diffraction data of the hydrated fibers. For a direct comparison between the dried and hydrated fibers, we subtracted circular symmetric backgrounds and scaled the intensity profiles on the basis of the intensity of 4.7 Å reflection. Whereas the dried fibers all show the equatorial diffuse peak at 9 Å (at 0.11 $Å^{-1}$ in Fig. 2(d) equator), the hydrated fibers show a flat profile in this region. These results indicate that the stack of β-sheets observed in the dried fiber is an artifact formed during the drying process and the native hydrated fibers do not have the stack of β-sheets in their structure.

Together with the evidence for parallel β-strands, a plausible core structure of Sup35 amyloid fibers is a bundle of β-helix nanotubes [4], as has been proposed by Perutz *et al*. for other amyloid fibers composed of Gln-rich peptides [5]. The central cavity of the β-helix tube would contain water molecules, and when the fibers are dried, these water molecules are removed, resulting in the collapse of the tube and formation of a stack of β-sheets, giving rise to the 9 Å equatorial reflections. The diameter of the β-helix nanotube proposed by Perutz *et al*. [5] is approximately 25 Å, much thinner than the amyloid fibers, and they modeled the fiber to be a twisted bundle of nanotubes. For the M domain of the NM fiber to be on the surface of the nanotube, the M domain has to be located on its one side. The M domain would be helically arranged on the periphery of the nanotube bundle due to a possible twisting of each nanotube as depicted in Fig. 3 [4].

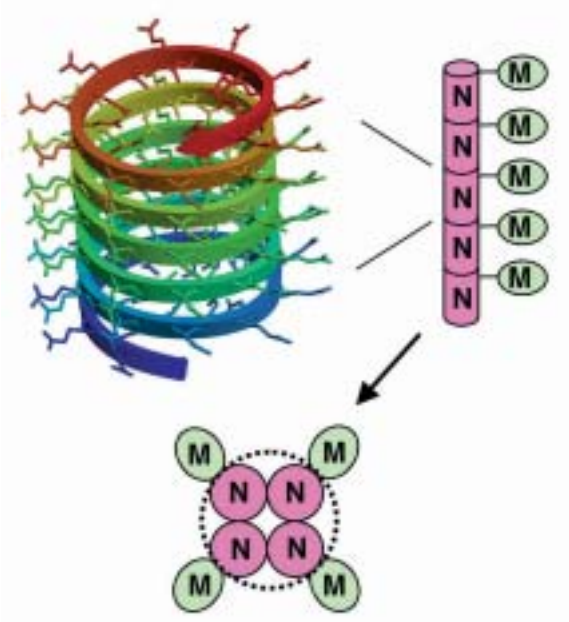

Fig. 3. Model of Sup35 NM fiber.

Aiko Kishimoto [a,b], Kazuya Hasegawa[c] and Keiichi Namba [b,d,*]

(a) Chemical Resources Laboratory, Tokyo Institute of Technology
(b) Graduate School of Frontier Biosciences, Osaka University
(c) SPring-8 / JASRI
(d) Dynamic NanoMachine Project, ICORP, JST

*E-mail: keiichi@fbs.osaka-u.ac.jp

References

[1] S.B. Prusiner: Proc. Natl. Acad. Sci. USA **95** (1998) 13363.
[2] J.W. Kelly: Curr. Opin. Struct. Biol. **8** (1998) 101.
[3] C.M. Dobson: Trends. Biochem. Sci. **24** (1999) 329.
[4] *A. Kishimoto, K. Hasegawa, H. Suzuki, H. Taguchi, K. Namba and M. Yoshida: Biochem. Biophys. Res. Comm.* ***315*** *(2004) 739.*
[5] M.F. Perutz *et al.*: Proc. Natl. Acad. Sci. USA **99** (2002) 5591.

Life Science
Medical Biology

Synchrotron radiation (SR) provides valuable techniques for investigating medical biological structures and functions. In this section, we selected five representative reports classified into two categories. The first category includes reports on the application of SR X-ray diffraction to the analyses of muscle and bone functions, and the second category includes reports on the application of SR microangiography and micro-CT to the imaging of tumor microvasculature and the peripheral lung structure.

(1) Wakayama *et al*. investigated the structural changes of contractile proteins in skeletal skinned muscle fibers during relaxation induced by the photolysis of caged ATP by the high-speed X-ray diffraction method. They showed that after the photolysis of caged ATP, myosin molecules simply detach from actin. (2) Pearson *et al*. analyzed actin-myosin crossbridge dynamics by the X-ray diffraction recording of beating rat hearts with left ventricular (LV) volume and pressure. They indicated that X-ray diffraction techniques offer more sensitive information on differences in crossbridge dynamics at the fiber level than at the macrolevel. (3) Todoh *et al*. showed wide-angle and small-angle scattering of X-ray diffraction from hydroxyapatite and collagen of cortical bone specimens, respectively. They analyzed the strain changes of both materials against applied dynamic strain, and results indicated differences in the maximum strain, elastic module and time response between the two materials. (4) Tokiya *et al*. performed an image analysis of the microvasculature of rat mammary adenocarcinoma transplanted to the inferior epigastric wall in athymic nude rats. They evaluated microvessels of 20~30 μm diameter and found differences in vascular density structure and extravasation among nontreated, b-FGF-treated, anti-VEGFR neutralizing antibody-treated and irradiated groups. (5) Ikura *et al*. analyzed the peripheral lung structure obtained from human autopsy specimens of pulmonary hypertension, emphysema and normal control. The 3D microstructures of alveolar walls, air-blood barriers and capillaries were obtained by SR CT. They found that the CT images well correlated with histological findings in both normal and pathological models.

Collectively, SR diffraction, microangiograhy and CT provide nano- and micron-level, novel information in medical biology.

Fumihiko Kajiya

Structural Transients of Contractile Proteins upon Sudden ATP Liberation in Skeletal Muscle Fibers

The molecular mechanism underlying muscle contraction remains one of the major unresolved problems in biology. A skeletal muscle is composed of bundles of muscle fibers (muscle cells). In a muscle fiber, myofibrils composed of a linear array of sarcomere running parallel to the fiber axis are packed (Fig. 1(a)). In each sarcomere, thin and thick filaments (contractile proteins) are regularly arranged in a hexagonal lattice (Fig. 1(b)). A thin filament is composed of helically polymerized actin monomers. The main constituent of a thick filament is myosin. Myosin is composed of two identical heads connected to a long tail (Fig. 1(c)). The myosin head contains all the components needed in the exertion of force, including the actin-binding site and ATP-binding pocket. The muscle contraction takes place by the interaction between actin and myosin utilizing the chemical energy produced by the hydrolysis of ATP. One of the major problems that need to be solved is to determine how force generation powered by the hydrolysis of ATP is associated with structural changes in the proteins actin and myosin when they interact with each other. Fiber X-ray diffraction is a useful technique for investigating structural events at appropriate spatial resolution (1-60 nm) and time resolution (milliseconds). Most of the X-ray diffraction studies have been done using either living muscle specimens or skinned muscle fibers. Usually, skinned muscle fibers, whose surface cell membrane has been removed or dissolved, have widely been used to study the effects of various reactants on the structural changes of contractile proteins. However, the use of skinned muscle fibers in the study of structural changes is open to the criticism that, due to the diffusion limit, the distributions of reactants are not uniform in muscle fibers because of their large diameter.

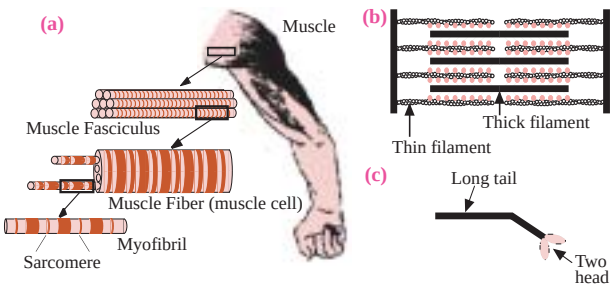

Fig. 1. **(a)** Schematic microanatomy of skeletal muscle. **(b)** Schematic drawing of sarcomere structure. **(c)** Schematic structure of myosin molecule.

One promising approach to overcome this difficulty is to use caged compounds. Caged compounds are inert when placed in a skinned fiber, but they can be split by an intense pulse of UV laser light to form biologically active substances, resulting in a sudden (within milliseconds) increase in their concentrations in the fiber. Some time-resolved X-ray diffraction studies have been carried out using caged compounds [1-3], but there have been limitations in both time resolution and the extent of reflections in X-ray diffraction pattern that can be analyzed. In these studies, only strong reflections (e.g., equatorial reflections and myosin meridional reflections) have been investigated, because the structural changes of contractile proteins caused by photolysis are fast (millisecond time scales) and the flux from X-ray source in these experiments was not high enough to measure intensities of weak reflections at millisecond time resolution. To understand fully the structural changes of contractile proteins induced by the flash of photolysis, one should investigate not only these strong reflections but also weak reflections (e.g. actin-based layer lines (ALL)), because they carry important information about the structure of the contractile proteins.

In the present study [4], we investigated the structural changes of contractile proteins in skeletal skinned muscle fibers during the relaxation induced by the flash photolysis of caged ATP by ultrahigh-speed time-resolved X-ray diffraction with a time resolution of 3.4 ms at high-flux **BL40XU** beamline. This beamline provides a photon flux of an order of 10^{15} s^{-1}, ~10^3 times higher than other undulator-based beamlines [5]. Thus, this beamline is suitable for time-resolved experiments at a high time resolution. As a material, overstretched skinned skeletal muscle fibers loaded with exogenous myosin heads were used.

Figure 2 shows the selected frame of the time series of diffraction patterns taken before and after the photolysis of caged ATP. Before photolysis, ATP was absent in the muscle fibers. This is the condition equivalent to the rigor state, and strong stereospecific interactions are known to occur between actin and myosin. In the diffraction pattern, all the ALL's between the first and sixth are strongly enhanced. The enhancement is caused by the myosin heads, which are bound to actin in a stereospecific manner. After photolysis, the concentration of ATP rapidly increases within the muscle fiber and the photorelease

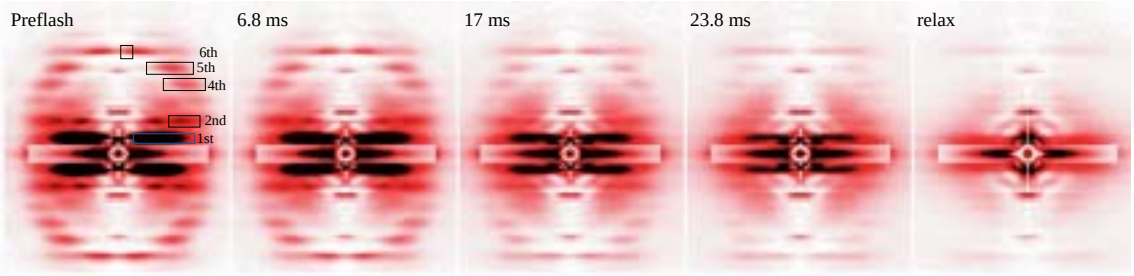

Fig. 2. Selected frames of time series of diffraction patterns taken during a caged ATP photolysis experiment (accumulation of multishots). The number in each pattern shows the time after flash. The boxes in the first pattern show the areas of intensity in Fig. 3. Time course of decay of integrated intensities of ALL's after photolysis.

of ATP allows the muscle fiber to enter into the relaxed state. In the diffraction patterns, these ALL's fade away, leaving the much weaker sixth ALL at the final stage of relaxation. The intensity of each ALL was integrated in the area indicated by a box shown in the first pattern in Fig. 2. The time courses of decay of the integrated intensities of ALL's are shown in Fig. 3. The decay of the lower-order ALL's (up to the fifth ALL) and the inner part of the sixth ALL was fast and was adequately fitted by a single exponential decay function. The rate constants for these ALL's were all similar. Also the changes in the intensity profiles of representative ALL's after photolysis, measured along the layer line, are shown in Fig. 4. It seems that the intensities of these ALL's decreased without changes in their profiles. These results suggest that after the photolysis of ATP (sudden ATP liberation) the myosin heads molecules simply detach from actin without passing through a state structurally distinct from the rigor state.

In this research, we found the structural changes of the contractile proteins during the course of relaxation caused by the photorelease of ATP.

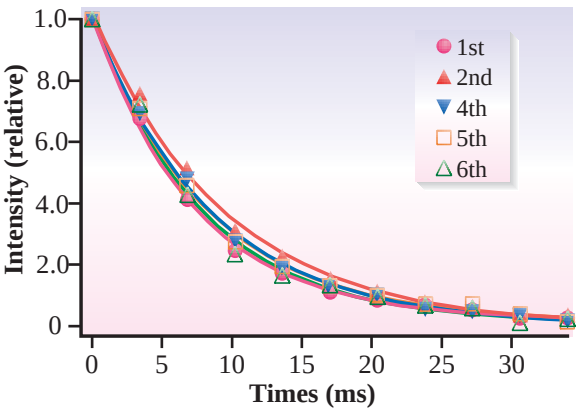

Fig. 3. Time course of decay of integrated intensities of ALL's after photolysis.

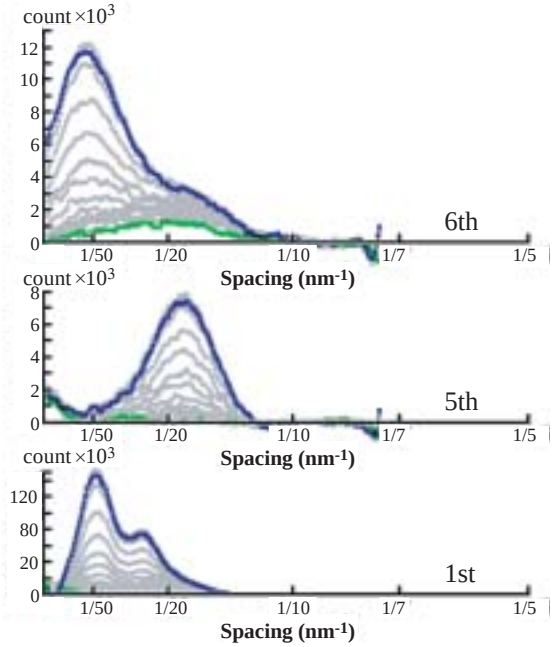

Fig. 4. Intensity profiles of representative ALL's before and after photolysis. The uppermost blue curve in each set of profiles represents the preflash level, and the lowermost green curve represents the relaxed level.

Jun'ichi Wakayama†

SPring-8 / RIKEN

E-mail: jwaka@nfri.affrc.go.jp

†Current address: Instrumentation Engineering Lab., National Food Research Institute

References

[1] K. J. V. Poole *et al.*: Adv. Biophys **27** (1991) 63.
[2] K. Horiuti *et al.*: J. Biochem. **115** (1994) 953.
[3] T. Yamada *et al.*: Biophys. J. **85** (2003) 1741.
[4] *J. Wakayama, T. Tamura, N. Yagi and H. Iwamoto: Biophys. J.* ***87*** *(2004) 430.*
[5] K. Inoue *et al.*: Nucl. Instrum. Meth. Phys. Res. A **467/8** (2001) 674.

Real Time *In Vivo* Measurements of Crossbridge Dynamics in Cardiac Muscle

Small angle X-ray scattering is one technique that is increasingly been used to investigate crossbridge cycling (formation of strong bonds between the major protein thick and thin filaments) in cardiac, skeletal and insect flight muscles. Recorded diffraction patterns indicate the proximity of myosin thick filaments to actin thin filaments within the filament lattice of myofibers, due to the large size, abundance and highly ordered arrangement.

In spite of the interest in investigating the cellular basis of heart function and dysfunction, whole-heart investigations at the fiber level had not been performed until recently [1,2]. Since the heart beats continuously throughout life, in contrast to skeletal muscle the heart alternates between rapid periods of contraction (referred to as systole) and relaxation (diastole, including LV filling) and has high metabolic demands, making it vulnerable to ischemia. As the heart, and in particular the left ventricle (LV), is controlled both by intrinsic and extrinsic factors it is of scientific interest and medical value to investigate how the cellular components of myofibers are modulated by endogenous hormones and hemodynamic changes (increased filling or heart rate).

There are several reasons why *in situ* cardiac measurements under physiological conditions are needed. First, in contrast to isolated muscle studies during isometric contractions, the beating heart performs work, i.e. contraction occurs under a load during systole. Factors such as temperature, fiber operating range (length is influenced by structure of the whole heart) and the extracellular chemical environment have major impacts on crossbridge formation *in vivo*. Finally, there is no *a priori* reason to assume that crossbridge dynamics will be uniform throughout the heart. It is for these reasons that we investigated how crossbridge dynamics are influenced by local ischemia in the anterior wall of the LV of rat hearts.

We used a narrow collimated quasi-monochromatic beam (0.2 mm × 0.2 mm) provided at beamline **BL40XU** for X-ray diffraction recordings of spontaneously beating Sprague-Dawley rat hearts (Fig. 1). Beam flux was ~10^{12} photons/s (reduced with 3 mm thick Al bar, 15 keV and ring current 60-100 mA). Beating hearts were continuously exposed for *ca*. 2 s to the X-ray beam and diffraction images recorded at a 15-ms sampling interval (about 8-11 consecutive heart beats per recording). Beam orientation was perpendicular to the fiber direction in the outermost layer of the LV (equatorial position reflections). Anesthetized rat models were prepared as detailed elsewhere [2]. Simultaneous macro-level determinations of LV performance were made using intracardiac catheters to determine LV pressure (LVP) and volume (LVV) changes. Thus the contribution of a specific LV region to the work performed by the whole LV (in addition to other important hemodynamic information) can be determined with the aid of pressure-volume (P-V) loops and *in situ* indices of crossbridge dynamics [3].

Myosin mass transfer to actin was determined as the decrease in intensity ratio (intensity of 1,0 reflection over 1,1) during the cardiac cycle (beat-to-beat interval identified from P-V loops). The distance between 1,0 reflections was converted to a lattice spacing between myosin filaments ($d_{1,0}$, nm) using a pixel calibration factor determined from a collagen sample.

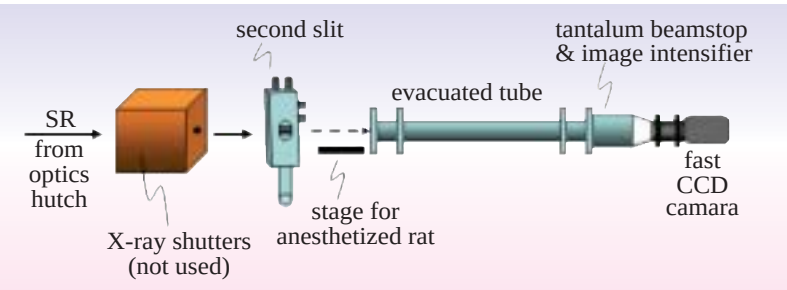

Fig. 1. Experimental set up for *in situ* whole-heart X-ray diffraction recordings. V5445P image intensifier and C4880-80-24A CCD camera (Hamamatsu Photonics) were used. Camera distance from the beating hearts was *ca*. 3 m during all experiments.

Increases in LVP during systolic contraction of the hearts correlated with a decrease in intensity ratio (i.e. mass transfer to actin during crossbridge formation) and an increase in $d_{1,0}$ spacing (Fig. 2). During relaxation, intensity ratio increased rapidly and $d_{1,0}$ spacing remained elevated until ventricular filling (LV refills with blood), when $d_{1,0}$ spacing decreased to a minimum, while intensity ratio remained stable. Thus under normal physiological conditions intensity ratio was high when the strong crossbridges were detached

from actin filaments, but decreased in direct proportion with the pressure formed during contraction (left panel *black line* in Fig. 3); i.e. the change in intensity ratio is proportional to mass transfer of crossbridges *in situ*, consistent with past studies in isolated cardiac muscle [4].

However, for the first time we found that *in vivo* hearts do not maintain constant lattice volume during contractions [2]. In all hearts examined under baseline conditions mass transfer was essentially completed before the maximal extent of the $d_{1,0}$ spacing change (2-5 nm between hearts). Significant lattice expansion occurs after the release of isometric tension, when the aortic valve opens and fiber shortening occurs (see expansion after asterisk in Fig. 3 middle panel). Since $d_{1,0}$ spacing during systole was larger than diastole at any given LVV (Fig. 3 right panel), we suggested that crossbridge formation might cause lattice expansion as the release of radial forces between the filaments has been shown to increase lattice spacing after release from isometric tension in skeletal muscle [see 5].

Left coronary artery occlusion eliminated increases in lattice spacing and severely reduced mass transfer in the ischemic region (Fig. 2 and Fig. 3). The latter is expected as crossbridge formation is dependent on aerobic metabolic pathways, however, the significantly increased intensity ratios of the ischemic region contrast the findings of *ex vivo* experiments (see ref. [2]).

X-ray diffraction techniques were more sensitive to fiber level differences in crossbridge dynamics than macro-level protocols and therefore have the potential to identify dysfunctional regions of the LV during cardiac disease.

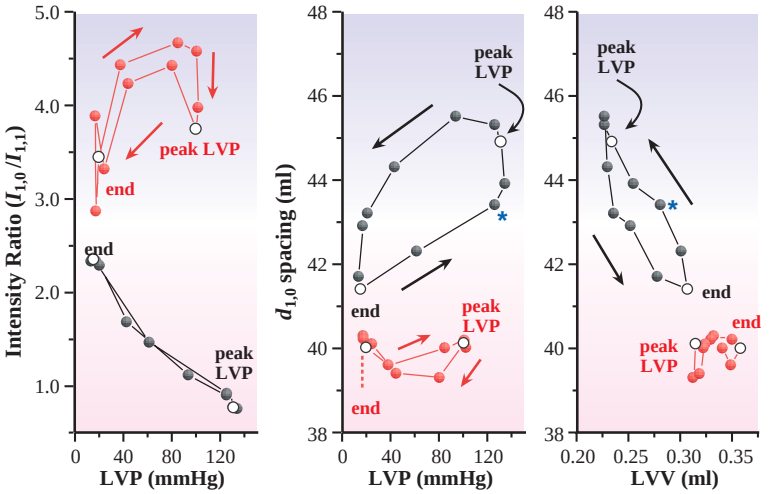

Fig. 3. Changes in the loop relationships between intensity ratio, myosin filament spacing ($d_{1,0}$), LVP and LVV of a typical heart before and after ligation of the left coronary artery (creating ischemia). Baseline conditions (black lines) and during regional ischemia (red lines) in the same heart are presented during average loops. Arrows indicate trajectories of the loops starting at the end of the cardiac cycle, through contraction (and peak LVP) and relaxation. Asterisks indicate the end of isovolumic contraction and the start of fiber shortening (see text).

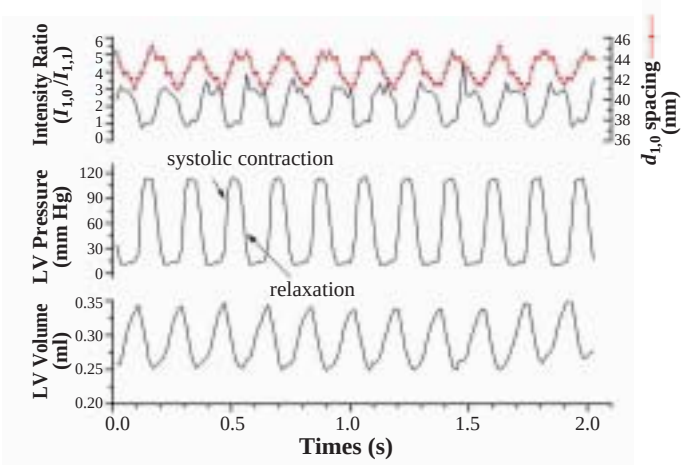

Fig. 2. Real time myosin filament spacing ($d_{1,0}$; red line) and intensity ratio changes calculated from X-ray diffraction patterns in relation to LVP and LVV recorded in a typical spontaneously beating rat heart under normal baseline conditions.

James T. Pearson [a,†,*], Mikiyasu Shirai [a,††] and Naoto Yagi [b]

(a) Department of Cardiac Physiology, National Cardiovascular Center
(b) SPring-8 / JASRI

*E-mail: james.pearson@med.monash.edu.au

†Current address: Department of Physiology, Monash University, Australia

††Current address: Department of Clinical Radiology, Hiroshima International University

References

[1] N. Yagi *et al.*: Biophys. J. **86** (2004) 2286.
[2] *J.T. Pearson, M. Shirai, H. Ito, N. Tokunaga, H. Tsuchimochi, N. Nishiura, D.O. Schwenke, H.I.-Ueda, R. Akiyama, H. Mori, K. Kangawa, H. Suga and N. Yagi.: Circulation **109** (2004) 2976.*
[3] H. Suga: Physiol. Rev. **70** (1990) 247.
[4] N. Yagi *et al.*: Pflügers Archiv. **448** (2004) 153.
[5] G. Cecchi *et al.*: Science **250** (1990) 1409.

Observation of Kinetic Response of Mineral and Collagen Phases in Bone by X-ray Diffraction

A bone has a hierarchical structure as shown in Fig. 1 [1]. Macroscopic bone properties are dependent on the microstructure and properties of structural elements. The bone is a composite material that consists of hydroxyapatite particles in a matrix of collagen fiber. Borsato *et al.* [2] measured the strain of hydroxyapatite by X-ray diffraction and obtained clear evidence of the stress concentration on hydroxyapatite in the bone. Sasaki *et al.* [3] reported the stress-strain curve for tendon collagen by X-ray diffraction. However, the relationship between the mechanical behavior of hydroxyapatite and that of collagen has been unclarified. In this study, the microscopic mechanical behavior of bone as a composite material was examined by measuring the strains of hydroxyapatite and collagen by wide-angle X-ray diffraction and small-angle X-ray scattering, respectively.

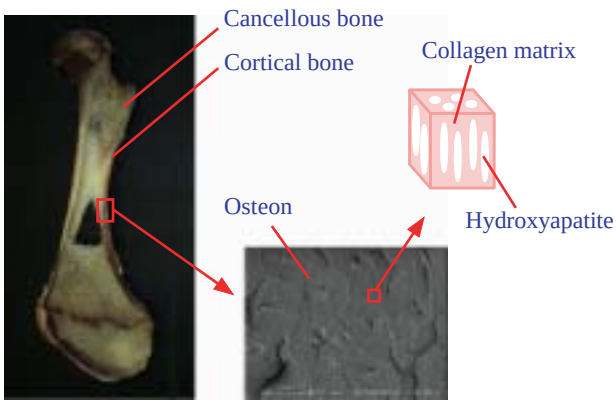

Fig. 1. Hierarchical structure of bone.

Twelve cortical bone specimens with an average size of 40 × 5 × 0.5 mm^3 were cut out from the mid-diaphysis of the bovine femur using a diamond cutter. The longer edges of the specimen were parallel to the longitudinal axis of the femur. Before the experiments, the specimens were preserved in a saline solution.

X-ray energy was 15.0 keV at beamline **BL40XU**. The experimental setup is shown in Fig. 2. The X-ray path length was about 9 cm in wide-angle diffraction for hydroxyapatite (Fig. 2(a)), and 3 m in small-angle scattering for collagen (Fig. 2(b)). The X-ray diffraction pattern was recorded with an X-ray image intensifier (Hamamatsu Photonics, V5445P) and a fast CCD camera (Hamamatsu Photonics, C4880-80). The time resolution was 30 frames/sec. The specimens were subjected to a load using tensile loading apparatus. The tensile loading was synchronized with the X-ray shutter and CCD camera.

Figures 3(a) and 3(b) show the images of X-ray diffraction from hydroxyapatite and collagen in the bone, respectively. In the wide-angle diffraction from hydroxyapatite in the bone, diffractions from (211) and (002) are strong (Fig. 3 (a)). As the (002) plane of hydroxyapatite in the bone has a preferred orientation in the bone axial direction, most of the *c*-axis of hydroxyapatite crystals is parallel to the bone axial direction. In the small-angle scattering from collagen in the bone, diffraction from *d* = 22.6 nm is strong (Fig. 3 (b)). The small-angle scattering pattern also contains a diffuse scattering perpendicular to the bone axial direction. Matsushima *et al*. [4] reported that this anisotropic diffuse scattering can be explained by the

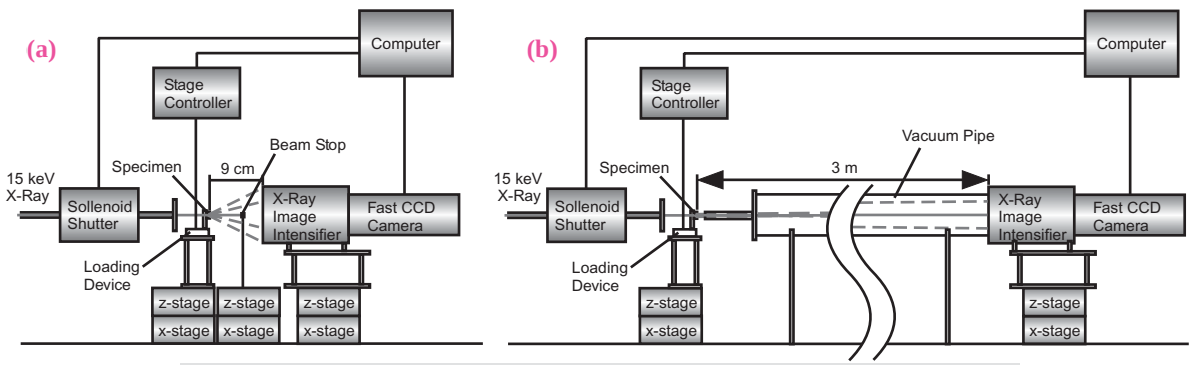

Fig. 2. Experimental setup for X-ray diffraction. **(a)** Wide-angle X-ray diffraction from hydroxyapatite in bone. **(b)** Small-angle X-ray scattering from collagen in bone.

shape and orientation of hydroxyapatite crystals.

Figure 4 shows the strain change of hydroxyapatite and collagen in the bone against the dynamic stress macroscopically applied to a bone specimen. The maximum strain of collagen is higher than that of hydroxyapatite. However, the difference in elastic modulus between hydroxyapatite and collagen is larger than that of the maximum strain. Therefore, it is estimated that hydroxyapatite is subjected to a larger stress. The strain of collagen changes quickly against the applied stress, however the strain of hydroxyapatite changes slowly. It is estimated that this difference in behavior is caused by the difference in elastic modulus between hydroxyapatite and collagen.

In summary, we could observe the mechanical behavior of hydoxyapatite and collagen in bone by wide-angle X-ray diffraction and small-angle X-ray scattering. A further study is now in progress to estimate the mechanical constitutive law for the hydroxyapatite – collagen composite material.

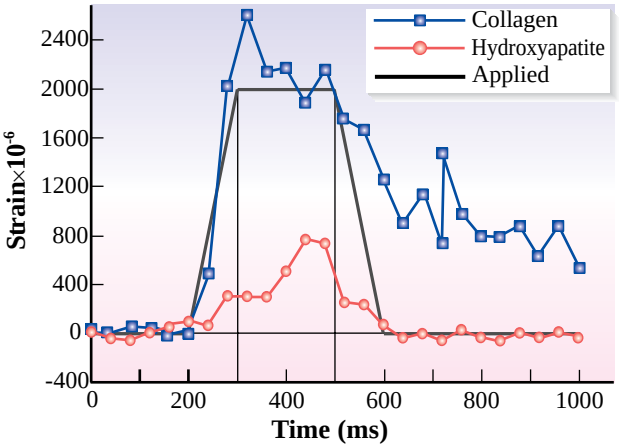

Fig. 4. Mechanical behavior of hydroxyapatite and collagen in bone by X-ray diffraction against macroscopically applied dynamic stress.

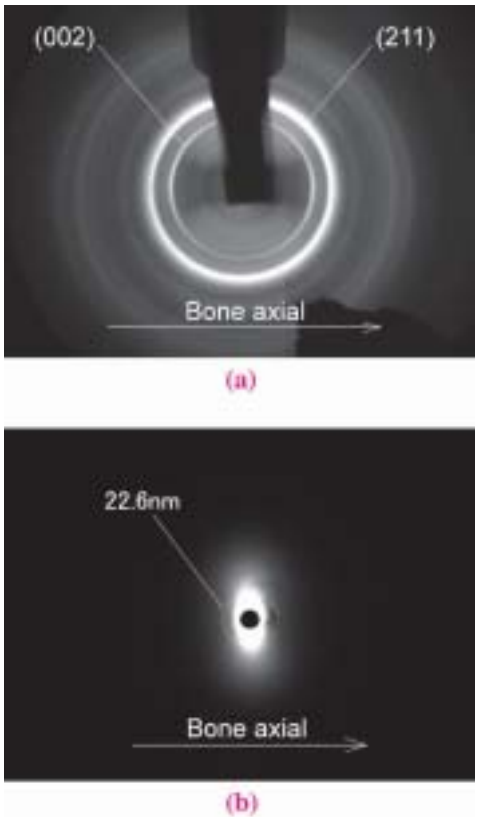

Fig. 3. X-ray diffraction images. **(a)** Wide-angle X-ray diffraction from hydroxyapatite in bone. **(b)** Small-angle X-ray scattering from collagen in bone.

Masahiro Todoh

Graduate School of Engineering, Hokkaido University

E-mail: todoh@eng.hokudai.ac.jp

References

[1] J. Y. Rho *et al.*: Med. Eng. Phys. **20** (1998) 92.
[2] K. S. Borsato *et al.*: J. Biomech. **30** (1997) 955.
[3] N. Sasaki *et al.*: J. Biomech. **29** (1996) 655.
[4] N. Matsushima *et al.*: Jpn. J. Appl. Phys. **21** (1982) 186.

Analysis of Microvasculature of Transplanted Rat Tumors using Synchrotron Radiation Microangiography System

In the 1970's, Folkman and colleagues [1] proposed a trail-blazing theory regarding tumor growth factors summarized as follows. Whereas an early-stage solid tumor can receive nutrients and oxygen through diffusion from mature vessels, in order for the tumor to grow larger than several millimeters, the induction of continuous angiogenesis is required (Fig. 1(a)). Since then, various *in vitro* and *in vivo* experimental models and observation methods have been developed to clarify the mechanism underlying tumor angiogenesis. However, there have been no techniques that enable the observation of micronsize tumor vessels by angiography, or the quantitative assessment of dynamic changes in the morphology of tumor vessels.

In the present study, N-nitrosomethylurea-induced rat mammary adenocarcinoma was transplanted to athymic nude rats, and tumor vessels in the transplanted tumor of 20-30 μm size were analyzed using a synchrotron radiation microangiography system (**BL20B2**). Furthermore, the effects of treatment with either basic fibroblast growth factor (b-FGF, an angiogenesis promoter) or anti-vascular endothelial growth factor receptor neutralizing antibody (anti-VEGFR neutralizing antibody, angiogenesis inhibitor), or irradiation on angiogenesis and microcirculation were determined morphologically. The results were as follows. (i) The minimal diameter of observable vessels in athymic nude rats with a tumor transplanted to the inferior epigastric wall was 20-30 μm (Fig. 2) [2,3]. (ii) As to microvessel density (MVD) 1-4 weeks after transplantation in the nontreated group, a significant correlation existed between histologic MVD, which was calculated histologically on the basis of the quantity of vessels, and angiographic MVD, which was calculated by binarization computation ($r = 0.944$, $p < 0.01$) (Fig. 3) [4]. (iii) In the nontreated group, the scores for dilatation, serpiginous vessels and encasement of tumor vessels were high 1-2 weeks after transplantation, whereas the scores for retiform vessels and extravasation were high 3-4 weeks after transplantation (Fig. 1(b)). (iv) Among the treated groups, at 4 weeks after the treatment, the scores for retiform vessels in the b-FGF-treated group and for extravasation in the irradiated group were high. However, in the anti-VEGFR neutralizing antibody-treated group, the scores for retiform vessels and extravasation were low (Fig. 4). (v) Finally, the time-density curve for each group was classified into the waning or recruiting response pattern; whereas the former was observed 1-2 weeks after transplantation in the nontreated and b-FGF-treated groups, the latter was observed 3-4 weeks after transplantation in the nontreated, anti-VEGFR neutralizing antibody-treated and irradiated groups (Fig. 5).

Using a totally new microangiography system based on monochromatic X-rays, (synchrotron radiation is 100,000 times brighter than X-rays from a standard medical X-ray source), we were able to observe and quantitatively assess the morphology of 20-30 μm tumor vessels, and results comparable to the conventional histological analyses were obtained. To date there have been no angiographic studies of the effects of treatment with an angiogenesis promoter or inhibitor, or irradiation on morphological changes in the tumor vessels, i.e., existing and

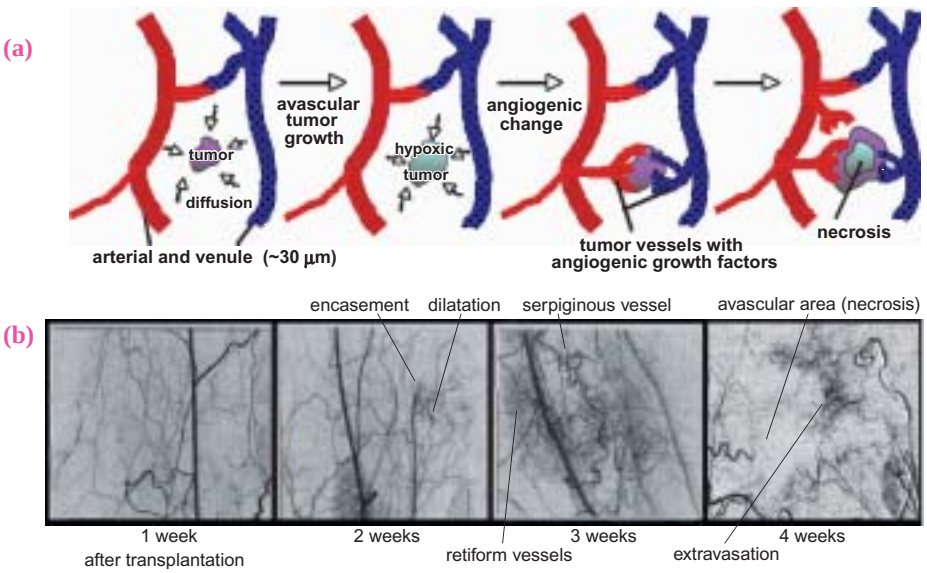

Fig. 1. **(a)** Tumor growth and modification of microvasculature with time. **(b)** Modification of tumor microvasculature according with time on microangiographic images.

new blood vessels (angiogenesis). The results obtained using the present technique are in close agreement with those obtained by molecular biological and histological analyses, indicating that the present technique is promising. In the present study, a rat tumor was transplanted, but with the present experimental system, human-derived tumor cell lines can be heterogeneously transplanted. Progress in human chemotherapy, molecular target therapy and radiotherapy will be realized with further technical advances.

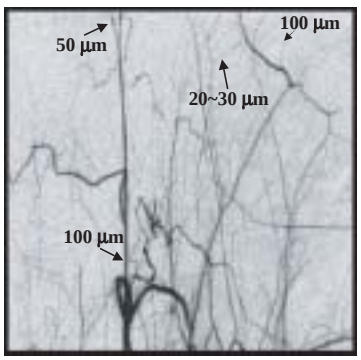

field of view : 9.5×9.5 mm / 1024×1024 pixel

Fig. 2. Microangiographic image of rat superficial inferior epigastric vessels.

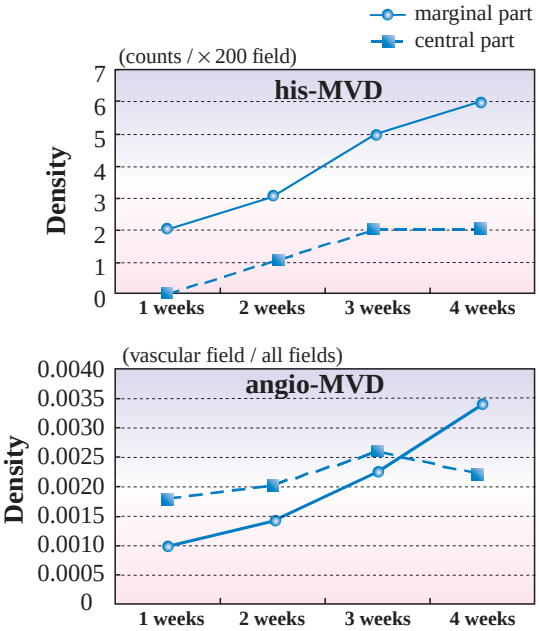

Fig. 3. Histological (his-) and angiological (angio-) microvessel densities (MVD) with tumor growth.

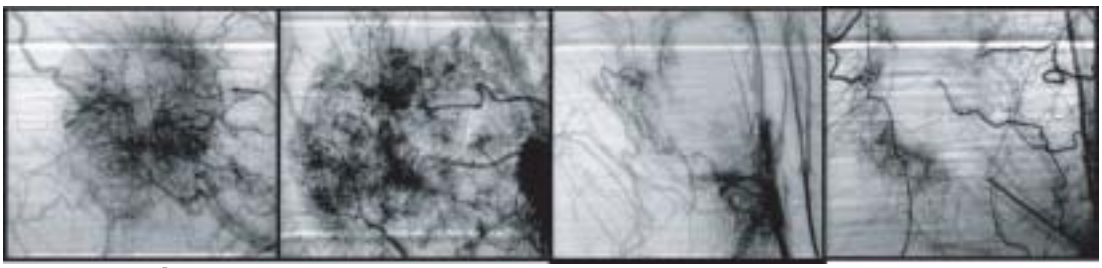

Fig. 4. Typical microangiographic changes recognized in tumors of the non-treated and treated groups (four weeks).

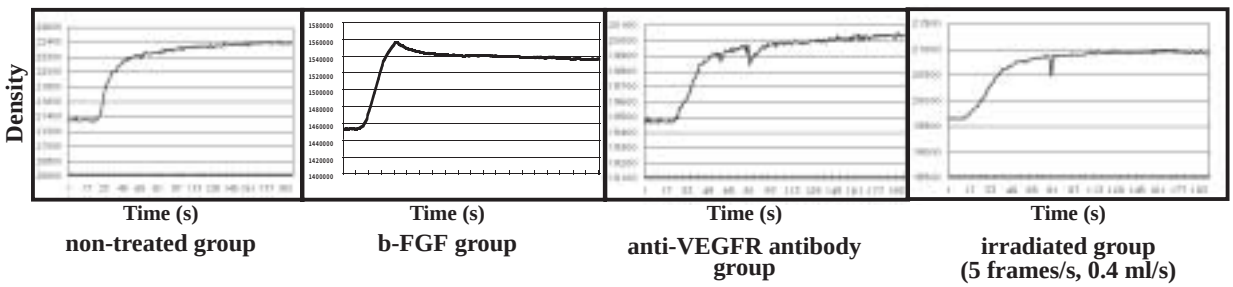

Fig. 5. Microangiographic time-density curves in tumors of non-treated and treated groups (four weeks).

Ryoji Tokiya [a,*], Keiji Umetani[b] and Yoshinari Imajo[a]

(a) Departments of Radiation Oncology, Kawasaki Medical School
(b) SPring-8 / JASRI

*E-mail: radoncol@med.kawasaki-m.ac.jp

References

[1] J. Folkman: Sci. Am. **234** (1976) 58.
[2] K. Umetani *et al.*: Bioimages **9** (2001) 97.
[3] T. Yamashita: Invest. Radiol. **36** (2001) 713.
[4] *R. Tokiya, K. Umetani, S. Imai, T. Yamashita, J. Hiratsuka, Y. Imajo: Acad. Radiol.* ***11*** *(2004) 1039.*

2D and 3D Visualization of Peripheral Lung Structure by Synchrotron Radiation CT

In many chronic lung diseases, the remodeling of the peripheral lung structure affecting peripheral ventilation often causes chronic respiratory failure. To precisely understand lung morphology and function, it is necessary to accurately visualize details of lung architecture. We demonstrated a new technique of 2D and 3D visualization the peripheral lung structure using isotropic volume data obtained by synchrotron radiation CT (SRCT) [1,3,4].

Lung specimens with pulmonary fibrosis and emphysema, and those without pulmonary diseases (normal) were obtained at autopsy, and were inflated and fixed. Each specimen was cut into a cylindrical shape of 6 mm diameter and 20 mm height. Projection images (360) of a specimen were captured using the SRCT system constructed at beamline **BL20B2** led from the source of synchrotron radiation. 2D SRCT images were reconstructed using these projection images on a workstation. Isotropic volume data with 12 μm voxel size were provided, stacked with 815 axial images of SRCT. 3D microstructures were obtained by automatic segmentation and combination of the surface and volume-rendering display technique on the workstation. For the 3D modeling of peripheral airflow, each point within the peripheral airway and airspace was assigned two values, one was the distance from the starting point, and other was the distance from the nearest airspace boundary. With these assigned values, the 3D model of air flow was demonstrated in the animation form.

SRCT images were correlated with the corresponding histopathologic images, point-by-point. SRCT demonstrated an approximately 10 μm area with clearly visualization of the alveolar wall, which was composed of two air-blood barriers of 0.5 μm thickness and a capillary of at least 8.6 μm diameter (Fig. 1) [2]. SRCT also demonstrated well the pathologic features. Each finding regarding various disease processes on SRCT images well correlated with histopathologic findings on microscopic images (Fig. 2) [3]. On the other hand, the 3D model of the peripheral lung structure could represent well the normal and pathologic lung structures (Fig. 3) [4]. In pulmonary fibrosis, the peripheral volume of airspace and beyond the respiratory bronchiole decreased compared with that in the normal model using animation. On the other hand, in emphysema, the volume increased compared with that in the normal model with animation. In both pathologic models, the difference in peripheral ventilation could be demonstrated clearly compared with that in the normal model.

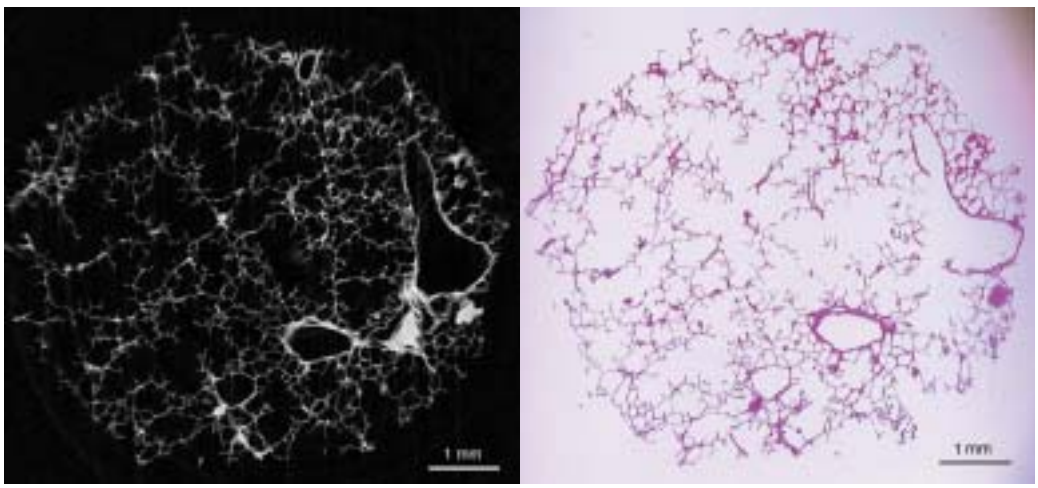

Fig. 1. Comparison between SRCT and microscopy images with normal human lung specimen. Synchrotron radiation CT image **(a)** with pixel resolution and thickness of 12 μm×12 μm, and 12 μm, respectively. Optical microscopy image **(b)** of a 6 to 12-μm-thick histologic section, which was stained with hematoxylin-eosin (original magnification, ×12.5). In the two figures, the scale bar corresponds to 1 mm.

In conclusion, the 2D and 3D analyses of the human peripheral lung structure by SRCT can provide important morphologic, physiologic, and pathologic information of the peripheral respiratory system. Currently, we cannot apply SRCT to patients in a clinical setting; however, important morphologic, pathophysiologic studies can be carried out using this ultrahigh resolution CT.

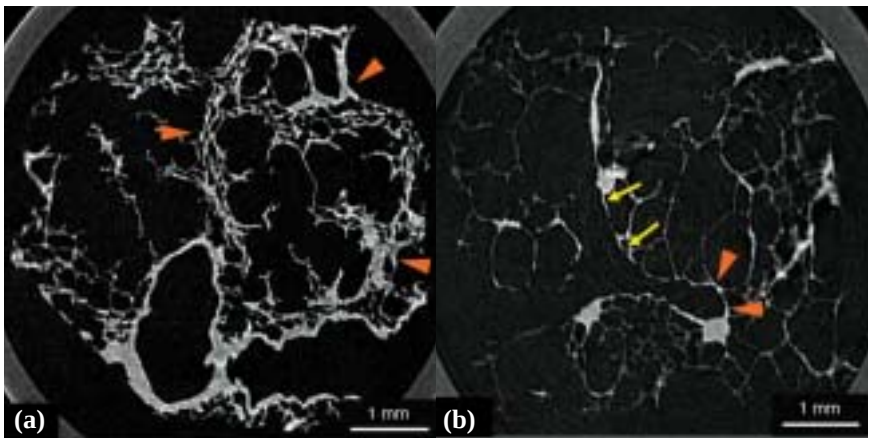

Fig. 2. SRCT images of pathologic lung specimen. SRCT images of pulmonary fibrosis **(a)** and emphysema **(b)**, with pixel resolution and thickness of 12 μm×12 μm, and 12 μm, respectively. For pulmonary fibrosis **(a)**, the dilatation of peripheral airspace due to interstitial fibrosis (arrowhead) can be observed clearly. SRCT can demonstrate the remodeling of the peripheral structure caused by interstitial fibrosis. For emphysema **(b)**, the peripheral airways and airspaces beyond the respiratory bronchiole (arrow) are dilated and destroyed. On the other hand, the terminal bronchiole in diseased specimens is narrower than that in the normal lung. SRCT also can demonstrate the pathologic features of emphysema on the microscopic order.

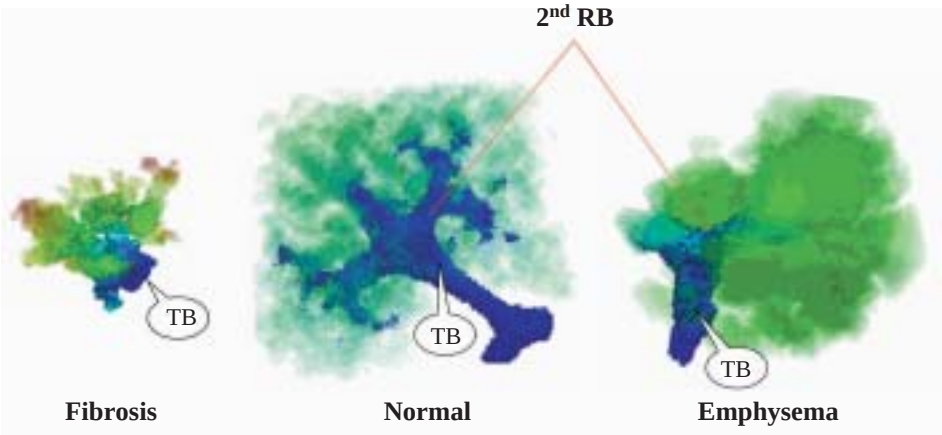

Fig. 3. Comparison of 3D models of the peripheral lung structure. These three models are adjusted to almost the same scale. Airflow is displayed with surface rendering (blue), when inspired air spreads into the bronchiole. Air diffusion is displayed with volume rendering (green), when inspired air spreads by diffusion in the more peripheral airspace. RB = respiratory bronchiole; TB = (most distal) terminal bronchiole.

Hirohiko Ikura[a,*] and Kenji Shimizu[b]

(a) Department of Radiology, Ehime University School of Medicine
(b) Department of Radiology, Tokai University School of Medicine

*E-mail: hikura@m.ehime-u.ac.jp

References

[1] *H. Ikura, K. Shimizu, J. Ikezoe, T. Nagareda, N. Yagi : J. Thorac Imaging* ***19*** *(2004) 8.*
[2] R.S. Fraser *et al.*: Synopsis of Diseases of the Chest, 2nd ed., Philadelphia, Pennsylvania, W.B. Saunders Company **9** (1994) 29.
[3] *H. Ikura and K. Shimizu: CT of the Chest, 2nd ed., Tokyo, Medical Science International (2004) 538.*
[4] K. Shimizu *et al.*: Proc. SPIE **5369** (2004) 439.

Materials Science
Structure

Materials science concerning structural aspects of materials is one of very active fields at SPring-8. Reflecting this fact, many papers concerned with Materials Science have been selected for the present issue, i.e., twelve papers. Although nanoscience and nanotechnology remain keywords for describing the focus of materials science activities at SPring-8, the present issue does not include any work dealing with typical nanomaterials such as fullerene compounds or nanotubes. This probably means that nanoscience at SPring-8 has become a continuous focus of research rather than topic of special interest. Instead, the present issue includes quite a few works concerning the study of the fluid state. In a very early stage of its existence, SPring-8 was not well equipped to study liquid or fluid state; this, however, is no longer true. The number of research areas of materials science, which SPring-8 covers, still seems to be growing.

From among many other studies, the following twelve works have been chosen. 1) "Direct observation of intermolecular interaction for organic magnet by low-temperature X-ray diffraction" by Y. Wang & J. J. Lee, 2) "Disordered zinc in thermoelectric material Zn_4Sb_3 with phonon-glass and electron-crystal properties" by E. Nishibori, G. J. Snyder, P. Rabillar, M. Christensen & B. B. Iversen, 3) "Doping effect of Cu-O bond stretching phonon in $La_{2-X}Sr_XCuO_4$ studied by inelastic X-ray scattering" by J. Mizuki, T. Fukuda & K. Yamada, 4) "Crystal structure of superconducting sodium cobalt oxide" by K. Takada & I. Nakai, 5) "High-quality as-grown MgB_2 film fabrication at low temperature using in-plane-lattice near-matched epitaxial-buffer layer" by O. Sakata, S. Kimura & S. Kubo, 6) "X-ray diffraction study of charge-density-wave phase transition on In/Cu(001)" by T. Aruga & S. Hatta, 7) "Strain field under the SiO_2/Si(001) interface revealed by phase-sensitive X-ray diffraction technique" by W. Yashiro, 8) "Structural determination of topological crystal" by S. Tanda, Y. Nogami & N. Ikeda, 9) "Glass forming at limit: how glass forms when there is insufficient network former ?" by S. Kohara, K. Suzuya & K. Takeuchi, 10) "Direct observation of macroscopic separation of dense fluid phase and liquid phase of phosphorus" by Y. Katayama, 11) "Observation of fast sound in expanded fluid mercury accompanying metal-nonmetal transition" by M. Inui, D. Ishikawa & K. Tamura, and 12) "Collective dynamics of super critical water" by T. Yamaguchi, K. Yoshida & S. Hosokawa.

Makoto Sakata

Direct Observation of Intermolecular Interaction for Organic Magnet by Low-temperature X-ray Diffraction

Hydrogen bonding plays an important role in the intermolecular interaction, recognition, and conformations of both small and large molecules. In the past decade, it has been recognized that weak C-H···O hydrogen bonds play important roles in the formation of molecular solids [1]. This also confirms the importance of C-H···O contacts for the transmission of magnetic interactions along a particular direction [2]. Now we performed a low-temperature X-ray diffraction (XRD) experiment on radical compounds in order to study such intermolecular interactions by high-resolution X-ray diffraction analysis at very low temperatures. To combine the multipole model of the atom in molecular and topological analyses, we can derive experimental bonding and weak interaction characters from the total electron density, which can be compared with those obtained from theoretical calculations. Taking advantage of the extremely low background of the vacuum chamber camera (VACC) at beamline **BL02B1**, the data quality is greatly improved. Therefore, a precise and accurate multipole model of the molecular solid can be obtained. In this experiment, the X-ray diffraction data was collected at 30 K [3].

The TEMPO (Tetramethyl Piperidin-1-Oxyl) series radical compounds are known to be relatively stable radical compounds. The (PNB-TEMPO) radical molecule as viewed from the b axis, is shown in Fig. 1(a), and the difference Fourier map of the molecular plane is shown in Fig. 1(b). In the case of PNB-TEMPO (Para-Nitronyl-4-Benzylideneamino-2,2,6,6-TEtraMethyl Piperidin-1-Oxyl), all the residual electron peaks are found to be in the middle of the interatomic regions, which means that the aspherical electron distribution can be well described in terms of the multipole model.

The molecule has a mirror plane that is perpendicular to the **b** axis; all atoms except the tetra methyl piperidin moiety are on the molecular plane, the distance between layers is 4.769(2) Å, the shortest distance between the different sites of O1 is 5.369(2) Å. The selected distances of the molecular solid are listed in Table 1. The O···H distance is shorter than the sum of the van der Waals' radii (2.72 Å), which makes the packing a pseudo-one-dimensional infinite chain system connected by hydrogen bonds. The spatial arrangement of the chains is in a zigzag configuration along **a** axis. From a polarized neutron diffraction (PND) experiment, we have observed the effect of the magnetic interactions along the chain via the hydrogen bonds, which connect neighboring molecules. The magnetic interactions induced the depletion of the spin density of the oxygen atoms of the hydrogen bonds and some spin density is found to be delocalized among hydrogen-bonded hydrogen atoms. This is reconfirmed by the *ab initio* DFT (Density Functional Theory) theoretical calculations: i.e., the depletion of the spin density of oxygen atoms is quantitatively identified; however, the delocalization of the spin density of the hydrogen-bonded hydrogen atoms can only be qualitatively described. These results clarify the mechanism of the magnetic interactions in these organic magnetic systems.

The theory of atoms in molecules [4] has been

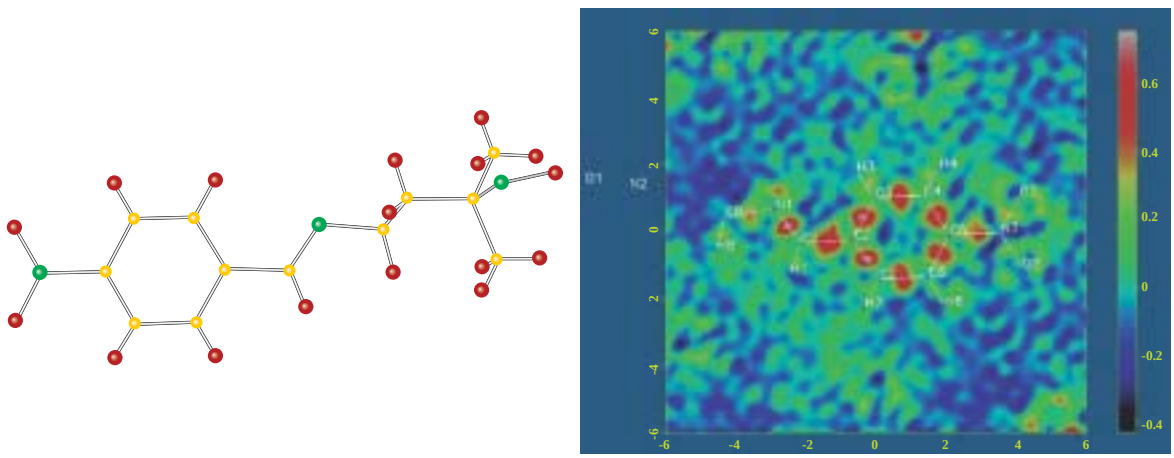

Fig. 1. **(a)** ORTEP (Oak Ridge Thermal Ellipsoid Plot) drawing of PNB-TEMPO monomer molecule. **(b)** Residual map of PNB-TEMPO at molecular plane. Data collected at 20 K.

Table 1. Selected intermolecular bond distances of PNB-TEMPO at 125 K, 30 K and 20 K(Neutron)

	X-ray (125K)	X-ray (30K)	Neutron (20K)
Bond	Distance	Distance	Distance
O1-H7A	2.423(1)	2.532(1)	2.411(1)
O1-H8B	2.483(1)	2.533(1)	2.446(1)
O1-C7A	3.414(2)	3.394(2)	3.385(1)
O1-C8B	3.553(2)	3.539(2)	3.523(1)

used to describe and characterize intramolecular and intermolecular hydrogen bonding solely from the total charge density for a large set of donor and acceptor molecules. This theory has also provided new insights to intermolecular hydrogen bonding. Even in the characterization of the C-H···O weak hydrogen bond, such interactions can still be recognized by applying topological analysis to an accurate experimentally determined electron density [5]. Bader classifies the hydrogen bond interactions as shared interactions and closed-shell interactions by the sign of $\nabla^2\rho(r_c)$ and the magnitude of $\rho(r_c)$. In addition to the properties associated with the bond critical point, the existence of the bond path between the bonded atoms is also necessary for the characterization of hydrogen bond interactions [6].

Table 2 shows the topological properties associated with the bond critical point of the O···H-C intermolecular hydrogen bond, as determined by experimental X-ray diffraction analysis (a) and theoretical calculation of the dimer (b) and infinite linear chain (c); all three results agree very well with one another. Based on Bader's theory, this interaction can be classified as a closed-shell interaction.

In conclusion, the magnetic interactions between organic radical molecules in a solid along a specific direction are mediated purely through C-H···O hydrogen bonds. Direct observation of such magneto-structural correlation includes use of magnetic measurements, highly accurate single crystal diffraction, and PND measurements.

Yu Wang[a] and Jey Jau Lee[b,*]

(a) Department of Chemistry, National Taiwan University, Taiwan
(b) National Synchrotron Radiation Research Center, Taiwan

*E-mail: jjlee@nsrrc.org.tw

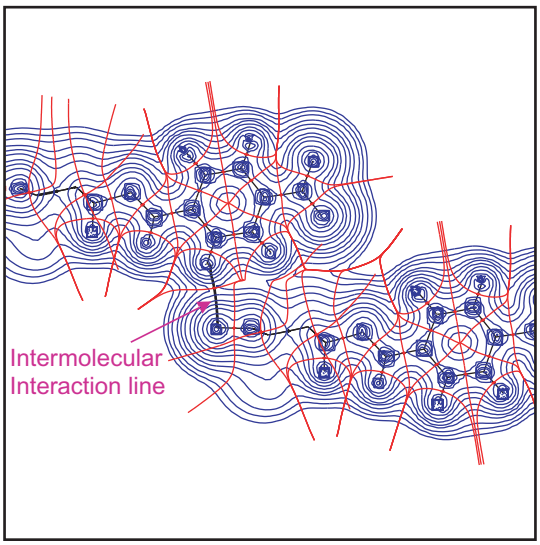

Fig. 2. Intermolecular interaction evidenced by bond path (black), atom domain (red) superimposed on total electron density (blue) at the molecular plane of PNB-TEMPO dimmer.

Table 2. Topological properties at bond critical point of O···H-C hydrogen bond on PNB-TEMPO:
(a) multipole model
(b) Gaussian98/UB3LYP (6-31G(D, P))
(c) crystal98/UB3LYP (6-31G(D, P))

Bond/ Bond distance	d1 (Å)	d2 (Å)	$\nabla^2\rho(r_c)$(eÅ^{-5})	$\rho(r_c)$(eÅ^{-3})
(a) O1-H7A /2.411(1)	1.516	1.042	0.80	0.040
(b)	1.449	0.974	0.76	0.068
(c)	1.452	0.971	0.75	0.070

References

[1] G. Desiraju: Acc. Chem. Res. **24** (1991) 290.
[2] F.M. Romero *et al.*: J. Am. Chem. Soc. **122** (2000) 1298.
[3] *J.-J. Lee, Y. Wang, K. Toriumi and Y. Ozawa - in preparation.*
[4] R.W.F. Bader: Atoms in Molecules. A Quantum Theory. Oxford University Press (1990).
[5] G.A. Jeffrey and J.F. Piniella: Eds. The application of charge density research to chemistry and drug design, Plenum Press, New York (1991).
[6] R.G.A. Bone and R.F.W. Bader: J. Phys. Chem. **100** (1996) 10892.

Disordered Zinc in Thermoelectric Material Zn_4Sb_3 with Phonon-glass and Electron-crystal Properties

By converting waste heat into electricity, thermoelectric generators could be an important part of the solution to today's energy challenges. The compound Zn_4Sb_3 is one of the most efficient thermoelectric materials known. Its high efficiency results from the extraordinarily low thermal conductivity in conjunction with the electronic structure of a heavily doped semiconductor. The efficiency of a thermoelectric generator depends on the thermoelectric figure of merit zT, where z is defined as $z = S^2\sigma/\kappa$ (S is the Seebeck coefficient, s the electrical conductivity, and κ is the thermal conductivity). S and s in Zn_4Sb_3 are not exceptionally high, and the power factor ($S^2\sigma$) is only half that of optimally doped $(Bi, Sb)_2Te_3$ [1]. It is the extremely low lattice contribution to the thermal conductivity, which gives Zn_4Sb_3 a very high zT. Previous structural studies have been unable to explain the unusual properties [2]. We have determined the maximum entropy method (MEM) electron density (ED) from synchrotron X-ray powder diffraction data, and Bader topological analysis [3] of the MEM density reveals that the origin of the remarkable physical properties is additional interstitial zinc atoms [1]. The discovery of glass-like interstitial sites uncovers a highly effective mechanism for reducing thermal conductivity. The analysis also leads to the identification of Sb^{3-} ions and Sb_2^{4-} dimers, and this shows that Zn_4Sb_3 is a Zintl semiconductor with ideal stoichiometry $Zn_{13}Sb_{10}$ [4].

Accurate diffraction studies of high symmetry inorganic solids containing heavy atoms are very challenging. Systematic errors such as absorption, extinction, anomalous scattering and twinning can seriously compromise the level of structural detail that can be extracted from the data. To overcome these problems we have used high energy synchrotron X-ray powder diffraction on a minute sample (0.2 mm capillary) at beamline **BL02B2**. The accuracy of the diffraction data is critical when MEM analysis is used, since the MEM has no "filter" to remove systematic discrepancies in the data [5]. The MEM has in recent years provided insight into the structure and chemical bonding in many interesting solids [6]. However, the limitation of the method has been that visualization of the thermally smeared ED only provides qualitative information. To quantify the electronic features we have used Bader topological analysis [4]. Our results show that important new information can be obtained by this method, and it greatly enhances the potential for extracting useful chemical and physical information from MEM EDs.

High-resolution synchrotron X-ray powder diffraction data were collected with λ = 0.42061 Å (d_{min} = 0.626 Å). The space group is R-3c with a = 12.22320(4), c = 12.41608(7) Å . The details of combined Rietveld/MEM analysis of powder diffraction data have been extensively presented in the literature [6]. In Figs. 1 and 2 the crystal structure and the corresponding MEM thermally smeared ED are shown. Interstitial zinc atoms are clearly observed as small secondary maxima in the MEM density. Based on bonding distances there are 18 free Sb^{-3} ions (Sb1) and 6 $(Sb2)^{-4}$ dimers (Sb2) in the unit cell requiring a total donation of 78 electrons from 39 Zn^{2+} ions for charge balance [1]. This is close to the stoichiometry of the present model, and Zn_4Sb_3 may be considered a Zintl phase. The MEM density provides direct evidence for the Zintl model, and the Sb-Sb dimer does indeed show covalent bonding density, Fig. 2. In contrast, the ED of the other Sb atom is more spherical. Bader topological analysis of the MEM ED establishes six maxima corresponding to two Sb atoms and one Zn atom forming the basic crystal structure, and three Zn interstitials. The positions of the maxima give a quite short Zn-Zn contact of 2.13 Å. However, since X-ray diffraction measures the average crystal structure, all the

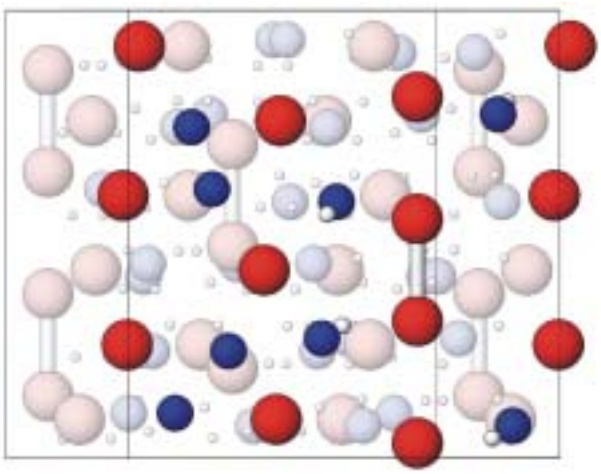

Fig. 1. The crystal structure of Zn_4Sb_3 including three interstitial Zn sites (small spheres). Sb atoms are red, Zn atoms on the main lattice site are blue. Atoms in or near the plane of Fig. 3 are highlighted.

interstitials are not necessarily present in the same unit cell. Nevertheless, we have refined a model with a restraint of 2.25 Å on the Zn-Zn distances. The restraint distance of 2.25 Å was determined from a series of refinements where the distance restraint on the Zn-Zn contacts was increased in steps between 2.0 to 2.5 Å. A minimum in Rietveld refinement reliability factors was found for 2.25 Å. Hg and Cd dimers are well known but only very recently firm experimental evidence for a Zn dimer was reported with a Zn-Zn distance of 2.30(3) Å [7]. There are other peculiar features in the MEM density. On the "back side" of the Sb dimer we locate a small maximum along the *c*-axis. This non nuclear maximum (NNM) is unlikely to be interstitial atoms, since the Sb sites are fully occupied and the Sb to NNM distance is very short. In Fig. 3 the Bader atomic basins are shown for the different types of atoms. The plot shows that the Sb atoms indeed have very different volumes and charge distributions. The atomic volume of the NNM fits perfectly into a void in the Sb_2 atomic volume along the *c*-axis. The NNM suggests that Zn_4Sb_3 may in fact also have Sb disorder along the *c*-axis. In summary the density contains one partly occupied main Zn site, three Zn interstitials and Sb disorder along the *c*-axis. These are all features which contribute to the drastic reduction of the thermal conductivity.

Fig. 3. Atomic surfaces defined by the Bader zero flux condition. The Zn_4Sb_3 structure is viewed nearly along the *c*-axis. The light shiny green basins along the *c*-axis correspond to the "dimer" Sb atom. At the top of the Sb dimer a non nuclear maxima (blue) fits exactly into the void. The red basin is the main Zn atom, the purple basins the interstitial Zn atoms, and the matt green basin is the Sb^{3-} ion.

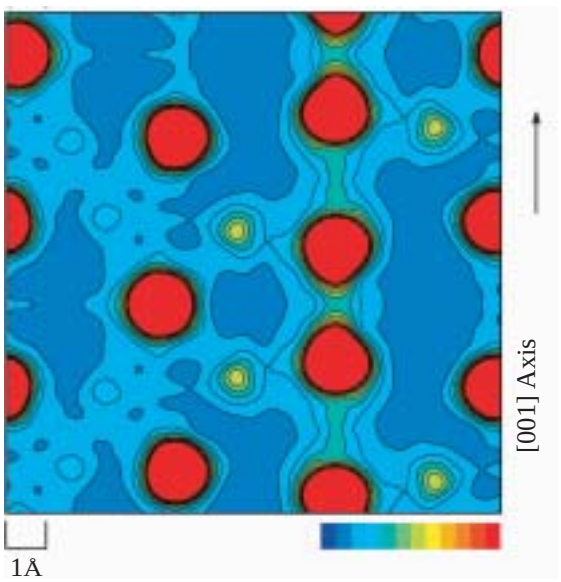

Fig. 2. Contour plot of the MEM density in the Sb_2^{4-} dimer region. The contour level is 0.2 e/Å^3.

Eiji Nishibori[a], G. Jeffrey Snyder[b], Philippe Rabiller[c], Mogens Christensen[d] and Bo Brummerstedt Iversen[a,*]

(a) Department of Applied Physics, Nagoya University
(b) Jet Propulsion Laboratory, California Institute of Technology, USA
(c) GMCM, UMR CNRS, France
(d) Department of Chemistry, University of Aarhus, Denmark

*E-mail: bo@chem.au.dk

References

[1] *G.J. Snyder, M. Christensen, E. Nishibori, T. Caillat and B.B. Iversen: Nature Materials* ***4*** *(2004) 458.*
[2] H.W. Mayer *et al.*: J. Less-Common Metals **59** (1978) 43.
[3] R.F.W. Bader: Atoms in Molecules, A Quantum Theory, Oxford University Press (1990).
[4] F. Cargnoni *et al.*: Chem. Eur. J. **10** (2004) 3861.
[5] B.B. Iversen *et al.*: Philos. Mag. A **72** (1995) 1357.
[6] M. Takata *et al.*: Z. Kristallogr. **216** (2001) 71.
[7] I. Resa *et al.*: Science **305** (2004) 1136.

Doping Effect of Cu-O Bond Stretching Phonon in $La_{2-X}Sr_XCuO_4$ Studied by Inelastic X-ray Scattering

Since the discovery of superconductivity in copper oxides in 1986 many different kinds of experiments have been carried out in order to investigate the mechanism of superconductivity, and also many different mechanisms have been suggested from a theoretical point of view to explain the high transition temperatures of cuprates. However, the driving mechanism for Cooper-pair formation in cuprates remains unclarified despite such large efforts from both experimental and theoretical sides for almost two decades. Since the critical temperature (TC) observed in various cuprates, including $La_{2-X}Sr_XCuO_4$, is too high to explain the Cooper-pair formation by the so called BCS theory, which is based on a phonon mechanism, only limited attention has been paid to phonons for the mechanism of superconductivity in cuprates. Recently, however, angular resolved photoemission spectroscopy (ARPES) [1] and inelastic neutron scattering (INS) measurements [2] led to a renewed interest in phonons. INS measurements show a strong softening in the highest energy LO phonon branch with hole doping of $La_{2-X}Sr_XCuO_4$ (LSCO) and $YBa_2Cu_3O_{7-\delta}$ (YBCO). However, since such softening is observed among other nonsuperconducting oxides such as manganites and nickelates, the relationship between the softening and high-T_C superconductivity is not clear. In order to clarify a clear correlation of this phonon mode with the superconductivity, one would like to see the behavior of this phonon softening in the over-doped region where superconductivity is degraded and normal metallic conductivity dominates. For this purpose, we study by IXS the Cu-O bond stretching LO phonon of LSCO, which has a simple layered structure with single CuO_2 planes and whose doping concentration X can be controlled readily from the nondoped insulator phase to the overdoped normal metallic phase through the superconducting phase (see Fig. 1(a)). Therefore, one can expect to successfully investigate the doping dependence of the phonon properties precisely. For this purpose, we used two types of sample: one with a uniform Sr concentration in the crystal, and an other in which the concentration varies smoothly along the cylindrical axis (gradient sample) (see Fig. 1(b)). These samples enable us to investigate the doping dependence easily because IXS requires a small sample size. In this report, we use the tetragonal notation, in which the main (a,b) axes are parallel to Cu-O bonds in the CuO_2 plane. The superconducting transition was observed by measurement of the diamagnetic susceptibility, and the results are consistent with those in the published literature.

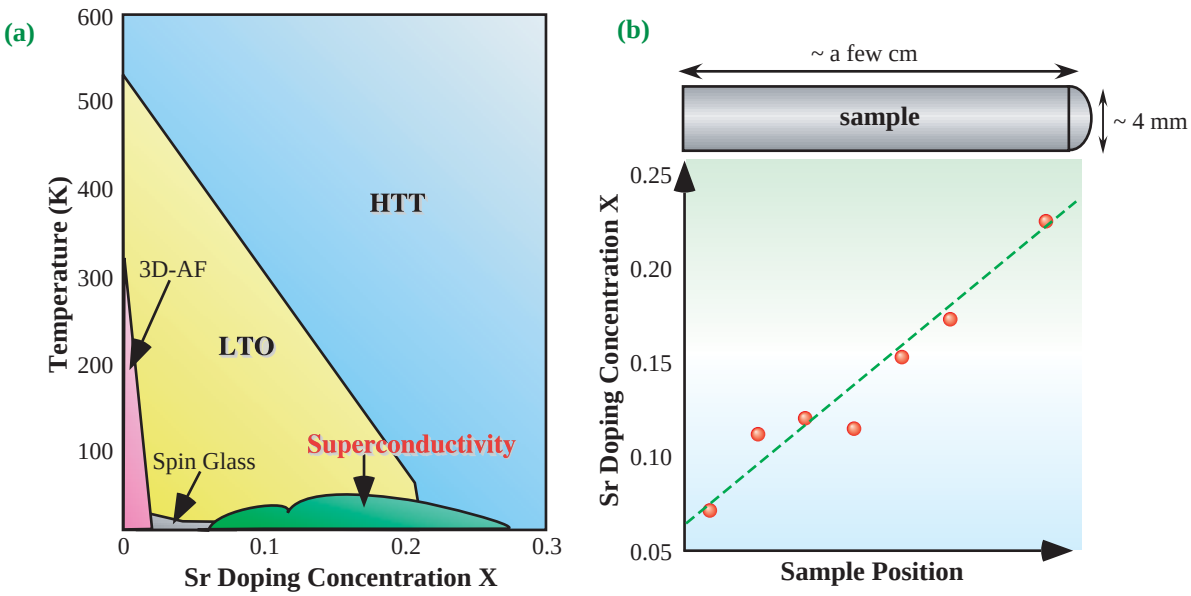

Fig. 1. **(a)** Schematic drawing of phase diagram of $La_{2-X}Sr_XCuO_4$ as a function of doping concentration X. **(b)** Doping concentration gradient of single crystal. X changes from 0.07 to 0.23 from one end to the other end of the single crystal.

The IXS experiments were performed at beamline **BL35XU**. The momentum and energy resolution in the experiment with 15.816 keV incident X-ray energy and about 100 μm spot size were about 0.076 $Å^{-1}$ and 6.0-6.2 meV (FWHM), respectively. The IXS measurements were performed with the sample in a reflection mode at 13 K and room temperature for X = 0.12, and at 60 K for X = 0.29. The reason for the measurements at low temperature is simply to reduce the tails of low energy phonons, and is not related to the measurement of superconducting transition. We focus on the LO high-energy Cu-O bond stretching phonons in the CuO_2 plane. Figure 2 shows the obtained dispersion of this mode for the samples with various doping concentrations together with neutron data, and Fig. 3 shows the amplitude of the softening, which is defined by the difference in energy between the maximum and minimum of the dispersion as a function of X [3], together with the results of recent theoretical calculations [4]. As can be seen, the softening shows a highly nonlinear dependence on X. Khaliullin and Horsch theoretically predicted that the softening simply depends linearly on X if no interaction between the low energy charge collective mode and the phonon is introduced [5]. Then, the anomalous softening can be defined as the deviation from the linear dependence of the softening on X, which is shown in Fig. 3 as a dashed line. The X dependence of T_C measured for the studied single crystals is also shown in Fig. 3. What should be noticed is that anomalous softening occurs near the superconducting region, and the maximum deviation is seen at around the optimum doping concentration. The present observation of the precise X dependence of the phonon softening in the normal metallic phase will evoke further discussion and studies to elucidate the reason for the anomalous softening in high-temperature superconducting cuprates.

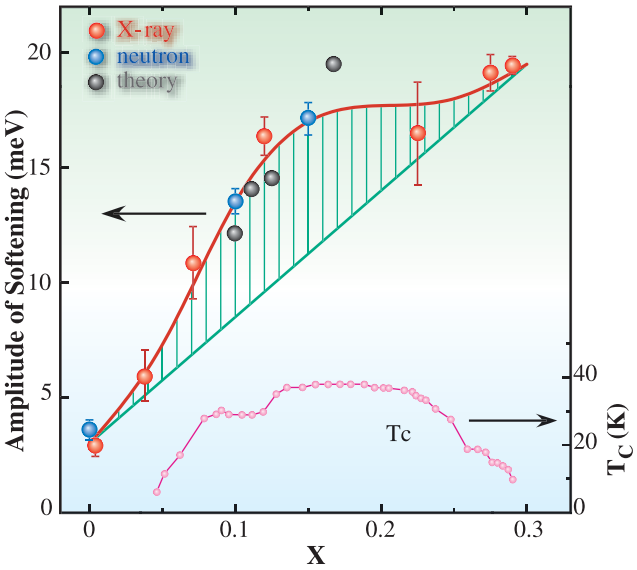

Fig. 3. Amplitude of softening as a function of doping concentration, X, together with results of theoretical calculations [4].

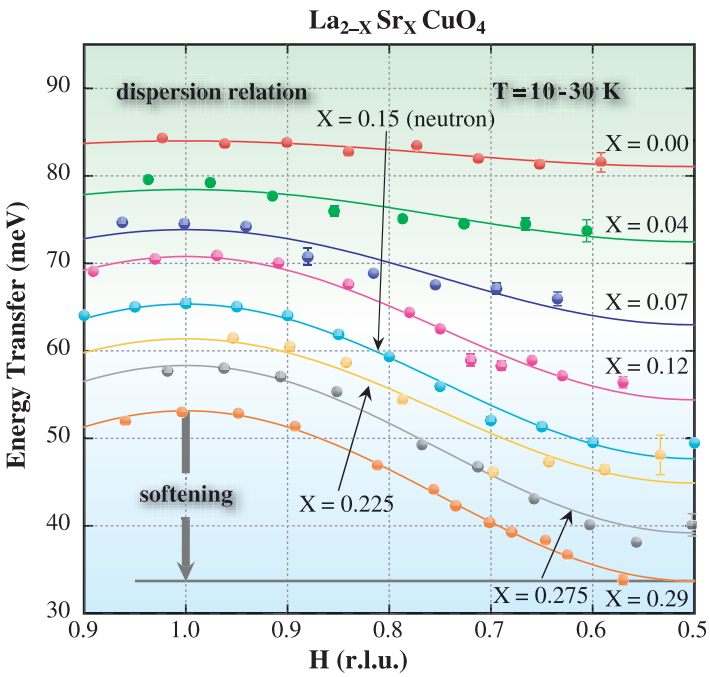

Fig. 2. Dispersion of Cu-O bond stretching LO mode for various doping concentrations, X.

J. Mizuki*, T. Fukuda and K. Yamada

SPring-8 / JAERI

*E-mail: mizuki@spring8.or.jp

References

[1] A. Lanzara *et al.*: Nature **412** (2001) 510.
[2] L. Pintschovius *et al.*: in Physical Properties of High Temperature Superconductors IV, (World Scientific, Singapore, 1994); L. Pintschovius *et al.*: Phys. Rev. B **60** (1999) R15039.
[3] *T. Fukuda, J. Mizuki, K. IKeuchi, K. Yamada, A.Q.R. Baron and S. Tsutsui: to be published in Phys. Rev. B: Rapid Comm.*
[4] O. Rosch and O. Gunnarsson: Phys. Rev. Lett. **92** (2004) 146403.
[5] G. Khaliullin and P. Horsch: Physica C **282-287** (1997) 1751; P. Horsch and G. Khaliullin: cond-mat/0312561 (2003).

Crystal Structure of Superconducting Sodium Cobalt Oxide

A sodium cobalt oxide with a bilayer-hydrate structure (BLH-Na_xCoO_2) was the first superconductor recently found in the cobalt oxide system [1]. It has a layered structure built up from CoO_2 layers with guest species in the galleries. Although the guest species had been believed to be Na^+ ions and H_2O molecules, the present structural analysis combined with our recent study based on chemical analysis and Raman spectroscopy has revealed that H_3O^+ ions are accommodated in the galleries as well [2].

The highly disordered arrangement of its guest species makes the structure analysis difficult. Diffraction data of higher quality will help us to clarify the complex structural aspects associated with guest species. In addition, we need to determine the crystal structure at low temperatures, where the superconducting transition takes place. The superconducting transition is, in general, not accompanied by a structural phase transition. However, in the present material, the crystal structure at low temperatures might be different from that at room temperature. Its guest species are mobile or diffusible; therefore, the structure may be modified by rearrangement of the guest species at low temperatures. In fact, the first-order phase transition was observed in $Na_{0.75}CoO_2$. If such a phase transformation occurs at a temperature higher than T_c, the superconducting mechanism should be discussed on the basis of the low-temperature phase. From the above requirements, the crystal structure of superconducting BLH-Na_xCoO_2 was reinvestigated using synchrotron radiation in the temperature range down to 12.5 K.

Synchrotron XRD data were measured using a Debye-Scherrer-type camera installed at beamline **BL02B2** [3]. The crystal structures were determined by Rietveld and maximum-entropy method (MEM) analyses using the computer programs RIETAN-2000 [4] and PRIMA [5], respectively.

Cooling BLH-Na_xCoO_2 down to 12.5 K did not bring about the appearance of any additional reflections in its diffraction patterns. All the reflections were indexable on the basis of hexagonal unit cells. Monotonous changes in lattice parameters given in Fig. 1 show the absence of phase transitions in this temperature range.

The structure parameters of BLH-Na_xCoO_2 were refined according to the previous structure model based on the space group $P6_3/mmc$ (No. 194) [1] with some modifications. In the present structure model, the 2*b* (0, 0, 1/4) and 2*d* (2/3, 1/3, 1/4) sites are occupied not only by Na^+ ions but also by H_3O^+ ions, because the Raman spectrum evidenced the presence of H_3O^+ ions at these sites. In the final refinement, Na^+ and H_3O^+ ions at the 2*b* site were split into the 4*e* (0, 0, z) site with $z \approx 0.24$, because MEM analysis showed that the isosurfaces for number densities, ρ, of electrons around the 2b site were elongated along the *c* axis as shown in Fig. 2. Figure 3 shows the Rietveld refinement pattern, and Table 1 lists the refined structure parameters at room temperature.

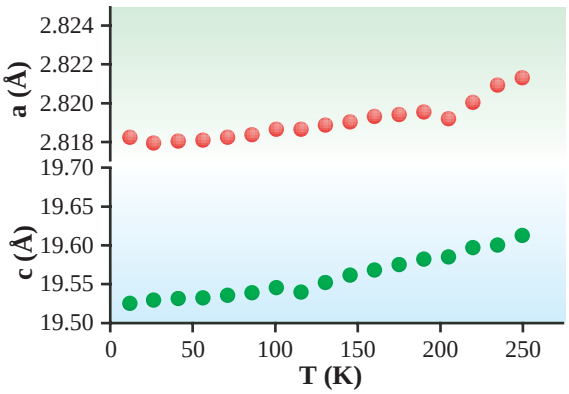

Fig. 1. Lattice parameters at various temperatures.

Table1. Structure parameters for BLH-Na_x CoO_2 at room temperature

Atom	Site	*x*	*y*	*z*	*g*	*U* / Å^2
Co	2*a*	0	0	0	1	0.0062(2)
O	4*f*	1/3	2/3	0.04578(12)	1	0.0091(5)
M1 (Na/H_3O)	4*e*	0	0	0.2413(12)	0.182(3)	0.047(4)
M2	2*d*	2/3	1/3	1/4	0.216*	0.030(4)
WO1(H_2O)	12*k*	0.137(2)	= 2*x*(WO1)	0.1700(5)	0.111(5)	0.026(5)
WO2	12*k*	0.875(6)	= *x*(WO2)/2	0.1757(6)	0.088*	0.023(8)

a = 2.82374(10) Å and *c* = 19.6576(8) Å; R_{wp} = 5.10% (S = 2.67), R_p = 3.28%, R_B = 1.75%, and R_F = 1.70%. Virtual chemical species, WO and M, were used in the refinement. WO denotes an H_2O molecule whose atomic scattering factor was set to be equal to the sum of one O atom and two H atoms. M has mean scattering amplitude of Na^+ ions and H_3O^+ ions with the atomic scattering factor set equal to the sum of one O atom and three H atoms. The Na^+:H_3O^+ amount-of-substance ratio was fixed at 0.591:0.409, and the total contents of M and WO were fixed at 0.580 and 1.19, respectively, which were determined by the chemical analyses.

In BLH-Na_xCoO_2, the guest species in the galleries are highly disordered. MEM is quite effective for detailed structure analysis of such a compound, because disordered structures are much better expressed by electron densities in the unit cell used in MEM than by structure parameters in Rietveld analysis. Indeed, MEM-based whole-pattern fitting, in which structure factors were fixed at those evaluated from the electron density distribution calculated by MEM, decreased the *R* factors from R_{wp} = 5.10%, R_B = 1.75% and R_F = 1.70% in the Rietveld analysis to R_{wp} = 4.99%, R_B = 1.34% and R_F = 1.25%.

Final R factors were low sufficiently, and most of the interatomic distances were consistent with those in other hydrates or Na^+-intercalation compounds, supporting this structure model.

The isotropic atomic displacement parameters, *U*, did not converge to reasonable values without any constraints, when the structure model did not include H_3O^+ ions. The introduction of H_3O^+ ions into the structure model made the values reasonable; they increased in the following order: *U* parameters for the heavy Co ion, for oxygen bonded to Co, and for guest species (Na^+, H_3O^+, and H_2O) bound loosely, which strongly suggests that BLH-Na_xCoO_2 accommodates H_3O^+ ions as well as Na^+ ions and H_2O molecules in its galleries.

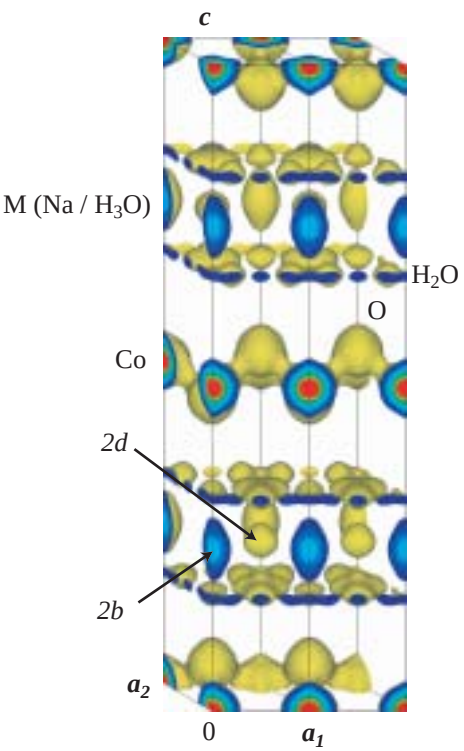

Fig. 2. Isosurfaces for number densities of electrons. Equidensity level: 1.0 A^{-3}.

An interesting structural feature was an unusually short Co—O bond length (1.8622(12) Å). It was much shorter than the value of 1.91 Å estimated by bond valence calculation on the basis of the analyzed Co oxidation state of +3.42. In addition, the formation of the BLH-phase from the anhydrous one during the hydration process is accompanied by the reductive insertion of H_3O^+ ions [2], which donate electrons to the Co ions. The donation should increase the ionic radii of Co ions and thus the Co—O bond length; however it decreased from 1.8875(15) Å in the anhydrous phase [2]. In this structure, the electrons are encaged in unusually narrow spaces, which may enhance the correlation between electrons and induce the superconductivity.

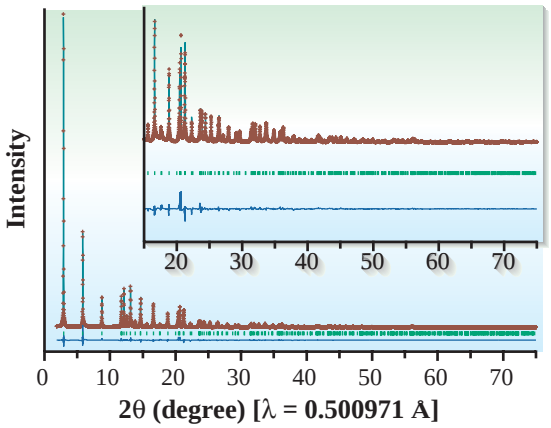

Fig. 3. Rietveld refinement pattern of BLH-Na_xCoO_2 at room temperature.

Kazunori Takada [a,c,*] and Izumi Nakai [b]

(a) Advanced Materials Laboratory, National Institute for Materials Science
(b) Faculty of Science, Tokyo University of Science
(c) CREST, Japan Science and Technology Agency

*E-mail: takada.kazunori@nims.go.jp

References

[1] *K. Takada, H. Sakurai, E. Takayama-Muromachi, F. Izumi, R.A. Dilanian and T. Sasaki: Nature* ***422*** *(2003) 53.*
[2] *K. Takada, K. Fukuda, M. Osada, I. Nakai, F. Izumi, R.A. Dilanian, K. Kato, M. Takata, H. Sakurai, E. Takayama-Muromachi and Takayoshi Sasaki: J. Mater. Chem.* ***14*** *(2004) 1448.*
[3] E. Nishibori *et al.*: Nucl. Instrum. Meth. A **467-468** (2001) 1045.
[4] F. Izumi and T. Ikeda: Mater. Sci. Forum **321-324** (2000) 198.
[5] F. Izumi and R.A. Dilanian: Recent Research Developments in Physics; Transworld Research Network, Trivandrum **3** (2002) 699.

High-quality As-grown MgB_2 Film Fabrication at Low Temperature using In-plane-lattice Near-matched Epitaxial-buffer Layer

To date a process for fabricating a superconducting MgB_2 [1] thin film has required a growth and/or annealing temperature higher than 600 ºC [2]. When such a process is applied to the fabrication of an integrated device, interdiffusion occurs at interfaces between the integrated layers, which degrades the quality of the device. This is one problem faced in fabricating a high-quality integrated device. We succeeded in the fabrication of high-quality as-grown MgB_2 films [3] and their structural and superconducting characterization [4]. One of the keys to success was the utilization of low-temperature crystal growth combined with a near-matched epitaxial buffer layer. We clarified the function of the buffer layer from a structural point of view.

A TiZr buffer layer was deposited on a sapphire Al_2O_3 (0001) substrate at 815 ºC by evaporation of a Ti-50 at % Zr alloy source. After the substrate was cooled to room temperature, MgB_2 films were deposited at 270 ºC by coevaporation of Mg and B metals, which were evaporated using an effusion cell and an electron beam gun, respectively. The film and buffer layer were determined to be about 300 and 100 nm in thickness, respectively, by high-resolution SEM observation. For a control experiment, we also prepared a MgB_2 film (without the buffer layer) grown on a sapphire (0 0 0 1) substrate.

Superconducting properties were examined resistively and magnetically. The critical temperature T_c of $MgB_2/TiZr/Al_2O_3$ was about 1 K higher than that of $MgB_2/TiZr/Al_2O_3$ (not shown here). The applied magnetic field dependences of magnetizations were measured under a perpendicular magnetic field to the film surface. The critical current density J_c was estimated from a magnetization hysteresis loop based on the Bean critical state model. The larger hysteresis loop for $MgB_2/TiZr/Al_2O_3$ in comparison with that for MgB_2/Al_2O_3 corresponds to a higher capacity for the flow of current in the former MgB_2 film. J_c at 5 K under 1 T magnetic flux density is 6×10^5 A/cm^2 for $MgB_2/TiZr/Al_2O_3$. J_c obtained from MgB_2/Al_2O_3 is much smaller than this value at 9×10^4 A/cm^2, suggesting that the crystallinity of the MgB_2 film in the $MgB_2/TiZr/Al_2O_3$ could be much improved.

X-ray measurements for film-structural analysis were performed with a six-circle diffractometer at beamline **BL13XU** [5]. An X-ray wavelength of 0.102 nm was used. We located the sample at the 0 1 $\bar{1}$ 1 Bragg position and rotated it around the [0 0 0 1] direction L (almost the surface normal) to record X-ray intensities diffracted from the film (Fig. 1). The MgB_2 film without the buffer layer was a *c*-axis oriented crystal and had no epitaxial relation. Accordingly, we concluded that the crystallinity of the film with the

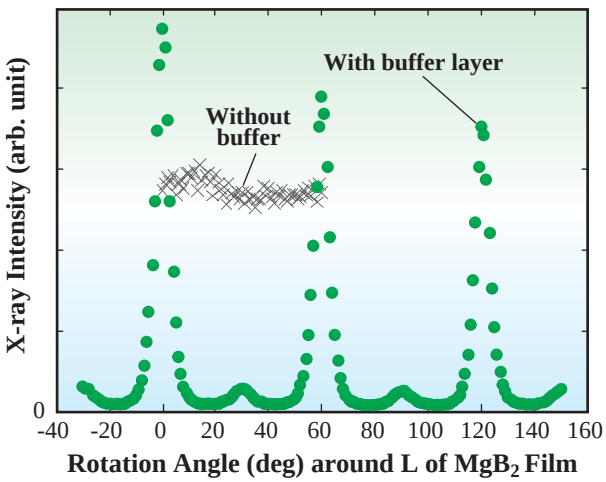

Fig. 1. L *vs.* X-ray intensity scattered from MgB_2 film on the buffer layer (solid circles) and without the buffer layer (crosses). The peaks came from the 0 1 $\bar{1}$ 1 reflection [4].

buffer layer was improved.

By similar measurements, it was determined that the buffer layer was also crystalline. The epitaxial relationship in a plane perpendicular to L was obtained: MgB_2 (majority domain) [0 1 $\bar{1}$ 0] // TiZr [0 1 $\bar{1}$ 0] and TiZr [0 1 $\bar{1}$ 0] // sapphire [1 1 $\bar{2}$ 0].

q_R, q_T and $q_\perp$ scans were carried out in the reciprocal-lattice space to determine in-plane lattice spacings of MgB_2 and the TiZr buffer layer. The q_R and q_T scans were parallel to the radius and tangential direction in the L-constant plane (almost in-plane) passing through a desired Bragg position, respectively. The $q_\perp$ scan was parallel to L around the position. The obtained in-plane lattice spacings, $d_{//}^{MgB_2}$, $d_{//}^{TiZr}$, and $d_{//}^{sapphire}$ are 0.268, 0.258, and 0.239 nm for the MgB_2 (0 1 $\bar{1}$ 0), TiZr (0 1 $\bar{1}$ 0), and sapphire (1 1 $\bar{2}$ 0) planes, respectively. It is noted that $d_{//}^{TiZr}$ was between $d_{//}^{MgB_2}$ and $d_{//}^{sapphire}$. The crystallinity of the film with the buffer layer became higher accordingly.

From FWHMs of Δq_R, Δq_T, and $q_\perp$, we estimated crystal mosaic spreads. The spreads are 6.1º and 0.38º for the MgB_2 film and the TiZr layer, respectively. We plot the spreads with respect to the in-plane lattice spacings (Fig. 2). The spread of the MgB_2 film was around 6º, while the film without the buffer layer was the *c*-axis oriented crystal. This suggests that the buffer layer improves the crystallinity of the MgB_2 film.

In summary, we have found that the in-plane-lattice near-matched TiZr buffer layer aided the fabrication of the as-grown MgB_2 crystalline film. This is because the in-plane lattice spacing of the buffer layer was between those of MgB_2 and the substrate crystal. T_c and J_c of MgB_2/TiZr/Al_2O_3 were found to be higher than those of MgB_2/Al_2O_3. The near-matched epitaxial crystallinity of the buffer-layered TiZr was of cardinal importance in the low-temperature growth of the high-quality as-grown MgB_2 film.

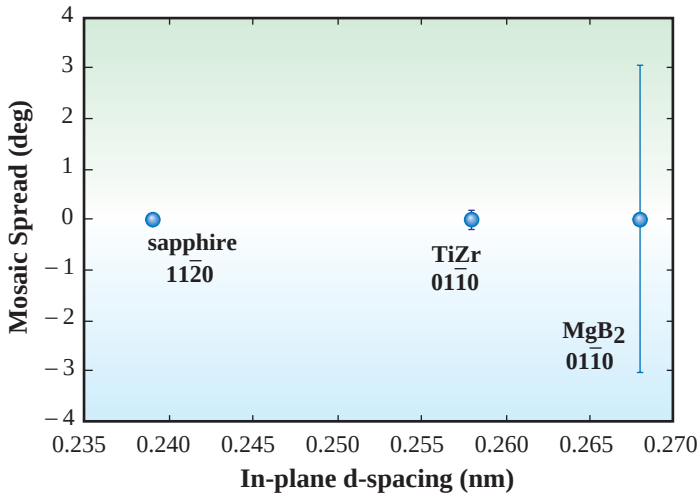

Fig. 2. Measured in-plane lattice spacings and mosaic spreads [4].

Osami Sakata[a,*], Shigeru Kimura[a] and Shugo Kubo[b]

(a) SPring-8 / JASRI
(b) Department of Materials Science, Shimane University

*E-mail: o-sakata@spring8.or.jp

References

[1] J. Nagamatsu *et al.*: Nature **410** (2001) 558.
[2] W.N. Kang *et al.*: Science **292** (2001) 1521.
[3] S. Yata *et al.*: Physica C **388-389** (2003) 155.
[4] *O. Sakata, S. Kimura, M. Takata, S. Yata, T. Kato, K. Yamanaka, Y. Yamada, A. Matsushita and S. Kubo: J. Appl. Phys.* ***96*** *(2004) 3580.*
[5] O. Sakata *et al.*: Surface Rev. Lett. **10** (2003) 543.

X-RAY DIFFRACTION STUDY OF CHARGE-DENSITY-WAVE PHASE TRANSITION ON In/Cu(001)

There is a growing interest in phase transitions in ultrathin films and wires. This is due in part to the technological trends toward electronic devices with dimensions much smaller than those of the currently used ones. The phenomena of interest include Peierls-type charge-density-wave (CDW) phase transitions, which are driven by the electron–phonon interaction in metallic materials with low-dimensional electron systems and are associated with changes in transport properties, which thus potentially useful in applications such as switching and memory.

As solid surfaces and interfaces provide quasi-two-dimensional electron systems, efforts have long been made to the observation of CDW transitions restricted to a few atomic layers on surfaces. Recently, intriguing surface phase transitions [1] have been found and a Peierls-type scenario was suggested as the driving mechanism. These phase transitions have received wide attention. However, in spite of extensive investigations, the driving mechanism is still a matter of intense controversy. The confusion is partly due to the difficulty of quantitatively characterizing phase transitions restricted to a few atomic layers on surfaces. Since the CDW phase transitions are driven by electronic and lattice degrees of freedom coupled with each other, it is desirable to study the dynamical behavior of the electrons and the lattice during the phase transition; this, however, has not yet been realized for these surface phase transitions.

Most recently, we have studied the phase transition on the Cu(001) surface covered with 0.63 ML of In. Grazing-incidence surface X-ray diffraction (GISXRD) [2] was used to observe the critical behavior of the lattice [3]. Angle-resolved photoelectron spectroscopy (ARPES) was used to study the temperature dependence of the CDW energy gap [4]. Only by combining these two classes of experimental data, we have succeeded in constructing a comprehensive picture of the CDW phase transition on this surface [3].

Figure 1 shows scanning-tunneling-microscopy (STM) images for the high-temperature (HT) p(2×2) and low-temperature (LT) c(4×4) phases. The phase transition is reversible. We have found by ARPES that the energy gap is formed at the Fermi level during the phase transition from the HT to LT phase. The energy gap coincided with the Brillouin zone of the LT c(4×4) phase, which indicates that the transition is a Peierls-type CDW transition. We also determined the temperature dependence of the absolute energy gap (energy interval between lower and higher bands). Upon elevating the temperature, the energy gap gradually decreases from 120 to ~300 K, decreases more significantly from 300 to ~370 K, and changes steeply above ~370 K to reach zero at $T_{c(elec)}$ = 405 K. The behavior is apparently in accordance with that predicted by the BCS gap equation and could be interpreted as indicative of the weak-coupling CDW phase transition, which assumes dominant contribution of electronic entropy. However, the GISXRD experiment carried out at beamline **BL13XU** clearly shows that this is not the case.

Typical diffraction profiles measured near the transition temperature are shown in Fig. 2. At low temperatures, the profiles can be well fitted with a single Lorentzian with a width of ~0.002 r.l.u., which corresponds to a transfer width of ~200 nm. Above 345 K, the profile gets broader and can be fitted with the sum of two components, a long-range one with the same width as those at low temperatures and a short-range one with a variable width, as shown in the middle panel of Fig. 2. The long-range component disappears just above 345 K and the short-range component decreases in intensity and gets broader with increasing temperature.

Typical diffraction profiles measured near the transition temperature are shown in Fig. 2. At low temperatures, the profiles can be well fitted with a single Lorentzian with a width of ~0.002 r.l.u., which corresponds to a transfer width of ~200 nm. Above 345 K, the profile gets broader and can be fitted with the sum of two components, a long-range one with the

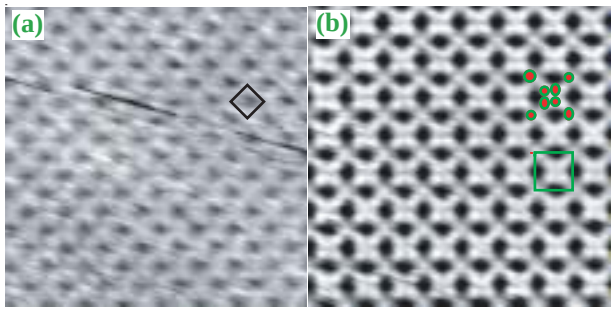

Fig. 1. STM images of **(a)** high-temperature p(2×2) and **(b)** low-temperature c(4×4) phases.

same width as those at low temperatures and a short-range one with a variable width, as shown in the middle panel of Fig. 2. The long-range component disappears just above 345 K and the short-range component decreases in intensity and gets broader with increasing temperature.

We deduced from these data the long-range order parameter, susceptibility, and correlation length, which are shown as functions of temperature in Fig. 3. Also shown are power-law curves with a sole fitting parameter of T_c and fixed exponents, β = 1/8, γ =7/4, and ν = 1. The curves are in good agreement with the data, which show unambiguously that an order-disorder phase transition classified into 2D using universality class takes place at $T_{c(lattice)}$ = 345 K.

The seemingly contradicting results of ARPES and GISXRD point to a scenario that suppose the cooperative roles of electronic and phonon entropy terms. The system is characterized by two energies: The zero-temperature CDW energy gap (~ 800 meV) determines the CDW condensation energy. A relatively large gap size leads to the enhanced effect of fluctuation. On the other hand, the energy separation of the upper CDW band from the Fermi level (< 200 meV) governs the excitation of bulk electrons to the upper band and thus the electronic entropy of the system. We thus conclude that the phase transition on the In/Cu(001) surface is a CDW phase transition driven concertedly by the electronic and phononic entropies.

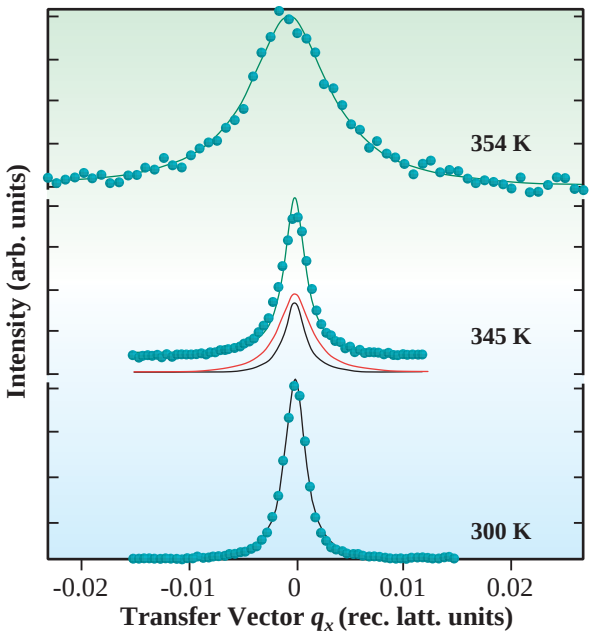

Fig. 2. Typical diffraction profiles measured for In/Cu(001) near the transition temperature.

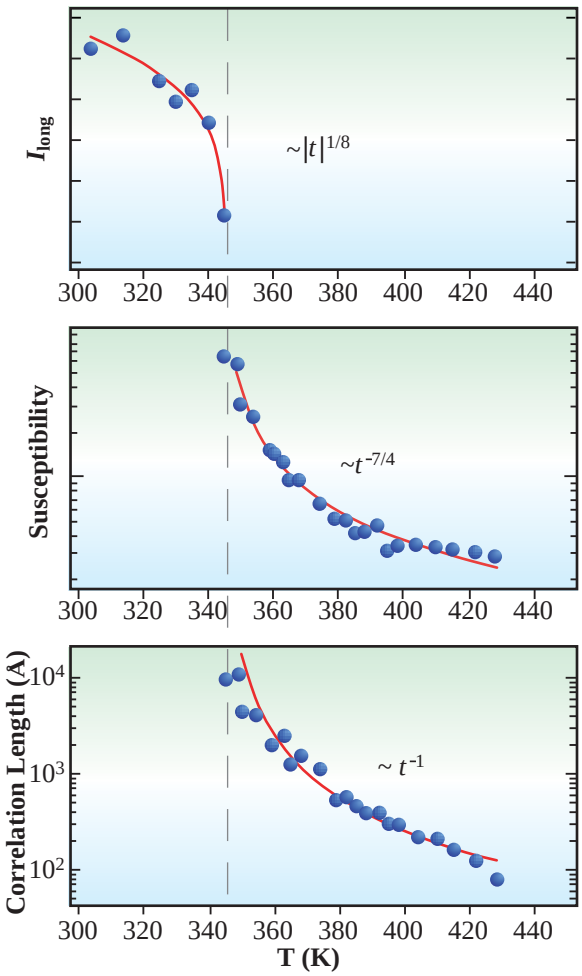

Fig. 3. Temperature dependences of long-range order parameter I_{long}, susceptibility, and correlation length. $t = (T - T_c)/T_c$, where T_c denotes the transition temperature.

Tetsuya Aruga* and Shinichiro Hatta

Department of Chemistry, Kyoto University

*E-mail: aruga@kuchem.kyoto-u.ac.jp

References

[1] T. Nakagawa *et al.*: Phys. Rev. Lett. **86** (2001) 854; Phys. Rev. B **67** (2003) 241401; and references therein.
[2] *S. Hatta, C.J. Walker, O. Sakata, H. Okuyama and T. Aruga: Surf. Sci.* ***565*** *(2004) 144.*
[3] S. Hatta *et al.*: to be published.
[4] *S. Hatta, H. Okuyama, M. Nishijima and T. Aruga: Phys. Rev. B* ***71*** *(2005) 041401.*

Strain Field under the SiO_2/Si(001) Interface Revealed by Phase-sensitive X-ray Diffraction Technique

Strain near an interface affects its electronic structure, but such a strain is still not completely understood even in the case of SiO_2/Si, which has been applied to electronic devices since the 1960s. We have developed a new powerful technique, the phase-sensitive X-ray diffraction (PSXD) technique, for characterizing strain fields near crystal surfaces, and applied it to a Si(001) wafer whose surface is covered with a thermal oxide layer [1]. It was revealed that there is a small strain field extending over a mesoscopic-range depth up to several hundreds nm under the SiO_2/Si interface and having a static fluctuation in the lateral direction.

The PSXD technique is an application of a phenomenon, that is, the modulation of the intensity of crystal-truncation-rod (CTR) scattering under an excitation of a Bragg reflection [1-5], which is an interaction between the CTR scattering, satisfying the two-dimensional diffraction condition, and the Bragg reflection, satisfying the three-dimensional diffraction condition. An example of the phenomenon in the case of using the Si(001) wafer is shown in Fig. 1, where the intensity of 50 rod CTR scattering is modulated by the excitation of 004 Bragg reflection. The experiment was carried out at beamline **BL09XU**. The experimental setup is shown in Fig. 2 (a). The arrangement was set to be particularly sensitive to strain fields extending over a mesoscopic-range depth (that is, Δl in Fig. 2 (b) was set to be very small).

In Fig. 1 the solid and open circles represent the experimentally obtained intensities corresponding to the 50 rod CTR scattering and the 004 Bragg reflection. The horizontal axis is the deviation of incident angle from the 004 Bragg angle. The broken line (green) is the best-fit curve of the experimentally obtained intensity of Bragg reflection.

We showed that the modulation profile can be characterized by two parameters: the phase shift, which represents the dip or peak position of the modulation profile, and the visibility. The solid line (red) in Fig. 1 is the best-fit curve calculated for the modulation profile, where the phase shift and the visibility are fixed at $-2\pi \times (0.117 \pm 0.001)$ and 0.521 ± 0.002, respectively. Both the experimentally obtained values were different from those of an ideal perfect crystal (0 and 0.711, respectively), which is shown by the dotted line (blue) in Fig. 1.

Figure 3 shows an illustration of the strain field under the SiO_2/Si(001) interface, which can explain the experimentally obtained modulation profile. The phase

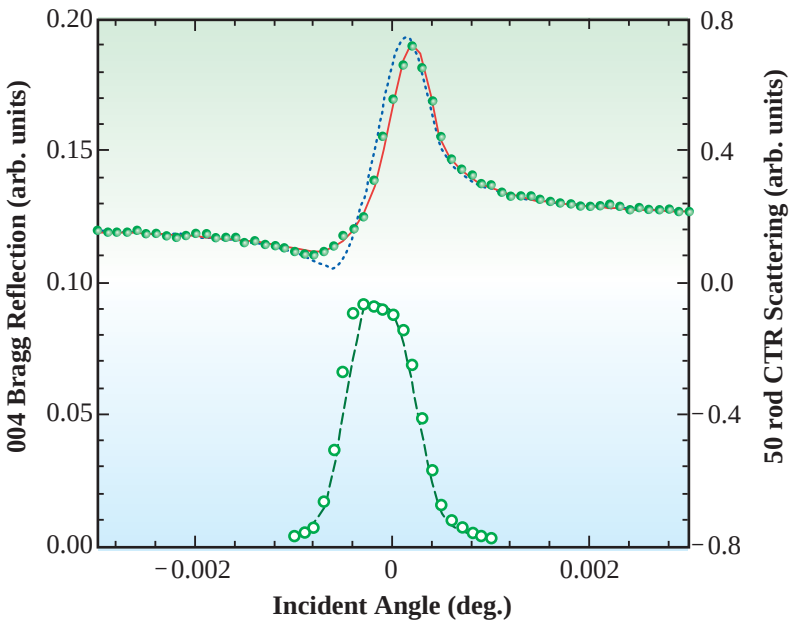

Fig. 1. Example of modulation of intensity of CTR scattering in the case of a Si(001) wafer covered with a thermal oxide layer. The intensity of 50 rod CTR scattering is modulated by the excitation of 004 Bragg reflection.

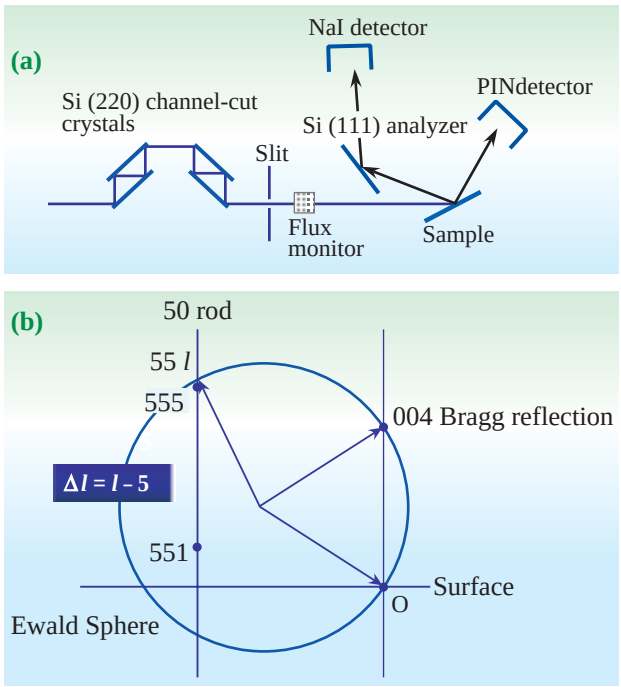

Fig. 2. **(a)** Side view of experiment setup. **(b)** Illustration of diffraction condition of experiment in reciprocal space.

shift can be simply interpreted as the sum of displacements of atomic planes under the interface projected onto the direction perpendicular to the 004 plane (–0.16 Å in Fig. 3). On the other hand, the experimentally obtained visibility indicates that the total displacement has a static fluctuation in the direction parallel to the interface. The visibility was interpreted as a static fluctuation of at least ±0.13 Å in the lateral direction. The features revealed by the PSXD technique are expected to provide a new aspect for understanding the mechanism of Si surface oxidation.

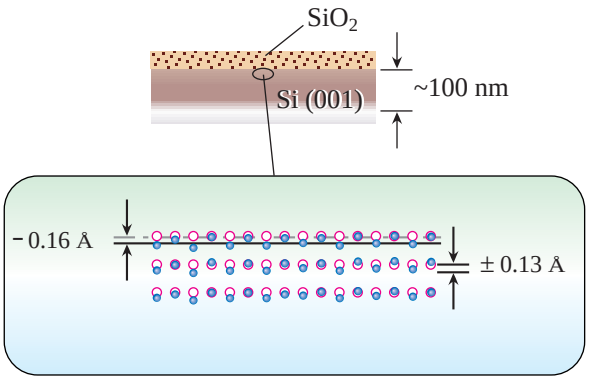

Fig. 3. Illustration of strain field under SiO_2/Si(001) interface, which can explain the experimentally obtained modulation profile. The open circles represent the sites of atoms or unit cells in a bulk crystal, and the solid circles represent the positions of atoms in the strained layer near the interface.

Wataru Yashiro [a,b]

(a) Nanomaterials Laboratory (NML), National Research Institute for Materials Science (NIMS)
(b) Department of Advanced Materials Science, The University of Tokyo

E-mail: yashiro@mml.k.u-tokyo.ac.jp

References

[1] *W. Yashiro, K. Sumitani, T. Takahashi, Y. Yoda and K. Miki: Surf. Sci.* ***550*** *(2004) 93.*
[2] T. Takahashi and S. Nakatani: Surf. Sci. **326** (1995) 347.
[3] T. Takahashi *et al.*: Phys. Rev. B **62** (2000) 3630.
[4] W. Yashiro *et al.*: Jpn. J. Appl. Phys. **41** (2002) L592.
[5] W. Yashiro *et al.*: Jpn. J. Appl. Phys. **42** (2003) 6658.

Structural Determination of Topological Crystal

To understand the physical, chemical and biological properties of novel functional materials, information on atomic arrangement in these materials has an indispensable role. The X-ray diffraction method is one of the most popular and powerful techniques in determining such atomic arrangement in a crystal cell. However, it has a limitation in structure determination. This is because X-ray diffraction is based on interference between waves scattered by atoms arranged coherently in space. For this reason, only crystals having a macroscopic translational symmetry can be analyzed by X-ray diffraction.

On the other hand, when the size of matter is reduced, its shape tends to bend and the macroscopic translational symmetry may be lost similar to carbon nanotubes and DNA wires. So our question is, "*Is it impossible to determine the atomic arrangement of a small matter with curved shape?* "

We attempt to answer the above question. Surprisingly, Tanda *et al*. produced entirely new crystals named "topological crystals" whose shapes are similar to a ring, a Möbius strip and a figure of eight [1]. Figure 1 shows the scanning electron microscopy images of $NbSe_3$ topological crystals [1]. Since *both ends of a crystal are bound and twisted*, these crystals are of an entirely different topological classes from ordinary crystals. Topological crystals can offer a chance of examining topological effects such as macroscopic interference in quantum mechanics.

From the crystallographic viewpoint, strains characteristic of each topological class will emerge in those crystals by joining two ends. In this report, we present the lattice parameter variation of topological crystals.

The difficulty in X-ray diffraction measurements of topological crystals lies in the nonuniformity of crystal orientation due to their curved shapes. If we divide or crush a topological crystal to obtain smaller crystalline powder with a macroscopic translational symmetry, we may lose important structural information originating from the topological shape. To overcome this difficulty, we decided to analyze the crystal structure without any sample treatment. To this end, we developed a two-axis sample rotator.

The sample rotator consists of two independent principal (P) and secondary (S) rotators crossing at an angle of 45 deg. The sample is mounted on the S axis (see inset of Fig. 2). With the rotation of S, one reciprocal lattice point traces a ring trajectory. With the distribution of reciprocal lattice points reflecting local crystal orientation originating from the curved shape, the assembly of ring trajectories nearly covers a part of a sphere in the reciprocal space. With the rotation of P, this part of the sphere intersects the Ewald sphere and the diffraction pattern will be similar to the Debye ring. Certainly, this is not the ideal Debye ring, which is found in powder crystals without a preferred orientation.

The effect of sample rotation on integrated reflection intensity (= Lorentz factor) should be taken into account. Since local crystal orientation varies continuously depending on the bent and the twist of a 'topological crystal', an accurate calculation of the Lorentz factor of a specific crystal is not realistic. Hence, we attempted to minimize the correction of the Lorentz factor by selecting the integration area in the imaging plate (IP) for estimating the diffraction intensity. Figure 2 shows the calculation of the Lorentz factor for the new two-axis rotator. With the rotation of S, one reciprocal lattice point forms a ring trajectory. With an increase in angle between the point and S axis, the nearest distance between the ring trajectory and the Ewald sphere decreases, where the Lorentz factor originating from another P axis rotation tends to diverge. We removed the contribution from the nearest part by selecting

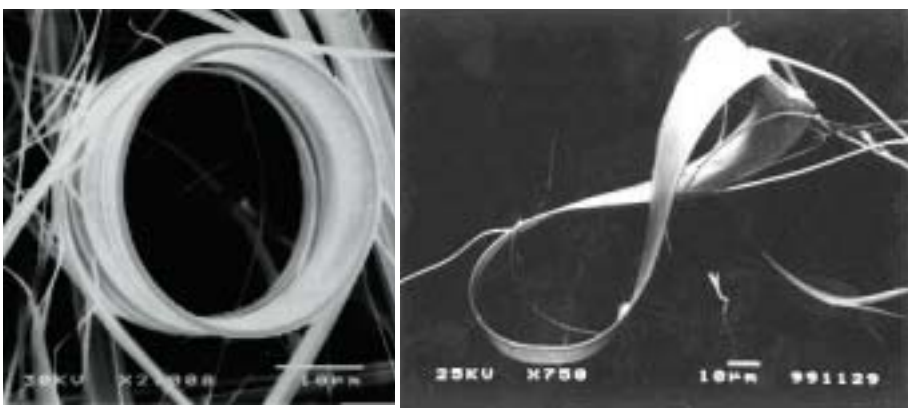

Fig. 1. Scanning electron microscopy images of topological $NbSe_3$ crystals, **(a)** ring crystal (no twist), **(b)** figure-of-eight crystal (2π twist).

the integration area of IP (see inset figure), and suppressed the singularity in the Lorentz factor.

We measured three rings (a tube, a thick ring and a thin ring) and two figures of eight and one cut ring. Owing to the smallness of the sample crystal (e.g., 50×10×5 μm^3), we used a low-temperature vacuum camera (LTVAC) at beamline **BL02B1** to diminish X-ray air scattering. To refine the unit cell parameter, we performed Rietveld analysis using RIETAN-2000 software.

The relationship between sample thickness and the ratio *a*/*c* are shown in Fig. 3. This change is caused by an *increase* in *c* length and a decrease in *a*. This unit cell deformation can be interpreted as a self-pressure effect in the thicker ring. The inner part of the thick ring can be pressurized from the outer part to maintain the sample shape. As compressibility along the one-dimensional *b* axis is nearly zero, the unit cell principally shrinks along the residual *a* axis (see Fig. 4). On the other hand, expansion in the *c* direction is reasonable because the direction is free from the above pressure effect. In the cut ring, the lattice parameter is not pressurized possibly owing to the relaxation caused by cutting. This success in the structure analysis of topological crystals encourages us to apply this developed method to other micro- or nanocrystals that do not have macroscopic translational symmetry.

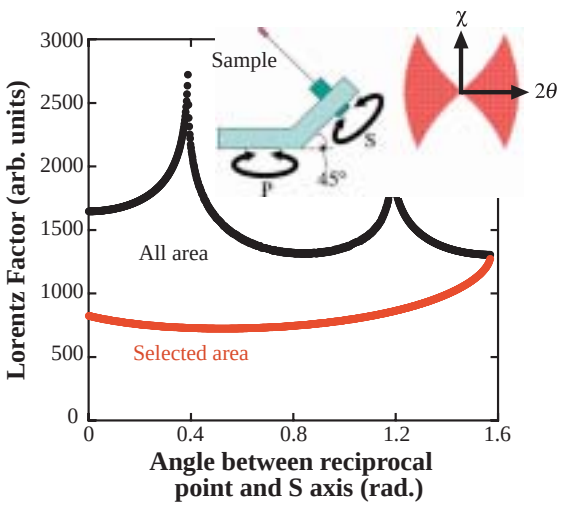

Fig. 2. Lorentz factor for the new two-axis rotator. Central inset: schematic view of two-axis rotator, right inset: selected integration area of IP.

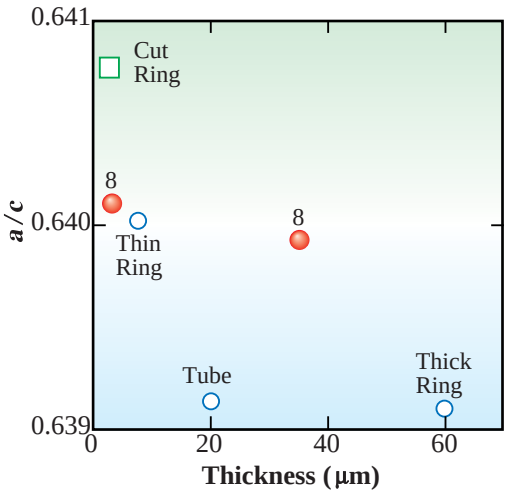

Fig. 3. Thickness dependence of *a*/*c* ratio.

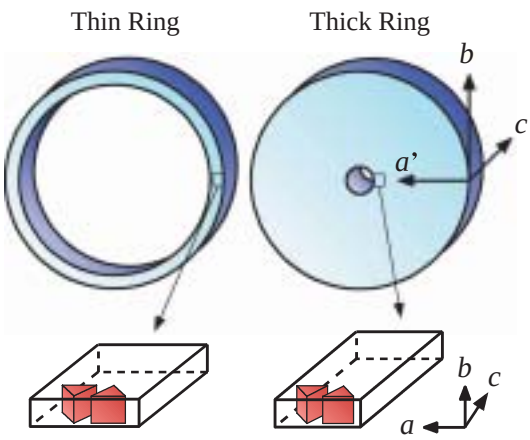

Fig. 4. Schematic view of unit cell deformation caused by self-pressure effect in the thick ring crystal.

Satoshi Tanda[a], Yoshio Nogami[b,c,*] and Naoshi Ikeda[d]

(a) Faculty of Engineering, Hokkaido University
(b) The Graduate School of Natural Science and Technology, Okayama University
(c) CREST, Japan Science and Technology Agengy
(d) SPring-8 / JASRI

*E-mail: nogami@psun.phys.okayama-u.ac.jp

References

[1] S. Tanda *et al.*: Nature **417** (2002) 397.
[2] *Y. Nogami, T. Tsuneta, K. Yamamoto, N. Ikeda, T. Ito, N. Irie and S. Tanda: to be published in Topology in Ordered Phases.*

Glass Forming at Limit: How Glass Forms when there is Insufficient Network Former ?

Vitreous forsterite (v-Mg_2SiO_4) is an important "prototypical" orthosilicate in the earth's magmas in the upper mantle and a model system for non-equilibrium low-silica-content binary melts. Experimental studies remain difficult due to the high melting point (~2150 K) and instability of forming a bulk glass. The low (33.33 mole%) SiO_2 content in v-Mg_2SiO_4 effectively prevents the formation of an extended SiO_4-based network, hence an interpretation based on the model structure of conventional silicate glasses. v-Mg_2SiO_4 can be considered as an extremely fragile glass as opposed to the strong characteristic of SiO_2-rich silicate network glasses [1]. Information regarding the structure of v-Mg_2SiO_4 is important for the development of refractory and laser host materials, formation of interplanetary and interstellar dust, prediction of thermodynamical properties of olivine minerals, and advancement of phenomenological theory of glass formation.

Experiments using the shock pressurization of olivine or the splat quenching of forsterite resulted in samples that contained a few percent glass. Only until recently Mg_2SiO_4-composition glasses prepared by containerless melting are available for structural characterization. In the present work, combined neutron and high-energy X-ray diffraction data obtained at beamline **BL04B2** and reverse Monte Carlo (RMC) modelling [2] were applied to the study of a bulk Mg_2SiO_4-composition glass formed by containerless processing of small droplets of a molten precursor [1].

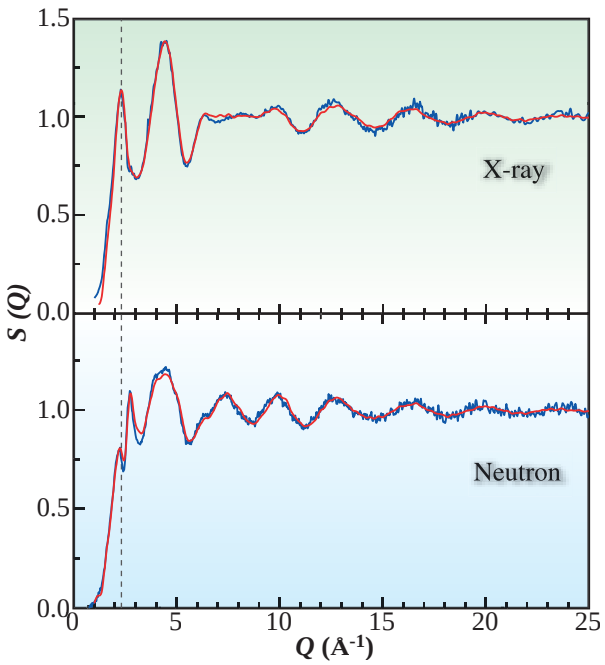

Fig. 1. Total structure factors $S(Q)$ of v-Mg_2SiO_4 (blue: experimental data; red: RMC simulation).

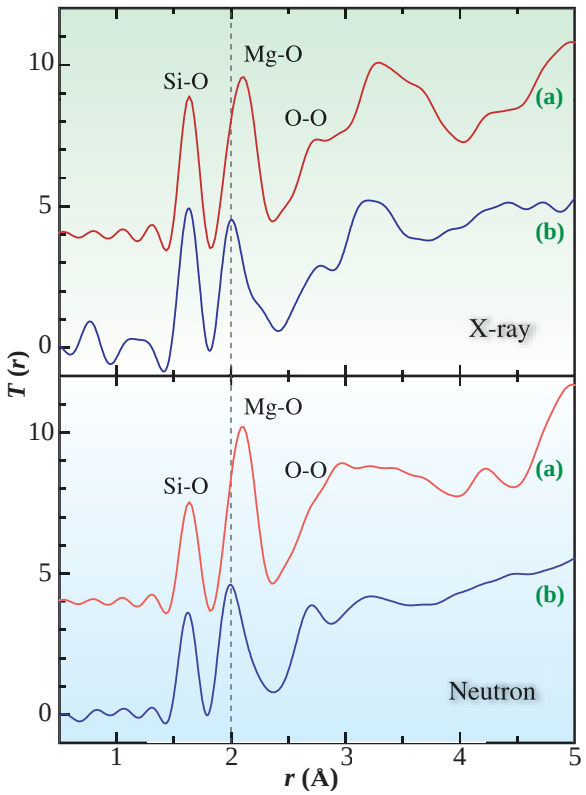

Fig. 2. Total correlation functions $T(r)$ of c-Mg_2SiO_4 **(a)** and v-Mg_2SiO_4 **(b)**. The curves of the crystal were calculated using the PDFFIT computer code according to the forsterite crystal structure. For clarity, they are displaced upward by 4 units from the baseline. The unphysical oscillations below 1.5 Å arose mainly from the Fourier transformation of truncated data at a finite Q.

The measured neutron and X-ray structure factors, $S(Q)$, [3] of bulk Mg_2SiO_4-composition glasses are shown in Fig. 1. The higher Q position (~2.2 $Å^{-1}$) of the first sharp diffraction peak than those in vitreous silica and typical non-orthosilicate glasses and melts (below 1.8 $Å^{-1}$) [4] indicates that v-Mg_2SiO_4 has a unique short-range order structure.

The derived total correlation functions, $T(r)$, are shown in Fig. 2. The well-resolved peak profiles corresponding to the Si-O and Mg-O nearest neighbors reveal details of the short-range order structure. The Si-O peak is sharp and symmetric and the Si-O coordination number, N_{Si-O}, is 4.05 ± 0.10, which indicates the presence of 4-oxygen coordinated silicon atoms as relatively regular SiO_4 tetrahedra typically found in silicate

glasses. The Mg-O peak in *T(r),* on the other hand, is broad and skewed towards the high-*r* side, indicating a distribution of Mg-O distances from 1.8 to 2.5 Å due to highly distorted MgO_x polyhedra. The average $N_{Mg\text{-}O}$ is 4.95 ± 0.20. This Mg-O peak differs markedly from that of crystalline forsterite, c-Mg_2SiO_4, (Fig. 2). The shift of the Mg-O peak towards smaller distances in v-Mg_2SiO_4 clearly implies a general relaxation of the MgO_6 octahedra of the crystalline state to include short Mg-O bonds corresponding to MgO_4 and MgO_5 local coordinations. The secondary shoulder near the nominal Mg-O bond length of crystalline MgO_6 octahedra and the tail at larger distances indicate an extensive distortion of polyhedra that include long Mg-O bonds.

To obtain a 3D representation of the glassy structure, particularly the "global" connectivity of SiO_4 and MgO_x polyhedra, we supplemented the measured data with computer simulation of diffraction data using the reverse Monte Carlo (RMC) technique. The converged configuration of the ensemble produced the calculated neutron and X-ray total structure factors *S(Q)* that agree well with the experimental data (see Fig. 1). Figure 3(a) shows a distribution of relatively regular SiO_4 tetrahedra, about 33% of which are isolated units. The remaining SiO_4 tetrahedra are connected to form corner-sharing dimers. There are almost no SiO_4 chains or cross-linked networks, in sharp contrast to the extensive 3D SiO_4 networking features in vitreous silica or in many silica-rich binary glasses. The Mg-O atoms, on the other hand, show a well-connected assembly featuring both edge- and corner-sharing MgO_x polyhedra (Fig. 3(b)). We found the presence of MgO_x polyhedra of x = 4, 5 and 6 corresponding to approximately the ratio of 3:5:2 according to the RMC snapshot representing the best fit of the data. Figure 3(c) shows a typical network element of MgO_x polyhedra. The MgO_4 units are relatively uniform tetrahedra whereas the MgO_5 and MgO_6 units have long mean bond lengths and contain one or two long bonds (observed as the shoulder and tail in Fig. 2).

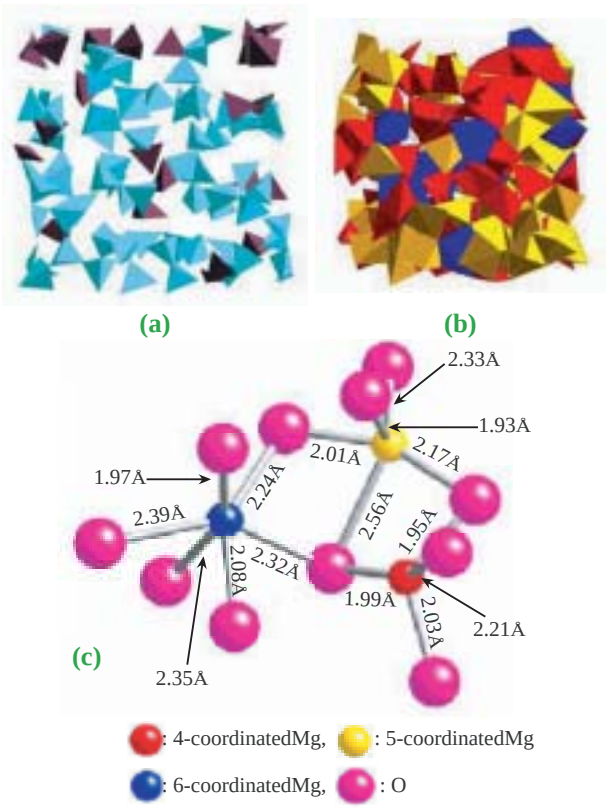

Fig. 3 **(a)** Configuration of SiO_4 tetrahedra obtained from the RMC snapshot. About 33% of tetrahedral are unconnected (purple). The remaining SiO_4 units are joined by an oxygen atom to form dimers (blue). **(b)** Network configuration of MgO_x polyhedra, x = 4 (red), 5 (yellow) and 6 (blue). The majority are MgO_5 units. **(c)** Typical network element containing MgO_4, MgO_5, and MgO_6 units obtained from the RMC snapshot.

Our findings concerning the glassy structure at the limit of insufficient network former have broad implications in the use of unconventional network former/modifier ratio in glass materials that may form new environments for dopant ions and offer potentials for tailored optical and electronic properties. In addition, the knowledge of the structure of glassy forsterite will aid in understanding the present and past magmatic processes in the earth's and moon's mantle. The present study of an unusual glass prepared by the containerless method may provide insights into the highly non-equilibrium material processing that occurs in interplanetary and interstellar environments [5].

Shinji Kohara[a,*], Kentaro Suzuya[b] and Ken Takeuchi[c]

(a) SPring-8 / JASRI
(b) Neutron Science Research Center, Japan Atomic Energy Research Institute (JAERI)
(c) Faculty of Industrial Science and Technology, Tokyo University of Science

*E-mail: kohara@spring8.or.jp

References

[1] J.A. Tangeman *et al.*: Geophys. Res. Lett. **28** (2001) 2517.
[2] R. L. McGreevy: J. Phys Condens. Matter. **13** (2001) R877.
[3] *S. Kohara, K. Suzuya, K. Takeuchi, C.-K. Loong, M. Grimisditch, J.K. Weber, J.A. Tangeman, T.S. Key: Science **303** (2004) 1649.*
[4] S. Kohara and K. Suzuya: Nucl. Instrum. Meth. B **199** (2003) 23.
[5] F.J. Molster *et al.*: Nature **401** (1999) 563.

Direct Observation of Macroscopic Separation of Dense Fluid Phase and Liquid Phase of Phosphorus

Many substances can exist in different crystalline structures. For example, graphite and diamond are both composed of carbon atoms. With a change in a parameter such as temperature or pressure, one crystalline structure transforms to another one. If the transformation is accompanied by a sudden change in density, it is called a first-order structural phase transition. While first-order phase transitions of crystalline solids are common, those in disordered states are extremely rare, with the exception of the liquid-gas transition [1]. The pressure- or temperature-induced structural change in the liquid state of a pure substance has been supposed to be gradual and continuous.

Phosphorus is an exceptional element that exhibits an abrupt structural change between two stable disordered states above its melting temperature when the pressure is changed to about 1 GPa at 1000°C [2]. From the structural features, the transformation is attributed to a conversion between a molecular form, comprising tetrahedral P_4 molecules at low-pressures, and a polymerized networked form at high-pressures. An abrupt change in the slope of the melting curve indirectly indicates that the two forms have different densities [3]. The transformation was supposed to be a liquid-liquid phase transition, but a later study [4] pointed out that the low-pressure phase is a dense molecular fluid phase because the pressure-temperature range was higher than the liquid-gas critical point of the molecular liquid. We call the two forms low-density fluid phosphorus (LDFP) and high-density liquid phosphorus (HDLP).

To obtain further evidence for the first-order phase transition, we have carried out in situ X-ray radiography experiments under high pressure and high temperature using a cubic-type multi-anvil apparatus, SMAP2, at beamline **BL14B1** [5]. Figure 1 shows a series of X-ray images. The dark area in Fig. 1(a) represents crystalline black P. The dark area became pale at 810°C as the sample was heated to 1000°C (Fig. 1(b)). X-ray diffraction measurements confirmed that LDFP was present. Then, the sample was gradually compressed. During compression, dark and round objects appeared in the radiograph. Figure 1(c) shows a large drop whose size is comparable to the diameter of the sample container. The diffraction pattern obtained for the drop was very different from that of LDFP, whereas the pattern measured for the area above the large drop showed that the sample was LDFP. The drop grew and finally filled the

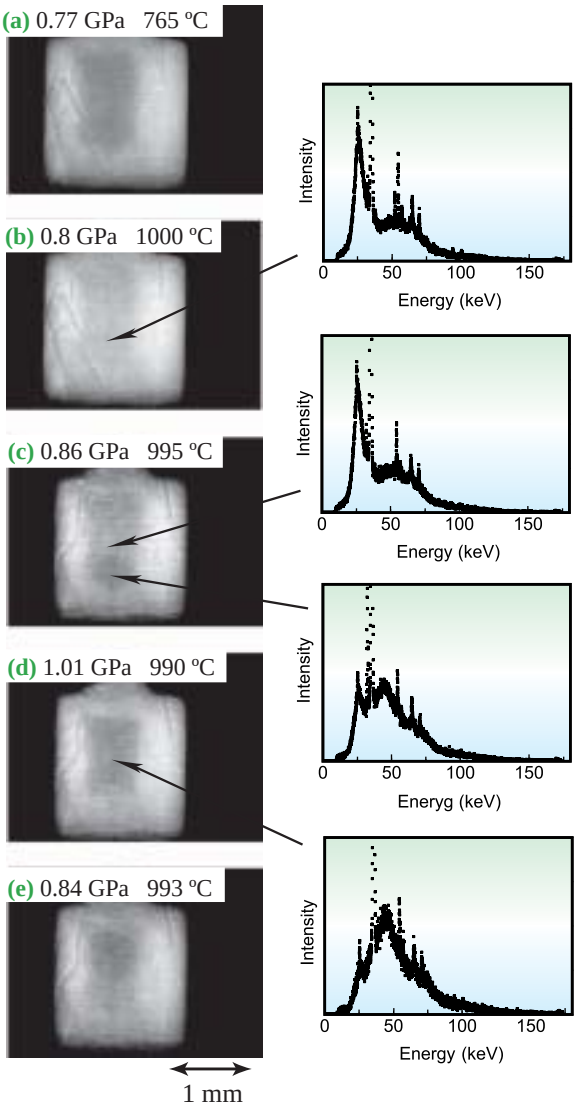

Fig. 1. Radiographs for phosphorus at various pressures and temperatures. Insets show X-ray diffraction patterns measured at the positions indicated by arrows. **(a)** Black P at 0.77 GPa and 765°C. **(b)** Low-density fluid phosphorus (LDFP) at 0.8 GPa and 1000°C. **(c)** A Drop of high-density liquid phosphorus (HDLP) in LDFP at 0.86 GPa and 995°C upon compressing. **(d)** The sample space filled with HDLP at 1.01 GPa and 990°C. **(e)** A drop of HDLP in LDFP at 0.84 GPa and 993°C upon decompressing. In the diffraction patterns, the broad peaks result from the liquid phase while sharp peaks mostly result from the high-pressure cell.

sample space (Fig. 1(d)) and the diffraction pattern at this stage was typical of that for HDLP. The diffraction pattern obtained for the drop shown in Fig. 1(c) was reproduced by the weighted sum of those of LDFP and HDLP in the ratio of 1:3. Hence, it was reasonable to suppose that the drop in shown Fig. 1(c) was HDLP. When the sample was decompressed, the dark area shrunk (Fig. 1(e)) and finally disappeared. The results demonstrate that LDFP and HDLP coexist and separate macroscopically. Moreover, the X-ray contrast between the two phases in the radiograph is direct evidence that the two phases have different densities.

To determine the densities of the two phases, we performed X-ray absorption experiments using a multi-anvil apparatus, SMAP180, and a monochromatic X-ray provided by beamline **BL11XU** [5]. The sample was placed in a sapphire ring with a 0.5 mm inner diameter, 1.0 mm outer diameter, and 1.0 mm height. The X-ray absorption of the sample was measured as a function of sample position and the profile was fitted to obtain the density. Figure 2 shows the density of liquid phosphorus at about 1000°C as a function of pressure. The density drastically decreased between 1.02 GPa and 0.84 GPa. The change in density corresponds to about 40% of the density of HDLP and about 60% of that of LDFP.

The observed macroscopic phase separation supports the existence of a first-order phase transition between two stable disordered phases besides the liquid-gas transition. Diffraction, absorption, radiography, and simulation studies revealed that LDFP and HDLP have very different structures, densities, and properties. The large difference in density stabilizes one structure against thermally induced fluctuations in density. The difference in the cohesive mechanism and, thus, in the electronic property probably contributes to the immiscibility of the two phases. These differences play an important role in the first-order fluid-liquid transition.

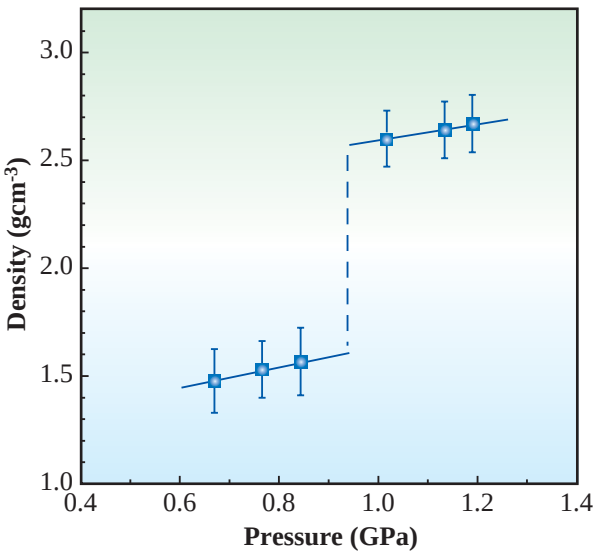

Fig. 2. Pressure dependence of density of liquid phosphorus at 1000°C. The solid and dashed lines are guides for eyes.

Yoshinori Katayama

SPring-8 / JAERI

E-mail: katayama@spring8.or.jp

References

[1] New Kinds of Phase Transitions: Transformations in Disordered Substances, V. V. Brazhkin, S. V. Buldyrev, V. N. Ryzhov, H. E. Stanley, Eds. (Kluwer, Dordrecht, 2002).

[2] Y. Katayama *et al.*: Nature **403** (2000) 170.

[3] G. Monaco *et al.*: Phys. Rev. Lett. **90** (2003) 255701.

[4] T. Mizutani *et al.*: Science and Technology of High Pressure, (Universities Press, Hyderabad, India, 2000) pp.525.

[5] *Y. Katayama, Y. Inamura, T. Mizutani, M. Yamakata, W. Utsumi, O. Shimomura: Science* ***306*** *(2004) 848.*

Observation of Fast Sound in Expanded Fluid Mercury accompanying Metal-nonmetal Transition

The metal-nonmetal (M-NM) transition has been an important subject in physics. Since the band picture of electronic states was established, it has been predicted that a divalent metal should transform to an insulating state with volume expansion. Among divalent metals, fluid Hg is the most suitable element for the study of the M-NM transition with volume expansion along the saturated vapor pressure curve because its critical constants are within those experimentally accessible (critical data of Hg: T_C = 1478 C, P_C = 1673 bar, ρ_C = 5.8 g·cm^{-3}). The M-NM transition in fluid Hg was first found in electrical conductivity and thermopower data by Hensel and Frank in 1966 and fluid Hg was determined to undergo the M-NM transition with decreasing density, ρ, from 13.6 g·cm^{-3} under ambient conditions to 9 g·cm^{-3} near the critical point. We first measured the dynamic structure factor $S(Q, \omega)$ of fluid Hg at densities from 13.6 to 1.0 g·cm^{-3}, including the M-NM transition region at 9.0 g·cm^{-3}, using a high resolution inelastic X-ray scattering (IXS) technique [1,2].

This work was carried out at the high-resolution IXS beamline **BL35XU** [3]. Backscattering at the Si (11 11 11) reflection was used to provide an incident beam of 21.747 keV energy and 0.8 meV bandwidth, which was incident onto the sample. Details of the experiments have been described in the literature [1,2].

Figure 1 shows selected IXS spectra, $S(Q, \omega)/S(Q)$, at 9.0 g·cm^{-3}. The resolution function is shown by a dashed curve at the bottom. The IXS spectra at 9.0 g·cm^{-3} have a single peak and the side peaks are not distinct from the central one. Note that the central peaks at 37.1 and 46.8 nm^{-1} are very broad at the M-NM transition at 9.0 g·cm^{-3}. The spectra were modeled as the sum of the Lorentzian at zero energy transfer and a damped harmonic oscillator (DHO) for the sound mode, with a statistical occupation factor. The optimized model function after convolution using the resolution function is denoted by the bold curves in Fig. 1. Figure 2 shows the Q dependence of the optimized excitation energy Ω_Q (squares) at 9.0 g·cm^{-3} obtained from a DHO term together with adiabatic sound velocity (dash-dotted line) obtained by the ultrasonic measurements. Also shown is a dotted line with a slope of 1500 ms^{-1}.

As can be seen in Fig. 2, the positive deviation of Ω_Q from the dash-dotted line of the adiabatic sound

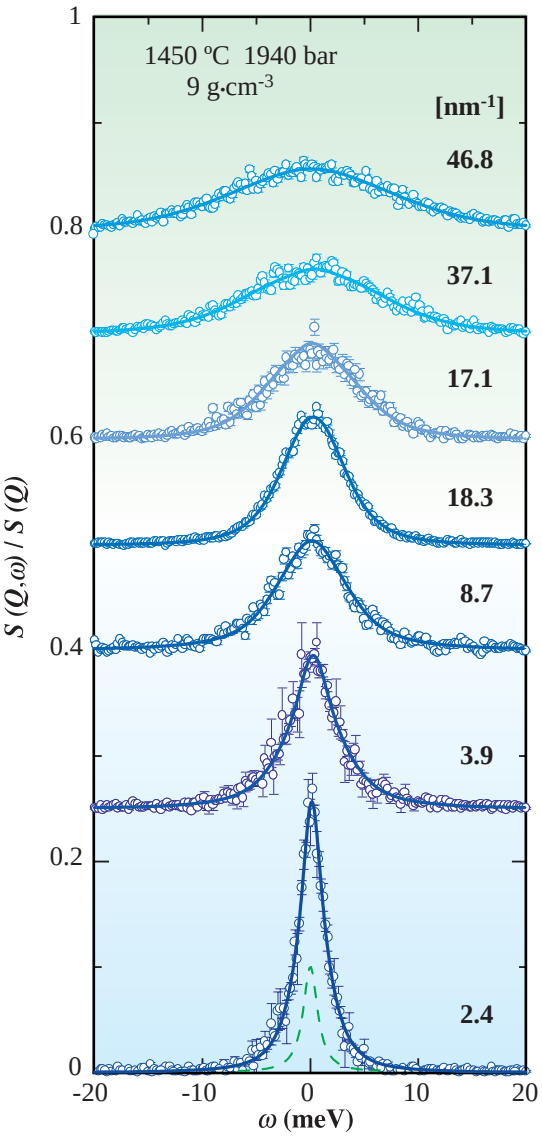

Fig. 1. IXS spectra (open circles) and fits (bold solid curves) of fluid Hg at a density of 9.0 g·cm^{-3} at 1450°C and 1940 bar. After subtracting the background, the experimental data were normalized to their integrated intensity.

velocity becomes very large at low Q and the effective velocity, $v_s(Q)=\Omega_Q/Q$, at 2 - 4 nm^{-1} is estimated to be 1500 ms^{-1}, which is triple the adiabatic sound velocity. We investigated the effective velocity estimated at low Q as a function of ρ and compared it with the adiabatic sound velocity. In the metallic region (13.6 - 9 g·cm^{-3}), the effective velocity does not decrease much with volume expansion and becomes three

times as large as the adiabatic sound velocity in the M-NM transition. With further volume expansion to the insulating state, the effective velocity becomes small and approaches the adiabatic sound velocity. Thus, a large positive dispersion, fast sound, is observed only in close vicinity of the M-NM transition.

We now discuss how fast sound is induced in the M-NM transition. The average number of nearest neighbors within the first coordination shell is reduced with volume expansion, while the nearest neighbor distance remains unchanged. On the basis of an assumption consistent with these experimental results, Franz [4] succeeded in explaining that the M-NM transition occurs at the correct density of 9 g·cm^{-3}. She pointed out the importance of the reduction and fluctuation of the coordination number in the M-NM transition. When the coordination number is substantially decreased, Hg atoms are considered to move more easily within interatomic distances and fluctuations in the nearest neighboring coordination number are enhanced. Then, a medium-range fluctuation between the metallic and insulating region appears, as schematically shown in Fig. 3. We consider that such fluctuations have a relatively large correlation length of around 1 nm in the M-NM transition and microscopic pressure fluctuations are enhanced due to the deformation of a pair potential that reversibly changes between the metallic and insulating states in a short period. We conclude that these fluctuations intrinsic to the M-NM transition were attributed to fast sound.

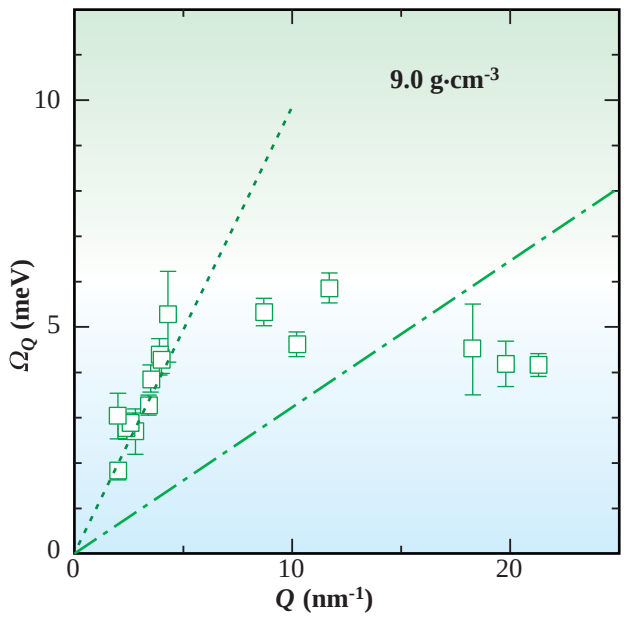

Fig. 2. Excitation energy, Ω_Q (squares) as a function of Q at 9.0 g·cm^{-3}. Dash-dotted and dotted lines correspond to the adiabatic sound velocity at 9.0 g·cm^{-3} and a slope of 1500 ms^{-1}, respectively.

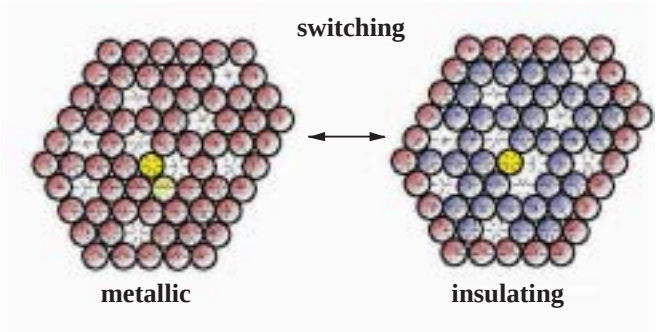

Fig. 3. A schematic illustration to relate the M-NM transition to the observed fast sound. Importance of fluctuations in the coordination number was first pointed out by Franz [4]. When a yellow atom in the left picture loses a neighboring atom (a half-tone yellow atom) and the coordination number becomes three, atoms in the medium range surrounding the central atom (denoted by half-tone blue in the right picture) should transform to an insulating state. Our IXS results suggest that such fluctuations between metallic and insulating states occur reversibly in coincident with free atomic motion under volume expansion. The central atom experiences fluctuations in pressure due to the deformation of a pair potential resulting mainly from the repulsive part. Switching of the potential on a picosecond time scale results in the high-frequency pressure fluctuations, i.e., fast sound.

M. Inui[a,*], D. Ishikawa[b] and K. Tamura[c]

(a) Faculty of Integrated Arts and Sciences, Hiroshima University
(b) SPring-8 / RIKEN
(c) Graduate School of Engineering, Kyoto University

*E-mail: inui@minerva.ias.hiroshima-u.ac.jp

References

[1] *D. Ishikawa, M. Inui, K. Matsuda, K. Tamura, S. Tsutsui and A.Q.R. Baron: Phys. Rev. Lett.* ***93*** *(2004) 097801-1-ibid-4.*
[2] D. Ishikawa *et al.*: J. Phys.: Condens. Matter **16** (2004) L45.
[3] A.Q.R. Baron *et al.*: J. Phys. Chem. Solids **61** (2000) 461.
[4] J.R. Franz: Phys. Rev. Lett. **57** (1986) 889.

Collective Dynamics of Supercritical Water

Supercritical water (SCW) is a fluid above the critical point (T_c = 647 K, P_c = 22.1 MPa, ρ_c = 0.322 g·cm^{-3}) of water, and its physicochemical properties, such as density, dielectric constant, and ionic product (= [H^+][OH^-]), vary continuously from gas-like to liquid-like properties as functions of temperature and pressure. For example, the dielectric constants of SCW are in a range of 3 ~ 30, comparable to those of hexane (1.8) and methanol (32.6), and thus SCW can dissolve organic compounds that are not soluble in ambient water. The ionic product of water increases from 1×10^{-14} (mol/dm^3)^2 under ambient conditions to a maximum of 1×10^{-11} (mol/dm^3)^2 at 34.5 MPa and ~573 K, i.e., ~30 times higher in hydrogen ion concentration in the latter thermodynamic state. Owing to its unique properties, SCW has recently drawn much attention as a medium for use in various reactions, such as decomposition of hazardous chlorinated organic compounds like dioxin and PCB and organic syntheses without acid catalysts, and production of nanometer scale metal oxides used as industrial materials. The unique properties of SCW should arise from the nature of hydrogen bonding that depends on pressure and temperature, and thus it is essential to investigate the structure and dynamic properties of hydrogen bonding in SCW as functions of temperature and pressure to understand the properties of SCW to enable the development of supercritical water technology.

In the present experiment, inelastic X-ray scattering (IXS) measurements were made using a high-resolution spectrometer installed at beamline **BL35XU** [1] on water from ambient to supercritical conditions to investigate the collective dynamics of water as a function of density. Sample water was inserted into a specially designed high-temperature and high-pressure cell made of Inconel 625 with single-crystal diamond windows (1 mm in thickness and 5 mm in diameter). The IXS measurements were carried out at eight Q values from 1.3 to 10.7 nm^{-1}, and a typical energy scan was in the range of ±40 meV.

Typical IXS spectra of water obtained at various temperatures and pressures are shown in Fig. 1 as a function of density. In ambient water (ρ = 0.997 g·cm^{-3}), the excitations are observed as shoulders on both sides of the central quasielastic peak, in good agreement with the literature data [2]. It is interesting to see that with decreasing density the shoulders corresponding to the inelastic excitation rapidly shift to the lower energies and merge into the central quasielastic peak. The observed spectra were analyzed by using a generalized Langevin formalism [3] convoluted with a resolution function, which was measured separately with a Plexiglas sample, to obtain the dynamic structure factor, $S(Q,\omega)$. The best-fitted values denoted by solid lines are compared with the observed ones denoted by open circles in Fig. 1.

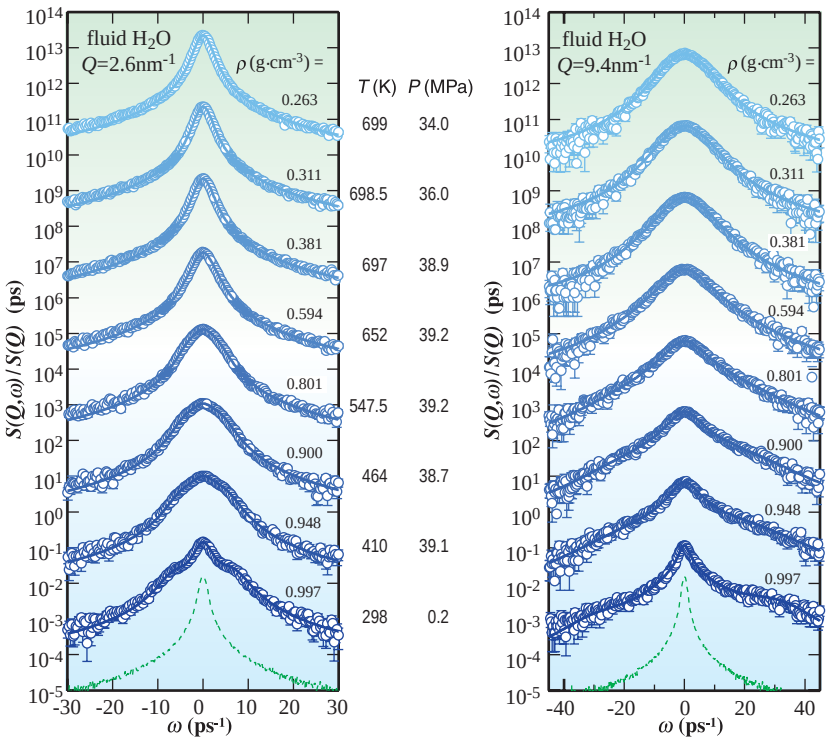

Fig. 1. Typical IXS spectra of water at various densities and at Q = 2.6 and 9.4 nm^{-1}.

The $S(Q,\omega)$ thus obtained was used to obtain the energy of the inelastic excitation, ω_1, of water as a function of density (Fig. 2) through the corresponding longitudinal current-current correlation function. The dashed lines show the hydrodynamic adiabatic velocity of sound of water in the corresponding thermodynamic states. In ambient water, the magnitude of the positive deviation of the high frequency inelastic excitations is almost 100% from the hydrodynamic values, as also reported in ref. [2]. One of the most interesting findings is the peculiar tendency of the positive deviation that gradually

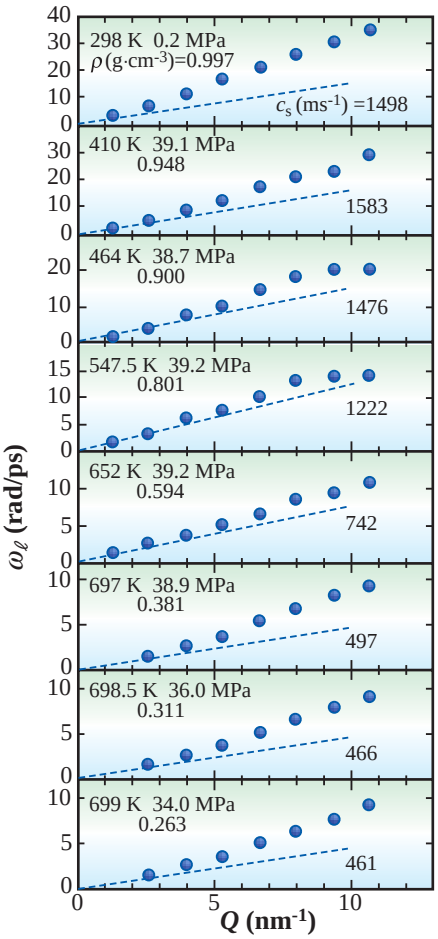

Fig. 2. *Q*-dependence of energy of inelastic excitation w1 of water at various densities.

decreases from ρ = 0.997 to 0.801 g·cm^{-3} in the subcritical state and then increases again up to ρ = 0.263 g·cm^{-3} in the supercritical state with a minimum at ρ = 0.801 g·cm^{-3}. Another characteristic to note is that the positive deviation of the inelastic excitation from the hydrodynamic data is not linear against Q, but appears to change with two different behaviors in the range of Q < ~ 5 nm^{-1} and Q > ~ 5 nm^{-1}.

In order to quantify the behavior, the apparent velocity of sound, which can be defined as $c_Q = \omega_1/Q$, was calculated at Q = 2.6 (open circles) and 9.4 nm^{-1} (solid circles) and the obtained results are shown in Fig. 3 together with the hydrodynamic velocity of sound c_s (dashed lines). Apparently, the ratios of c_Q / c_s rapidly decrease with lowering density and approach to unity at ~0.8 g·cm^{-3}. In the supercritical state, however, the c_Q /c_s ratios at Q = 9.4 nm^{-1} increase with decreasing density and reach a value of ~80% for the positive deviation near the critical density of 0.32 g·cm^{-3}, whereas those at Q = 2.6 nm^{-1} are practically independent of density. It should be noted that large density fluctuations occur near the critical point, which probably reflects the present finding of a large positive deviation of sound velocity.

In conclusion, IXS experiments on sub- and supercritical water were performed to investigate the collective dynamics of water over a wide range of densities. Analysis of the IXS data by using a generalized Langevin formalism has shown that a high apparent sound velocity of water decreases from ~3000 m·s^{-1} in ambient water at ρ = 0.997 g·cm^{-3} to a hydrodynamic value of ~1100 m·s^{-1} at ρ = 0.801 g·cm^{-3} and that in the supercritical regime a positive deviation of sound velocity from the hydrodynamic velocity of sound gradually evolves when the density approaches the critical value, probably reflecting large density fluctuations in supercritical water [4].

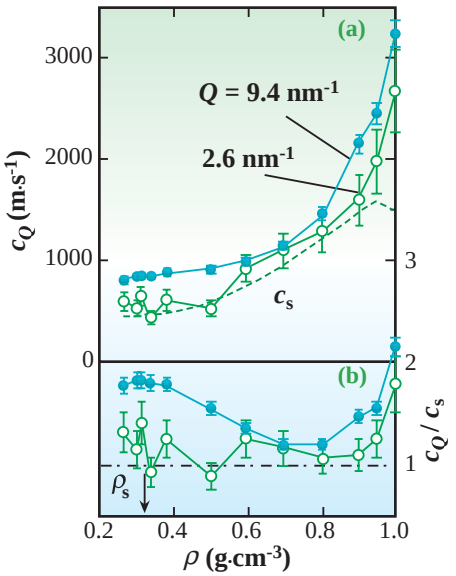

(a) Density dependence of apparent sound velocity c_Q of water as a function of density at Q = 2.6 (open circles) and 9.4 (solid circles) nm^{-1} and the hydrodynamic values c_s (dashed line), **(b)** Density dependence of the ratio of c_Q / c_s.

T. Yamaguchi[a,*], K. Yoshida[a] and S. Hosokawa[b]

(a) Department of Chemistry, Fukuoka University
(b) Faculty of Engineering, Hiroshima Institute of Technology

*E-mail: yamaguch@fukuoka-u.ac.jp

References

[1] A.Q.R. Baron *et al.*: J. Phys. Chem. Solids **61** (2000) 461.
[2] F. Sette *et al.*: Phys. Rev. Lett. **75** (1995) 850; ibid. **77** (1996) 83.
[3] R. Zwanzig: J. Chem. Phys. **39** (1963) 1714; H. Mori: Prog. Theor. Phys. **33** (1965) 423.
[4] *T. Yamaguchi, K. Yoshida, N. Yamamoto, S. Hosokawa, M. Inui, A.Q.R. Baron and S. Tsutsui: Nucl. Instrum. Meth. Phys. Res. B (2005) - in press.*

Materials Science
Electronic & Magnetic Properties

The nanotechnology support project is now in progress as one of the priority research programs. This project provides substantial support for research on Electronic & Magnetic Properties of matter. Some interesting achievements have been reported. From both the basic and technological points of view, these activities concerning nanotechnology indeed show the pioneering world in these scientific fields. Certainly, the activities proposed for general and long-term proposal categories are also high. Representative activities are introduced here. The key techniques used at SPring-8 in investigating the electronic and magnetic properties of matter are high-resolution spectroscopy (including X-ray scattering) and microscopy. The experiments carried out used the high brilliance of the SPring-8 storage ring very efficiently. Bulk-sensitive photoemission spectroscopy in soft and hard X-ray regions, microscopy, magnetic dichroism measurements and inelastic X-ray scattering are widely used for materials science in SPring-8, namely, for investigating the real bulk-, interface-, and nanosize particle information. Evidence of the existence of a magnetic moment in nanosize gold particles was obtained by magnetic circular dichroism without any ambiguity originating from the impurity and background effects usually observed in the SQUID measurement (see report by Yamamoto *et al.*). Phase separation evidence in strongly correlated organic systems was observed clearly by infrared microspectroscopy (see report by Sasaki *et al.*). The controversy in spin-charge separation in strongly correlated systems seemed to be solved by bulk-sensitive angle-resolved photoemission studies (see report by Suga *et al.*). Further bulk-sensitive studies have become possible by hard X-ray photoemission spectroscopy (see report by Makino *et al.*). The fact that bulk-sensitive techniques need no surface treatments is of great benefit to industrial science. The attendance of a variety of users from many fields holds much promise for the development of a new field and for greater activities. Those who have new ideas and/or materials are welcome as users in the materials science field at SPring-8.

Toyohiko Kinoshita

Magnetic Compton Profiles of Co/Pd Multilayers

Metallic multilayers, such as Co/Pd, exhibit large positive uniaxial anisotropies when the magnetic layer thickness is reduced to a few monolayers [1]. The presence of perpendicular magnetic anisotropy in metallic multilayers has attracted much interest because of technological advances in high-density magnetic recording. In spite of many experimental and theoretical studies related to the understanding of magnetic anisotropy, the origin of perpendicular anisotropy in multilayered magnetic thin films has not yet been clarified. Theoretical investigations to clarify this have pointed out the importance of the anisotropy of wavefunctions [2].

A magnetic Compton profile (MCP), $J_{mag}(p_z)$, is expressed by a projection of a spin density map to the p_z axis in the momentum space. Here, p_z denotes the z component of the electron momentum $\boldsymbol{p}$ in the solid. Then the MCP probes the anisotropies of spin-dependent wavefunctions [3]. However, there are few MCP measurements of thin films. This is because scattering photons from the film substrates are rather strong in comparison with those from the films. Recently, we have suggested a novel and convenient technique for reducing background scattering from the substrates, in which the film sample is deposited on a thin substrate, such as polyethylene terephthalate (PET), and have succeeded in observing for the first time the anisotropy of magnetic Compton profiles in Pd/Co multilayers [4]. In this paper, we report on the anisotropies of MCPs in Co/Pd multilayers and discuss the anisotropy of wavefunctions and electronic structures.

Three multilayer films (Pd(x nm)/Co(0.8 nm), x = 0.8, 1.6, 4.0) were fabricated on PET film substrates of 4 μm thickness by RF sputtering. The total film thickness of the multilayers was adjusted to about 1 μm. The thin-film samples were folded 16 times to increase their effective thickness; the effective thicknesses of the films and the PET substrate were 16 μm and 64 μm, respectively.

The crystal structure was confirmed by $\theta - 2\theta$ X-ray diffraction measurement. The (111) texture of the fcc structure or the (0001) texture of the hcp structure was observed in the middle angle region. Satellite peaks, which were observed around the middle angle region, confirm the designed period of the multilayers. Magnetizations were measured in an out-of-plane configuration (applied fields were perpendicular to the sample surface) and an in-plane configuration (applied fields were parallel to the sample surface). The anisotropy energies, obtained from magnetization measurement, were –0.1 Merg/cc, 0.67 Merg/cc and 1.57 Merg/cc for the Pd(0.8 nm)/Co(0.8 nm) multilayer, Pd(1.6 nm)/Co(0.8 nm) multilayer and Pd(4.0 nm)/Co(0.8 nm) multilayer, respectively (a positive energy shows a perpendicular anisotropy).

MCPs were measured on the high-energy beamline **BL08W**. Figure 1 shows the experimental setup of the MCP measurements for the in-plane configuration and the out-of-plane configuration. The circularly polarized X-ray energy was selected to be 174 keV. The degree of circular polarization was about 0.76. The scattered X-rays were detected by a 10-segment Ge solid-state detector (SSD) with a scattering angle of 178 degrees. The SSD was installed at a distance of 1 m from the sample. The momentum resolution was 0.43 atomic units (a.u.). The applied magnetic field, which was supplied by a superconducting magnet, was ±2.5 T for magnetization saturation in both the in-plane and out-of-plane configurations. All the measurements were carried out under vacuum at room temperature.

Figure 2 shows MCPs of Pd(x nm)/Co(0.8 nm) multilayers in the in-plane configuration ((a), (b), (c)) and out-of-plane configuration ((d), (e), (f)). Changes in the MCP shapes are significant in the out-of-plane configuration, but not in the in-plane configuration. Figure 3 shows the anisotropies of the MCPs. The anisotropies depend on Pd thickness and are observed up to 2 a.u. Although spin magnetic moments have been reported for both Co 3d electrons and Pd 4d electrons [5], the anisotropies of the MCP are due to

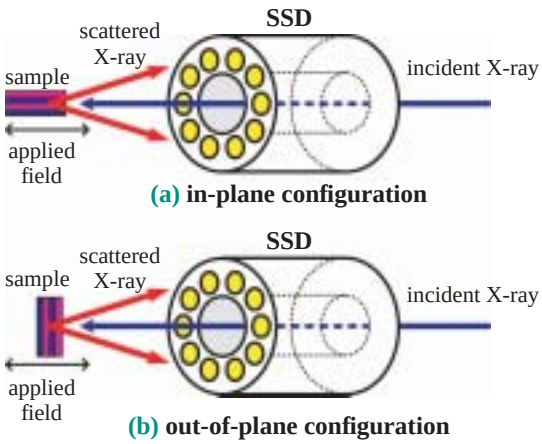

Fig. 1. Experimental setup of MCP measurements for in-plane configuration (applied fields are parallel to the sample surface) and out-of-plane configuration (applied fields are perpendicular to the sample surface).

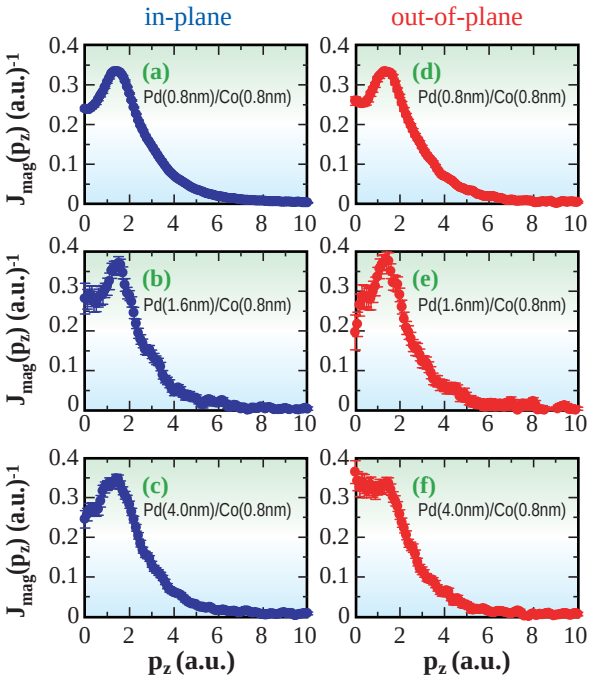

Fig. 2. Magnetic Compton profiles (MCPs) of Pd/Co multilayers in out-of-plane and in-plane configurations. MCPs are normalized to a unit area.

Co 3*d* electrons. This is because of the following two reasons. The first is the difference in momentum distribution between Co 3*d* electrons and Pd 4*d* electrons. Model MCPs of Co 3*d* and Pd 4*d* that assumed an atomic wavefunction with uniaxial crystal field symmetry show that the anisotropies are obtained up to 2 a.u. for Co 3*d* electrons but within 1 a.u. for Pd 4*d* electrons. This suggests that the observed experimental anisotropies reflect features of Co 3*d* anisotropies. The second is that Pd 4*d* spin moment contributions are small compared with the total magnetization [5]. This suggests a minor contribution of Pd 4*d* electrons to the anisotropies.

Fitting analyses using the model MCPs reproduce the experimental anisotropy as shown in Fig. 3 (yellow solid lines). The analyses give the population of each Co 3*d* state (|*m*| = 0, 1 and 2, *m*: magnetic quantum number) as summarized in Table 1. Electron density maps for each 3*d* state are shown in Fig. 4. Pd(0.8 nm)/Co(0.8 nm) with isotropic magnetization has an isotropic wavefunction. Pd(1.6 nm)/Co(0.8 nm), which has a weak perpendicular anisotropy, is dominated by |*m*| = 1 state. Pd(4.0 nm)/Co(0.8 nm), which has a strong perpendicular anisotropy, is dominated by |*m*| = 2 state.

These results shows that perpendicular anisotropy is dominated by both the |*m*| = 1 and |*m*| = 2 states.

Table 1. Populations of |*m*|=0, |*m*|=1 and |*m*|=2 states (*m*: magnetic quantum numbers) of Co 3*d* states in Pd/Co multilayers.

	$\|m\| = 2$	$\|m\| = 1$	$\|m\| = 0$
Pd 0.8 nm/ Co 0.8 nm	40%	40%	20%
Pd 1.6 nm/ Co 0.8 nm	30%	60%	10%
Pd 4.0 nm/ Co 0.8 nm	50%	20%	30%

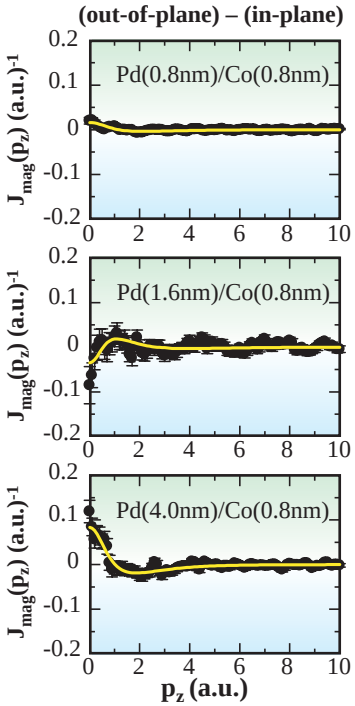

Fig. 3. Anisotropies of magnetic Compton profiles (MCPs) in Pd/Co multilayers. $\Delta J_{mag}(p_z)$ are obtained from differences in MCP between the in-plane and out-of-plane configurations.

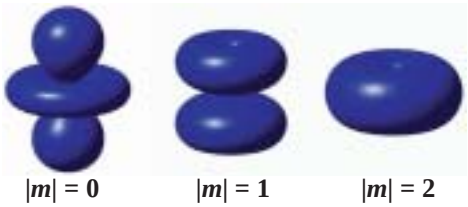

Fig. 4. Electron density maps of |*m*| = 0, |*m*| = 1 and |*m*| = 2 states (*m*: magnetic quantum numbers) of 3*d* states.

Hiroshi Sakurai

Dept. Electronic Engineering, Gunma University

E-mail: sakuraih@el.gunma-u.ac.jp

References

[1] P.F. Carcia *et al.*: Appl. Phys. Lett. **47** (1989) 178.
[2] K. Kyuno *et al.*: Phys. Rev. B **54** (1996) 1092.
[3] A. Koizumi *et al.*: Phys. Rev. Lett. **86** (2001) 5589.
[4] *M. Ota, H. Sakurai, F. Itoh, M. Itou and Y. Sakurai: J. Phys. Chem. of Solids* ***65*** *(2004) 2065.*
[5] H. Sakurai *et al.*: J. Magn. Magn. Mat. **198-199** (1999) 662.

Direct Evidence of Ferromagnetic Spin Polarization in Gold Nanoparticles

It is believed that bulk gold metal is chemically inert and the most stable metal in nature. However, its properties in the nanosize region might be different from its bulk nature because the electronic structure may be modified significantly. In fact, recent experiments have shown that gold nanoparticles exhibit an enhancement in catalytic activity at a diameter of approximately 2 nm [1]. Moreover, superparamagnetic behavior has been reported for gold nanoparticles stabilized by a polymer (Fig. 1) for diameters below 3 nm [2], although bulk gold metal has non-magnetic (diamagnetic) properties. This indicates that individual Au particles possibly have ferromagnetic moments. However, no clear evidence has been provided showing that the ferromagnetism of Au particles is intrinsic because conventional magnetometry may include magnetization from trivial origins, such as magnetic impurities. Therefore, it is essential to measure the element-specific magnetization of gold atoms to confirm that their magnetism is intrinsic.

In this study, we have presented direct evidence of the intrinsic ferromagnetism of Au nanoparticles protected by polyallyl amine hydrochloride (PAAHC) (abbreviated as PAAHC-Au) by means of element-specific magnetization (ESM) measurements based on the X-ray magnetic circular dichroism (XMCD) technique. The XMCD technique allows the detection of the magnetic moments of a particular element through sensitivity to the difference between the up- and down-spin densities at approximately the Fermi level. This element selectivity is the most important advantage of this technique over conventional magnetometry and is essential in the present study of extracting the magnetization of Au nanoparticles.

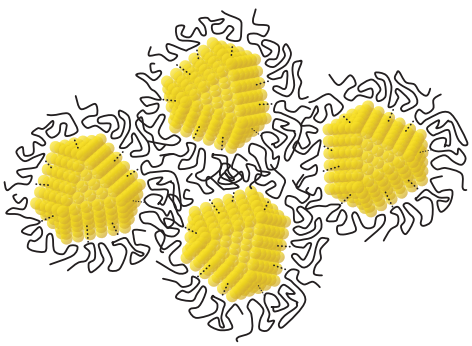

Fig. 1. Schematic of gold nanoparticles protected by linear polymer. Each nanoparticle (cluster of Au metal) is surrounded by a matrix polymer, which prevents further aggregation and oxidation of Au nanoparticles.

XMCD spectra were recorded using a highly sensitive spectrometer installed at beamline **BL39XU**. External magnetic fields up to 10 T were applied along the X-ray beam direction using a split-type superconducting magnet. The experimental resolution was high enough to detect XMCD signals of 10^{-5} parts of the spin-averaged X-ray absorption coefficients. This high sensitivity is achieved through the helicity modulation technique based on lock-in detection [3], and the high brilliance of a third generation synchrotron radiation source. We emphasize that the modulation technique is crucial for the detection of very small ferromagnetism in Au nanoparticles because this technique markedly improves the signal/noise ratio of the XMCD signal.

Figure 2 shows the X-ray absorption spectroscopy (XAS) and XMCD spectra of Au at the L_3- ($2p_{3/2} \rightarrow 5d_{5/2}$, $6s_{1/2}$ dipole-allowed transitions) and L_2-edge ($2p_{1/2} \rightarrow 5d_{3/2}$, $6s_{1/2}$) at 2.6 K in an applied magnetic field of 10 T. A negative XMCD signal was clearly observed at the L_3-edge (11.917 keV), whereas the XMCD signal at the L_2-edge (13.730 keV) was positive. As shown by the dotted line in Fig. 2, the sign of the XMCD signal reversed when the magnetic field direction was changed. This result confirms that the observed signal is truly of magnetic origin and does not arise from any artificial effects. To the best of our knowledge, this is the first observation of an evident XMCD signal arising from Au within a nonmagnetic matrix.

Considering the XMCD signal to be proportional to the magnetization, ESM is obtained by recording the peak amplitude of the XMCD spectra at the Au L_3-edge as a function of external magnetic field and temperature. Figure 3 shows ESM measurements scaled arbitrarily for comparison with the magnetic field variation of SQUID magnetization in the same figure. ESM increases with increasing magnetic field without saturation. This behavior is similar to the magnetization process obtained by SQUID magnetization measurements. The temperature dependence of ESM was also investigated and compared to the temperature variation of SQUID magnetization. ESM increases rapidly with decreasing temperature, although it seems that a finite constant value remains at high temperatures. The steep increase in ESM at low temperatures is consistent with the temperature variation of SQUID magnetization and does not

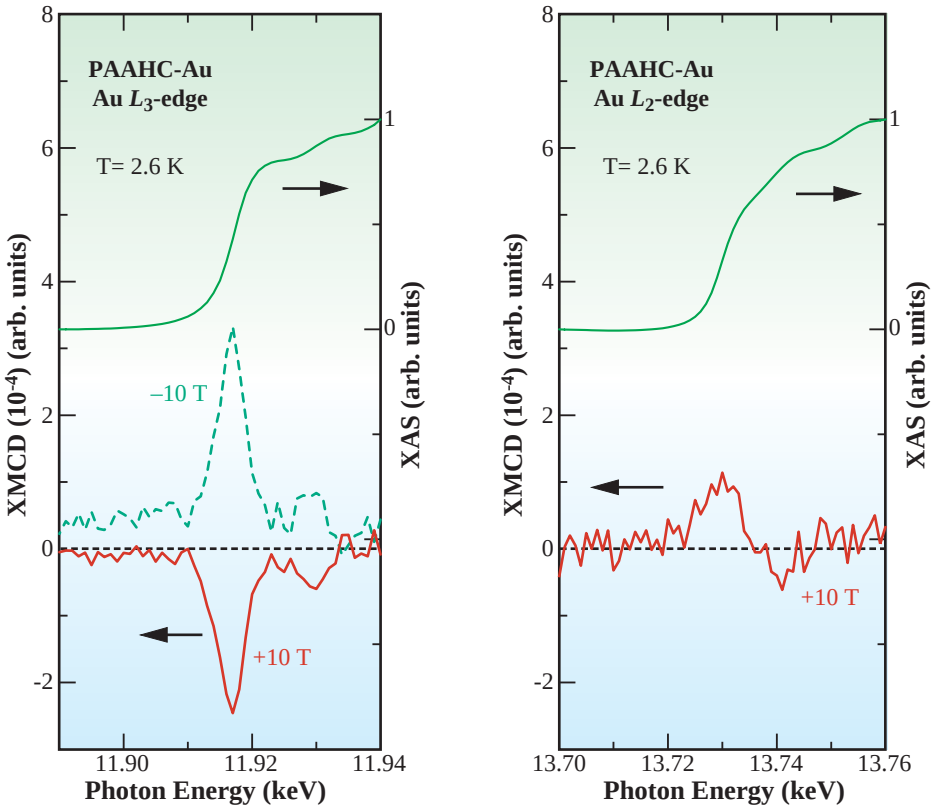

Fig. 2. XMCD and XAS spectra at Au L_3- and L_2-edge with applied magnetic fields of 10 T (red solid line) and –10 T (broken line). The XMCD and XAS spectra include the same scale factor so that the heights of the edge jumps of the XAS spectra (solid lines) are unity.

contradict the characteristics of the superparamagnetic model. If one assumes that superparamagnetism and Pauli paramagnetism arise from surface atoms and core atoms in Au nanoparticles respectively, the observed mixture of superparamagnetism and Pauli paramagnetism is reasonably explained.

In summary, our XMCD and ESM experiments have revealed the intrinsic magnetic polarization in Au nanoparticles with a mean diameter of 1.9 nm [4]. The external magnetic field and temperature dependences of the ESM signal suggest that the magnetization of Au nanoparticles consists of a superparamagnetic part and a temperature-independent Pauli paramagnetic part. The mixture of these components is reasonably explained by the picture that the surface atoms are ferromagnetic and the core atoms are Pauli paramagnetic.

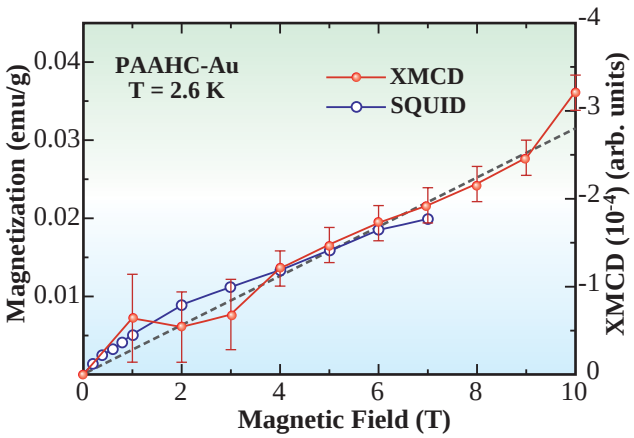

Fig. 3. ESM of PAAHC-Au as a function of applied magnetic field and magnetization process obtained using SQUID magnetometer. The integral of the peak intensity yields similar results. The dashed line is the fit to the data assuming a Langevin function plus a linear field-dependent term.

Y. Yamamoto* and H. Hori

School of Materials Science, Japan Advanced Institute of Science and Technology (JAIST)

*E-mail: y-yamamo@jaist.ac.jp

References

[1] M. Valden *et al.*: Science **281** (1998) 1647.
[2] H. Hori *et al.*: Phys. Lett. A **263** (1999) 406.
[3] M. Suzuki *et al.*: Jpn. J. Appl. Phys. **37** (1998) L1488.
[4] *Y. Yamamoto, T. Miura, M. Suzuki, N. Kawamura, H. Miyagawa, T. Nakamura, K. Kobayashi, T. Teranishi and H. Hori: Phys. Rev. Lett.* ***93*** *(2004) 116801.*

Real-space Imaging of Phase Separation Near Mott Transition in Organic Superconductor κ-(BEDT-TTF)$_2$Cu[N(CN)]$_2$Br

Microscopic spatially inhomogeneous electronic states have attracted much attention recently in many kinds of correlated electron systems. Materials with such intrinsic electronic inhomogeneity tend to have a criticality of changes in charge, spin, orbital, and lattice degrees of freedom in correlated electrons.

Organic charge transfer salts based on the BEDT-TTF molecule have been recognized as one of the highly correlated electron systems. Among them, κ-(BEDT-TTF)$_2X$ with X = Cu(NCS)$_2$, Cu[N(CN)$_2$]Y (Y = Br and Cl), etc. (Fig. 1(a)), have attracted considerable attention from the point of view of a strongly correlated electron system. The strong BEDT-TTF dimer structure effectively makes the conduction band half-filling. In such a strongly correlated electron system, several electronic phases appear and the transitions among these phases are controlled by the applied pressure and slight chemical substitution of the donor and anion molecules, as shown in Fig. 1(b), which must change the conduction bandwidth with respect to the effective Coulomb repulsion between two electrons on a dimer. The Mott first-order metal-insulator transition divides the superconducting and antiferromagnetic Mott insulator phases. Thus, the κ-(BEDT-TTF)$_2X$ family has been considered to be the bandwidth-controlled Mott system in contrast to the filling-controlled one in inorganic perovskites, such as high-T_c copper oxides. Therefore, an intrinsic electronic inhomogeneity has been expected to appear in the vicinity of the Mott transition.

Scanning microregion infrared reflectance spectroscopy (SMIS) was applied to perform a two-dimensional imaging of the local electronic state in the organic Mott system κ-[(h-BEDT-TTF)$_{1-x}$(d-BEDT-TTF)$_x$]$_2$Cu[N(CN)$_2$]Br [1], whose bandwidth is controlled by the substitution ratio x between the hydrogenated BEDT-TTF molecule (h-BEDT-TTF) and the deuterated one (d-BEDT-TTF). This deuterated molecule substitution makes it possible to control the bandwidth continuously at ambient pressure with minimal disorder effect. SMIS using synchrotron radiation were performed at beamline **BL43IR**. An IR microscope with a controlled precision x-y stage and a

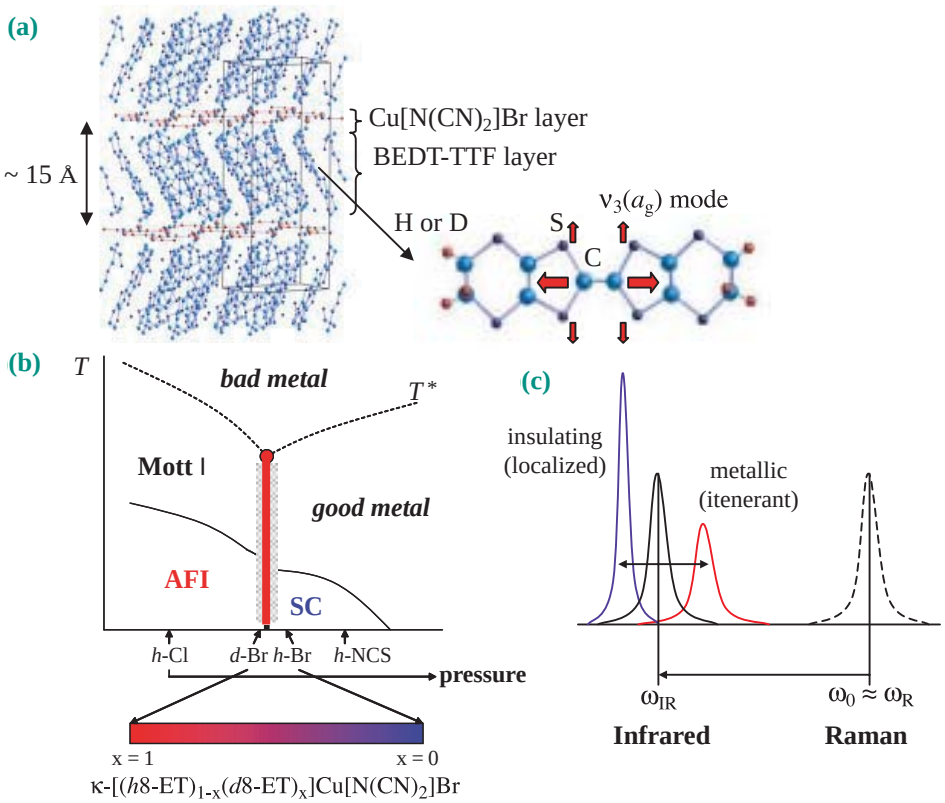

Fig. 1. **(a)** Crystal structures of κ-(BEDT-TTF)$_2$Cu[N(CN)$_2$]Br and BEDT-TTF molecules. **(b)** Schematic phase diagram of κ-(BEDT-TTF)$_2X$. (c) IR molecular vibration shifted by EMV coupling.

high brilliance SR light enable us to obtain a two-dimensional reflectance spectrum map with a spatial resolution of ~10 μm with no apertures. To obtain the real space image of the electronic states by SMIS, we use the shift in the frequency ω_3 of a molecular vibration mode, $\nu_3(a_g)$. The specific $\nu_3(a_g)$ mode, which is a symmetric stretching mode of the central double-bonded carbon atoms of the BEDT-TTF molecule (Fig. 1(a)), has been found to be very sensitive to the difference between metallic and insulating states due to the large electron-molecular vibration (EMV) coupling [2]. The peak of the $\nu_3(a_g)$ mode should shift to a lower frequency and exhibit a sharper shape in the insulating state, while it should show an opposite shift in the metallic state (Fig. 1(c)).

Figure 2 shows the two-dimensional contour maps of the reflectivity peak frequency ω_3 of the $\nu_3(a_g)$ mode at 4 K. In the contour maps, a bright region indicates the higher frequency of ω_3 which demonstrates a metallic feature. In the samples with small substitution ratios of x = 0 and 0.2, an almost homogeneous metallic state is realized in their entire area. In contrast, the sample of the opposite end member x = 1 shows a homogeneous insulating state. In the intermediate substitution, however, an inhomogeneous feature, that is, phase separation on a micrometer scale can be found in the maps. The insulating domains appear on the dominant metallic background in the x = 0.5 sample. Such insulating domains have a tendency to grow with increasing x. In the x = 0.8 sample, the insulating region becomes dominant and the metallic domains are found to remain.

Experimental evidence of the electronic phase separation is obtained in the organic Mott system using the real space imaging technique. SMIS using SR enables us to show the macroscopic size of the domain structure of the insulating and metallic regions. The observation of the micrometer scale phase separation is different from the recent findings of nanoscale electronic inhomogeneity in a strongly correlated inorganic system. The origin of the phase separation must be the strong electronic correlation near the Mott transition.

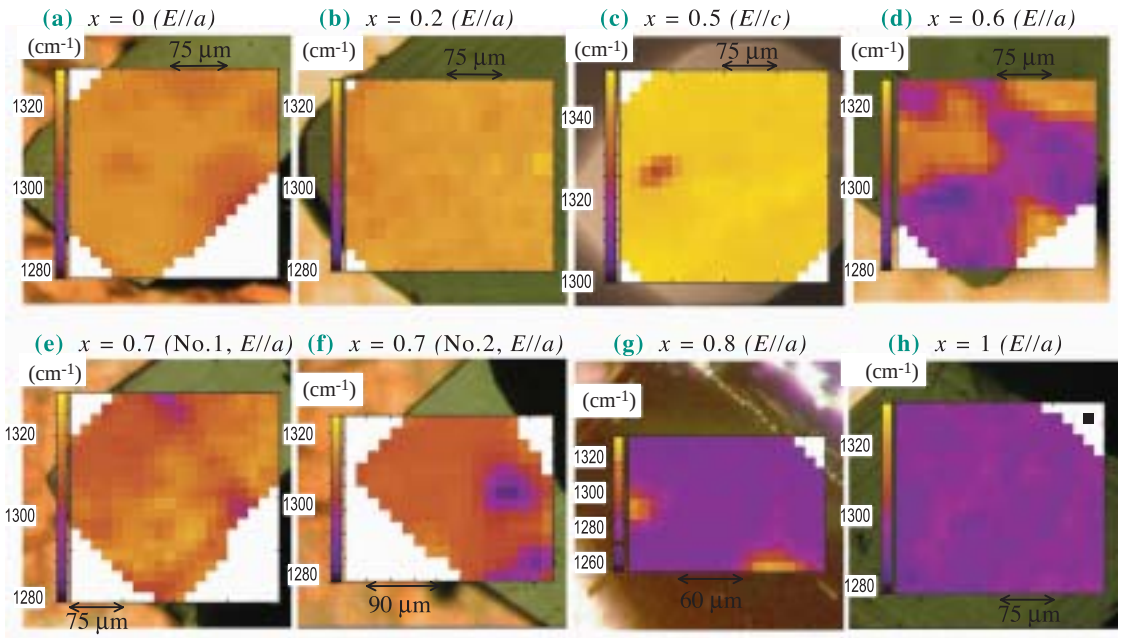

Fig. 2 Two-dimensional contour maps of peak frequency of $\nu_3(a_g)$ for various substitution ratios x in κ-[(*h*-BEDT-TTF)$_{1-x}$(*d*-BEDT-TTF)$_x$]$_2$Cu[N(CN)$_2$]Br. The left colored bar corresponds to the peak frequency.

Takahiko Sasaki

Institute for Materials Research, Tohoku University

E-mail: takahiko@imr.tohoku.ac.jp

References

[1] *T. Sasaki, N. Yoneyama, N. Kobayashi, Y. Ikemoto and H. Kimura: Phys. Rev. Lett.* ***92*** *(2004) 227001.*
[2] *T. Sasaki, I. Ito, N. Yoneyama, N. Kobayashi, N. Hanasaki, H. Tajima, T. Ito and Y. Iwasa: Phys. Rev. B* ***69*** *(2004) 064508.*

Soft X-ray Angle-resolved Photoemission Spectroscopy of Strongly Correlated Bulk Electronic Structures of $SrCuO_2$ and Sr_2RuO_4

Angle-resolved photoemission spectroscopy (ARPES) with high resolutions in energy and momentum (or wave number k) realized at low photon energies (hν) between ~20 and ~100 eV has been extensively applied to correlated electron systems such as high-T_c cuprates to study their electronic structures [1]. However, it is known that such a low-hν photoemission spectroscopy (PES) is surface sensitive and often provides spectral shapes which are not consistent with bulk electronic structures in several transition metal and rare earth compounds [2,3]. Therefore, caution is required to suppress surface effects sensitively probed by the short photoelectron mean free path (λ). For this purpose, the bulk-sensitive ARPES above several hundred eV with λ > 10 Å has been strongly desired. Pioneering ARPES with high-hν X-ray was performed many years ago. However, the unsatisfactory angular (±2°) and energy (0.35 - 0.85 eV) resolutions made it impractical for band mapping and Fermiology.

By virtue of recent instrumental developments at beamline **BL25SU**, soft X-ray ARPES is successfully performed for the valence bands of quasi-one-dimensional (quasi-1D) $SrCuO_2$ and quasi-two-dimensional (quasi-2D) Sr_2RuO_4. Above several hundred eV, the photoionization cross section of the Cu 3*d* or Ru 4*d* states is much higher than that of the O 2*p* states. Clear differences from the results of low-hν ARPES have been observed for both materials.

In contrast to various misconceptions, the large photon momentum q (0.36 $Å^{-1}$ at hν = 700 eV) is simply transferred to the photoelectron momentum. Then $q_{//}$ = 0.25 $Å^{-1}$ is transferred to the photoelectron momentum parallel to the surface ($k_{//}$). For a lattice constant of c = 3.9 Å ($SrCuO_2$), for example, $k_{B//}$ at the Brillouin zone edge is π/c = 0.80 A^{-1} and the instrumental angular resolution of 0.25° corresponds to the sufficiently high $k_{//}$ resolution of ~0.06 A^{-1}.

It was proposed in quasi-1D $SrCuO_2$ by low-hν ARPES that the so-called "spin-charge separation" might be taking place. We have performed Cu 3*d*-sensitive and bulk-sensitive ARPES on a cleaved surface at room temperature and found a clear dispersion in the valence band region (Fig. 1(a)). In the so-called O 2*p* bands in the range of 2 - 4 eV, the Cu 3d and O 2*p* states are strongly hybridized. The band near 1 eV has a strong Cu 3*d* component. As shown in the density plot in Fig. 1(b), the V-shaped dispersion up to 1 eV is very prominent in k = 0 (or 2π) ± π/2. Dispersion is much less prominent in the region of π ± π/2. Although both spinon and holon branches are expected in the region of 0 (or 2π) ± π/2 according to the spin-charge separation scenario, there is no trace of the spinon branch irrespective of the present Cu 3*d* sensitivity. The larger dispersion due to the holon is also not observed in the region of π ± π/2. These results demonstrate that the spin and charge are not fully separated in the bulk of $SrCuO_2$ due to the finite magnitude of U/t = 7.5 (U is the Coulomb repulsive energy and t is the transfer energy) [4].

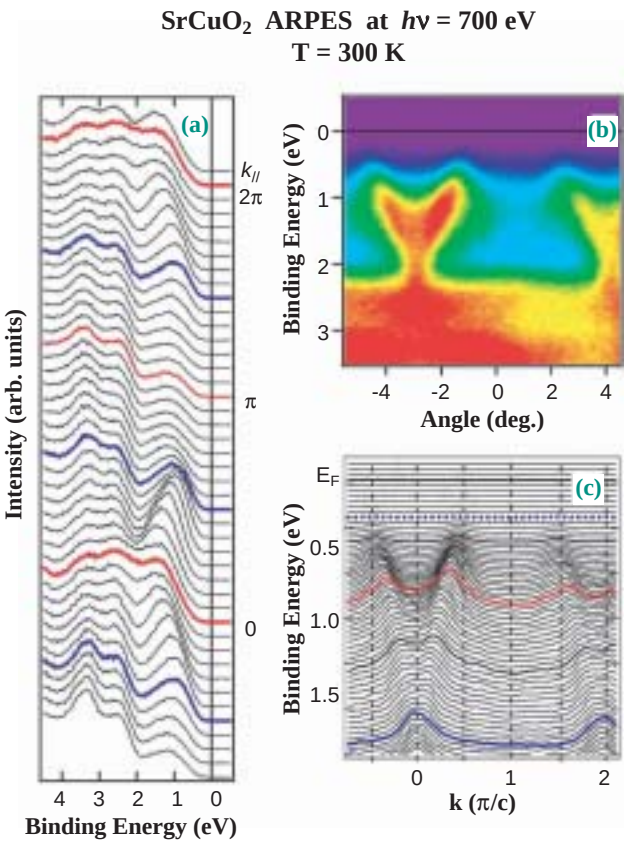

Fig. 1. Soft X-ray (*h*ν=700 eV) ARPES along the c-axis of 1D $SrCuO_2$ at 300 K. **(a)** Energy distribution curves. **(b)** Density plot of the measured photoemission intensity. **(c)** Momentum distribution curves.

Fermi surfaces (FSs) are key issues in understanding the physical properties of new functional materials. Soft X-ray ARPES is applied to the "triplet" superconductor Sr_2RuO_4. Quantum oscillation measurements and band-structure calculations suggest one holelike FS sheet centered at (π,π) (α sheet) and two electron-like FS sheets centered at (0,0) (β and γ sheets). On the other hand, Yokoya *et al*. have first concluded two holelike and one electron-like FSs from low-hν ARPES. A following low-hν ARPES on degraded surface suggests that the earlier finding originates from surface states and surface reconstruction, and that the bulk FSs are qualitatively similar to the result of band calculation.

ARPES spectra are here measured at hν = 700 eV along the (π,0)-(π,π) direction, demonstrating a holelike FS sheet α. Then ARPES spectra are measured along the (0,0)-(π,0) cut. They are complicated because the a sheet band is located at ~0.5 eV, while the β and γ sheet bands show dispersion crossing E_F. The behavior of the E_F crossing of the β and γ branches is also confirmed by the momentum distribution curves (MDCs). Thus the genuine bulk FSs are revealed in Figs. 2(a) and 2(b) without serious distortion owing to the bulk-sensitivity of the soft X-ray ARPES. This technique is further applied to high-T_c cuprates and other strongly correlated electron systems.

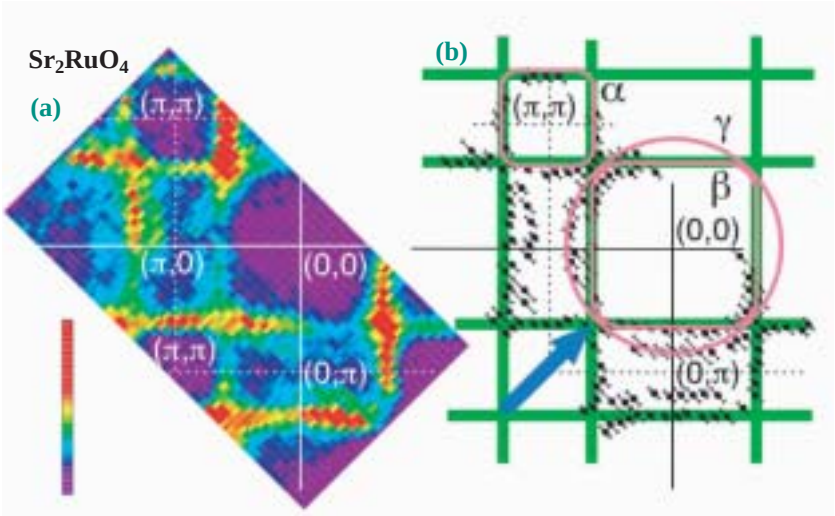

Fig. 2. Bulk Fermi surfaces of Sr_2RuO_4 probed by soft X-ray ARPES at 700 eV and 20 K. **(a)** Intensity integrated from E_F to –0.1 eV. **(b)** Estimated k_F and schematic drawing of FSs.

Shigemasa Suga* and Akira Sekiyama

Graduate School of Engineering Science,
Osaka University

*E-mail: suga@mp.es.osaka-u.ac.jp

References

[1] A. Damascelli *et al.*: Rev. Modern Phys. **75** (2003) 473.
[2] A. Sekiyama *et al.*: Nature **403** (2000) 396.
[3] A. Sekiyama *et al.*: Phys. Rev. Lett. **93** (2004) 156402.
[4] *S. Suga et al.: Phys. Rev. B **70** (2004) 155106.*
[5] *A. Sekiyama, S. Kasai, M. Tsunekawa, Y. Ishida, M. Sing, A. Irizawa, A. Yamasaki, S. Imada, T. Muro, Y. Saitoh, Y. Onuki, T. Kimura, Y. Tokura and S. Suga: Phys. Rev. B **70** (2004) 060506(R).*

Hybridization of Cr 3*d*-N 2*p*-Ga 4*s* in the Wide-Band-Gap Diluted Magnetic Semiconductor $Ga_{1-x}Cr_xN$

Diluted magnetic semiconductors (DMS) have been of much interest because of their potential application to spintronics. In semiconductor spintronics, two degrees of freedom, charge and spin, have been explored to realize novel functionalities in semiconductors [1]. For practical device applications, it is desirable to synthesize materials with high Curie temperatures. Transition-metal-doped group-III nitrides have been considered to be one of the promising candidates for high-temperature ferromagnetic DMS. However, the origin of magnetism in the material system is still controversial. In order to get insight into the mechanism of the magnetism, an electronic structure investigation of GaN-based DMS is necessary.

We report on the electronic structure of $Ga_{1-x}Cr_xN$ observed by hard X-ray photoemission spectroscopy (HX-PES) at the excitation energy of 5.95 keV to understand a possible origin of the magnetism. Soft X-ray PES is very surface sensitive due to the short mean free paths of electrons at measurable kinetic energies. There is no method of forming an ideal surface after exposure to atmosphere even once. This problem is more critical for the case of epitaxial thin films because surface cleaning procedures are not well established. The photoemission spectra of $Ga_{1-x}Cr_xN$ in this research are actually bulk sensitive, and also almost free from distortion due to inelastic scattering at high energies [2,3]. Thus, we are able to precisely analyze the difference of the spectra between doped and undoped GaN.

The HX-PES experiments were performed at **BL29XU** and **BL47XU**. The large escape depth at a high energy allow determination of bulk electronic states with high precision owing to the negligibly small contribution from the surface; therefore, no surface cleaning was done. Photoelectrons were collected using a Gammadata Scienta SES2002 electron analyzer, which is modified to accommodate higher photoelectron kinetic energies up to 6 keV.

Figure 1 shows the energy distribution curves (EDC) of undoped GaN and that of $Ga_{0.899}Cr_{0.101}N$, and the difference spectrum between them. The origin of binding energy (BE) is set to the valence band maximum (VBM). Cr doping introduces new electronic states in the band gap (**A**) and causes some change in the valence band structure (**B** and **C**). In addition, the intensity of the in-gap state increases in proportion to the Cr concentration (inset in Fig. 1). Thus, the in-gap states should be related to the doped Cr.

In order to elucidate the origin of the new electronic states, we have calculated the electronic band structure for Cr-doped GaN by the first-principles calculation based on the density functional theory using the generalized gradient approximation. On the basis of the calculation considering the intensity ratio of the atomic subshell photoionization cross sections of Cr 3*d* and Ga 4*s* at the high excitation energy [4], the observed in-gap state is interpreted to originate dominantly from Ga 4*s* states by hybridization with Cr 3*d* [5].

Core level spectra of N 1*s* and Ga $2p_{3/2}$ are also modified by Cr doping. Open circles, solid gray circles, and solid black circles in Fig. 2(a) show N 1*s* core level spectra of undoped GaN, $Ga_{0.937}Cr_{0.063}N$, and $Ga_{0.899}Cr_{0.101}N$, respectively. Gray and black solid lines are the difference spectra between the undoped

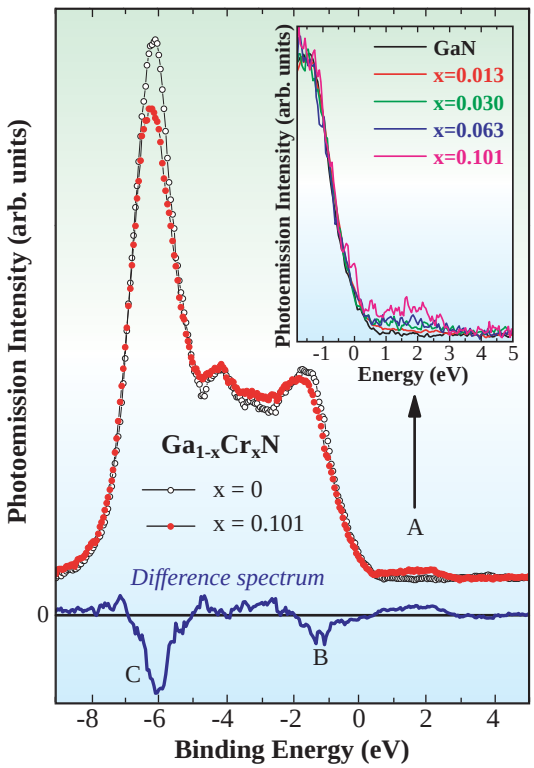

Fig. 1. EDCs for undoped GaN (open circles) and $Ga_{0.899}Cr_{0.101}N$ (filled circles) at hν = 5.95 keV. These EDCs are obtained by subtracting the trivial background from the experimental spectra. The solid line at the bottom panel shows the difference spectrum. The inset shows the intensity of the in-gap state *versus* Cr concentration.

GaN and $Ga_{1-x}Cr_xN$ (x = 0.063 and 0.101, respectively). The main peak at 394.5 eV decreases and the tail at 393.8 eV increases with Cr doping. The rates of the decrease and the increase are proportional to the Cr concentration. Namely, Cr doping causes a decrease of N 1*s* in the matrix and introduces a new chemically shifted component at the low BE region. Because the electronegativities (EN) of Ga, Cr, and N atoms are 1.81, 1.56, and 3.07, respectively, the EN difference of the Cr-N bond is larger than that of the Ga-N bond. Therefore, the N atoms bonded with Cr are more shielded by electrons than the N atom bonded with Ga atoms. Accordingly, Cr doping causes a chemical shift of N 1*s* to the low BE region.

Figure 2(b) shows Ga $2p_{3/2}$ core level spectra. Gray and black solid lines are the difference spectra between undoped GaN and $Ga_{1-x}Cr_xN$ (x = 0.063 and 0.101, respectively). The intensity of the peak decreases with Cr doping. The decrease of the intensity is almost linearly proportional to the increase of Cr content. The line shape in difference spectra is evidently asymmetric, suggesting the existence of an unresolved chemically shifted component at the low BE side. This is reasonably expected from the EN differences between Ga-Cr and N-Cr. The linear increase of the full width at half maximum (FWHM) with increasing Cr content (inset in Fig. 2(b)) is taken as further evidence of the existence of the increasing chemically shifted component, supporting the Ga-Cr hybridization discussed above.

We have investigated the electronic structure of $Ga_{1-x}Cr_xN$ by bulk-sensitive HX-PES. We have observed for the first time the electronic states in the GaN band-gap region induced by Cr doping. This is the Ga 4*s* contribution raised by the hybridization with Cr 3*d*. We have also observed that the Cr doping influences the second neighbor Ga via the formation of Cr-N bonds.

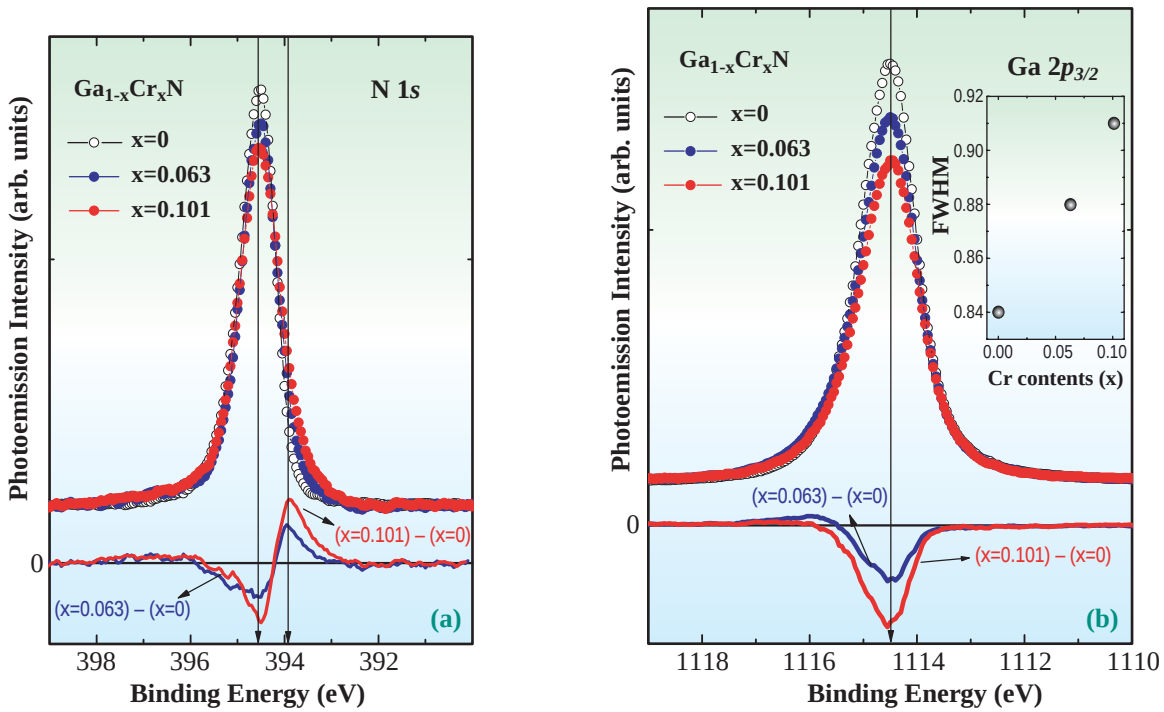

Fig. 2. Core-level photoemission spectra of **(a)** N 1*s* and **(b)** Ga $2p_{3/2}$ of undoped GaN (open circles) and $Ga_{1-x}Cr_xN$ (x = 0.063 (solid blue circles), 0.101(solid red circles). The inset on the right in (b) shows the FWHM variation of the Ga $2p_{3/2}$ spectra with Cr concentration. The more Cr doped, the broader the FWHM of Ga $2p_{3/2}$ spectra.

Jung-Jin Kim[a], Hisao Makino[b,*] and Takafumi Yao[a,b]

(a) Center for Interdisciplinary Research, Tohoku University
(b) Institute for Materials Research, Tohoku University

*E-mail: makino@cir.tohoku.ac.jp

References

[1] Y. Ohno *et al.*: Nature **402** (1999) 709.
[2] K. Kobayashi *et al.*: Appl. Phys. Lett. **83** (2003) 1005.
[3] Y. Takata *et al.*: Appl. Phys. Lett. **84** (2004) 4310.
[4] J.J. Yeh *et al.*: Atomic Data and Nuclear Data Tables **32** (1985) 1.
[5] *J.J. Kim, H. Makino, K. Kobayashi, Y. Takata, T. Yamamoto, T. Hanada, M.W. Cho, E. Ikenaga, M. Yabashi, D. Miwa, Y. Nishino, K. Tamasaku, T. Ishikawa, S. Shin and T. Yao: Phys. Rev. B* ***70*** *(2004) 161315(R).*

Electronic Excitations in $La_{1-x}Sr_xMnO_3$ Studied by Resonant Inelastic X-ray Scattering

Strongly correlated electron systems, such as transition metal oxides, have been an attractive issue in recent condensed matter physics [1]. Strong on-site Coulomb repulsion separates a partially filled band into the occupied lower Hubbard band (LHB) and the unoccupied upper Hubbard band (UHB), and the system becomes an insulator with a charge gap, known as the Mott gap. In the vicinity of the metal-insulator transition by carrier doping, these systems show not only novel physical properties such as high-temperature superconductivity in cuprates and colossal magnetoresistance (CMR) in manganites, but also a variety of electronic phases from the interplay of different degrees of freedom of charge, spin, orbital and lattice. The carrier doping in the strongly correlated electron systems affects the electronic structure in a wide energy range, and its reconstructions occur up to a few eV across the metal-insulator transition as well as at the magnetic or orbital ordering. Therefore, it is quite important to examine the electronic excitations in a wide energy-momentum space to understand the electronic properties of these compounds. In this respect, the resonant inelastic X-ray scattering (RIXS) in the hard X-ray regime is an ideal tool for the elucidation of the electron excitations around a few eV since it gives momentum-dependent spectra, unlike the conventional optical experiments. Here we report on a RIXS study of CMR materials, $La_{1-x}Sr_xMnO_3$.

The excitation across the Mott gap in the RIXS process at the Mn *K*-edge is schematically shown in Fig. 1. The initial state is (a). When the incident X-ray is absorbed, a core hole is created in the 1*s* orbital of an Mn site (b). Then, an electron transfers from surrounding atoms to an unoccupied Mn orbital to screen the core hole potential (c). After emitting the X-ray, the transferred electron remains in the Mn orbital as a final state (d).

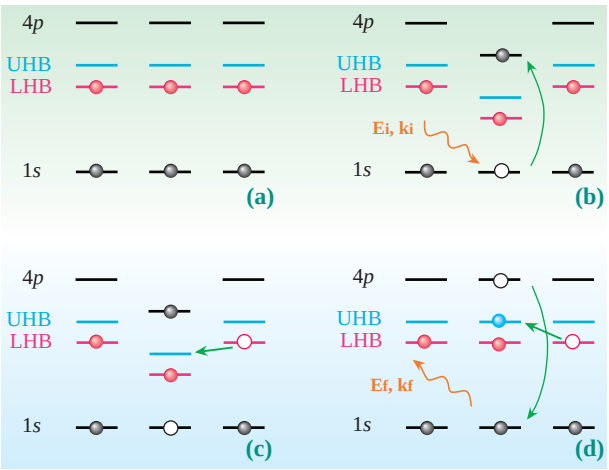

Fig. 1. Schematic picture of the Mn *K*-edge RIXS process.

The RIXS experiments were carried out at beamline **BL11XU**. A spectrometer for inelastic X-ray scattering is installed in this beamline [2]. The total energy resolution was 230-500 meV, depending on the selection of monochromators. The energy of the incident X-ray was tuned at 6556 eV, where the excitation across the Mott gap is most enhanced.

RIXS spectra of $LaMnO_3$ and $La_{0.6}Sr_{0.4}MnO_3$ are shown in Fig. 2. $LaMnO_3$ is a Mott insulator, while $La_{0.6}Sr_{0.4}MnO_3$ has enough holes to be metallic. In $LaMnO_3$, the peak at 2.5 eV corresponds to the excitation from the effective LHB hybridized with the O 2*p* orbital to UHB across the Mott gap, which shows a weak dispersion in momentum dependence and an apparent polarization dependence of scattering intensity. These experimental facts are related to the orbital order in $LaMnO_3$ and are consistent with theoretical calculation. The peaks at higher energies of 8 and 11 eV are the charge transfer excitations from O 2*p* to Mn 3*d* and from O 2*p* to Mn 4*s*/4*p*, respectively [3]. It should be emphasized that a salient peak remains even in metallic $La_{0.6}Sr_{0.4}MnO_3$, as seen in Fig. 2(a). We show the spectra at a higher scattering angle in Fig. 2(b), where the elastic scattering decreases and the spectral shape at low energy can be seen more clearly. Since we confirmed that the momentum dependence of energy dispersion for the Mott gap excitation is small in both compounds, the difference of momentum between two spectra is not important. A gap feature was observed in insulating $LaMnO_3$, while the gap is partially filled in metallic $La_{0.6}Sr_{0.4}MnO_3$. Even though the Mott gap is filled in $La_{0.6}Sr_{0.4}MnO_3$, a fairly large spectral weight remains at the excitation from the LHB to the UHB even in the metallic state. The momentum and polarization dependences of the Mott gap excitation are qualitatively similar to those of $LaMnO_3$, even though a static orbital order disappears in $La_{0.6}Sr_{0.4}MnO_3$. These results indicate that the strong Coulomb repulsion and the orbital correlation robustly persist

even in the metallic state of $La_{0.6}Sr_{0.4}MnO_3$.

Figure 3 shows the temperature dependence of the Mott gap excitation in $La_{0.8}Sr_{0.2}MnO_3$, which shows a metal-insulator transition accompanied by a ferromagnetic transition at Tc = 309 K [4]. The RIXS intensity of Q = (2.7, 0, 0) increases with decreasing temperature, whereas that of Q = (2.2, 2.2, 0) is independent of temperature. The temperature dependence of intensity depends on the direction of the scattering vector, and the intensity along the <h00> direction roughly accords with the bulk magnetization. We consider that the difference in temperature dependence between the <h00> and <hh0> directions may be attributed to the anisotropy of the magnetic interaction related to the orbital correlation, as is often discussed. The present result indicates again that the orbital degree of freedom is important for electronic properties in $La_{1-x}Sr_xMnO_3$.

In summary, our results demonstrate that the momentum-dependent spectra of RIXS are important in studying electronic structure and in elucidating the underlying interactions of electronic degrees of freedom in strongly correlated electron systems.

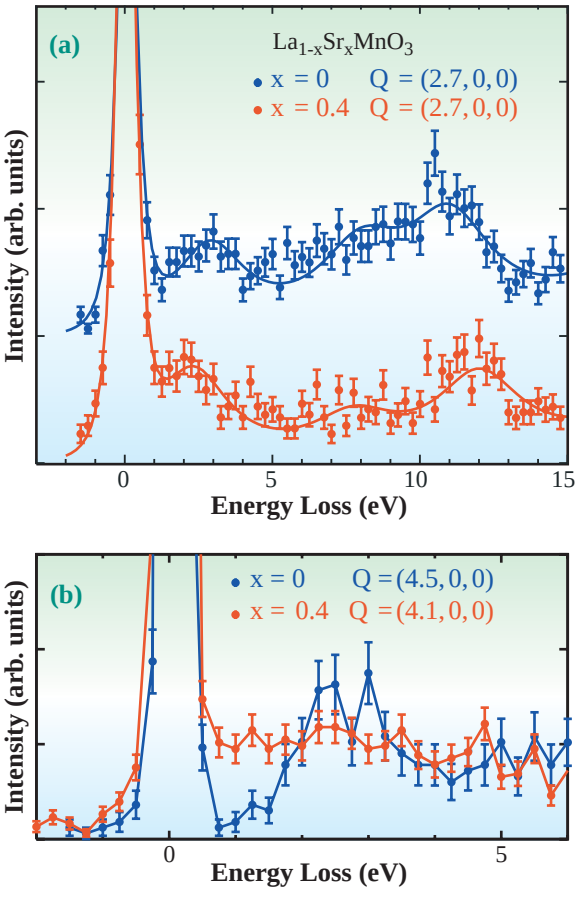

Fig. 2. RIXS spectra of $LaMnO_3$ and $La_{0.6}Sr_{0.4}MnO_3$ at Q = (2.7, 0, 0) **(a)** and at higher scattering angle **(b)**. The energy resolution is 230 meV.

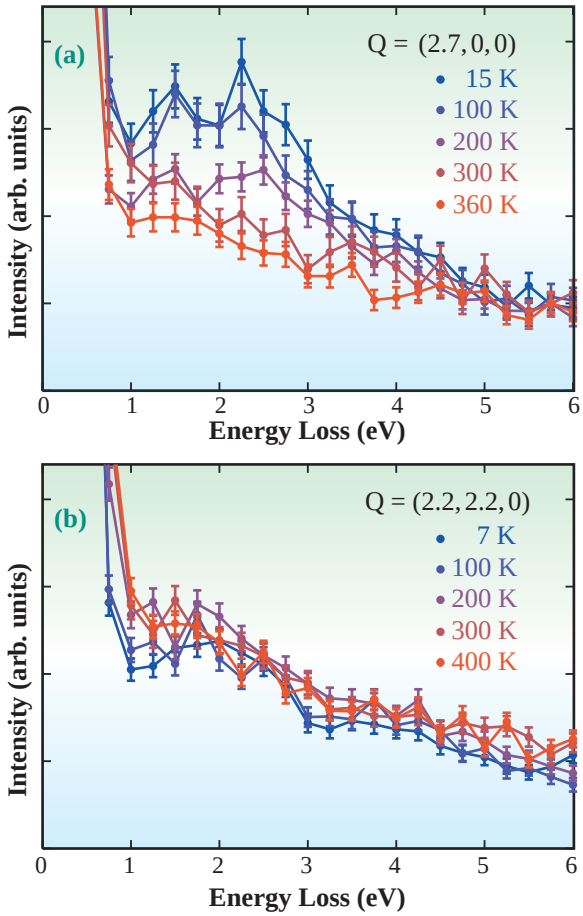

Fig. 3. RIXS spectra of $La_{0.6}Sr_{0.4}MnO_3$ at some temperatures. The scattering vectors are Q = (2.7, 0, 0) for **(a)** and Q = (2.2, 2.2, 0) for **(b)**, respectively. The energy resolution is about 500 meV.

Kenji Ishii* and Toshiya Inami

SPring-8 / JAERI

*E-mail: kenji@spring8.or.jp

References

[1] Y. Tokura and N. Nagaosa: Science **288** (2000) 462.
[2] T. Inami *et al.*: Nucl. Instrum. Meth. Phys. Res. A **467-468** (2001) 1081.
[3] T. Inami *et al.*: Phys. Rev. B **67** (2003) 045108.
[4] A. Urushibara *et al.*: Phys. Rev. B **51** (1995) 14103.
[5] *K. Ishii, T. Inami, K. Ohwada, K. Kuzushita, J. Mizuki, Y. Murakami, S. Ishihara, Y. Endoh, S. Maekawa, K. Hirota and Y. Moritomo: Phys. Rev. B* ***70*** *(2004) 224437.*

Extended Spin-polarized X-ray Absorption Near-edge Spectra of MnO

Spin-polarized XANES (SPXANES) gives a direct approach to resolve the spin dependence of excited electronic states of non-ferromagnetic materials [1]. It is based on the assumption that one can separate the $K\beta_{1,3}$ ($3p \rightarrow 1s$) emission spectrum into an internally referenced spin-up part and a spin-down part [2], and hence one can achieve a local-spin selectivity in the *K*-edge XANES by measuring the emission from either the main (spin-down, $K\beta_{1,3}$) or satellite (spin-up, Kβ') bands as a function of incident X-ray energy.

At beamline **BL47XU**, X-ray emission in the MnKβ region of MnO powder was measured at room temperature using a multicrystal spectrometer [3]. The radiation was horizontally dispersed and vertically focused with five cylindrically bent Ge (440) crystals having a 550 mm radius of curvature. Analyzed X-rays from different crystals were focused on different vertical positions of a two-dimensional position-sensitive proportional counter. The overall energy resolution was 1.4 eV.

Figure 1(a) shows a $K\beta_{1,3}$(spin-down)- and Kβ'(spin-up)-emission contour map of MnO [3,4], where the abscissa (ω_1) and the ordinate (ω_2) are excitation and emission energies, respectively. Here, the $1s \rightarrow 3d$ resonant excitation appears as an island,

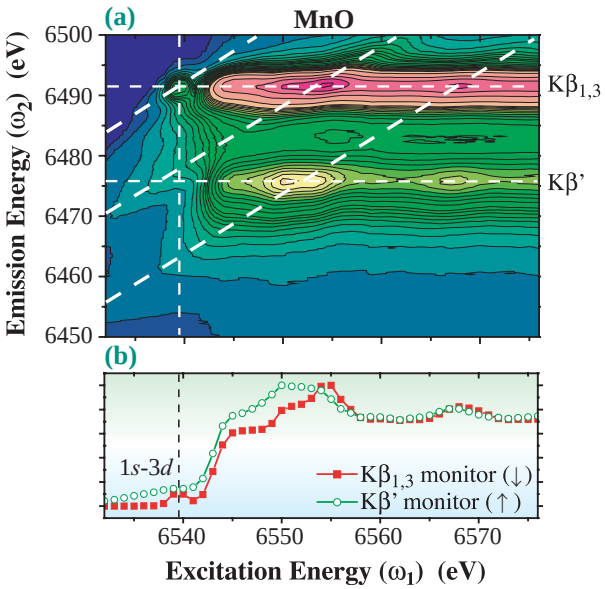

Fig. 1. **(a)** A Kβ-contour map of MnO; emission intensities as functions of excitation (ω_1) and emission (ω_2) energies are plotted. Two horizontal and three diagonal ridges are indicated by broken lines. **(b)** Cross sections of the map at ω_2 = 6476 eV (solid squares) and ω_2 = 6491 eV (open circles).

and the existence of two prominent ridges extending parallel to the abscissa, indicated by broken lines, is evident. The energy ω_2 of each ridge is the same as that of regular $K\beta_{1,3}$ and Kβ' emissions. In addition, three ridges stretching diagonally (constant energy loss), also indicated by broken lines, are also conspicuous.

By traversing the contour map along a constant ω_2 axis, one obtains an excitation spectrum for the constant final state energy, which is equivalent to measuring excitation spectra while monitoring the part of fluorescence spectra, the conventional method of observing SPXANES [1]. Shown in Fig. 1(b) are two such excitation spectra obtained along the lines ω_2 = 6491 eV ($K\beta_{1,3}$ peak) and ω_2 = 6476 eV (Kβ' peak), which are essentially the same as the SPXANES reported previously [1]. Here, non-vanishing components were noted in the energy region of $1s \rightarrow 3d$ transition not only in the spin-down polarized spectrum but also in the spin-up spectrum. Since all five 3*d*-electrons of Mn^{2+} in MnO are known to be spin-up, the transition is forbidden from Hund's rule in the latter spectrum. This casts some doubts on the validity of the underlying assumption of the conventional SPXANES method.

The Kβ-contour map, shown in Fig. 1(a), can be analyzed using the following equation based on the Kramers-Heisenberg formula [4]

$$\frac{d\sigma(\omega_1)}{d\omega_2} \propto \int \frac{(\Omega_{1s}+\omega)\{(dg_{1s}^{up}/d\omega)f^{up} + (dg_{1s}^{down}/d\omega)f^{down}\}}{(\Omega_{1s}+\omega-\omega_1)^2+\Gamma_{1s}^2/4\hbar^2} d\omega \quad (1)$$

Here, $\hbar\omega$ is the energy of the excited electron in the intermediate state, and Γ_{1s} is the widths of the 1*s* levels, the energy of which is represented by $\hbar\Omega_{1s}$. $dg_{1s}^{up}/d\omega$ and $dg_{1s}^{down}/d\omega$ are spin-dependent oscillator strength distributions for spin-up and spin-down 1*s* electrons, respectively. The shape of the Kβ-emission spectra is determined also by final-state effects, such as lifetimes and multiplet structures. In equation (1), they are taken into consideration by functions f^{up} and f^{down}.

In Fig. 2(a), Kβ-emission spectra observed at the excitation energies indicated are shown by solid lines. Calculated Kβ-spectra by using equation (1) and by assuming that the two spectra in Fig. 1(b) represent $dg_{1s}^{up}/d\omega$ and $dg_{1s}^{down}/d\omega$ are also shown in Fig. 2(a) by broken lines. Agreements between the observed and calculated spectra are not very good, in particular

below the absorption edge excitation. This result reveals that the two spectra of Fig. 1(b) do not well represent the $dg_{1s}/d\omega$'s. Subsequently, by modifying $dg_{1s}^{up}/d\omega$ and $dg_{1s}^{down}/d\omega$, similar calculations were repeated by trial and error until satisfactory agreements were reached. The 'best-fit' $dg_{1s}/d\omega$'s thus obtained are shown in Fig. 2(b).

In Fig. 2(a), best-fit calculated RIXS spectra at each excitation energy are shown by circles. The calculated spectra almost completely overlap the observed ones at every spectrum. It must be stressed that a single set of $dg_{1s}^{up}/d\omega$ and $dg_{1s}^{down}/d\omega$ has been employed to generate all the emission spectra, in spite of the fact that observed spectra vary enormously with excitation energy.

The best-fit $dg_{1s}^{up}/d\omega$ and $dg_{1s}^{down}/d\omega$ are considerably different from the excitation spectra obtained by monitoring Kβ' or $K\beta_{1,3}$ in Fig. 1(b). Major features are labeled; $1s \rightarrow 3d$ (pre-edge peak), A and B (shoulders), C and E (peaks), and D (valley), which well correspond to those in the spectra calculated by Soldatov *et al.* [5]. It is evident that $1s \rightarrow 3d$ transition is completely missing in the $dg_{1s}^{up}/d\omega$, as is expected from Hund's rule. It is immediately understood from Fig. 1(a) that the non-vanishing intensity apparent in the Kβ' excitation spectrum is due to the diagonal component that originates from the main peak of the $K\beta_{1,3}$ ridge.

The present results indicate that analyses of emission maps in terms of the Kramers-Heisenberg equation (eq. (1)) are crucially important for a correct determination of SPXANES.

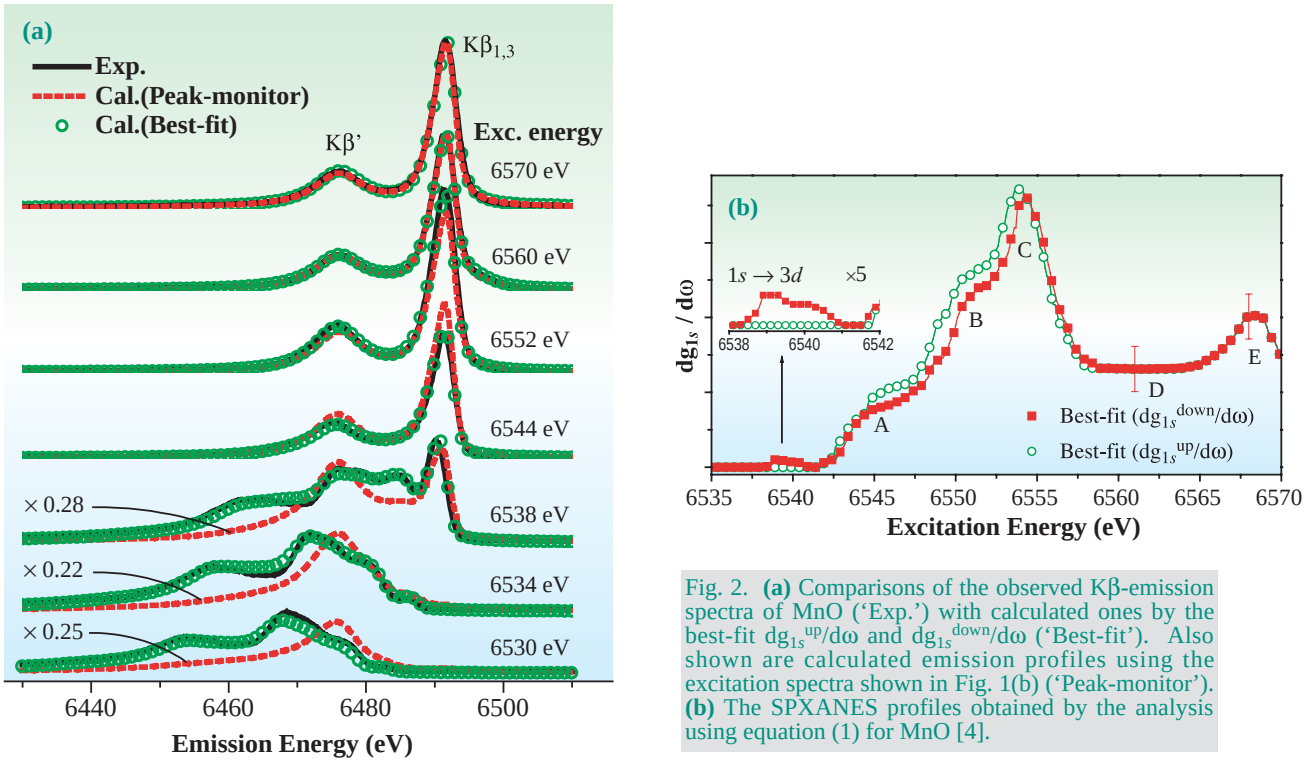

Fig. 2. **(a)** Comparisons of the observed Kβ-emission spectra of MnO ('Exp.') with calculated ones by the best-fit $dg_{1s}^{up}/d\omega$ and $dg_{1s}^{down}/d\omega$ ('Best-fit'). Also shown are calculated emission profiles using the excitation spectra shown in Fig. 1(b) ('Peak-monitor'). **(b)** The SPXANES profiles obtained by the analysis using equation (1) for MnO [4].

Hisashi Hayashi

IMRAM, Tohoku University

E-mail: hayashi@tagen.tohoku.ac.jp

References

[1] K. Hämäläinen *et al.*: Phys. Rev. B **46** (1992) 14274.
[2] K. Tsutsumi *et al.*: Phys. Rev. B **13** (1976) 929.
[3] *H. Hayashi, M. Kawata, R. Takeda, Y. Udagawa, Y. Watanabe, T. Takano, S. Nanao and N. Kawamura: J. Electron Spectrosc. Relat. Phenom.* ***136*** *(2004) 191.*
[4] *H. Hayashi, M. Kawata, Y. Udagawa, N. Kawamura and S. Nanao: Phys. Rev. B* ***70*** *(2004) 134427.*
[5] A.V. Soldatov *et al.*: Phys. Rev. B **52** (1995) 11757.

Actively-controlled Oxidation of Cu(100) with Hyperthermal O_2 Molecular Beam

The dissociation process of an oxygen molecule (O_2) on a metal surface is of considerable research interest, both because many important industrial oxidation processes are heterogeneously catalyzed by transition metals (TMs) and because O_2 dissociation is the first step towards the corrosion of various TMs. Among TMs, Cu is one of the most important metals. Cu oxidation process must be elucidated because of the important role of Cu oxides in materials science, for example, high-T_c superconductors of cuprates and solar cells.

A Cu(100) can be oxidized in its bulk when exposed to ambient thermal O_2 molecules at temperatures above 450 K, and Cu_2O films can be grown epitaxially. However, high exposures of 10^5-10^6 L O_2 (1L = 1.33×10^{-4} Pa·s) are required for an oxide-film growth on Cu(100) under a thermal O_2 atmosphere, suggesting the low efficiency of oxidation. Here, we demonstrate actively-controlled oxidation of Cu with a hyperthermal O_2 molecular beam (HOMB) [1-4].

All experiments were performed using the surface reaction analysis apparatus (SUREAC~2000) constructed at beamline **BL23SU**. After the irradiation of a proper amount of HOMB along the surface normal, high-resolution X-ray photoemission spectroscopy (XPS) spectra were measured at ~300 K using synchrotron radiation (SR) with the photon energy of 760.3 eV.

Figures 1(a) and 1(b) show the oxygen-coverage (Θ) dependence of representative O-1*s* XPS spectra and the O-uptake curve determined from the integration of such O-1*s* spectra in the 2.3-eV-HOMB irradiation on the Cu(100) surface at ~300 K, respectively. In Region I in Fig. 1(b), the O-1*s* peak, fitted well with a symmetric single component (see the spectrum at Θ = 0.47 ML in Fig. 1(a)), decreases in its full width at half maximum (FWHM) with increasing Θ. In $\Theta \geq 0.5$ ML (Region II), the oxidation of Cu progresses very slowly as seen in Fig. 1(b). We have tried to separate the O-1*s* peak into two components (see the spectrum at Θ = 0.95 ML in Fig. 1(a)). One component (blue solid line) located at the binding energy of 529.5 eV corresponds to the surface O atoms and has the same line shape as the single component (red solid line) at Θ = 0.47 ML, as shown in Fig. 1(a). The other component (blue dashed line in Fig. 1(a)) centered at 530.1 eV with nearly the same FWHM as the surface

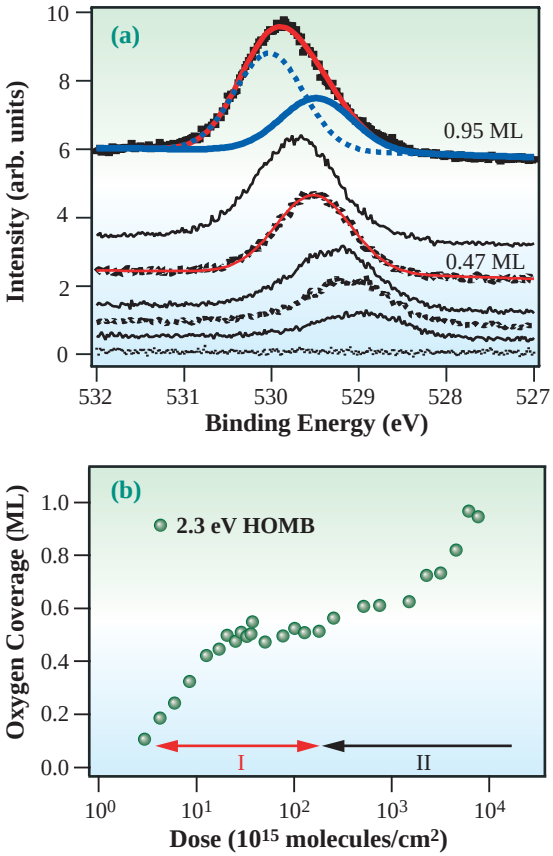

Fig. 1. **(a)** O-coverage dependence of the O-1*s* XPS spectra for the 2.3-eV-HOMB incidence along the surface normal on Cu(100) at ~300 K. The spectra correspond to 0, 0.19, 0.32, 0.42, 0.47, 0.73, and 0.95 ML from the bottom. The spectra at Θ = 0.47 and 0.95 ML are separated into single (red solid line) and double components (blue solid and dashed lines), respectively. The red solid line at Θ = 0.95 ML indicates the sum of the double components. **(b)** O-uptake curves on Cu(100) for 2.3 eV HOMB incidence. Regions I and II are indicated by the arrows.

component is assigned to the subsurface and/or bulk O atoms that initiate a growth of Cu_2O.

What happens in the slow oxidation into subsurface and/or bulk? We propose that *a collision-induced-absorption mechanism may explain the slow* oxidation process of Cu in Region II. In this mechanism, an incident O_2 molecule collides with a preadsorbed O atom impulsively with a small impact parameter. The energy transfer from the incident particle to a

preadsorbed O atom occurs effectively and as a result, the produced energetic O atom penetrates into the subsurface leaving a vacant site for further dissociative adsorption on the surface.

We directly confirmed this collision-induced-absorption mechanism as follows. Figure 2 shows the O-1*s* spectra measured with a high resolution after the 3-eV-Ar-beam incidence along the surface normal on the $2\sqrt{2} \times \sqrt{2}$ R45º surface (Θ = 0.5 ML) at ~300 K. The symmetric O-1*s* shape (see the spectrum at Θ = 0.47 ML in Fig. 1(a)) turned into an asymmetric shape after the exposure of the $2\sqrt{2} \times \sqrt{2}$ R45º surface to 3-eV Ar. This asymmetric shape is attributed to the above-mentioned two components; one at 529.6 eV for surface O atoms and the other at 530.0 eV for the subsurface and/or bulk O atoms. This is the first example of the collision-induced-absorption mechanism in the oxidation process, although it is known that the energetic-collision process induces the dissociation of the preadsorbed O_2 molecule at low temperatures.

In summary, oxidation of Cu(100) by HOMB was investigated by high-resolution XPS with SR. We apply for the first time a collision-induced absorption mechanism to the oxidation of Cu into Cu_2O with the HOMB irradiation. Thus, we demonstrated the possibility of the actively-controlled oxidation by HOMB.

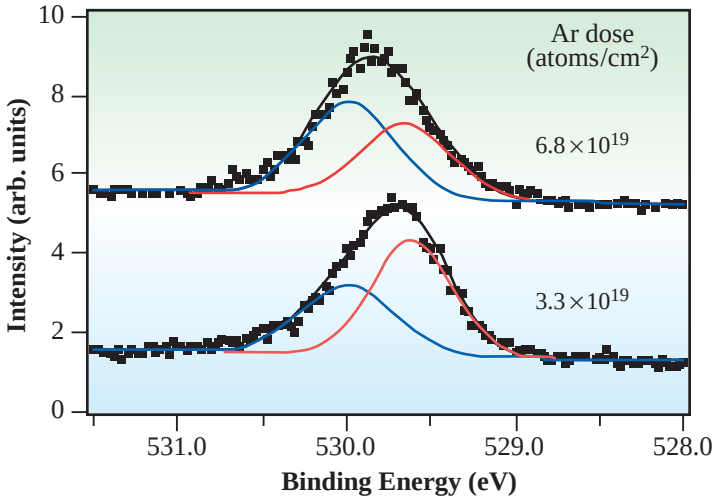

Fig. 2. O-1*s* XPS spectra measured after the 3 eV Ar-beam incidence along the surface normal on the $2\sqrt{2} \times \sqrt{2}$ R45º surface (Θ = 0.5 ML) at ~300 K. The lower and upper spectra correspond to the 3-eV-Ar exposures of 3.3×10^{19} and 6.8×10^{19} atoms/cm^2, respectively. Each spectrum can be separated into two components of surface (red line) and the subsurface and/or bulk (blue line) O atoms. Black lines indicate the fitted curves corresponding to the sums of the red and blue curves.

Michio Okada[a,*], Toshio Kasai[a] and Yuden Teraoka[b]

(a) Department of Chemistry, Osaka University
(b) SPring-8 / JAERI

*E-mail: okada@chem.sci.osaka-u.ac.jp

References

[1] M. Okada *et al.*: J. Chem. Phys. (Communications) **119** (2003) 6994.
[2] *M. Okada, K. Moritani, A. Yoshigoe, Y. Teraoka, H. Nakanishi, W.A. Diño, H. Kasai and T. Kasai: Chem. Phys.* ***301*** *(2004) 315.*
[3] K. Moritani *et al.*: J. Vac. Sci. Tech. A **22** (2004) 1625.
[4] K. Moritani *et al.*: Thin Solid Films **464-465** (2004) 48.

Depining Process and Dynamic Phase Transition of Charge-density Wave in $K_{0.3}MoO_3$

The homogeneous phase in low-dimensional materials, such as $K_{0.3}MoO_3$, $NbSe_3$, 2H-$NbSe_2$ and TMTSF molecules, undergoes a phase transition to charge-density waves (CDWs) at low temperatures. The instability toward spontaneous formation of charge-density modulations is driven by electron-phonon or electron-electron interactions [1]. Among many other interesting aspects of CDWs, the transport property has attracted much attention from both experimental and theoretical sides. It is generally believed that current is suppressed at a small bias voltage, where the CDW is pinned by impurity potential. Above some threshold voltage, the sliding motion along the applied electric field starts and the current increases significantly. It is known that this dynamic behavior involves the phase slippage of the density waves [2]. In addition, the dynamics of the disordered state driven by an external force in a periodic medium are also of the characteristic common to many physical systems, such as density waves and vortex lattices [3].

An interesting question naturally arises: How does the internal structure of density modulations change in the presence of the applied electric field? In particular, in the non-equilibrium sliding motion the robust periodic structure, originally developed in static limit, might become unstable. In this report, we address this issue by applying the techniques of multiple (three-wave) X-ray diffraction and X-ray scattering to measure the changes in the CDW lattice and its internal structure with respect to the applied electric fields. From the extracted phase $\delta_3(V)$ of the three-wave diffraction and the peak profile of the CDW satellite reflection, we demonstrate that the occurrence of nonlinear conductivity caused by the periodic media is through the internal deformation of the CDW lattice, i.e., a phase jump of 2π, as the applied voltage exceeding the threshold. From the evolution of the measured peak width of satellite reflections as a function of the field strength, we also report that the CDW lattice can be driven to move and undergo a dynamic phase transition from a disordered pinning state to an ordered moving solid state and then to a disordered moving liquid.

A good-quality single-crystal $K_{0.3}MoO_3$ was first characterized and oriented at room temperature. The non-linear conductivity [4] was confirmed by measuring the *I-V* curve at 70 K, as shown in Fig. 1(a), indicating the dynamic transition from the pinned CDWs to sliding motions at the threshold observed at $V_c \approx 0.165$ V. It is noteworthy that the nonlinearity is not as robust as that at low temperature due mainly to the thermal fluctuations smearing out the switching behavior.

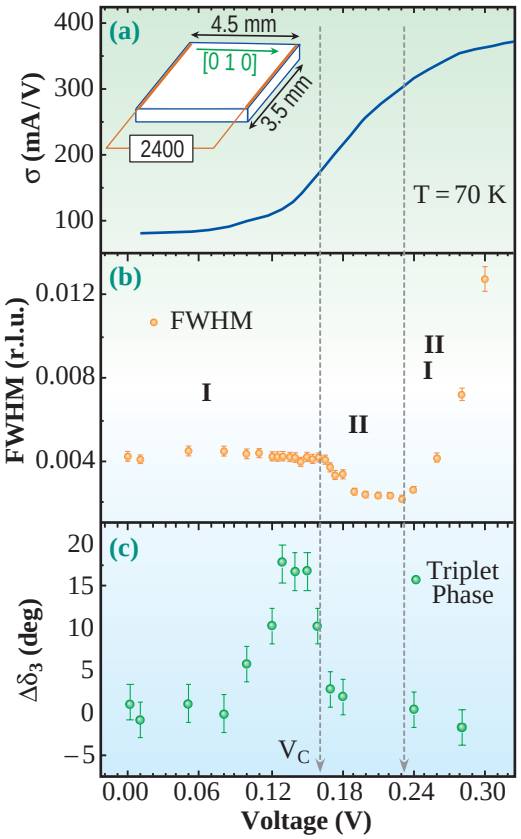

Fig. 1. **(a)** Resistance versus voltage at 70 K. The curve shows the nonlinear behavior with a threshold voltage $V_c \approx 0.165$ V. The inset shows the dimensions of the sample and the experimental setup. **(b)** Evolution of the FWHM of the CDW satellite reflection as a function of applied voltage. One can classify CDW into three phases: (I) the creeping CDW state, (II) the moving solid and (III) the moving liquid. **(c)** Triplet phase $\Delta\delta_3$ at different voltages. Note that in the sliding phase, $\Delta\delta_3 = 0$ is direct evidence that the pinning forces become irrelevant.

The *in situ* measurements were carried out in the Taiwan beamline **BL12B2**. The incident X-ray wavelength was selected to be 1 Å. Satellite reflections signal the formation of CDW, located at the Bragg position G = (13 q 6.5), where $q \approx 0.748$. Scans were performed through the longitudinal direction of [2 0 -1], and the data was convoluted with the resolution function obtained from the nearby Bragg peak (12 0 -6). Figure 1(b) shows the evolution of the peak width of CDW reflection as a function of applied voltage at T = 70 K.

As shown in Fig. 1(b), the FWHM of the satellite reflection, (13 q -6.5), remains more or less unchanged below the critical voltage $V_c \approx 0.165$ V determined from the transport measurement. Above the critical voltage, where the CDW enters the sliding phase, the FWHM decreases as predicted by previous theoretical investigations. As the voltage exceeds 0.18 V, the lattice shows a long-range ordered state; namely, the moving solid phase [5]. This interesting dynamical narrowing of FWHM is a strong indication that the pinning forces due to random potentials become irrelevant (or less efficient) when the CDW begins to slide. When the voltage exceeds 0.22 V, nonequilibrium effects, amplitude fluctuations and other factors become important and the Bragg peaks disappear. This is clearly evidenced by the sharp increase of FWHM.

The other key quantity we studied is the triplet phase δ_3 of a 3-wave multiple diffraction at different bias voltages. To set up a 3-wave ($\boldsymbol{O}$,$\boldsymbol{G_1}$,$\boldsymbol{G_2}$) multiple diffraction experiment, the crystal is first aligned for a primary reflection $\boldsymbol{G_1}$. It is then rotated around the reciprocal lattice vector $\boldsymbol{G_1}$ with an azimuthal angle ψ to bring in the secondary reflection $\boldsymbol{G_2}$, that also satisfies Bragg's law. Namely, both $\boldsymbol{G_1}$ and $\boldsymbol{G_2}$ reflections take place simultaneously. $\boldsymbol{O}$ stands for the incident reflection. The interaction of the multiply diffracted waves modifies the intensity of the primary reflection. Intensity variation showing an asymmetric distribution versus y gives the required information about δ_3, which is the triplet phase of $F_{G2}\,F_{G3}\,/\,F_{G1}$ involved in the 3-wave diffraction. Previously [6], we demonstrated that the triplet phase δ_3 due to the coupling between the CDW lattice and its host lattice can be probed using multiple diffraction. Here we further demonstrate that measuring the relative change in δ_3 , $\Delta\delta_3$, caused by a driving force makes the study of the internal deformation of the CDW lattice possible.

Through the azimuthal scan around the primary reflection $\boldsymbol{G_1}$ = (13 q -6.5) at T = 70 K, we obtained the 3-wave diffraction pattern containing numerous multiple diffraction peaks. We concentrated here only on a particular 3-wave diffraction, (0 0 0), (13 q -6.5) and (4 -8 4) at ψ = 108.53º, where the primary reflection is (13 q -6.5) and the coupling reflection is (9 8 +q 10.5). The profile asymmetry of the diffraction intensity of (13 q -6.5) versus ψ at V = 0 is typical for δ_3 = 0. The phase variation $\Delta\delta_3$ due to nonzero applied voltages was analyzed based on the dynamical theory for multiple diffractions [7]. In Fig. 2, the profile develops different asymmetries at different finite voltages. In the static CDW state, the crystal lattice possesses a centrosymmetric structure, and a change in the peak profile means that this centrosymmetry is broken due

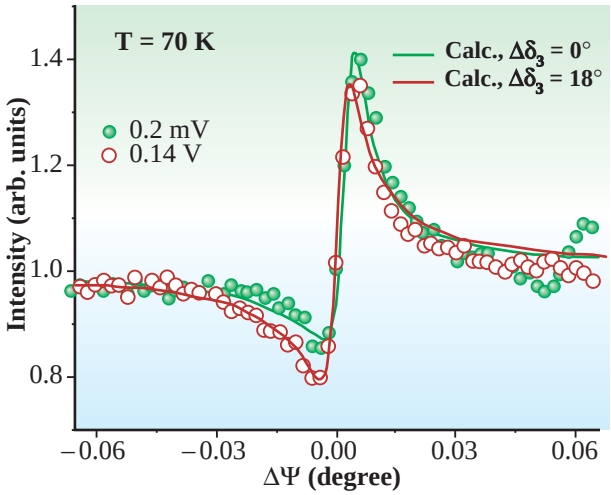

Fig. 2. Triplet phase change $\Delta\delta_3$ extrapolated from curve fitting of the 3-wave diffraction profiles of the primary reflection $\boldsymbol{G_1}$ = (13 q -6.5) at V = 0.2 mV and 0.14 V. The analysis is based on the dynamical theory for multiple diffractions [7].

to the relative motion of ions by a driving force. This results in a nonzero $\Delta\delta_3$, suggesting the internal deformation of the original charge density distribution by the driving force. As shown in Fig. 1(c), the estimated $\Delta\delta_3$ values from curve fitting at 0.1, 0.12 0.13, 0.14, 0.15, and 0.16 V are about 6º, 10º, 18º, 17º, 17º, and 10º respectively, and then back to 0º for $V > 0.18$ V. This proves experimentally that the occurrence of nonlinear transport behavior is through a phase jump of 2π at the sliding threshold, i.e., from the pinned to sliding states [8].

Chao-Hung Du[a,*], Mau-Tsu Tang[b] and Shih-Lin Chang[b,c]

(a) Department of Physics, Tamkang Univ., Taiwan
(b) National Synchrotron Rad. Research Center, Taiwan
(c) Dept. of Physics, National Tsing Hua Univ., Taiwan

*E-mail: chd@mail.tku.edu.tw

References

[1] A. W. Overhauser: Adv. Phys. **27** (1978) 343.
[2] S. Brazovskii *et al.*: Phys. Rev. B **61** (2000) 10640.
[3] U. Yaron *et al.*: Nature **376** (1995) 753.
[4] N. Ogawa *et al.*: Phys. Rev. Lett. **87** (2001) 256401.
[5] R. Danncau *et al.*: Phys. Rev. Lett. **89** (2002) 106404.
[6] C.-H. Du *et al.*: Acta Cryst. A **60** (2004) 209.
[7] S. L. Chang: X-ray multiple-wave diffraction - theory and application, Springer-Verlag, Berlin (2004); R. Colella: Acta Crystallogr. A **30** (1974) 413; Q. Shen: Phys. Rev. Lett. **80** (1998) 3268.
[8] *C.-H. Du, M.-T. Tang, Y.-R. Lee, Y.P. Stetsko, C.-Y. Lo, J.-J. Lee, H.-H. Lin and S.-L. Chang - submitted to Phys.Rev. Lett.; published in cond-mat/0412696.*

Chemical Science

Observation of reactions involving the variation of states and phases induced by external forces, and clarification of the nature of chemical bonds are the eternal subjects of chemistry. What we human beings have found, analyzed, uncovered and understood is only the tip of the iceberg of vast chemical knowledge. The variety of facilities installed in SPring-8 and the variety of scientists gathering there are now unveiling the mysteries of chemistry. The present section compiles eight highlighted outcomes of the excellent experiments carried out during the period of 2003B and 2004A.

The 1st article features the *femtosecond* nuclear motion that occurs when a core-excited CF_4 molecule happens to dissociate entirely to form an F^+ ion and an electron. This ultrafast process has been observed by measurement of electron-ion momentum correlation. The 2nd article introduces the application of two-dimensional ultra-small-angle X-ray scattering (2D-USXAS) to the *in situ* study of the aggregated structure of stretched rubber using X-ray scattering by silica particle fillers containing in an elastomer. The phenomenon of structural variation on a size scale of 100 nm-10 μmol is observed for the first time here, though its existence has been speculated on the basis of viscoelastic experiments. The following three articles are the outcomes of X-ray powder diffraction experiments carried out with the large Debye-Scherrer camera installed at BL02B2 combined with analyses by the maximum entropy method (MEM) and the Rietveld method. The porous coordination polymers are thought to be promising as an alternative material of zeolites, and the synthetic method and its properties are being extensively studied. The skeletal framework has been thought to be rigid but careful analysis of X-ray diffraction (XRD) patterns in the 3rd article reveals that the framework shrinks when guest molecules are incorporated into the pores of the coordination polymers. The porous coordination polymer adsorbs hydrogen molecules effectively and the authors of the 4th article are the first to succeed in determining the position of hydrogen molecules by the XRD technique. The 5th paper is the first to report that a charge ordering pattern in an organic conductor can be observed before and after the metal-insulator (M-I) transition known as the 'Peierls transition' by the same XRD technique. The 6th article deals with a new technique, nuclear resonant inelastic scattering (NRIS). The change in the spin state donated by the electronic configuration in the t_{2g} and eg orbitals of octahedrally coordinated iron complexes including ^{57}Fe was fully analyzed by NRIS. The nature of the chemical bonds are discussed in the 7th and 8th articles. The former article reports that shape resonance energy is dependent on intramolecule distance in core-level molecular photoionization as well as on the ionization cross section observed by high-resolution photoelectron spectroscopy. The latter clarifies the electronic structure of the hydrogen bond in various phases of H_2O at low temperatures by oxygen *K*-edge absorption fine structure technique and the spectra may suggest the presence of an unknown phase of ice at the temperatures of 4-50 K.

Tsunehiro Tanaka

Ultrafast Fragmentation Processes of CF_4 Studied by Electron-Ion Momentum Coincidence Spectroscopy

While purely spectroscopic methods like XPS yield information about the electronic and geometrical structure of materials, dynamic phenomena like chemical reactions can only be investigated using time-resolved or coincidence methods. One class of model reactions is ultrafast fragmentation of core excited small molecules. In the pre-edge region soft X-ray absorption spectra show a rich structure due to the excitation of a core electron to unoccupied molecular orbitals. This excitation leads to well defined initial states which can be considered a model of an intermediate state of a chemical reaction, even though the excitation energy involved is much higher than those in typical chemical reactions. Nuclear relaxation of the core-excited state takes place on a femtosecond time scale, in competition with the electronic relaxation. This femtosecond nuclear motion can be studied using an electron-ion momentum correlation measurement.

In the present work we focus on a specific Auger electron emission that belongs to atomic like Auger transition from the core excited F atom produced via ultrafast dissociation of a core excited CF_4 molecule [1]. We consider the following sequence of reactions:

(1) $CF_4 + h\nu \rightarrow CF_4^*$ $(F\ 1s^{-1})\ a_1^*$
(2) $CF_4^* \rightarrow CF_3 + F^*$ $(1s\ 2p^6\ ^2S)$
(3) F^* $(1s\ 2p^6\ ^2S) \rightarrow F^+ + e^-$

In step (1), a F(1*s*) electron in the CF_4 molecule is promoted into the lowest unoccupied antibonding molecular orbital. In step (2), the core-excited molecule dissociates into a core-excited F atom and a CF_3 fragment. We do not analyze the neutral molecular fragments. Thus, in the present work, CF_3 may be considered a symbol summarizing all possible excited or fragmented states involving an C atom and three F atoms. We will show that this part of the system absorbs most of the excess energy. In step (3), the F* atom emits an Auger electron with a kinetic energy close to 656.5 eV. The time scale of this decay is about 3 fs.

The experimental setup and the data acquisition system are described in detail elsewhere [2,3]. Briefly, the setup consists of a hemispherical electron spectrometer (Gammadata-Scienta SES-2002) and an ion time-of-flight (TOF) spectrometer mounted inside a vacuum chamber. The CF_4 is introduced as an effusive beam. Electrons that are emitted in the direction of the electron spectrometer are detected by a delay-line detector. Triggered by the electron detection, rectangular high voltage pulses are applied to the pusher and extractor electrodes. The ions are detected by another delay-line detector. All data are recorded in a TDC module and stored in the list-mode for off-line analysis. The experiment has been carried out on the c-branch of the high resolution photochemistry beamline **BL27SU**. The radiation source is a figure-8 undulator. We used first-order harmonic light generated by this undulator which has horizontal linear polarization (Fig. 1).

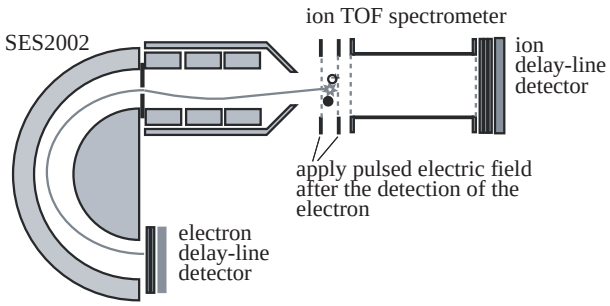

Fig. 1. Experimental setup for electron-ion momentum correlation measurements.

Figure 2 shows an example data set of the coincidence experiment belonging to the reactions (1),(2) and (3). Each point in the map corresponds to one electron-F^+ ion event. Below the Auger peak two clusters of points can be seen. They occur due to the fact that the Auger electron is emitted by a fast core excited F-atom and thus gets additional momentum compared with an emission from an F-atom at rest. The corresponding energy shift is termed Doppler shift. By analyzing the momentum distribution of the F^+ ions coincident with the atomic Auger line, the kinetic energy release of the F CF_3 fragmentation is determined.

Changing the excitation energy from 688.80 to 690.90 eV increases the excess energy of the excited CF_4 molecule. As we consider reactions where the Auger decay takes place in the atomic regime the excess energy can distribute among the fragmentation energy and the excitation of the CF_3 fragment. The slope of the curve in Fig. 3(a) indicates that more than half of the excess energy goes into excitation of the

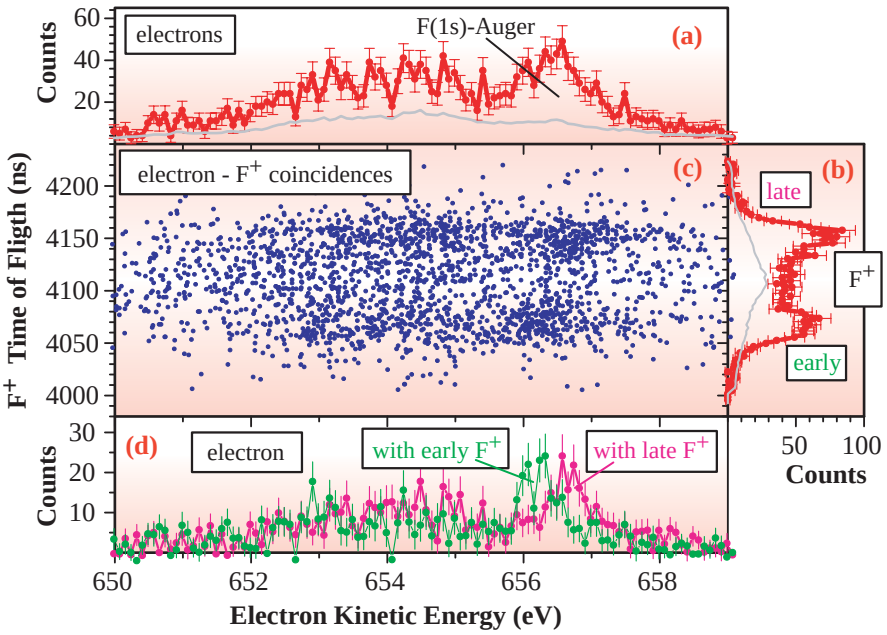

Fig. 2. The electron **(a)** and ion **(b)** spectrum of the coincidence events, together with the coincidence map **(c)**. Each dot represents one event. The grey lines in **(a)** and **(b)** are the contributions from the random coincidences. The two curves in **(d)** are the electron spectra that belong to a F^+ emission towards and away from the ion detector.

CF_3 fragment. The most probable channel for this excitation is the vibrational motion of CF_3, as the CF_3 remainder originates from a tetrahedral configuration it will vibrate around its almost planar ground state. Additionally the momentum analysis of the F^+ ions yields the amount of back-scattering at the CF_3 fragment. For the photon energies considered here we found an average molecular back scattering of 4.7 ± 1.7 percent. Our estimate for the C-F separation is an almost constant value of 1.5×10^{-10} m for all photon energies considered.

We have shown that electron-ion momentum correlation measurements combined with detuning from the excitation is a versatile tool to study the femtoseconds nuclear relaxation processes of core excited molecules. Our data provides a consistent picture of the time scales and magnitudes of the involved processes. Further systematic studies involving other molecules and electron-ion-ion coincidence are in progress.

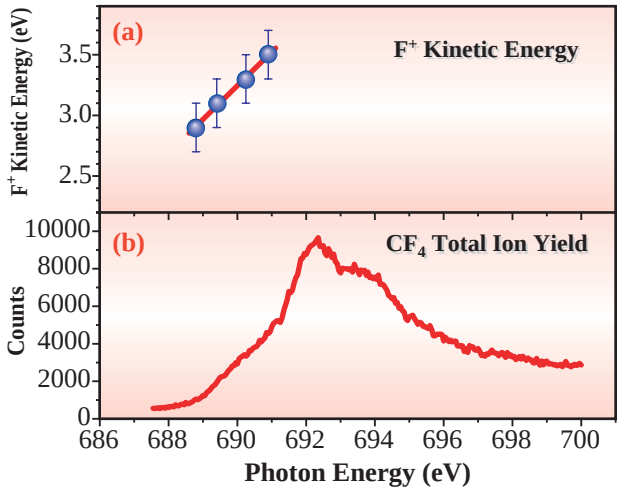

Fig. 3. Total ion yield and the kinetic energy of the F^+ ion as a function of the photon energy.

Georg Pruemper [a,*], Kiyoshi Ueda[a] and Yusuke Tamenori [b]

(a) Institute of Multidisciplinary Research for Advanced Materials, Tohoku University
(b) SPring-8 / JASRI

*E-mail: pruemper@tagen.tohoku.ac.jp

References

[1] *G. Prümper, K. Ueda, Y. Tamenori, M. Kitajima, N. Kuze, H. Tanaka, C. Makochekanwa, M. Hoshino and M. Oura: Phys. Rev. A* ***71*** *(2005) 052704, (also available at: June 1, 2005 issue of Virtual J. of Ultrafast Science).*
[2] *G. Prümper, Y. Tamenori, A. De Fanis, U. Hergenhahn, M. Kitajima, M. Hoshino, H. Tanaka and K. Ueda: J. Phys. B* ***38*** *(2005) 1.*
[3] *G. Prümper, K. Ueda, U. Hergenhahn, A. De Fanis, Y. Tamenori, M. Kitajima, M. Hoshino and H. Tanaka: J. Elec. Spectrosc.* ***144-146*** *(2005) 227.*

Real-time Observation of Filler Aggregate Structure using Two-dimensional Ultra-small-angle X-ray Scattering

The addition of fillers such as carbon black and silica to an elastomer shows reinforcement effects, which increase modulus of elasticity, tear strength, tensile strength, cracking resistance, and fatigue resistance [1]. The reinforcement effects have been extensively investigated since 1904, when S.C. Mote discovered the effect with carbon black. However, the mechanism of the reinforcement has not yet been understood. A filler composes a hierarchical structure in rubber, where *primary particles form aggregates*, and the aggregates form *agglomerates*, as shown in Fig. 1. The structures of the aggregate and agglomerate, on a size scale of 100 nm - 10 μm, are considered to be the origins of the reinforcement. However, conventional methods of studying the structure on such a size scale, such as light scattering and transmission electron microscopy (TEM), are inappropriate for the study of aggregate structure: the light scattering method is not suitable for an opaque specimen such as filled rubbers, and TEM is not suited to the study of three-dimensional (3D) structures under elongation because it requires thin samples.

Two-dimensional ultra-small-angle X-ray scattering (2D-USAXS) is a promising tool for the observation of structural change on a size scale of 100 nm - 10 μm and is now available at the "medium-length" beamline **BL20XU**. The combination of the high brilliance and long sample-to-detector distance used makes it possible to observe *in situ* 2D-USAXS patterns, which is not possible by conventional USAXS using a Bonse-Hart camera [2]. In the present study, we performed 2D-USAXS of filled rubber under elongation and investigated the change of the aggregate structure.

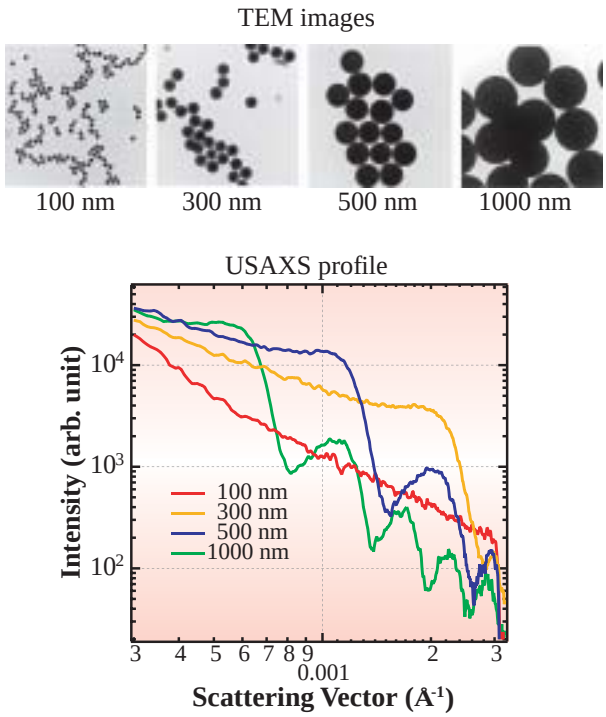

Fig. 2. USAXS profiles and TEM images of silica particles with monodisperse size distribution.

The sample used is styrene-butadiene rubber (SBR) filled with spherical silica particles with a volume fraction of 20% (Seahoster, Nippon Shokubai, Osaka, Japan), which have a monodispersed size distribution. This enables us to separate the structure factor (scattering from aggregates) and the form factor (scattering from a primary particle). A schematic view of the experimental setup at BL20XU is shown in Fig. 1. The X-ray energy is 23 keV and the camera

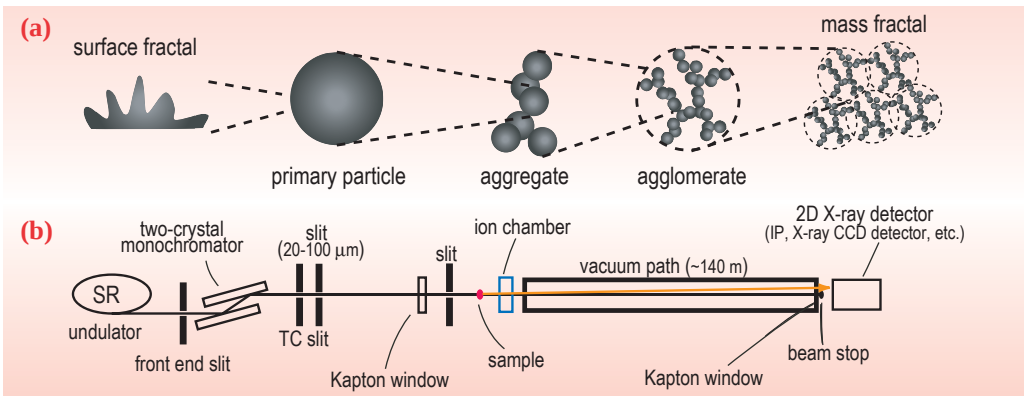

Fig. 1. **(a)** Hierarchical structure of filler in rubber. **(b)** Schematic view of experimental setup. The sample is set at the first experimental hutch in the experimental hall of the storage ring building. The detectors are set at the second hutch in the Biomedical Imaging Center. The sample-to-detector distance is 160.5 m.

length is 160.5 m. In this setup, the USAXS in a q-range of 4×10^{-4} - 2.5×10^{-3} Å^{-1} is recorded, where q is the scattering vector defined as $q = 4\pi \sin\theta / \lambda$, λ is the X-ray wavelength and 2θ is the scattering angle. As area detectors, an imaging plate and an X-ray CCD detector coupled with X-ray image intensifier (XRII) [3] are used. Figure 2 shows the USAXS profiles of the particles and the corresponding TEM images. The exposure time for each 2D-USAXS image is around 100 ms.

Figure 3(a) shows the 2D-USAXS images of rubber filled with silica particles (diameter: D = 540 nm) under elongation. The structural information on a size scale of 250 nm - 1500 nm is available from the images. It corresponds to that on the distribution of the silica particles inside the aggregates in this sample. When the samples are stretched, four spots appear and then change their positions, while the scattering angle is kept constant. This indicates that the distance between neighboring silica particles remains constant in stretched rubber (approximately 860 nm). A sample filled with small particles (D = 100 nm) shows different scattering patterns, as shown in Fig. 3(b). In this case, the USAXS patterns have information on the distances between the aggregates rather than on those between the particles. When the sample is stretched, the distance between the aggregates increases in the direction of the elongation. This suggests that the rubber between the aggregates is mainly stretched.

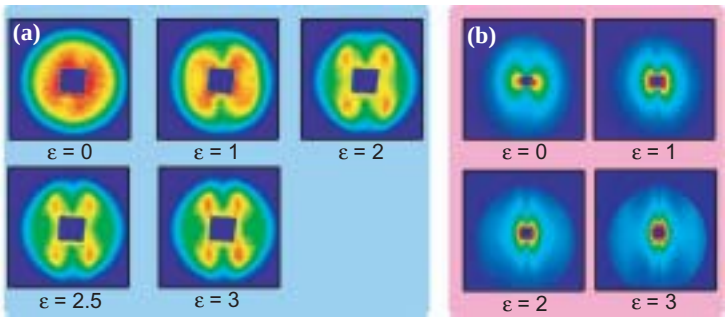

Fig. 3. **(a)** 2D-USAXS images of stretched rubber filled with silica particles (diameter = 540 nm). e is the elongation ratio defined as $\varepsilon = \Delta L/L$, where L is the initial length of the sample and ΔL is the elongation length of the sample. The sample is stretched in the horizontal direction. **(b)** 2D-USAXS images of stretched rubber filled with silica particles (diameter = 100 nm). The sample is stretched in the horizontal direction.

The combination of 2D-USAXS and viscoelastic measurements reveals the relationship between the aggregate structure and reinforcement, as shown in Fig. 4, which records the stress-strain curve of rubber filled with silica particles (D = 300 nm) and corresponding 2D-USAXS images. The images showed the hysteresis corresponding to that of the stress-strain curve. Therefore, the morphology of the aggregation is found to affect the hysteresis of stress-strain curve.

In summary, by *in situ* 2D-USAXS, the structural change of aggregates in stretched rubber has been observed for the first time, which, previously, had only been speculated on the basis of viscoelastic experiments. Further study by 2D-USAXS will elucidate the long-time unresolved mechanism of the reinforcement in filled rubber.

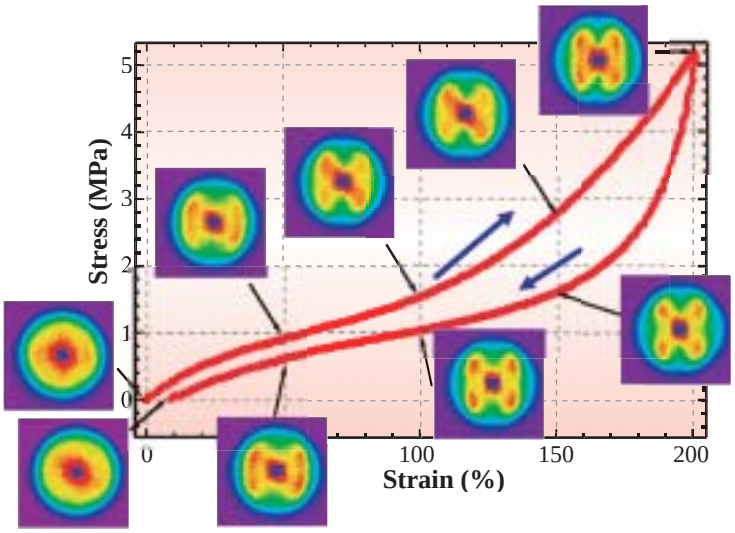

Fig. 4. 2D-USAXS images and stress-strain curve of rubber filled with silica particles (diameter = 300 nm). The sample is stretched in the horizontal direction.

Yuya Shinohara [a], Hiroyuki Kishimoto [b] and Yoshiyuki Amemiya [a,*]

(a) Department of Advanced Materials Science, The University of Tokyo
(b) SRI Research & Development Ltd.

*E-mail: amemiya@k.u-tokyo.ac.jp

References

[1] J. D. Ferry: "Viscoelastic Properties of Polymers", John Willy & Sons, New York, 1980.
[2] U. Bonse and M. Hart: Appl. Phys. Lett. **7** (1965) 238.
[3] Y. Amemiya *et al.*: Rev. Sci. Instrum. **66** (1995) 2290.

Guest Shape-responsive Fitting of Porous Coordination Polymer with Shrinkable Framework

In the past decade, porous coordination polymers have attracted the attention of chemists due to scientific interest in the creation of nanometer-sized spaces and the finding of novel phenomena, as well as commercial interest in their application for storage and heterogeneous catalysis. This new feature is based on their robust open frameworks ascribed to a permanent porosity in the crystal structure so as to accommodate various guest molecules. It has been believed that the robustness of host porous frameworks is a prerequisite for their successful performance while flexibility is incompatible with porous properties. On the other hand, bioenzymes such as metalloproteins take advantage of their structural flexibility, which appears to be essential for their superb molecular recognition. For porous coordination polymers , we could also expect that host flexibility, so-called structural dynamism, is a key principle for the highly selective recognition, accommodation and separation of a target molecule, which, at present, is a new class of practical materials [1]. Herein, we have chosen a microporous coordination polymer ($[Cu_2(pzdc)_2(bpy)]$) (**CPL-2**) (pzdc = pyrazine-2,3-dicarboxylate; bpy = 4,4'-bipyridine) as a host porous framework [2] and a benzene molecule as a guest. We have demonstrated the reversible structural change on guest adsorption/desorption by monitoring X-ray diffraction patterns, which detected "shape-responsive fitting" profiles on guest adsorption with large crystalline shrinking.

For the anhydrous **CPL-2** without a guest (**apohost**), adsorption isotherms of benzene were measured at 300 K. The adsorbed amount of benzene is saturated at just one molecule per unit pore. When an integer number of guest molecules are densely packed within a periodic unit pore, structures for both guest and host gain a good matching in periodicity. In this case, only one molecule can be accommodated in the unit pore of the channel. As a result, **CPL-2** affords a single pocket in the "unit pore" for benzene. The X-ray powder diffraction (XRPD) patterns at 300 K of as-synthesized **CPL-2** (**CPL-2** ⊃ $\mathbf{H_2O}$), **apohost** under reduced pressure, and **CPL-2** with benzene (**CPL-2** ⊃ **benzene**) at 1.0 kPa are shown in Fig. 1. After being exposed to benzene vapor, the peak characterized by 020 at the lowest 2θ moves to a higher-angle region, indicative of a contractive structure transformation. On removal of the guest water from **CPL-2** ⊃ $\mathbf{H_2O}$, the *b*-axis decreases by 0.82%. Surprisingly, the further

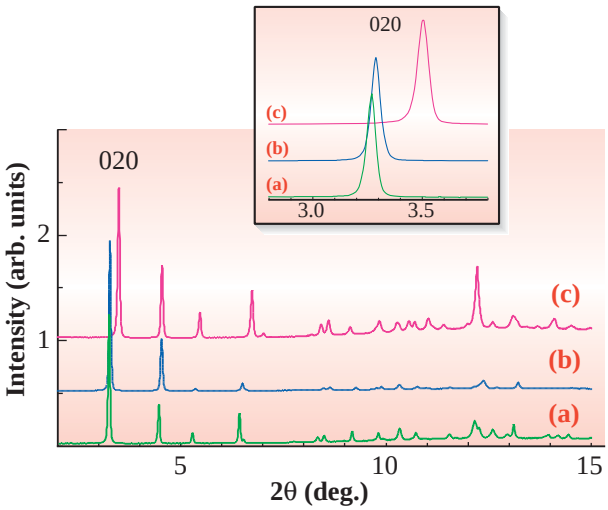

Fig. 1. Synchrotron XRPD patterns at 300 K of **(a) CPL-2** ⊃ $\mathbf{H_2O}$, which contains water molecules as guests, **(b) apohost** under reduced pressure and **(c) CPL-2** ⊃ **benzene** at 1.0 kPa vapor pressure of benzene. The X-ray wavelength is 0.80087 Å and 2θ ranges from 2° to 15°. The inset shows the peak 020 at the lowest 2θ in the range of 2.8° to 3.8°.

decrease of the unit cell dimensions is recognized when benzene molecules are adsorbed in **apohost**. The large reduction of the *b*-axis by 6.8% is observed, although the benzene molecules occupy the channels.

The crystal structures of **apohost** at 293 K and **CPL-2** ⊃ **benzene** at 273 K are determined by Rietveld analysis. In both structures, a neutral two-dimensional layer of $[Cu(pzdc)]_n$ forms in the *ac* plane, whose layers are connected by bpy as pillar ligands, resulting in a 3D pillared layer structure. In the structure of **CPL-2** ⊃ **benzene**, shown in Fig. 2, the benzene molecule, as the guest, is located in the channel, indicative of a saturated amount, 1.0 molecule per unit pore for adsorption, in good agreement with that obtained from the adsorption isotherm.

The pillared layer framework undergoes such a deformation that the channel cavities suit benzene molecules very well, resulting in an appreciable difference in the channel shape with and without benzene. The channel without benzene has a nearly rectangular shape with dimensions of 5.6 Å × 7.2 Å, whereas that with benzene is no longer rectangular

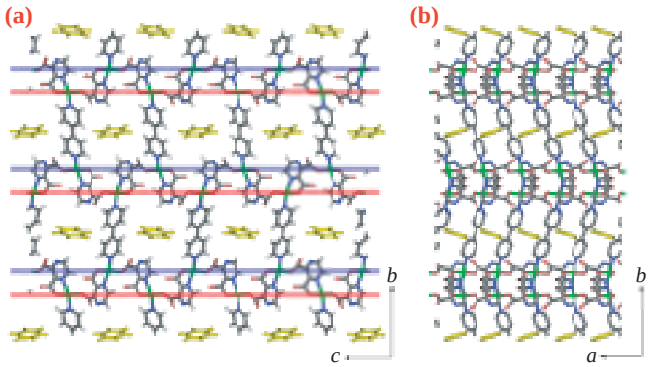

Fig. 2. Crystal structure of $\{[Cu_2(pzdc)_2(bpy)]\cdot C_6H_6\}n$ (**CPL-2** ⊃ **benzene**). The benzene molecules are located in each channel. **(a)** Crystal view of **CPL-2** along the *a*-axis. **(b)** Crystal view of **CPL-2** along the *c*-axis. Hydrogen atoms are omitted for clarity. The blue and red lines indicate the copper atom sheets projected down to the *a*-axis, which practically form layers.

but takes a "Z" letter-shape, as shown in Fig. 3. In the absence of benzene, the geometry around the copper ion is square pyramidal, while that with benzene shows a square planar form. Eventually, the deformation produces a large contact area to the benzene plane.

Dynamic pores are subject to a guideline for a flexible framework, that is, building units (or motifs) with flexible moiety are linked with strong bond, or stiff building blocks (or motifs) are connected with weaker bonds. These combinations would afford a subtly balancing porous framework, namely, a soft framework. Herein, the structural rearrangement of the framework proceeds from the "open" phase to the "contact" phase responding to guest molecules. In the case of **CPL-2**, the gadgets are bpy and pzdc rings as stiff motifs, the rotatable carboxyl group in pzdc and the fluxional coordination geometry of the Cu ion, all of which provide a contrivance for a unique flexible channel structure: the dynamic structural transformation of **CPL-2** is derived from the change of the coordination mode based on the cleavage of the apical long Cu-O bond in the Cu geometry and on the rotation of the carboxyl group subsequently [3].

The host flexibility can improve the efficiency of the adsorption by aid of the host structural transformation suited for the guest molecules. Most porous materials have been synthesized with the aim of a robust structure. However, we believe that a flexible framework proves to have a pore structure suited for a certain guest molecule, which is much more useful for molecular recognition or selective guest inclusion than the robust porous structure. This "shape-responsive fitting" property, would afford a novel recognition system for crystal materials.

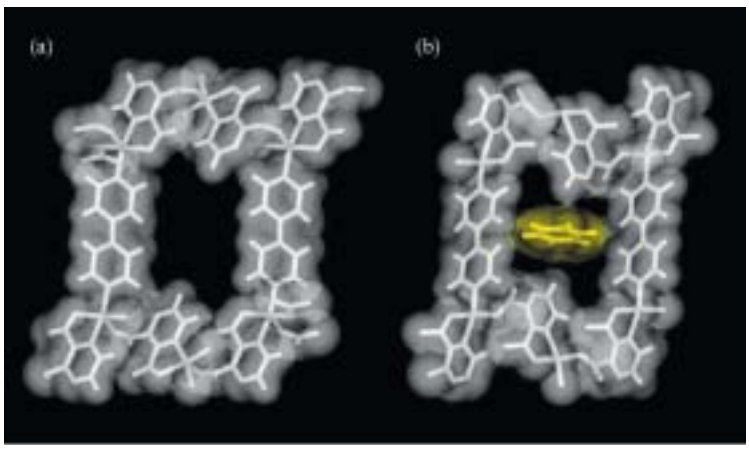

Fig. 3. Representation of the pore structures of **(a) apohost** and **(b) CPL-2** ⊃ **benzene**. Both views are looking down from the *a*-axis, displayed by stick and van der Waals surface models.

Ryotaro Matsuda

Department of Synthetic Chemistry and Biological Chemistry, Kyoto University

E-mail: ryotato@sbchem.kyoto-u.ac.jp

References

[1] S. Kitagawa *et al.*: Angew. Chem. Int. Ed. **43** (2004) 2334.
[2] M. Kondo *et al.*: Angew. Chem. Int. Ed. **38** (1999) 140.
[3] *R. Matsuda, R. Kitaura, S. Kitagawa, Y. Kubota, T.C. Kobayashi, S. Horike and M. Takata: J. Am. Chem. Soc.* ***43*** *(2004) 14063.*

Direct Observation of Hydrogen Molecules Adsorbed in Microporous Coordination Polymer

Hydrogen storage is an important technology and is indispensable for the establishment of clean hydrogen energy systems. Although various kinds of materials have been studied as hydrogen-storage materials, there is as yet no decisive way to store and release H_2 molecules efficiently. The adsorption of H_2 molecules in metal-organic porous materials [1] is one of the most promising candidates. To develop a rational synthetic strategy for novel metal-organic porous materials that can adsorb large amounts of H_2 molecules, the elucidation of the intermolecular interaction between H_2 molecules and pore walls is essential. Despite several investigations into novel metal-organic porous materials for hydrogen storage [2], little is known about the effective interaction mechanism and the fundamental structural characteristics of the adsorbed H_2 molecules. In our previous work [3], we determined the assembled structure of O_2 molecules in nano-channels by *in situ* synchrotron powder diffraction, which allowed a good understanding of the magnetic and adsorption behaviors of O_2 molecules. Therefore, the structure determination of adsorbed H_2 molecules should also provide us with much information on their physicochemical properties to enable the rational design and synthesis of high-performance hydrogen-storage materials. Although the weakest X-ray scattering amplitude of hydrogen made it difficult to determine their structure, we have succeeded in the first direct observation of elusive H_2 molecules adsorbed in the nano-channels of a metal-organic porous material by the *in situ* synchrotron powder diffraction experiment of gas adsorption and by MEM (maximum entropy method)/Rietveld charge-density analysis [4].

The sample used in this study is microporous coordination polymer 1 with a pillared layer structure (CPL-1) with uniform ordered nano-channels of 4 Å × 6 Å. The *in situ* synchrotron powder diffraction experiment for hydrogen gas adsorption was carried out using the large Debye-Scherrer camera installed at beamline **BL02B2**. The hydrogen gas was dosed into the capillary sample through a stainless steel tube connected to the gas-handling system. The amount of adsorbed gas was controlled by adjusting the sample temperature under a constant hydrogen gas pressure of 102 kPa.

The structure was investigated by MEM/Rietveld analysis [5]. The amount of H_2 molecules adsorbed in CPL-1 at 90 K at 102 kPa was determined to be 0.3 molecules per Cu atom from the hydrogen adsorption isotherm. The reliability (R) factors based on the powder profile R_{WP} and the Bragg integrated intensities R_I were 2.45% and 3.33%, respectively. The cell parameters for CPL-1 with H_2 gas were determined as a = 4.7101(1) Å, b = 20.0289(2) Å, c = 10.7704(1) Å, and β = 95.472(2)° (space group $P2_1/c$). The R factor based on the structure factors in the final MEM analysis R_F was 1.86%.

In the MEM charge density of CPL-1 without H_2 molecules shown in Fig. 1(a), only the nano-channel structure was clearly seen and no electron density was observed in the nano-channels, even at lower electron-density levels. On the other hand, in the MEM charge density of CPL-1 with H_2 molecules (Fig. 1(b)), the small peak maxima of the electron densities with an elongated shape distribution, which are due to the adsorbed H_2 molecules, were observed in the nano-channels. It should be noted that the position and orientation of the H_2 molecules are mean values obtained by statistical analysis. The

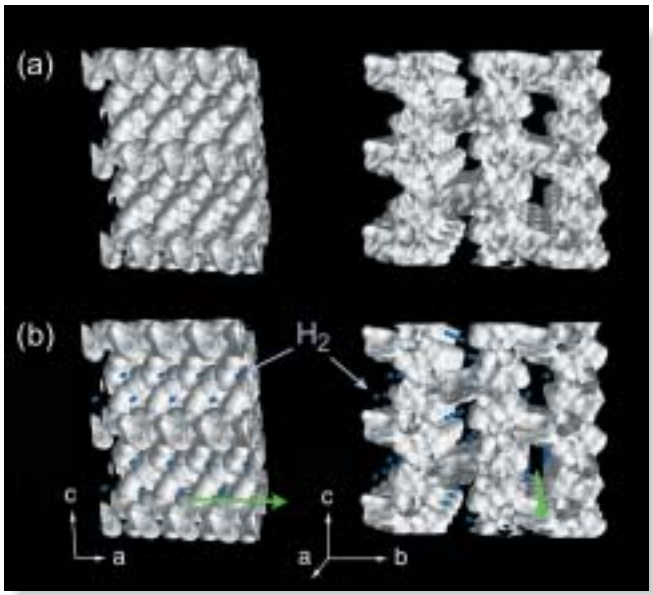

Fig. 1. MEM charge density maps of CPL-1 at 90K as equi-density contour surfaces **(a)** without H_2 molecules and **(b)** with adsorbed H_2 molecules. The equi-contour level is 0.11 eÅ^{-3}. The charge densities of the adsorbed H_2 molecules are colored blue. The green arrows indicate the nano-channel direction.

charge density distribution of the adsorbed H_2 molecules is broader than that of hydrogen atoms of pyrazine in CPL framework as a result of the large thermal motion. The H_2 molecules align in a zigzag pattern to form a one-dimensional array along the nano-channels. The position of each H_2 molecule is found to be displaced from the center of the nano-channel and is near a corner of the rectangular nano-channels. The H_2 molecule is positioned closely to the oxygen atom (O1) of the carboxylate group (Fig. 2). The O1 atom forms a coordination bond with the Cu^{II} ion and is slightly negatively charged. The Cu-OOC moiety is associated with an attractive interaction site for H_2 molecules. Interestingly, most metal-organic porous compounds reported to date that behave as hydrogen- gas-storage materials have similar metal-oxygen (M-O) bonded units. The possibility that the interaction between the hydrogen molecules and the M-O units is essential for H_2 adsorption will be examined in the next stage of this work. Moreover, the H_2 molecule seems to be trapped in the concave space formed by the O1 atom and the hydrogen atom H1 of the pyrazine molecules of the CPL framework. The pocket of the cavity formed by the carboxylate group and the pyrazine unit is suited to the size of adsorbed H_2 molecules in CPL-1.

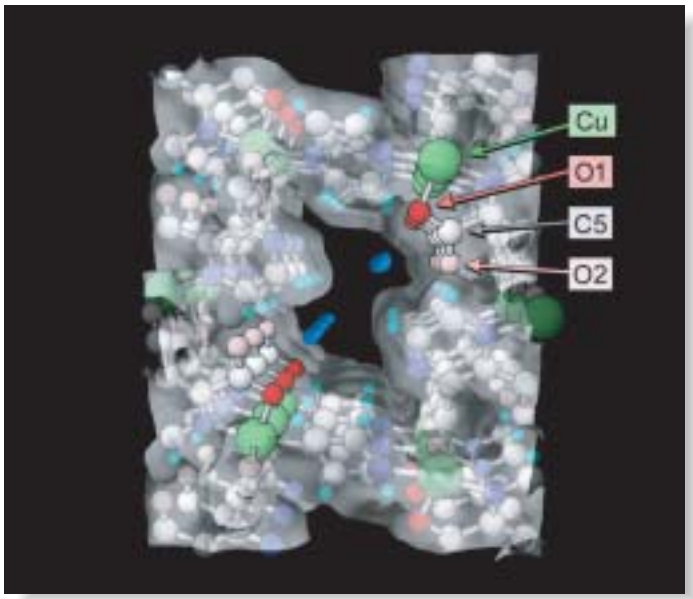

Fig. 2. Close-up view of MEM charge density map around an adsorbed H_2 molecule. The equi-contour level is 0.11 $eÅ^{-3}$. The structural model of the CPL framework is superimposed on the charge density map.

At a lower temperature and/or a higher gas pressure, more H_2 molecules are expected to be adsorbed into CPL-1. In the case of the adsorption of dilute hydrogen gas, it is interesting and important to know where the first adsorbed H_2 molecule is located in the nano-channel, because that will provide us with structural information on the initial stage of adsorption in this system. A pocket that is well suited to the size of the adsorbed molecule *and* a functional site from the Cu-OOC moiety could have an effect on H_2 adsorption in this system. The first direct observation of H_2 molecules adsorbed in the nano-channels of CPL-1 could give us promising guidelines for designing hydrogen-gas-storage materials.

Yoshiki Kubota[a,*], Masaki Takata[b,c] and Susumu Kitagawa[d]

(a) Department of Environmental Sciences, Osaka Women's University
(b) SPring-8 / JASRI
(c) CREST, Japan Science and Technology Agency
(d) Department of Synthetic Chemistry and Biological Chemistry, Kyoto University

*E-mail: kubotay@center.osaka-wu.ac.jp

References

[1] S. Kitagawa *et al.*: Angew. Chem. Int. Ed. **43** (2004) 2334.
[2] J.L.C. Rowsell *et al.*: J. Am. Chem. Soc. **126** (2004) 5666.
[3] R. Kitaura *et al.*: Science **298** (2002) 2358.
[4] *Y. Kubota, M. Takata, R. Matsuda, R. Kitaura, S. Kitagawa, K. Kato, M. Sakata and T.C. Kobayashi: Angew. Chem. Int. Ed.* ***44*** *(2005) 829.*
[5] M. Takata *et al.*: Z. Kristallogr. **216** (2001) 71.

Direct Observation of Charge Ordering Pattern in an Organic Conductor $(EDO\text{-}TTF)_2PF_6$

Tetrathiafulvalene (TTF) and its derivatives have provided numerous kinds of conducting charge-transfer complexes that show phase transitions such as superconducting, metal-insulator (MI), and magnetic ones. They have been extensively studied to understand the mechanisms and develop new functional systems along with the aim to afford molecular devices. The 1/4-filled-band conductor $(EDO\text{-}TTF)_2PF_6$ (EDO-TTF = ethylenedioxytetrathiafulvalene) is one of them and shows quite a peculiar MI transition at T_{MI} = 280 K accompanying the changeover from para- to diamagnetism. The MI transition has been considered as a particular example that shows the cooperative actions of Peierls distortion, charge ordering and anion ordering together with molecular deformation [1,2]. Recently, ultrafast photoswitching from the insulator to the metallic phase has also been reported [3,4]. The peculiar phase transition in $(EDO\text{-}TTF)_2PF_6$ is quite an attractive for a better understanding of cooperative and coherent phenomena in organic conductors.

The charge ordering pattern in the insulating phase has been suggested to be [0,0,+1,+1,...], despite the fact that in most 1/4-filled-band conductors the ordering pattern [0,+1,0,+1,...] is found as a result of strong neighbor-site Coulomb repulsion [1,2]. However, there has been no direct evidence of the charge ordering pattern. In this study, we present direct evidence for an ordering of $(EDO\text{-}TTF)^+$ and $(EDO\text{-}TTF)^0$ visualized in $(EDO\text{-}TTF)_2PF_6$ charge density distributions [5].

The charge density distributions were obtained from the synchrotron radiation powder diffraction data by a combination of the maximum entropy method (MEM) and the Rietveld method. The experiment was carried out using the large Debye-Scherrer camera at beamline **BL02B2**. The wavelength of incident X-ray was 1.0 Å. Data were measured for the metallic phase at 285 K and for the insulator phase at 260 K. In the structure analysis procedures, the reliability factors based on the Bragg intensities of the final Rietveld fitting were 3.75% and 3.38% for the metallic and insulator phases, respectively. The reliability factors based on the structure factors for the final MEM charge densities were 2.85% and 5.28% for the metallic and insulator phases, respectively.

The equi-charge-density surfaces at 260 K are shown in Fig. 1 at 0.7 eÅ^{-3}. In both the metallic and the insulator phases, the layers of EDO-TTF molecules form columns by a head-to-tail stacking perpendicular to the molecular plane; PF_6^- anions are located at the cavities between the EDO-TTF layers. Compared with the metallic phase, the unit cell is doubled in the insulator phase, corresponding to the Peierls instability. The PF_6^- anions are disordered in the metallic phase (the overlapping of two octahedra with a tilt of about 50°), whereas they are ordered in the insulator phase. Two types of EDO-TTF molecule are present in the insulator phase (flat and bent molecules) while only one EDO-TTF is crystallographically unique in the metallic phase.

The charge states of EDO-TTF and PF_6 can be examined from the charge density distributions by counting the number of electrons around them. In the metallic phase, EDO-TTF has +0.6(1) e and PF_6 has -1.2(1) e. In the insulator phase, flat EDO-TTF has

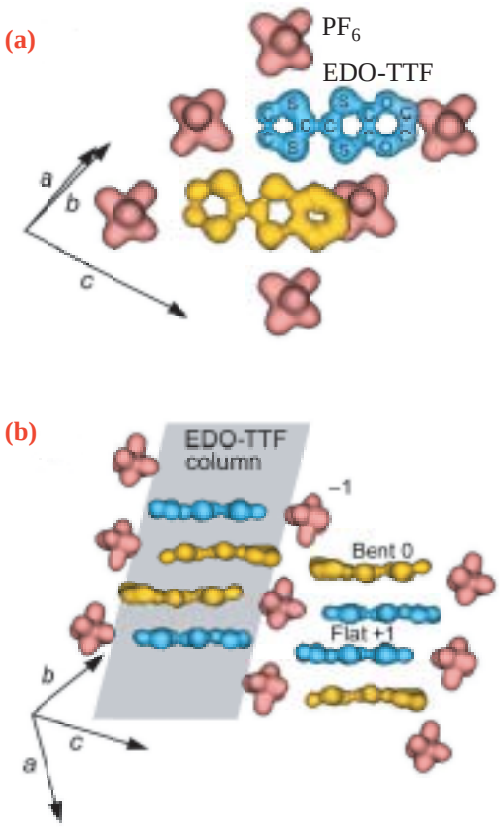

Fig. 1. MEM equi-charge-density surfaces of insulator phase of $(EDO\text{-}TTF)_2PF_6$ at 0.7 eÅ^{-3}. The view in **(a)** is along the EDO-TTF stacking direction; **(b)** the side view of the EDO-TTF column is shown. PF_6 is colored in red. The flat and bent EDO-TTF molecules are colored in blue and yellow, respectively.

+0.8(1) e, bent EDO-TTF has +0.2(1) e, and PF_6 has -1.0(1) e. Thus, flat EDO-TTF in the insulator phase has an excess charge concentration close to +1 e. The positive charge is concentrated mainly on one sulfur atom in the flat molecule, the nearest sulfur atom to the PF_6^- anion. The distance between the sulfur atom and the anion is shortened by the molecular displacement caused by the MI transition. Therefore, it is considered that the local electrostatic interaction between the sulfur atom and the anion contributes to the hole trapping on the sulfur atom and to anion ordering. The charge-rich and -poor EDO-TTF molecules alternate with a periodicity of $2k_F$ nesting vector of the Fermi surface due to the Peierls instability. As a result, the [0,0,+1,+1,...] ordering of charges is along the nesting vector as shown in Fig. 2.

The lower equi-charge-density surface of the EDO-TTF column in the insulator phase at 0.13 eÅ^{-3} is shown in Fig. 3. A weak intermolecular overlapping of charge density between flat molecules can be observed as two S-S bonds, whereas it cannot be observed between flat and bent molecules and between bent molecules. In other words, the flat $(EDO\text{-}TTF)^+$ molecules in the insulator phase are dimerized to provide a spin singlet state. From the viewpoint of intermolecular orbital interactions, this dimerization assists the neighboring of two $(EDO\text{-}TTF)^+$ causing the [0,0,+1,+1,...] charge-ordering pattern.

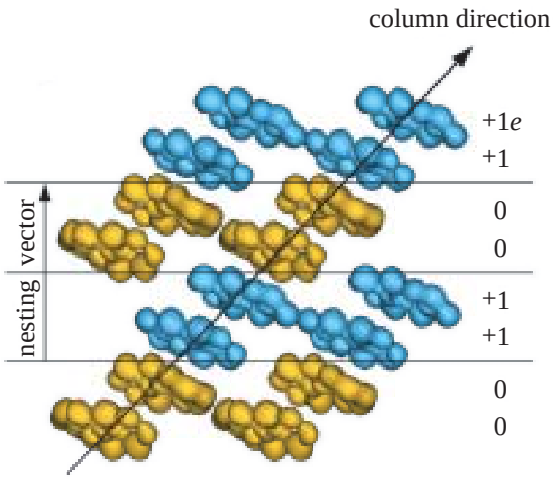

Fig. 2. MEM equi-charge-density surface of EDO-TTF layer at 0.7 eÅ^{-3} and charge ordering pattern in the insulator phase viewed along *c*-axis.

This study revealed that the molecular displacements observed in the MI transition of $(EDO\text{-}TTF)_2PF_6$ assist the anion ordering and the electrostatic and electronic stabilization of the crystal structure in the insulator phase. The cooperation in this peculiar MI transition shall be regarded as a result of the displacement and deformation of EDO-TTF molecules during the phase transition.

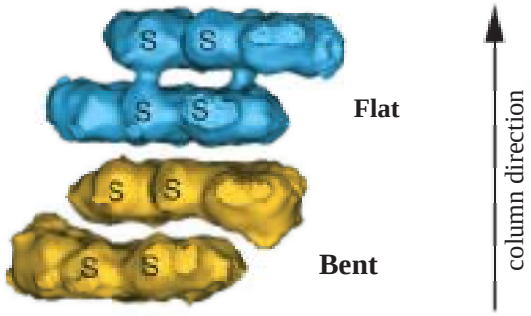

Fig. 3. Side view of lower MEM equi-charge-density surface of EDO-TTF column in the insulator phase. The surface is at 0.13 eÅ^{-3}.

Shinobu Aoyagi[a,*], Hideki Yamochi[b] and Gunzi Saito[c]

(a) Department of Applied Physics, Nagoya University
(b) Research Center for Low Temperature and Materials Sciences, Kyoto University
(c) Division of Chemistry, Kyoto University

*E-mail: aoyagi@mcr.nuap.nagoya-u.ac.jp

References

[1] A. Ota *et al.*: J. Mater. Chem. **12** (2002) 2600.
[2] O. Drozdova *et al.*: Phys. Rev. B **70** (2004) 075107.
[3] N. Uchida *et al.*: J. Phys. IV France **114** (2004) 143.
[4] M. Chollet *et al.*: Science **307** (2005) 86.
[5] *S. Aoyagi, K. Kato, A. Ota, H. Yamochi, G. Saito, H. Suematsu, M. Sakata and M. Takata: Angew. Chem. Int. Ed.* ***43*** *(2004) 3670.*

Study on $[FeN_6]$ Core of $[Fe(2\text{-pic})_3]Cl_2 \cdot Et\,OH$ in Photo-induced High-spin State by Nuclear Resonant Inelastic Scattering

As a consequence of the splitting of d orbitals into t_{2g} and e_g orbitals, octahedral transition metal compounds with d^4 to d^7 electronic configurations may exist either in the low-spin (LS) or high-spin (HS) state. Compounds that show a transition between different spin states upon external perturbation, e.g., variation in temperature and light-irradiation, are of great importance due to their possible industrial uses such as in photo-switches, memories and display devices.

$[Fe(2\text{-pic})_3]Cl_2 \cdot EtOH$ (**1**) is one of the most well known among these compounds. The lattice of compound **1** is built from $[Fe(2\text{-pic})_3]^{2+}$ units (Fig. 1), in which each iron(II) ion is surrounded by six nitrogen atoms belonging to three 2-pic ligands (2-pic: 2-picolylamine). Recently, Tayagaki *et al*. reported that for compound **1**, the Raman and IR spectra of the photo-induced HS state are remarkably different from the spectra of the thermally induced HS state [1]. The observed differences suggest a distortion of molecules in the photo-induced phase, which according to the authors is most probably due to a cooperative Jahn-Teller effect. In order to confirm these conclusions, we performed ^{57}Fe nuclear resonant inelastic scattering (NRIS) measurements on the light-induced and thermally induced spin transition of compound **1** [2]. The NRIS is a novel technique for monitoring the vibration states isotope-selectively, and yields only the vibration modes that are associated with a significant displacement of the resonant isotope, in this case ^{57}Fe. This selectivity simplifies data analysis, and is especially effective for the direct investigation of the vibrational states of $[FeN_6]$ in compound **1**. These vibration modes were not in the energy range of the IR and Raman measurements of Tayagaki *et al*.; therefore, the result of the NRIS measurement complements their previous findings.

The measurements were carried out at **BL09XU** beamline, on a ^{57}Fe-enriched sample of compound **1** placed in a cryostat. For the light-irradiation experiment, a Hg-arc lamp was used as a light source, and its light was directed through the cryostat window using a glass fiber. Figure 2 shows the spectra of compound **1** under various conditions. Upon irradiation at 35 K, the sample exhibits an almost complete photoinduced phase transition from the LS (t_{2g}^6) state (Fig. 2(a)) to a light-induced HS, LHS ($t_{2g}^4\ e_g^2$) state (Fig. 2(b)), and the most intense peaks of the spectra move from 320-360 cm^{-1} (LS state) to 200-270 cm^{-1} (LHS state). The reason for this shift is that the spin-transition is associated with the transfer of two electrons from the nonbonding t_{2g} to the antibonding e_g orbital. The observed LS-HS conversion is reversible by switching off the light source; after a short annealing of the sample at 100 K, the peaks attributed to HS disappear from the spectrum remeasured at 35 K.

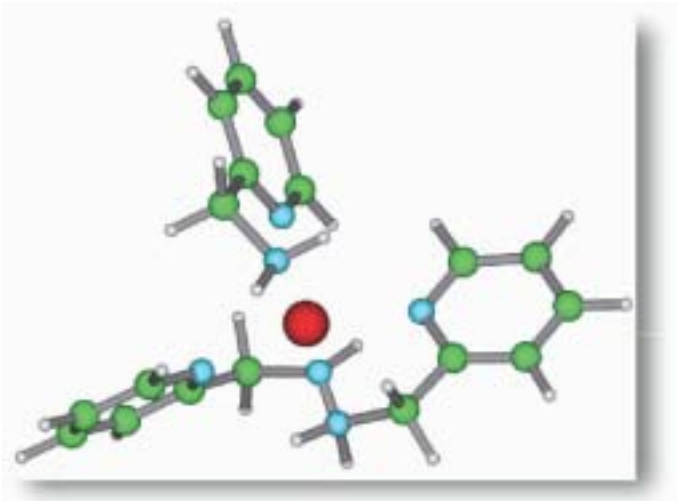

Fig. 1. Structure of $[Fe(2\text{-pic})_3]^{2+}$. Red: iron atoms; blue: nitrogens atoms; green: carbons atoms; gray: hydrogens atoms.

The thermally induced spin-transition was observed at 115 K (Fig. 2(c)), and upon further elevating the temperature to 150 K, the spectra of thermally induced HS were also recorded (Fig. 2(d)). The spin-transition is manifested as a decrease in the intensity of the peaks at 320-360 cm^{-1}, characteristic to the LS state, and the occurrence of new peaks at 200-270 cm^{-1}. The spectra of the thermally induced HS phase show only minor differences compared with the light-induced HS phase (Fig. 2(b)).

The geometry and vibrational modes of an isolated $[Fe(2\text{-pic})_3]^{2+}$ in the LS and HS states were calculated by the BLYP DFT method, and the NRIS spectra were simulated using the results of DFT calculation (Fig. 3). The results of the simulation are in good qualitative agreement with the measurements, although the calculation is less accurate for the LS state, most probably due to the neglected solid-state effects. We are currently trying to extend our studies by taking into account intermolecular interactions.

In summary, we found that the distortion in the light-induced HS phase of compound **1** reported by Tayagaki *et al*. [1] has only a minor effect on the dynamics of the $[FeN_6]$ core, as was also suggested by recent X-ray crystallographic reports on **1** [3].

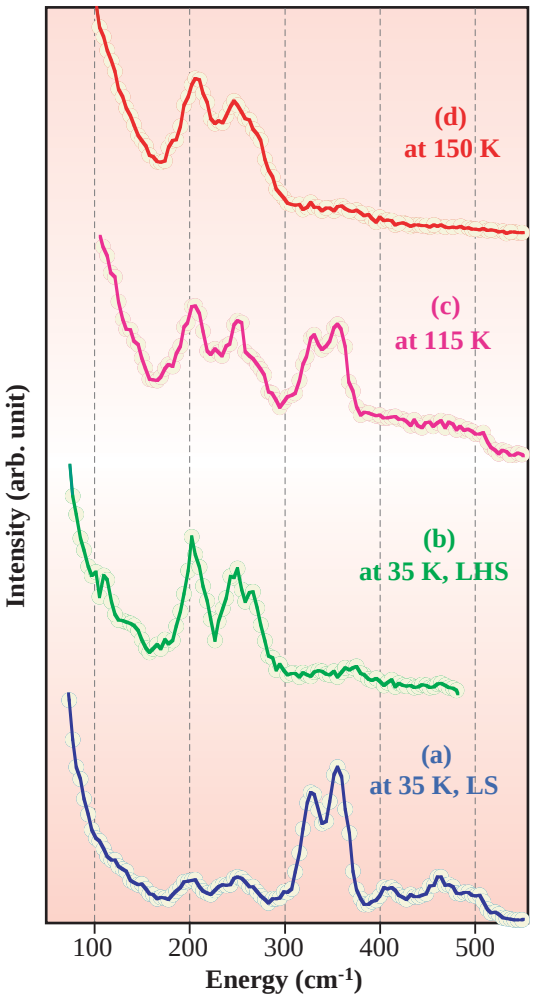

Fig. 2. NRIS spectra of $[Fe(2\text{-pic})_3]Cl_2$•EtOH **(1)** at 35 K before **(a)** and after light-irradiation **(b)**; around the spin transition at 115 K **(c)**; and in thermally induced HS state at 150 K **(d)**.

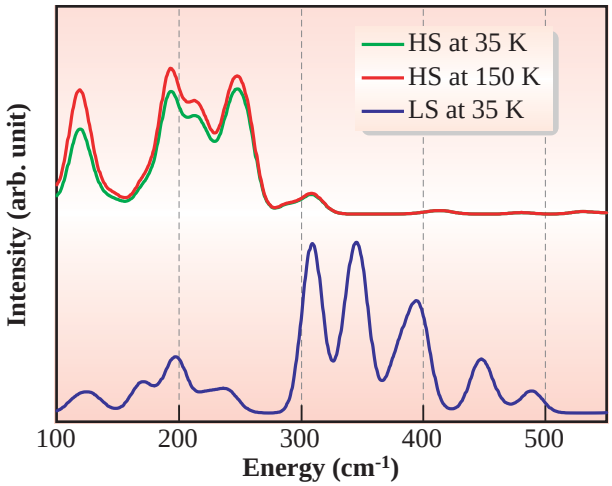

Fig. 3. Simulated NRIS spectra for LS state (at 35 K) and HS state (at 35 K and 150 K).

Gergely Juhász[a,†,*], Makoto Seto[b] and Yonezo Maeda[a]

(a) Department of Chemistry, Kyushu University
(b) Research Reactor Institute, Kyoto University

*E-mail: gergely@andrew.cmu.edu

†Current address: Chemistry Department, Carnegie Mellon University, USA

References

[1] T. Tayagaki and K. Tanaka: Phys. Rev. Lett. **86** (2001) 2886; T. Tayagaki *et al.*: Phys. Rev. B **69** (2004) 064104.
[2] *G. Juhász, M. Seto, Y. Yoda, S. Hayami and Y. Maeda: Chem. Comm. (2004) 2574.*
[3] N. Huby *et al.*: Phys. Rev. B **69** (2004) 020101(R).

Dependence of Molecular Shape Resonance Energy on Inter-nuclear Distance Probed by High-resolution Core-level Photoelectron Spectroscopy

The advent of third generation synchrotron radiation facilities has provided a wealth of information about inner shell photoionization processes because they offer a combination of high-resolution and high-intensity beams.

Shape resonances are one of the most interesting features observed in core-level molecular photoionization. By definition, shape resonances arise from the temporal trapping of a photoelectron in the intermediate states by a centrifugal barrier. The resonance can be viewed as a broad enhancement in the ionization cross section where the photoelectron is resonantly scattered. As illustrated in Fig. 1, one can infer that the shape resonance positions should be sensitive to the intramolecular distances [1].

Köppe *et al*. [2] showed that the C $1s^{-1}\sigma^*$ shape resonance in CO that appears at the photon energy $h\nu \approx 305$ eV in the photoabsorption spectrum is not only present in the C $1s^{-1}$ single-hole ionization (SHI) partial cross sections for the individual vibrational components v', but also that the energies of the shape resonances decrease with increasing vibrational quantum number, i.e., from ~307 eV for $v' = 0$ to ~302 eV for $v' = 2$.

In this work carried out on the C branch of the soft X-ray photochemistry beamline **BL27SU**, the CO O 1*s* photoelectron spectra were recorded at photon energies across the σ* shape resonance region [3]. The O $1s^{-1}$ SHI cross sections for the vibrational components $v' = 0$, 1 and 2 are shown together with the C $1s^{-1}$ SHI cross sections from Köppe *et al*. [2] in Fig. 2. It is clear that the O $1s^{-1}\sigma^*$ shape resonance energies increase with increase in v', i.e., opposite to the C $1s^{-1}\sigma^*$ shape resonance. The corresponding displacements of the nuclear separation from the equilibrium distance R_e of the ionic states were determined to be + 0.025, + 0.068 and + 0.111 Å for C 1*s* and - 0.020, - 0.074 and - 0.109 Å for O 1*s* for

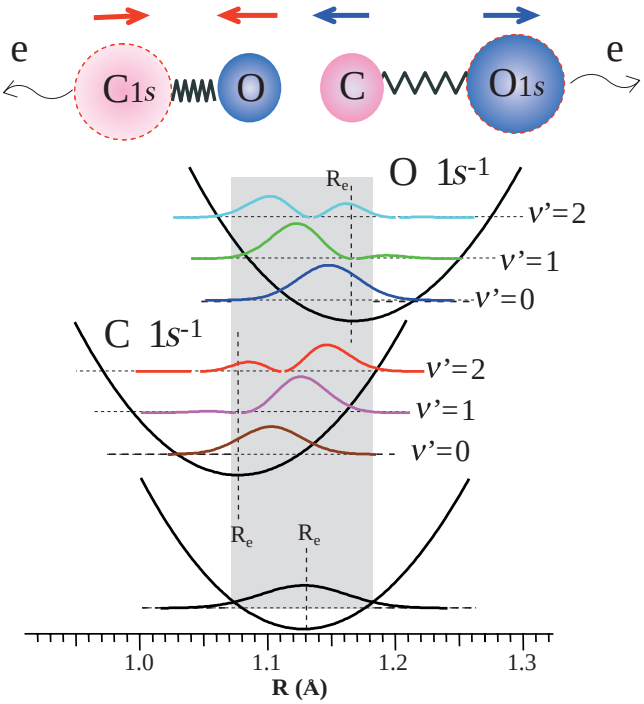

Fig. 1. Schematic diagram of nuclear motion upon photoionization-induced vibrational excitation showing potential curves for the ground and core-ionized C $1s^{-1}$ and O $1s^{-1}$ in CO, respectively. R_e is the equilibrium internuclear distances: R_e = 1.128 Å, 1.167 Å and 1.079 Å for the ground and core-ionized C $1s^{-1}$ and O $1s^{-1}$ states, respectively.

v' = 0, 1 and 2, respectively. This indicates that the photoelectron is trapped by a compressed ion and the compression increases with increasing v' for O 1*s* in contrast with an elongation that increases with n' in the case of C 1*s* [3] (see Fig. 1).

This work on CO has been extended to other molecules (H_2CO [4], CO_2, N_2O, C_2H_2, C_2H_4 and C_2H_6), which offers an interesting systematic study of these effects. The g-u symmetry-resolved C 1*s* σ_g and $1\sigma_u$ SHI partial cross sections of C_2H_2 are shown in Fig. 3 for v' = 0, 1 and 2 vibrational components. The shape resonance appears only in the C 1*s* σ_g photoionization and can be assigned to σ_g*. The energy of the C 1*s* σ_g^{-1} σ_u* shape resonance decreases with the increase in the vibrational quantum number ν', i.e., in a way similar to the result of CO C $1s^{-1}\sigma$* shape resonance discussed above. This is the first observation of the vibrational effects on shape resonance energy in the g-u symmetry-resolved SHI cross sections [5].

The analysis of the results for the other molecules is still in progress.

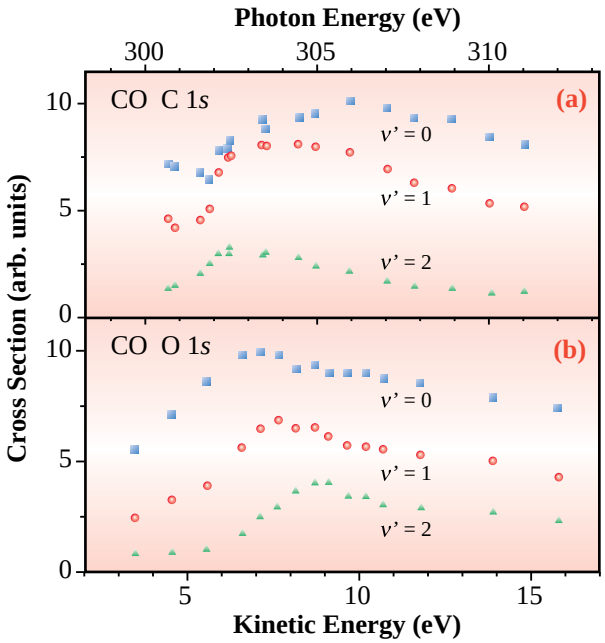

Fig. 2. SHI cross sections for vibrational components v' = 0, 1 and 2 for **(a)** C $1s^{-1}\sigma$* from Köppe *et al.* [2] and, **(b)** current results for O $1s^{-1}$ 1σ*. The photon energy scale above the top panel applies only to the CO C 1*s* data, whereas the kinetic energy scale applies to both panels.

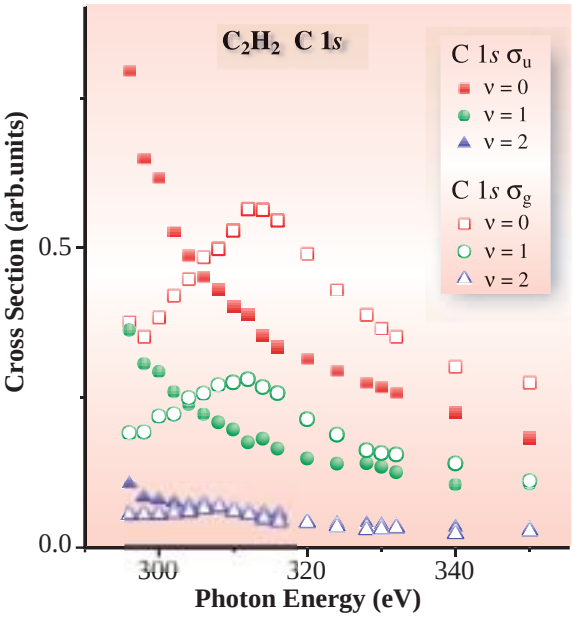

Fig. 3. g-u symmetry-resolved C 1*s* σ_g and $1\sigma_u$ SHI partial cross sections of C_2H_2 for ν' = 0, 1 and 2 vibrational components.

Casten Makochekanwa[a], Hiroshi Tanaka[a,*] and Kiyoshi Ueda[b]

(a) Department of Physics, Sophia University
(b) Institute of Multidisciplinary Research for Advanced Materials, Tohoku University

*E-mail: h_tanaka@sophia.ac.jp

References

[1] J. L. Dehmer and D. Dill: Electron-Molecule and Photon-Molecule Collisions, edited by T. Rescigno, V. McKoy and B. Schneider (Plenum Publishing Corporation) (1979) 225.
[2] H. M. Köppe *et al.*: J. Phys. B **30** (1997) L741.
[3] D. A. Mistrov *et al.*: Phys. Rev. A **68** (2003) 022508.
[4] A. De Fanis *et al.*: Phys Rev. A **71** (2005) 052510.
[5] *K. Nakagawa, T. Tanaka, C. Makochekanwa, N. Kuze, M. Kitajima, H. Tanaka, A. De Fanis, Y. Tamenori, M. Matsumoto, K. Fujiwara and K. Ueda: - to be published.*

Ordering of Hydrogen Bonds in High-pressure Low-temperature Ices

The hydrogen bonds linking the water molecules are known to give rise to a rich variety of stable and metastable phases of H_2O under specific temperature and pressure conditions (Fig. 1) [1]. Study of the electronic structure of the hydrogen bonds in various phases of H_2O provides valuable information on the change of hydrogen, covalent and ionic bonding of the H_2O framework that is essential for understanding the icy planetary interiors as well as the physical and chemical properties of organic and biological systems at high pressure. Such information can in principle be obtained from analysis of the near-edge fine structure from X-ray absorption spectroscopy (XAS). For low-*Z* materials whose core-level electrons are in the soft X-ray region, however, conventional XAS is difficult to perform. An alternative technique, based on the inelastic scattering of hard X-rays (~ 10 keV) by core-level excitations, known as X-ray Raman scattering (XRS), provides the same information as XAS when the momentum transfer of XRS is small enough that the dipole approximation is valid. As our work demonstrated, the inherent bulk sensitivity and good penetration depth of XRS make it especially valuable for studies under extreme conditions such as high pressure.

We have studied the near *K*-edge structure of oxygen in liquid water and ices III, II, and IX at 0.25 GPa and several low temperatures down to 4 K on the Taiwan Inelastic X-ray Scattering Beamline **BL12XU** [2]. The spectra obtained are summarized in Fig. 2, which reveal detailed spectral changes across the various phases that contain important information on the change of the hydrogen bonds of the H_2O framework.

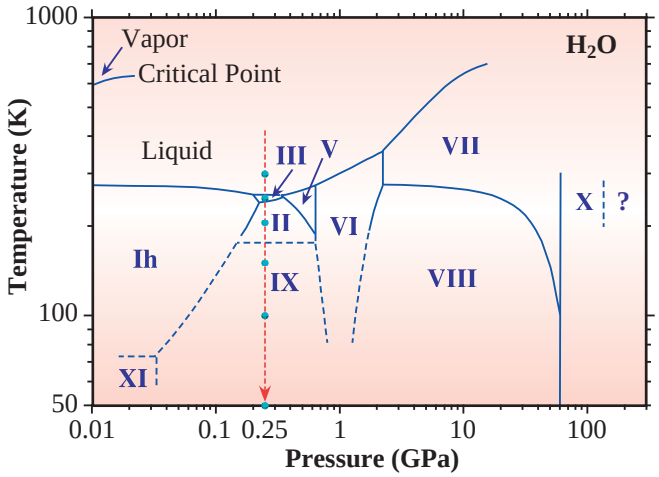

Fig. 1: Phase diagram of H_2O.

The most prominent changes are observed in the pre-edge region (535-537 eV). First-principles density functional calculations (DFT) for liquid water [3] have identified that the pre-edge feature is caused by oxygen 2*p* and 2*s* orbital hybridization in water molecules with an uncoordinated (broken or distorted) donor hydrogen bond. The observed increase of the pre-edge intensity in liquid water upon high-pressure compression at 300 K therefore suggests the increase of the number of uncoordinated hydrogen bonds with pressure.

With decreasing temperature at 0.25 GPa, the H_2O framework undergoes structural changes firstly from liquid to ice III with the ordering of the oxygen network, then from ice III to ices II and IX. Ice IX is the low-temperature proton-ordered phase of ice III with an identical tetragonal crystal structure, whereas ice II has a *completely* proton-ordered rhombohedral lattice. From Fig. 2, the ordering of the oxygen network causes only a small decrease of the pre-edge intensity, whereas the ordering of the proton network, or equivalently the ordering of the hydrogen bonds, dramatically reduces the pre-edge intensity, which can be interpreted as a result of the diminishing number of uncoordinated hydrogen bonds in the proton-ordered lattice of ices II and IX.

The remaining pre-edge intensities observed in ices II and IX are, however, unexpected as all (most) of the water molecules in the proton-ordered lattice of ice II (IX) are fully coordinated with symmetric hydrogen bonds, which should lead to a diminishing pre-edge intensity. Our DFT calculations of the near-edge XAS spectrum for ice IX indicate that the remaining intensity may be due to the influence of the local electronic structure by the Madelung potential of the crystal lattice, estimated by point charges placed at the hydrogen and oxygen periodic lattice positions. The calculated XAS spectrum including the point charges reproduces qualitatively the major features of the experimental spectrum (Fig. 3). We therefore conclude that the Madelung potential of the proton-ordered lattice causes the remaining pre-edge intensity. This is in contrast to liquid water where the near-edge structure is determined pre-dominantly by the first coordination shell of the water molecules [4]. These results can be reconciled, however, by

considering that the ordered proton network creates a long-range anisotropy in the H_2O framework and introduces the necessary orbital asymmetry in the hydrogen bonds of the water molecules, causing the observed pre-edge intensity. A randomly distributed proton network smears out the anisotropy, and the pre-edge intensity is dominated by uncoordinated donor hydrogen bonds.

At temperatures between 4 and 50 K, substantial spectral changes from ice IX are observed, which suggest substantial changes of the H_2O framework in this *P-T* regime and the formation of a possible new ice phase. Further structural characterization is however required to confirm this finding.

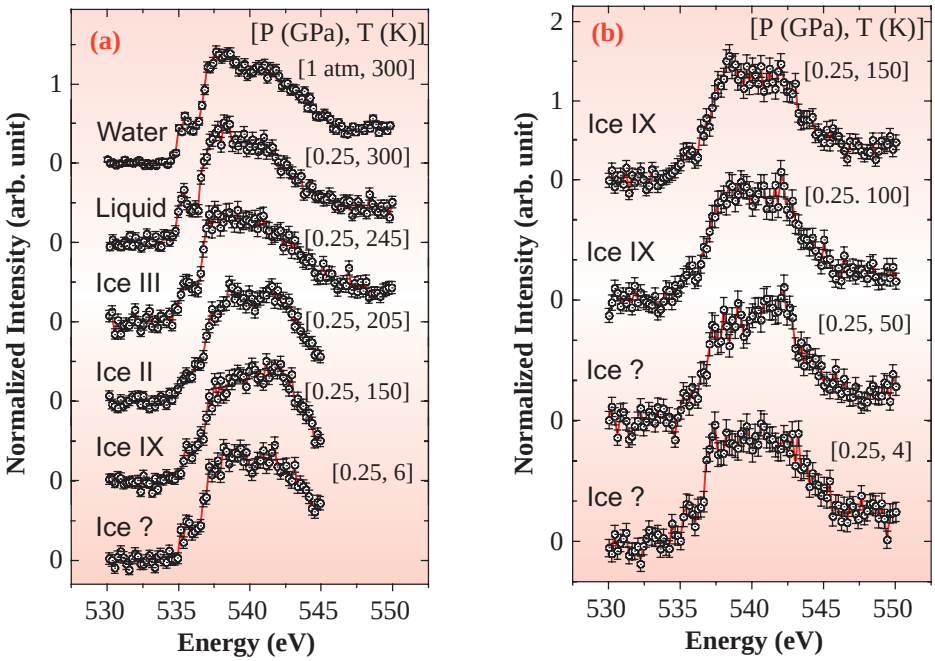

Fig. 2. Near *K*-edge spectra of the oxygen in various phases of H_2O obtained with a total energy resolution of 305 **(a)** and 175 meV **(b)** at E_0 = 9884.7 eV. The pressure and temperature conditions are indicated.

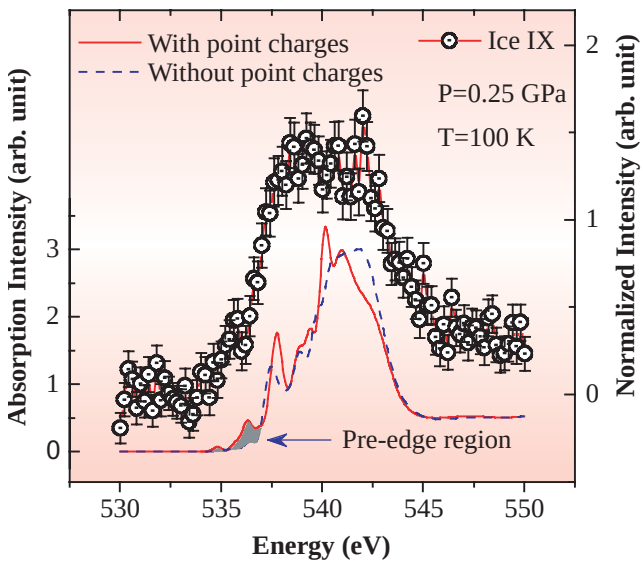

Fig. 3. Comparison of the near *K*-edge spectrum of ice IX with DFT calculations.

Y.Q. Cai[a,*], H.-K. Mao[b], J.S. Tse[c] and C.C. Kao[d]

(a) National Synchrotron Radiation Research Center, Taiwan
(b) Geophysical Laboratory, Carnegie Institution of Washington, USA
(c) Department of Physics, University of Saskatchewan, Canada
(d) National Synchrotron Radiation Light Source, Brookhaven National Laboratory, USA

*E-mail: cai@spring8.or.jp

References

[1] See, for example, P.V. Hobbs: Ice Physics, Clarendon, Oxford, 1974.
[2] *Y.Q. Cai, H.-K. Mao, P.C. Chow, J.S. Tse, Y. Ma, S. Patchkovskii, J.F. Shu, V. Struzhkin, R.J. Hemley, H. Ishii, C.C. Chen, I. Jarrige, C.T. Chen, S.R. Shieh, E.P. Huang and C.C. Kao: Phys. Rev. Lett.* ***94*** *(2005) 025502.*
[3] S. Myneni *et al.*: J. Phys. Condens. Matter **14** (2002) L213.
[4] Ph. Wernet *et al.*: Science **304** (2004) 995.

EARTH & PLANETARY SCIENCE

Developments in both scientific instruments and techniques are vital to advance experimental studies. Great efforts have been directed toward developing high-pressure technology combined with synchrotron radiation at some beamlines related to Earth & Planetary Sciences, and *in situ* X-ray diffraction measurements under P-T conditions approaching those of the Earth's core are now possible using the laser-heated diamond anvil (LHDAC) system. Researchers at the Tokyo Institute of Technology and JAMSTEC have largely contributed to constructing such a system and to developing relevant techniques at BL10XU.

On the basis of this technology, Hirose, Murakami and coworkers reported a new polymorph of $MgSiO_3$-perovskite, the most important high-pressure phase in the lower part of the mantle, at pressures greater than 120 GPa, equivalent to those near the mantle-core boundary (136 GPa). An independent study by Ono *et al*. at the same beamline also confirmed the formation of this new phase at similar pressures. The discovery of the "post-perovskite (PP) phase" has attracted researchers in wide fields of Earth Sciences, including mineral physics, seismology, geochemistry, mantle dynamics simulation, etc., and the roles of the PP phase in the Earth's deep interior have been actively discussed in some recent international conferences.

Technological progress has also been made using a combination of sintered diamond (SD) anvils and a large-volume multianvil apparatus (MA) at BL04B1, mostly by researchers at ISEI, Okayama University and GRC, Ehime University. Ito and coworkers reported the generation of pressures exceeding 60 GPa at room temperature, and have been working on the determination of phase transition pressures of some materials. They demonstrated that the wurtzite to rocksalt transition in GaN occurs at pressures of approximately 50 GPa, with a negative Clapeyron slope, based on *in situ* X-ray diffraction observations conducted at room temperature and also at high temperatures up to 850 K.

The stable generation of higher temperatures in MA with SD anvils has been challenged by Irifune, Sueda *et al*., and temperatures up to 2400 K are now comfortably produced for a long duration (e.g., several hours) at pressures up to ~45 GPa. They found that hollandite-type $KAlSi_3O_8$, an important constituent in subducted crust or sediment materials, transforms to a new structure in the upper part of the lower mantle, on the basis of this technique. This result is in contrast to earlier results with LHDAC, demonstrating the advantage of using MA with sample volumes far larger than those available in DAC.

The relatively large volume in MA permits precise measurements of some physical properties and of materials structures under high pressure. Ohtaka, Arima, Yoshiasa and coworkers made XAFS spectra measurements of GeO_2 melt under high pressure (up to 15 GPa) and temperature, and found a rather abrupt change in Ge-O distance, suggesting the occurrence of an oxygen coordination change from four- to six-fold at about 3 GPa. This method can be applied to evaluate structural changes in silicate melts under high pressure, which should provide important information on the viscosity changes in magmas in Earth's deep interior.

Technological development in computer tomography (CT) using synchrotron radiation allows three-dimensional imaging of very small (< 0.1 mm) materials. Tsuchiyama and coworkers developed a microtomography technique, named SR-based projection microtomography (SP-μCT), and first applied it to minute cosmic dusts collected from ice and snow or in the stratosphere. Based on the SP-μCT imaging of a variety of cosmic dusts at BL20XU and BL47XU, they evaluated the nature and origin of the three-dimensional shapes of some microspherules. This technique has also been applied to quantitatively evaluate the porosity of some micrometeorites. These results should provide important constraints on the origin of such cosmic dusts, leading to a deeper understanding of the physical and chemical processes in the interplanetary space of our solar system.

Tetsuo Irifune

Post-perovskite Phase Transition in $MgSiO_3$

$MgSiO_3$ is a representative chemical composition of the Earth's mantle. The upper/lower mantle boundary is marked by the formation of orthorhombic $MgSiO_3$-rich perovskite (space group: *Pbnm*). The $MgSiO_3$ perovskite was first synthesized at 30 GPa in 1975 [1]. Later, the conservation of perovskite structure was confirmed up to 127 GPa [2]. It has been believed that the perovskite-type $MgSiO_3$-rich phase is a predominant mineral in the lower mantle and is stable to 135 GPa a condition corresponding to the bottom of the mantle. However, phase transition of $MgSiO_3$ perovskite was once suggested from the seismic anomalies near the base of the mantle around 2700-km depth [3].

In order to investigate the stability and possible phase transition of $MgSiO_3$ perovskite, we performed *in situ* X-ray observation of pure $MgSiO_3$ composition at high pressure and temperature up to 134 GPa and 2600 K corresponding to the conditions of the lowermost mantle [4]. Angle-dispersive X-ray diffraction spectra were collected at beamline **BL10XU**. High pressure and temperature conditions were generated in a laser-heated diamond anvil cell (LHDAC). Temperature was measured by the spectroradiometric method. Pressure was determined from the unit-cell volume of platinum mixed with the sample using *P-V-T* equation of state.

Results demonstrate that the *Pbnm* perovskite structure is stable at least to 114 GPa and 2300 K (Fig. 1). Above 127 GPa and 2500 K, fifteen new peaks were observed in the diffraction pattern. These new peaks from a new $MgSiO_3$ polymorph (post-perovskite phase) can be indexed by an orthorhombic cell with lattice parameters of a = 2.456(0) Å, b = 8.042(1) Å, and c = 6.093(0) Å. In order to determine the crystal structure that possesses these lattice parameters, molecular dynamics (MD)-aided crystal structure design was performed. The appropriate number of atoms (8 Mg + 8 Si + 24 O; Z=8) were positioned randomly in a double unit cell because of the small a-parameter. Classical MD calculations were carried out with the (NTV) ensemble of this system at high temperature (5000 K), and then the system was quenched to 0 K. The calculations were repeated, each time checking and correcting the atomic positions until the crystal structure became consistent with the crystal chemistry and the calculated XRD pattern matched the observed one. The result revealed a crystal structure of a new phase (post-perovskite phase) with a space group of *Cmcm* (Fig. 2). This is isostructural with $UFeS_3$ or $CaIrO_3$. The post-perovskite phase is denser than perovskite by 1.0-1.2 % at 121 GPa and 300 K.

The post-perovskite phase has six-fold Si and

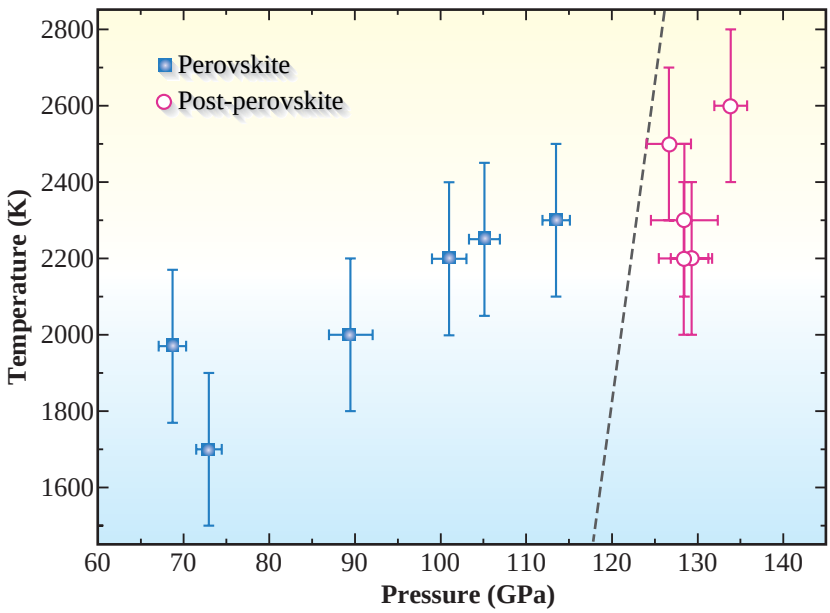

Fig. 1. Phase diagram of $MgSiO_3$. Solid squares and open circles indicate the stabilities of *Pbnm* perovskite and post-perovskite phase, respectively. A broken line shows the transition boundary.

eight-fold Mg coordination, and the SiO_6-octahedra share the edges to make an octahedral chain like rutile-type structure. These chains run along *a*-axis and are interconnected each other by apical oxygen atoms in the direction of *c*-axis to form edge and apex shared octahedral sheets. The octahedral sheets are stacked along *b*-axis with interlayer Mg^{2+} ions. This crystal structure was further optimized by the first-principles calculations [5]. The calculations also indicated that the post-perovskite phase stabilizes relative to perovskite above 98 GPa and 0 K.

These results show that the $MgSiO_3$ post-perovskite is a predominant mineral in the Earth's lowermost mantle (D" region) at 2700 to 2900-km depth. Phase transition can cause large seismic heterogeneities. The D" seismic discontinuity is observed in many regions around the world about 200-300-km above the core-mantle boundary (119-125 GPa). The post-perovskite phase transition occurs at depths matching those of the D" discontinuity (Fig. 1) and is most likely responsible for the cause of seismic velocity increase up to 3%. A large S-wave polarization anisotropy ($V_{SH} > V_{SV}$) is also observed below the D" discontinuity. It can be explained by a strong preferred orientation of the post-perovskite phase under the strong horizontal shear flow [5]. The D" region has long been the most enigmatic region in the Earth's interior. The newly discovered $MgSiO_3$ post-perovskite phase provides a consistent way to explain a number of seismic anomalies observed in this region.

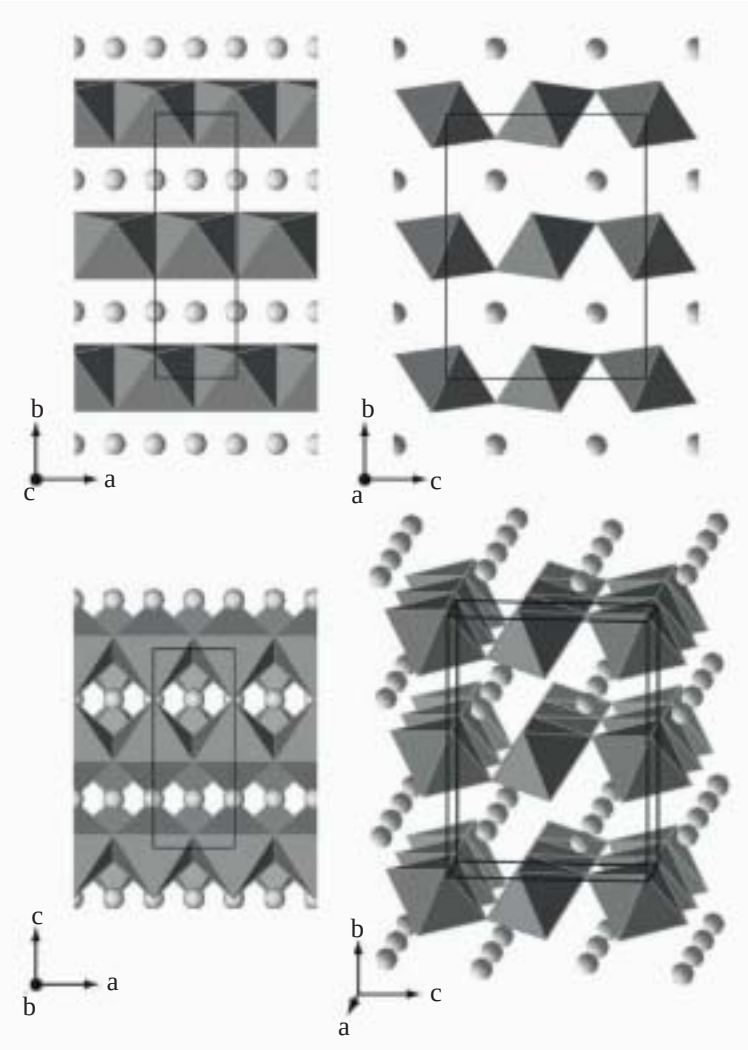

Fig. 2. Crystal structure of the post-perovskite phase projected along [001], [100], and [010] directions, and a stereoscopic view showing the layer stacking structure. Coordination polyhedra of oxygen atoms around Si atoms are shown as octahedra, and the Mg^{2+} ions are shown as balls. Bold line indicates the unit cell.

Kei Hirose

Department of Earth and Planetary Sciences,
Tokyo Institute of Technology

E-mail: kei@geo.titech.ac.jp

References

[1] L. Liu: Geophys. Res. Lett. **2** (1975) 417.
[2] E. Knittle and R. Jeanloz: Science **235** (1987) 668.
[3] I. Sidorin *et al.*: Science **286** (1999) 1326.
[4] *M. Murakami, K. Hirose, K. Kawamura, N. Sata, Y. Ohishi: Science **304** (2004) 855.*
[5] *T. Iitaka, K. Hirose, K. Kawamura and M. Murakami: Nature **430** (2004) 442.*

Ultrahigh Pressure Generation in the Kawai-type Apparatus: Application to the Wurztite-rocksalt Transition in GaN

The Kawai-type high-pressure apparatus has been widely utilized in the mineral physics field because of its ability to keep a sample of at least several milligrams under controlled pressure and temperature conditions for a desired duration. Nevertheless, the maximum attainable pressure has been limited to *ca*. 28 GPa when tungsten carbide (WC) is used as the anvil material. Recently, by utilizing sintered diamond (SD) as the cubic anvil of the apparatus, the attainable pressure range has been remarkably extended. We [1] have carried out experiments to evaluate the maximum attainable pressure of the Kawai-type apparatus equipped with the SD anvil and to examine whether the wurzite (W)-rocksalt (R) transition in GaN can be usable as a pressure fixed point.

An assembly of eight SD cubes with an edge length of 14 mm and a truncated corner length of 1.5 mm compressed an octahedral pressure medium of MgO+5%Cr_2O_3 using the DIA type press SPEED-Mk.II installed at beamline **BL04B1**. Both the phase identification of the GaN sample and pressure determination were performed by *in situ* energy-dispersive X-ray diffraction analysis. Two experimental runs, M139 and M148, were performed at 300 K and at temperatures up to 850 K, employing the specimen assemblies schematically shown in Fig. 1. A white X-ray beam was introduced to the sample and the MgO capsule (pressure standard), independently. The diffracted beam was detected by a Ge solid-state detector with a diffraction angle 2θ of *ca*. 6.0°. In run M139, measurement of the electrical resistance of GaN was also carried out by inserting two Pt wires at opposite positions on the cylindrical outer surface of the sample.

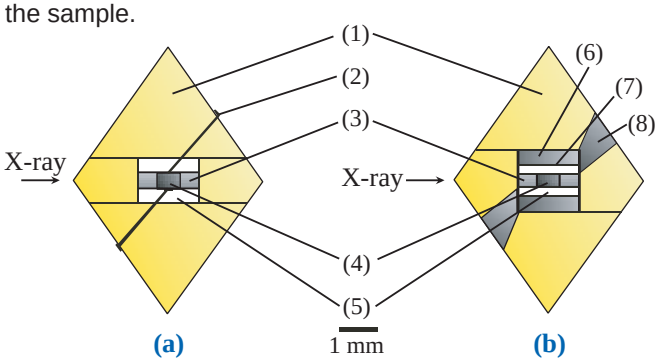

Fig. 1. Cross sections of the specimen assemblies employed in experiments at 300 K **(a)** and at high temperatures **(b)**. (1): Pressure medium; (2): Pt wire; (3): Diamond powder; (4): GaN sample; (5): MgO capsule; (6): $LaCrO_3$; (7): Nichrome heater; (8): TiC electrode.

Pressure generation: The pressures generated at 300 K are plotted against press load in Fig. 2 for runs M139 and M148 and independent runs M162 and M181 carried out using similar assemblies (Fig. 1). Pressure is generated with a repeatable accuracy of 2-3% up to *ca*. 60 GPa over the four runs. The maximum pressure of 63.3 ± 0.4 GPa was achieved at load of 8.6 mega Newtons (MNS). However, stagnation of generated pressure at higher loads may be a sign of onset of deformation or fracture of SD anvils. To achieve higher pressures higher-quality SD is urgently required.

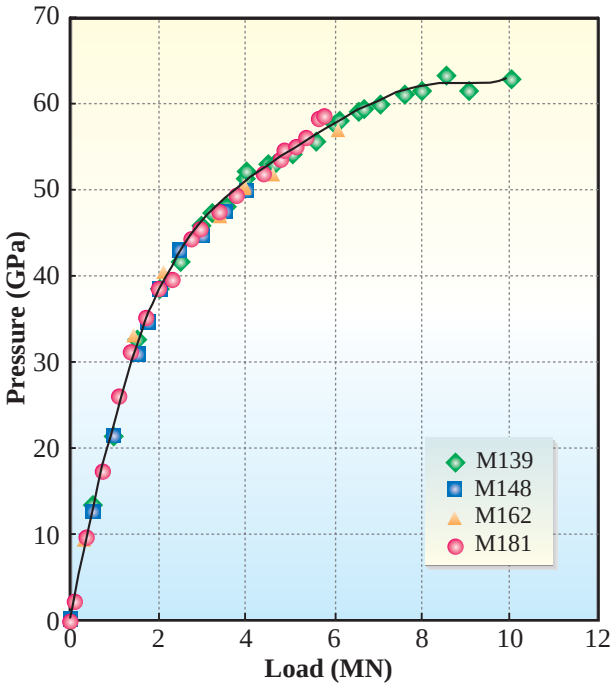

Fig. 2. Pressure *versus* press load at 300 K. Pressure values are based on the MgO scale.

Phase transition of GaN: Some characteristic diffraction patterns are reproduced in Fig. 3. At pressures higher than 50 GPa, it was difficult to acquire the diffraction profile of the sample separately from that of the MgO capsule. Diffraction profiles in run M139 were further complicated by the coexistence of Ga_2O_3 (see Figs. 3(a) to 3(d)). Fortunately, the complexity due to the additional phases did not cause any difficulty in identifying the phases of GaN. The

onset of the W-R transition was observed at 54 GPa (Fig. 3(b)), consistent with the previous work [2]. A very quick transition from the W- to R-types, however, took place at 51.4 GPa and 750 K in the course of heating at a fixed press load (4.1 MNS). We monitored the sample by X-ray diffraction analysis during the heating at lower press loads, paying special attention if the reverse transition could be observable. Growth of the R-types was not observed under conditions up to 49 GPa and 850 K. However, the dashed line connecting points a and b in Fig. 4 would be close to the equilibrium phase boundary, because both denote the onset conditions of transition from the W- to R-types at 300 K and 750 K, respectively. The Clapeyron slope for the phase boundary is suggested to be negative at approximately dT/dP = –170 K/GPa.

The electrical resistance of the GaN sample showed no significant change upon the W-R transition. This observation and the very slow reaction rate prevent the W-R transition in GaN from being used as a fixed point.

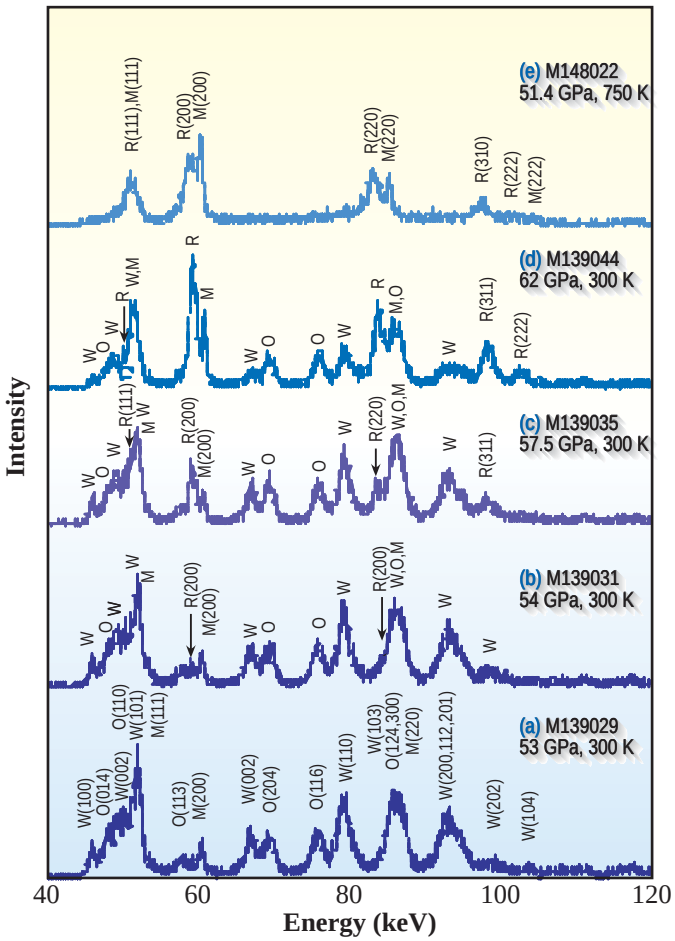

Fig. 3. Selected diffraction profiles of GaN sample with indices. W: wurzite-type GaN; R: rocksalt-type GaN; M: MgO; O: Ga_2O_3.

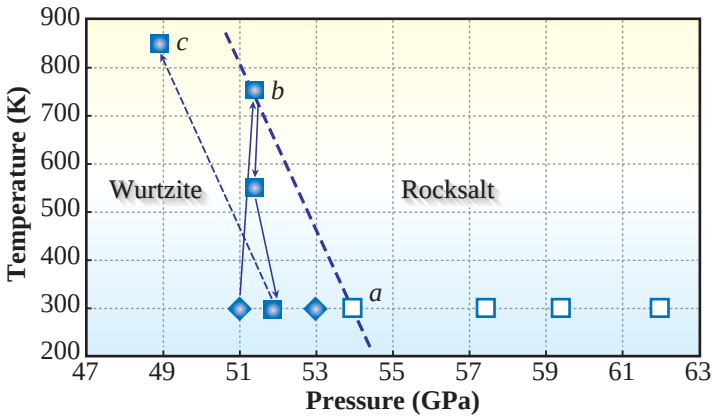

Fig. 4. Results of synthesis experiments on GaN. Solid diamond: wurzite-type; solid square: rocksalt-type; open square: composite of wurzite- and rocksalt-types.

Eiji Ito

Institute for Study of the Earth's Interior,
Okayama University

E-mail: eiito@misasa.okayama-u.ac.jp

References

[1] *E. Ito, T. Katsura, Y. Aizawa, K. Kawabe, S. Yokoshi, A. Kubo, A. Nozawa and K. Funakoshi: Frontiers in High Pressure Research, Geophysical Applications (2005) - in press.*
[2] S. Uehara *et al.*: J. Phys. Chem. **58** (1997) 2093.

New High-pressure Form of $KAlSi_3O_8$ Hollandite under Lower Mantle Conditions

We have developed an *in situ* X-ray diffraction technique for the precise determination of phase transitions and the P-V-T relations of high-pressure phases under lower mantle conditions (P = 25-130 GPa), combining sintered diamond (SD) anvils for a multianvil apparatus with synchrotron radiation. As a result, we are now able to conduct routine-basis *in situ* X-ray diffraction measurements at simultaneous high pressures up to 45 GPa and high temperatures up to 2100°C with markedly improved accuracy and on a sample volume significantly larger than those available in a diamond anvil cell (DAC). Here, we report the formation of a new high-pressure form of $KAlSi_3O_8$ [1], as an example of the recent experimental results based on this technique.

$KAlSi_3O_8$-rich feldspar is a major mineral in continental crust, which is known to transform to the hollandite structure at approximately 9 GPa via a mixture of $K_2Si_4O_9$ wadeite + Al_2SiO_5 kyanite + SiO_2 coesite. The K-rich hollandite was shown to be stable at pressures up to 95 GPa and temperatures up to 2300°C using a laser-heated DAC (LHDAC) [2], but no *in situ* X-ray diffraction studies have been carried out under simultaneous high-pressure and high-temperature conditions.

We used both synthetic K-hollandite and glass starting materials in our *in situ* X-ray diffraction study. The cell assembly was basically the same as that used in our earlier studies (e.g. [3]), as shown in Fig. 1,

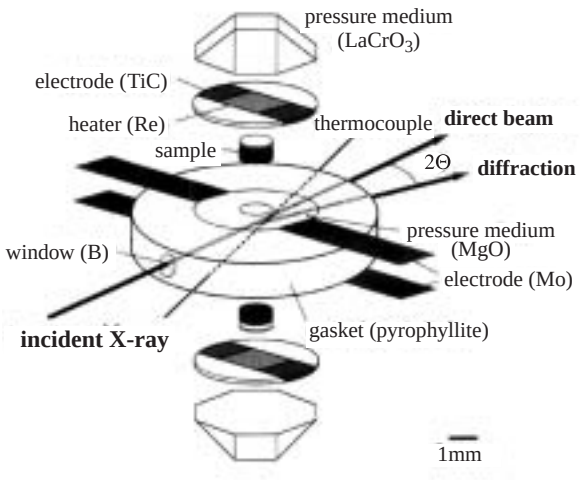

Fig. 1 Illustration of the cell assembly used for *in situ* X-ray diffraction measurements using sintered diamond anvils.

and sintered diamond cubes of 14 mm edges with truncations of 1.5 mm (TEL=1.5) were used as the second-stage anvils. An energy-dispersive method was adopted for X-ray diffraction measurements with a white X-ray beam of ~50 μm, and a new 1500 ton MA (SPEED-Mk.II [4]) constructed at beamline **BL04B1** was used for high-pressure experiments with SD anvils.

Pressure was first increased, and diffraction data were acquired for every ~2 GPa upon compression. We found that some of the diffraction peaks of K-hollandite (Fig. 2(a)) became significantly broader at pressures above 22-23 GPa in the course of compression, which partially split at pressures greater than ~25 GPa (Fig. 2(b,c)). Upon increasing temperature at a maximum press load, at ~35 GPa, the diffraction peaks became sharper and completely split into several peaks at more than ~800°C (Fig. 2(d)). The new phase was preserved after quenching under pressure (Fig. 2(e)), but was converted back to K-hollandite upon release of pressure (Fig. 2(f)). The diffraction pattern of the new high-pressure form of K-hollandite, named hollandite II, was reasonably indexed on the basis of a monoclinic symmetry with the I2/m space group, and yielded a density of 4.39 g/cm^3 under a pressure of 27.5 GPa at room temperature.

The P-T conditions of the present study and the plausible phase boundary between K-hollandite and hollandite II is shown in Fig. 3. The formation of hollandite II was confirmed when we used a glass starting material, and was also demonstrated by independent experiments using DAC with a helium pressure medium by Prof. T. Yagi's group of ISSP, University of Tokyo [5]. The present result of the transformation of K-hollandite to hollandite II is inconsistent with the results of earlier studies, which concluded that hollandite is stable at pressures up to 95 GPa, equivalent to depths of almost the entire lower mantle. However, the latter results are based mainly on the quench experiments, and the present results demonstrated the superiority of *in situ* measurements over the traditional quench experiments in the identification of a truly stable phase under high pressure and temperature.

K-hollandite is the major host for geochemically important trace elements, such as K, Ba, La, Pb, Sr, etc. in subducted crust and marine sediments, and is

believed to play a fundamental role in the fractionation of these elements in the deep mantle. It follows that chemical fractionation due to partial melting in the presence of K-hollandite should introduce some distinctive geochemical signatures in the deep mantle, which may be related to the origin of the enriched mantle reservoirs for EMI, EMII, and HIMU ocean island basalts. The present finding of the new phase transition of K-hollandite to hollandite II may significantly affect the partitioning behavior of these elements and thereby lead to a reconsideration of the origin of such reservoirs in the deep mantle.

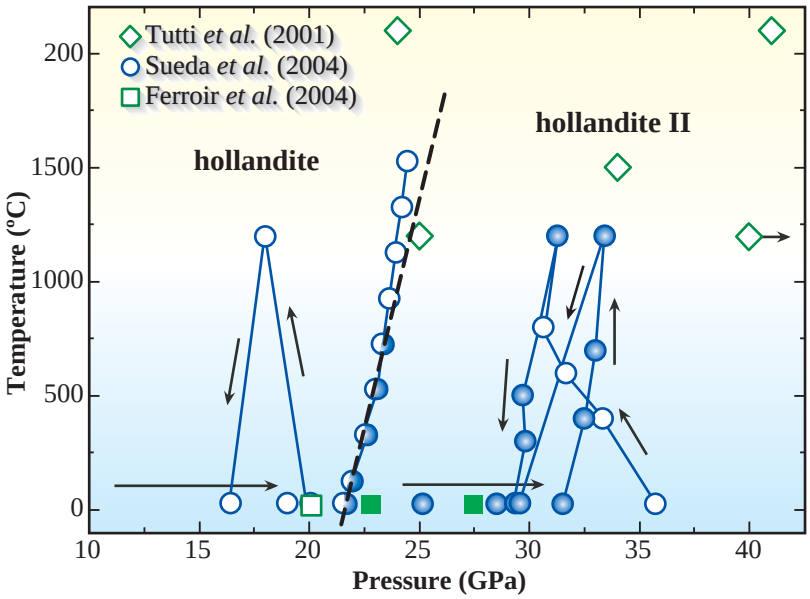

Fig. 3 P-T conditions of *in situ* X-ray diffraction measurements of the present study (circles). Squares denote those of a corresponding study with DAC at room temperature [5]. Diamond symbols denote the P-T conditions where hollandite was reported to be stable in an earlier study based on DAC [2].

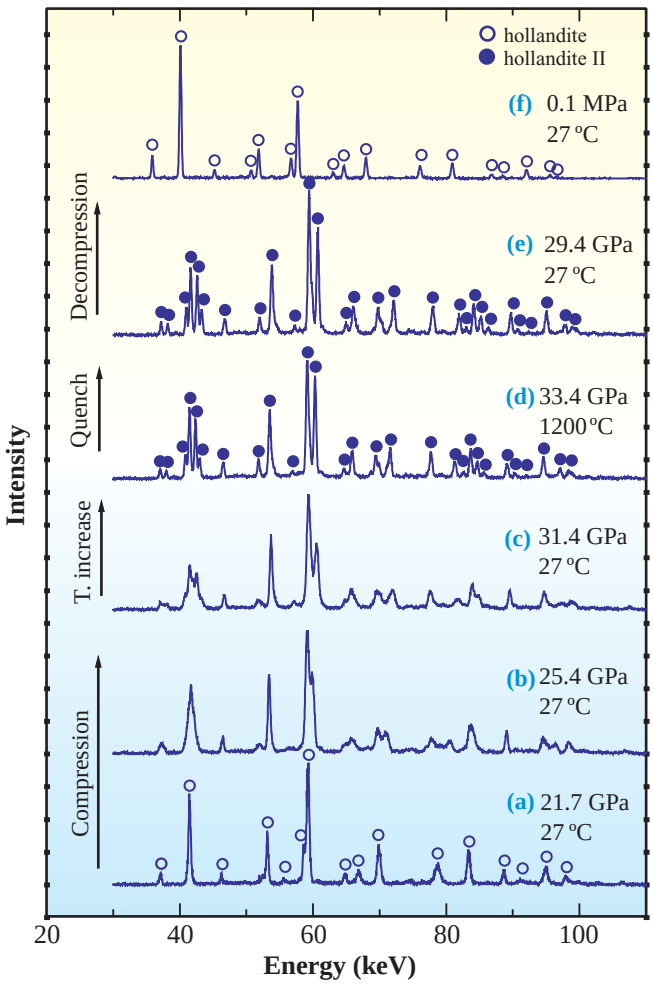

Fig. 2 Variations of X-ray diffraction profile of $KAlSi_3O_8$ with increasing pressure **(a-c)**, and at high temperature under fixed load **(d)**. Hollandite II was quenchable under pressure **(e)**, but converted back to hollandite upon release of pressure **(f)**.

Yu-ichiro Sueda and Tetsuo Irifune*

Geodynamics Research Center,
Ehime University

*E-mail: irifune@dpc.ehime-u.ac.jp

References

[1] *Y. Sueda, T. Irifune, N. Nishiyama, R.P. Rapp, T. Ferroir, T. Onozawa, T. Yagi, S. Merkel, N. Miyajima, K. Funakoshi: Geophys. Res. Lett.* ***31*** *(2004) L23612.*
[2] F. Tutti *et al.*: Geophys. Res. Lett. **28** (2001) 2735.
[3] T. Irifune *et al.*: Phys. Chem. Miner. **29** (2002) 645.
[4] T. Katsura *et al.*: Phys. Earth Planet. Inter. **143** (2004) 497.
[5] T. Ferroir *et al.*: submitted to Am. Miner.

XAFS Study of Liquid Germanate under Pressure

A crystalline solid can exist in different polymorphs with different structures and bonding patterns, whereas the idea of polymorphism in liquids was not considered seriously for a long time because of the view that liquids have rapidly changing structures that vary smoothly with temperature and pressure. Liquids with a locally tetrahedral molecular structure, such as Si, Ge, C, SiO_2, and GeO_2, have possibilities for observing pressure-induced polymorphism [1]. Because the glasses retrieved from high pressures and high temperatures do not fully preserve their high-density liquid structure, direct structural observations are essential for further understanding of pressure-induced structural changes in these liquids. However, direct structural studies have not been successful to date. Crystalline GeO_2 has two polymorphs, a quartz-type structure with fourfold Ge and a rutile-type structure with sixfold Ge. The rutile-type phase is stable at ambient conditions. With increasing temperature at atmospheric pressure, it transforms to the quartz-type phase and then melts to form a network-structured liquid in which Ge ions are tetrahedrally coordinated. Since the rutile-type phase directly melts at pressures above 1 GPa, it is most plausible that liquid GeO_2 at pressures of several GPa shows local structures different from those of the ambient-pressure liquid. We have investigated the local structures around Ge in liquid germanate by means of *in situ* X-ray absorption measurements up to 9 GPa for the first time [2].

High-pressure and high-temperature conditions were realized using a cubic-type multi-anvil press (SMAP180) installed at beamline **BL14B1**. The main experimental obstacles to studying liquid GeO_2 are the high melting temperature (e.g., 2000 K at 3 GPa) and the easy decomposition of GeO_2 into Ge and O. Accordingly, we used an alkali germanate (Li_2O-$4GeO_2$ composition) instead of pure GeO_2 and an additive of B_2O_3 in order to lower the melting temperature and suppress the decomposition of GeO_2. XAFS spectra near the Ge *K*-edge with an energy range of 1000 eV above the edge were successfully measured up to 9 GPa at 1273 K. EXAFS data analysis is described in detail elsewhere [3].

The XANES spectra of liquid germanate recorded at 4, 6 and 9 GPa and 1273 K are shown in Fig. 1 together with those of the rutile-type and quartz-type crystalline GeO_2 at ambient conditions. As shown in the spectrum of the rutile-type structure, the characteristic of the sixfold coordination of Ge is that the near-edge spectra show two shoulders discernible on both the lower- and higher-energy sides of the most intense peak, which are indicated by the two arrows in the figure. The observed spectra of liquid germanate have the pronounced shoulders, indicating that the sixfold coordination is dominant at these pressures.

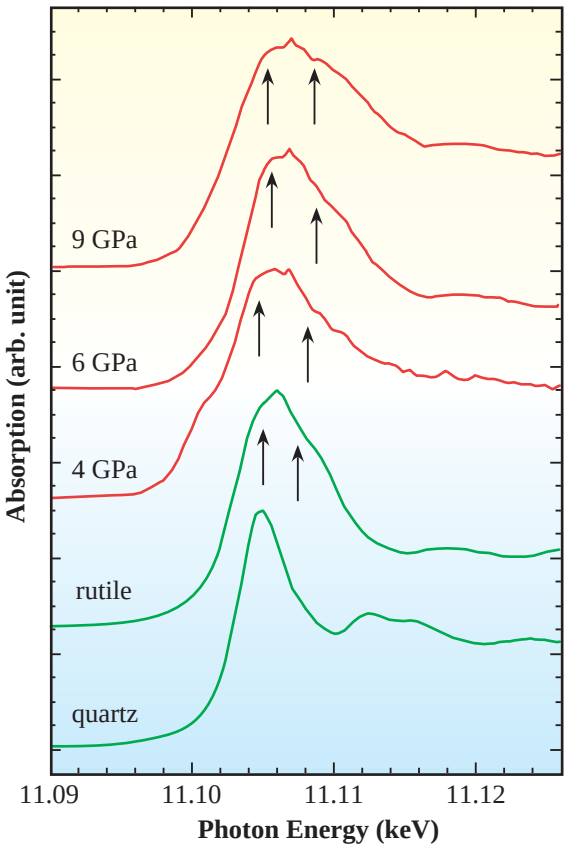

Fig. 1. Experimental Ge *K*-edge XANES spectra of liquid germanate recorded at 4, 6 and 9 GPa and 1273 K (red), together with those of the rutile- and the quartz-type crystalline GeO_2 at ambient conditions (green). The arrows indicate the shoulders as discussed in the text.

Figure 2 shows the variation of the first-neighbor Ge-O distances in the present liquid germanate at various pressures and 1273 K, as well as those in Li_2O-$4GeO_2$ glass at room-temperature compression [4,5]. The distance in the liquid remains almost unchanged up to 2.5 GPa, indicating that the fourfold coordination is dominant. At 3 GPa, the distance increases abruptly, which indicates that components with a higher coordination than fourfold are introduced.

The distance shows a maximum at 4 GPa and then decreases monotonically with pressure. The observed distances between 4 and 9 GPa are comparable to those calculated for the rutile-type crystalline GeO_2 at 1273 K (solid line). Also, the XANES spectra of this pressure region, as shown in Fig. 1, indicate the characteristics of sixfold coordination. Therefore, we conclude that the transition to sixfold coordination is completed below 4 GPa and then a high-density polymorph of liquid germanate in which Ge is octahedrally coordinated is stabilized. It should be noted that the coordination change occurs in a narrow pressure range of less than 1 GPa, although the densification accompanied by the coordination change has long been assumed to proceed monotonically over a wide pressure range. The present result reveals that the transition can be a first-order type.

As shown in Fig. 2, anomalous compressibility of the GeO_6 octahedron in the present liquid (solid circles) is observed. The compressibility of the GeO_6 octahedron in Li_2O-$4GeO_2$ glass (solid diamond) is consistent with that in the rutile GeO_2 at room temperature (dashed line), whereas the GeO_6 octahedron in the present liquid is more compressible than those in the crystal and glass; the GeO_6 octahedron in the liquid contracts and expands with pressure more easily than that in the crystalline rutile GeO_2. This anomalous compression behavior of the GeO_6 octahedron is presumably due to the lack of long- and medium-range order in liquid.

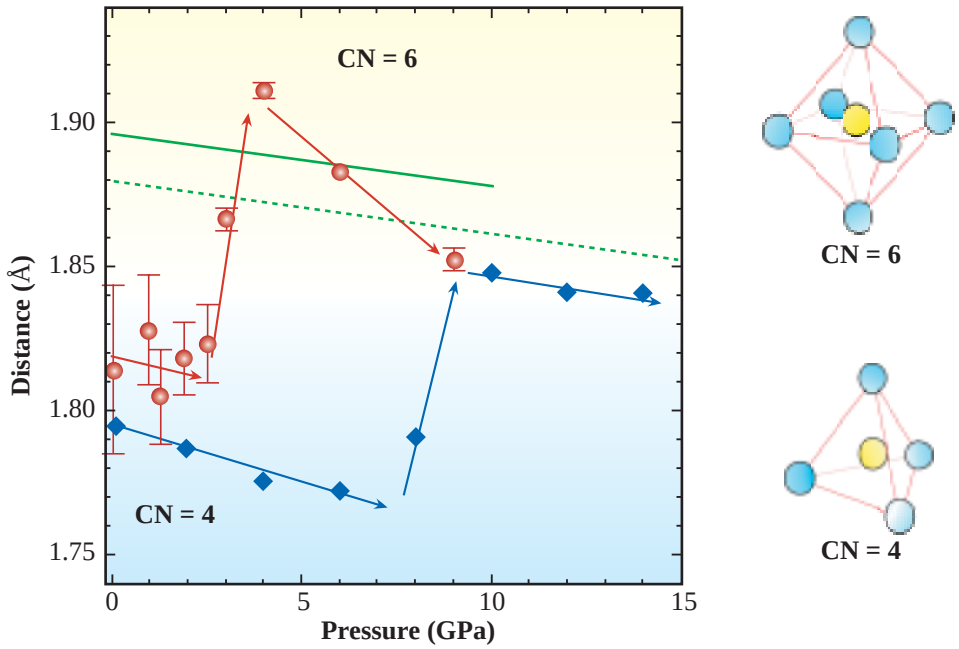

Fig. 2. Variation of the first-neighbor Ge-O distances in the present liquid germanate at 1273 K (red solid circles) and in Li_2O-$4GeO_2$ glass at room temperature (blue solid diamond). Errors for the distances are estimated from the statistical fitting errors. The arrows are guides for the eye. CN indicates the coordination number. Averaged Ge-O distances (4 short bonds and 2 long bonds in distorted GeO_6 octahedron) in rutile-type crystalline GeO_2 at room temperature and 1273 K are shown by green dashed and green solid lines, respectively.

Osamu Ohtaka[a,*], Hiroshi Arima[a] and Akira Yoshiasa[b]

(a) Department of Earth and Space Science, Osaka University
(b) Department of Science, Kumamoto University

*E-mail: ohtaka@ess.sci.osaka-u.ac.jp

References

[1] P. H. Poole *et al.*: Science **275** (1997) 322.
[2] *O. Ohtaka, H. Arima, H. Fukui, W. Utsumi, Y. Katayama and A. Yoshiasa: Phys. Rev. Lett.* ***92*** *(2004) 155506.*
[3] A. Yoshiasa *et al.*: J. Synchrotron Rad. **6** (1999) 1051.
[4] O. Ohtaka *et al.*: J. Synchrotron Rad. **8** (2001) 791.
[5] O. Ohtaka *et al.*: J. Phys. Condens. Matter **14** (2002) 10521.

Three-dimensional Structures of Cosmic Dust by Microtomography

X-ray computed tomography (CT) is a nondestructive technique for obtaining the internal structures of objects using the X-ray absorption of the materials. Three-dimensional structures can be obtained by constructing a number of successive CT images. Uesugi *et al*. [1] have developed an SR-based projection microtomography system named SP-μCT. A calculated value of the linear attenuation coefficient (LAC), which is called a CT value, is stored in each pixel of a CT image. The relationship between the CT and LAC values obtained for SP-μCT [2] enables the quantitative estimation of materials using their CT values and elemental mapping using the absorption edges of elements [3].

Extraterrestrial materials of < 1 mm in size are called cosmic dust, in contrast to meteorites (> 1 mm). They are classified into cosmic spherules, micrometeorites (MMs) and interplanetary dust particles (IDPs). Cosmic spherules are objects made spherical by melting due to heating during their entry into the Earth's atmosphere; they are collected from snow and ice in the polar region and from mud on oceanic floors. MMs are irregularly shaped particles of a few tens to a few hundreds μm in size and collected from snow and ice in the polar region. Most of them are more or less suffered from heating during atmospheric entry. IDPs are particles of about 10 μm in size and are collected in the stratosphere. They are not affected by any heating due to their small size. Cosmic dust originates from primitive materials of the solar system, which are similar to primitive meteorites, named carbonaceous chondrites. However, they probably have a wider variety of origins than meteorites (cosmic dust might come from asteroids and comets while carbonaceous chondrites come from asteroids). Accordingly, it is expected that specific information that cannot be obtained from meteorites alone can be extracted from cosmic dust. As cosmic dust is small, research has usually been done using scanning and transmission electron microscopes. We have applied microtomography to cosmic dust for the first time.

Cosmic spherules (50-300 μm) collected from Antarctica by the National Institute of Polar Research (NIPR) were imaged by SP-μCT at beamlines **BL20XU** and **BL47XU** with the pixel size of 0.5 μm [4]. Their three-dimensional external shapes were extracted from CT images (Fig. 1) and approximated as three-dimensional ellipsoids with the axial diameters of A, B and C ($A \geq B \geq C$). The axial ratios are plotted together with the data for another type of extraterrestrial spherical object characteristically included in primitive meteorites, chondrules, whose data have already been obtained by SP-μCT (Fig. 2). The shapes of cosmic spherules are recognized as belonging to three groups. For group (1), the aspect ratios ($p = C/A$) are larger than 0.8 and many of them are oblate ($B/A < C/B$ or $\log n > 0$: $(C/B)=(B/A)n$); group (2), $0.6 < p < 0.8$ and they are prolate ($B/A > C/B$ or $\log n < 0$); and group (3), are dumbbell shaped ($p \sim 0.3$-0.4). Groups (1) and (2) were also recognized in chondrules. These shapes can be explained by a high-speed rotation of the spherical objects: flattening of molten droplets during melting (oblate), deformation by shape instability (prolate), and further deformation (dumbbell shaped). As the cosmic spherules were formed by shock wave heating during their atmospheric entry, the common shape features might indicate that chondrules were also formed by shock wave melting in the primordial solar nebula. The rotation rates estimated from the oblate cosmic spherules are >1000 rps (50-300 rps for chondrules). Such extremely high rotation rates might be related to cometary dust, which

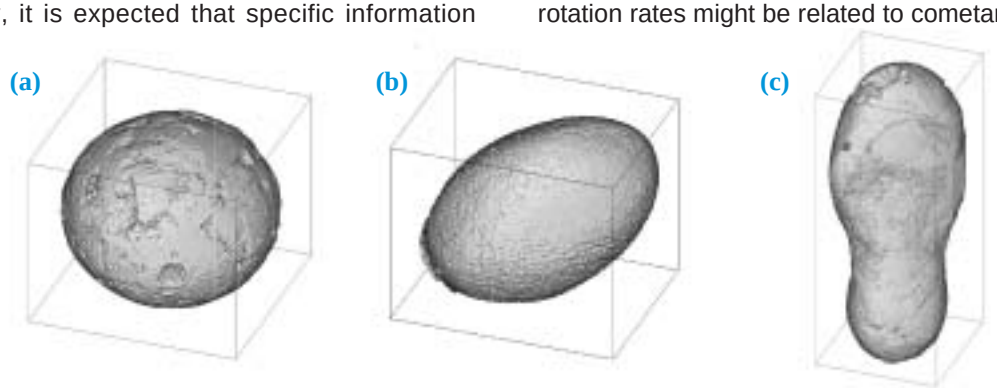

Fig. 1. Bird's-eye-views of cosmic spherules. **(a)** Oblate spherule ($133 \times 162 \times 164$ μm^3). **(b)** Prolate spherule ($80 \times 88 \times 124$ μm^3). **(c)** Dumbbell shaped spherule ($88 \times 114 \times 314$ μm^3).

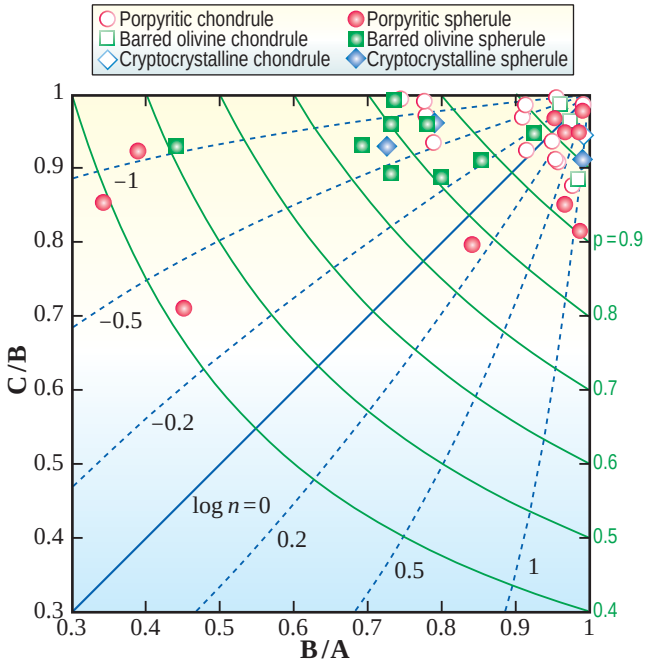

Fig. 2. Diagram showing external shapes of cosmic spherules (solid symbols) and chondrules (open symbols). Cosmic spherule and chondrule textures are also shown.

enters into the atmosphere much faster than asteroidal dust.

MMs (70-320 μm) collected from Antarctica by NIPR were also imaged by SP-μCT at BL20XU and BL47XU with the pixel size of 0.5 μm [5]. If an MM is heated during entry into the atmosphere, hydrous silicates, which were originally present in the MM, are dehydrated and become porous (scoriaceous MM: Fig. 3), while non-scoriaceous MMs suffer from slight heating. Solid portions (e.g., the white portion in Fig. 3(b)) were extracted three-dimensionally by binarization from CT images. We can also recognize voids included in the solid portions (e.g., the green portions in Fig. 3(b)). The porosities of scoriaceous and non-scoriaceous MMs are 5-28% and < 6%, respectively.

As the size of the voxel (pixel in 3D) is known in the CT images, bulk and solid volumes with and without internal voids, respectively, were obtained by counting the number of voxels belonging to the objects. The masses of the samples were also measured using an ultra-microbalance, which can measure masses of > 0.1 μg (> 50-100 μm), and their densities were calculated. The bulk and solid densities were 2.0±0.4 and 2.1±0.4 g/cm^3 for the non-scoriaceous MMs and 2.2±0.1 and 2.6±0.3 g/cm^3 for the scoriaceous MMs, respectively. The bulk densities are almost identical irrespective of vesiculation. Discrepancy between the solid density of a non-heated MM (1.8 g/cm^3) and the grain density (~2.6 g/cm^3) roughly estimated from their constituent mineral phases and their modes strongly suggests that numerous submicron pores smaller than the spatial resolution of the CT images are present. This might explain the observed low densities of asteroids.

We are now applying this technique to IDPs to obtain their fractal dimensions and enable 3D Fe mapping. This technique is also useful for small samples, which will be retrieved from an asteroid (Hayabusa mission by JAXA) and a comet (Stardust mission by NASA) by spacecrafts in the near future.

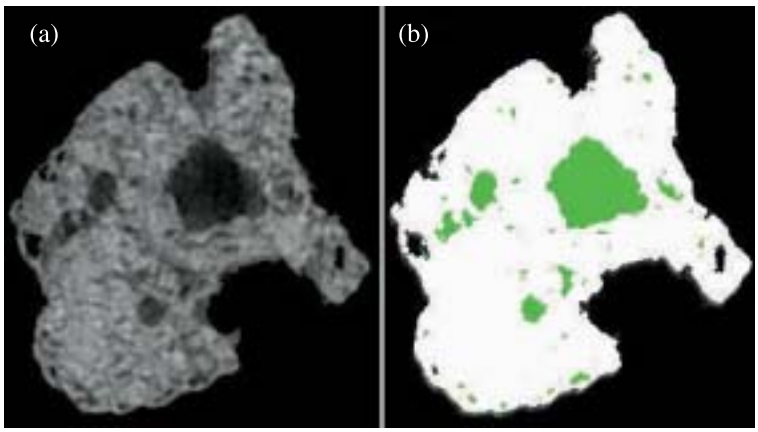

Fig. 3. Antarctic micrometeorites. **(a)** CT image. **(b)** Solid portions extracted by binarization. The width of each image is 75 μm.

Akira Tsuchiyama[a,*], Tsukasa Nakano[b] and Kentaro Uesugi[c]

(a) Department of Earth and Space Science, Osaka University
(b) AIST/GSJ
(c) SPring-8 / JASRI

*E-mail: akira@ess.sci.osaka-u.ac.jp

References

[1] K. Uesugi *et al.*: Nucl. Instrum. Meth. Phys. Res. A **467-468** (2001) 853.
[2] *A. Tsuchiyama, K. Uesugi, T. Nakano and S. Ikeda: American Mineralogist **90** (2004) 132.*
[3] S. Ikeda *et al.*: American Mineralogist **89** (2004) 1304.
[4] A. Tsuchiyama *et al.*: Chondrites and the Protoplanetary Disk (2004) 9033.
[5] A. Tsuchiyama *et al.*: Meteor. Plant. Sci. Suppl. **39** (2004) A107.

Environmental Science

As I mentioned in a previous issue, a powerful X-ray beam from the SPring-8 has enabled microanalysis, microarea analysis, and chemical state analysis for almost all elements. These techniques, realized as a result of great efforts, have yielded fruitful results in Environmental Science.

The first topic concerns the unique structures of palladium species in a heterogeneous catalyst that have been clarified by Pd *K*-EXAFS, TEM, and so on. Heterogeneous catalysts, offering the advantages of unprecedented reactions based on specific surface ensemble sites and a simple operation for the separation of products from catalysts, are considered to be promising materials for Green and Sustainable Chemistry.

Regarding the second topic, the chemical states of copper, the compounds of which are considered to be catalysts implicated in the generation of dioxins, have been studied in the case of real fly ash samples by XAFS using an *in situ* cell. Evidence of oxychlorination, which may generate dioxins, has been found in real fly ash. The mechanism of dioxin generation in fly ash is being clarified.

In the third topic, a scanning electron microscope with an energy-dispersive X-ray spectrometer (SEM-EDX) has been combined with a synchrotron radiation X-ray fluorescence (SR-XRF) spectromicroscope for the first time. Such a sophisticated observation system like SEM-EDX, is necessary for microarea analysis by SR-XRF. The combined system has been applied to the element analysis of individual micrometer-size aerosol "kosa" particles sampled in northeastern China.

Momoko Takemura

XAFS Analysis of Fine Structure of Palladium Species Immobilized on Hydroxyapatite Surface

The evolution of environmentally acceptable organic synthesis routes is an ultimate goal of the present-day chemistry. One of the promising approaches to "Green & Sustainable Chemistry" is the replacement of conventional methods employing toxic and/or hazardous stoichiometric reagents by atom-efficient catalytic alternatives. Heterogeneous catalysts have the advantages of being operationally simple, as well as enabling unprecedented reactions based on specific surface ensemble sites within a regular arrangement. Achieving precise architectures of active metal species on solid surfaces is one of the most important challenges in creating highly functionalized heterogeneous catalysts. Currently, we are developing high-performance metal catalysts using unique properties of clay minerals as macroligands for catalytic active centers [1].

Hydroxyapatites (HAPs) possess Ca^{2+} sites surrounded by PO_4^{3-} tetrahedra parallel to the hexagonal axis, as shown in Fig. 1, and are of considerable interest in many areas because of their ion-exchange ability, adsorption capacity, and acid-base properties. The chemical composition of HAPs can be varied from the stoichiometric form to the Ca-deficient one. Here, we present two new classes of HAP-bound Pd complexes designed with strict compositional and structural control [2]. Both stoichiometric and Ca-deficient HAPs are employed, and the catalysts exhibit specific novel functions as heterogeneous Pd catalysts. The precise construction of Pd species described here also represents a great contribution to modern palladium chemistry.

HAPs were synthesized from $Ca(NO_3)_2{\cdot}4H_2O$ and $(NH_4)_2HPO_4$ by a precipitation method. Selecting appropriate Ca/P molar ratios yielded the stoichiometric $Ca_{10}(PO_4)_6(OH)_2$ (Ca/P=1.67, HAP-0) and Ca-deficient $Ca_9(HPO_4)(PO_4)_5(OH)$ (Ca/P= 1.50, HAP-1). The treatment of the HAP-0 and HAP-1 with an acetone solution of $PdCl_2(PhCN)_2$ yielded HAP-bound Pd complexes, PdHAP-0 and PdHAP-1, respectively (Pd content: 0.02 mmol·g^{-1}).

The characterization of the PdHAPs using physicochemical methods such as X-ray diffraction, X-ray photoelectron spectroscopy, and inductively coupled plasma spectrometry revealed that the palladium species are immobilized by adsorption on the HAP surface. Furthermore, the results of Pd *K*-edge X-ray absorption near-edge structure spectra of both PdHAPs confirmed the divalent state of all Pd species. A monomeric Pd species was evidenced by the absence of peaks at around 2.5 Å in the Fourier transform (FT) of k^3-weighted extended X-ray absorption fine structure (EXAFS) data for the PdHAPs (Figs. 2(a) and 2(b)) (**BL01B1**).

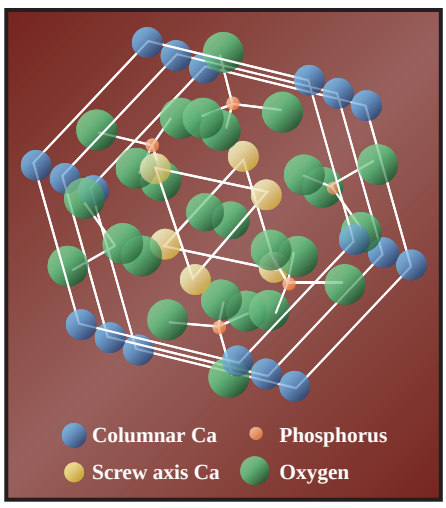

Fig. 1. Structure of hydroxyapatite.

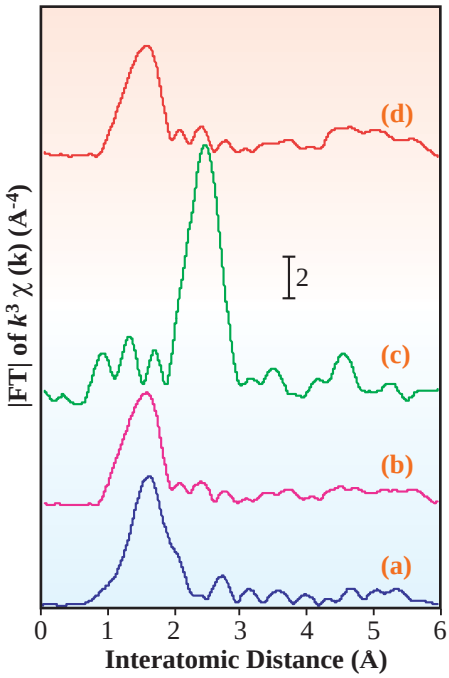

Fig. 2. FTs of k^3-weighted Pd *K*-edge EXAFS experimental data for **(a)** PdHAP-0, **(b)** PdHAP-1, **(c)** recovered PdHAP-0 and **(d)** recovered PdHAP-1 for the oxidation of 1-phenylethanol. The phase shift was not corrected.

The inverse FT of the peaks at around 1-2 Å for the PdHAP-0 was well fitted using Pd-Cl and Pd-O shells, whereas the best fit for the PdHAP-1 was achieved using only a Pd-O shell. It was conclusively established that a monomeric $PdCl_2$ species was grafted by chemisorption on the HAP-0 surface (Fig. 3(a)), and a monomeric Pd^{II} phosphate complex surrounded by four oxygens was formed at a Ca-deficient site of the HAP-1 (Fig. 3(b)). Two unique monomeric Pd species with intrinsically different surroundings can be created on the solid surfaces through the precise control of the Ca/P ratios of the parent hydroxyapatites.

The oxidation of alcohols into carbonyl compounds is one of the most pivotal functional group transformations in organic synthesis. The PdHAP-0 was an effective heterogeneous catalyst for the aerobic oxidation of a wide variety of alcohols, giving the corresponding ketones and aldehydes in high yields. In a 250 mmol scale reaction of 1-phenylethanol without organic solvents, the oxidation proceeded smoothly and the turnover number (TON) of acetophenones based on Pd approached 236,000. This TON is three orders of magnitude larger than those previously reported for any catalyst systems under an atmospheric O_2 pressure.

The FT EXAFS for the recovered PdHAP-0 exhibited a single peak at approximately 2.5 Å due to the formation of Pd metal, as shown in Fig. 2(c). TEM also revealed the presence of Pd nanoparticles with a diameter of *ca*. 40 Å and a narrow size distribution (σ = 5.7 Å) (Fig. 4). The ICP analysis of the filtrate confirmed that no leaching of Pd species occurred during the above oxidations. Notably, the above oxidations hardly occurred in the presence of the PdHAP-1, and that there were no structural changes at around the PdII center (Fig. 2(d)).

Recently, we have also found that the PdHAP-0 can be an efficient heterogeneous catalyst for the dehalogenation of aryl halides, deprotection of the *N*-benzyloxycarbonyl group from amino acids using 1 atm of H_2, and the dehydrogenation of indolines into indoles that serve as versatile intermediates for the synthesis of pharmaceuticals and agrochemicals [3].

The Heck coupling reaction has received considerable attention due to its enormous synthetic potential to form new carbon–carbon bonds. Commercial applications have, however, been limited by low TONs. We found that the PdHAP-1 is an outstanding catalyst for the Heck reaction. For example, the TON based on Pd reached 47,000 for 24 h in the reaction of bromobenzene with styrene. The recovered PdHAP-1 kept an original monomeric Pd^{II} structure and was recyclable with retention of its catalytic activity. It can be concluded that the high catalytic activity of the PdHAP-1 is ascribed to the exceptional robust structure of monomeric Pd^{II} species.

We expect that our immobilizing protocol using hydroxyapatites will offer an attractive route for the design of high-performance nanostructured catalysts at the atomic level with the aim of realizing environmentally friendly chemical processes. XAFS measurement gives us precise and reliable information about the local structure of infinitesimal metal species immobilized on the solid surface.

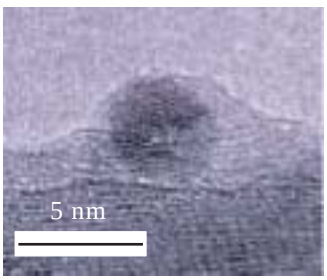

Fig. 4. Transmission electron micrograph of the Pd nanoparticle for the recovered PdHAP-0 catalyst after the oxidation of 1-phenylethanol.

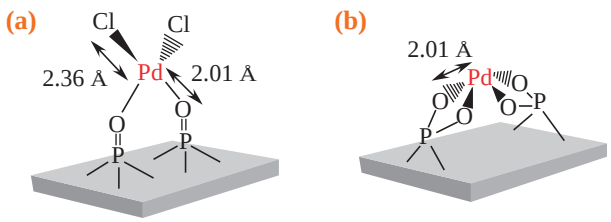

Fig. 3. Proposed surface structures around Pd^{II} of PdHAP-0 **(a)** and PdHAP-1 **(b)**. The nearest oxygen and chlorine atoms around the Pd^{II} are shown.

Kiyotomi Kaneda

Graduate School of Engineering Science,
Osaka University

E-mail: kaneda@cheng.es.osaka-u.ac.jp

References

[1] K. Kaneda *et al.*: J. Am. Chem. Soc. **121** (1999) 4526; **122** (2000) 7144; **125** (2003) 10486; **125** (2003) 11460; **126** (2004) 5662.
[2] *K. Mori, T. Hara, T. Mizugaki, K. Ebitani and K. Kaneda: J. Am. Chem. Soc.* ***126*** *(2004) 10657;* ***124*** *(2002) 11572.*
[3] *T. Hara, K. Mori, M. Oshiba, T. Mizugai, K. Ebitani and K. Kaneda: Green Chem.* ***6*** *(2004) 507; Tetrahedron Lett.* ***44*** *(2003) 4981;* ***44*** *(2003) 6207.*

Change in Chemical Form of Copper in Fly Ash at Temperatures Suitable for Dioxin Formation

Understanding the mechanisms involved in the formation of dioxins in fly ash is necessary in the control of dioxin emission. Dioxins are secondarily formed in a post-combustion zone, which is considered to occur primarily on and in fly ash, as first described by Stiegltiz and Vogg [1]. According to many studies, copper compounds are regarded as influential catalysts that generate large amounts of dioxins in heat experiments involving model fly ash. Nevertheless, only limited information on the chemical forms of copper or their changes in real fly ash is available in the literature. Previously, we investigated the chemical forms of copper in eight types of real fly ash before heating experiments using XANES [2]. However, to understand the exact formation mechanism, it is necessary to study the reaction that takes place with Cu compounds during the heating of fly ash. Here, we conducted *in situ* XANES experiments using real fly ash.

Real fly ash was sampled from a bag filter in a normal stoker-type municipal solid-waste incinerator (MSWI). The measured copper, chlorine, and total organic carbon levels were 2600 mg/kg, 14%, and 1.5%, respectively. The direct speciation of copper in fly ash was examined using XANES with an *in situ* cell (see Fig. 1) at beamline **BL01B1**. The heating procedure and atmospheric conditions are shown in Fig. 2. The spectra were collected in a fluorescence mode using a 19-element Ge solid-state detector with a Si(111) monochromator. Species have also been distinguished using the linear combination fit (LCF) technique, in which the spectra of known reference species are fitted to the spectrum of an unknown sample.

Fig. 1. XANES experiment using *in situ* cell.

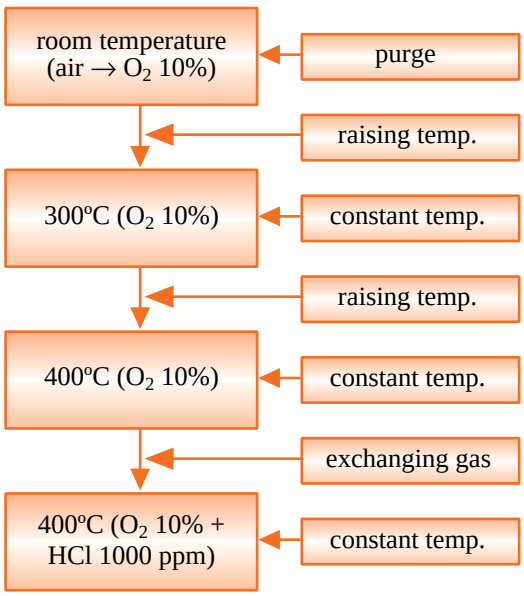

Fig. 2. Heating procedure of *in situ* XANES experiment.

The change in the chemical form of copper in real fly ash during heating is shown in Fig. 3. At room temperature, the XANES spectra indicated that the copper compounds consisted of 75% $CuCl_2{\cdot}3Cu(OH)_2$, 14% CuCl, and 11% $Cu(OH)_2{\cdot}$ $CuCl_2{\cdot}3Cu(OH)_2$ is one of the species present as a catalyst in the chlorination of ethylene [3] and as the main species in real fly ash [2]. In the second temperature increase, the shape of the XANES spectra dramatically changed and the edge position of the spectra shifted to a low energy. Hence, it was found that the reduction of cupric compounds begins below 200°C. When the fly ash was heated to 300°C, the chemical forms of copper dramatically changed to 45% CuCl, 29% Cu, and 26% Cu_2O. We did not recognize $CuCl_2{\cdot}3Cu(OH)_2$ in the heated fly ash. Heating the fly ash to 300°C transformed the cupric compounds in the fly ash into cuprous compounds or elemental copper. This indicates that the atmosphere

surrounding the fly ash is very reductive. When the temperature of the fly ash increased to 400°C, the ratio of CuCl increased to 61% of the total Cu, while the ratios of Cu and Cu_2O decreased to 20%. The atmosphere was then changed from 10% O_2 (90% N2) gas to 10%O_2 + HCl 1000 ppm (balance of N_2) to observe the effect of chlorination by HCl at 400°C. The ratios of CuCl and Cu_2O decreased to 49 and 14% of the total Cu, respectively, and CuO appeared. Oxidation of Cu^+ compounds to CuO occurred rather than the chlorination of copper in fly ash by HCl. *In situ* XANES showed that the chemical form of copper in the fly ash depends on the temperature, and that cupric compounds at room temperature are transformed into cuprous compounds or elemental copper by heating. The trend observed in the XANES spectra of an oxychlorination catalyst is similar to those obtained by us [3]. Thus, we can conclude that oxychlorination occurs in real MSWI fly ash. Some researchers have suggested that oxychlorination occurs in real fly ash [4], although until now, only limited evidence of this is available. However, in this study, we found stronger evidence for this in our *in situ* XANES experiment. Since it is thought that the state of copper in fly ash depends on the temperature, fly ash composition, and surrounding environment, research on its effects on the chemical forms of copper is required. Furthermore, the correspondence between the amount of dioxin generated and the change in the chemical form of copper should also be investigated.

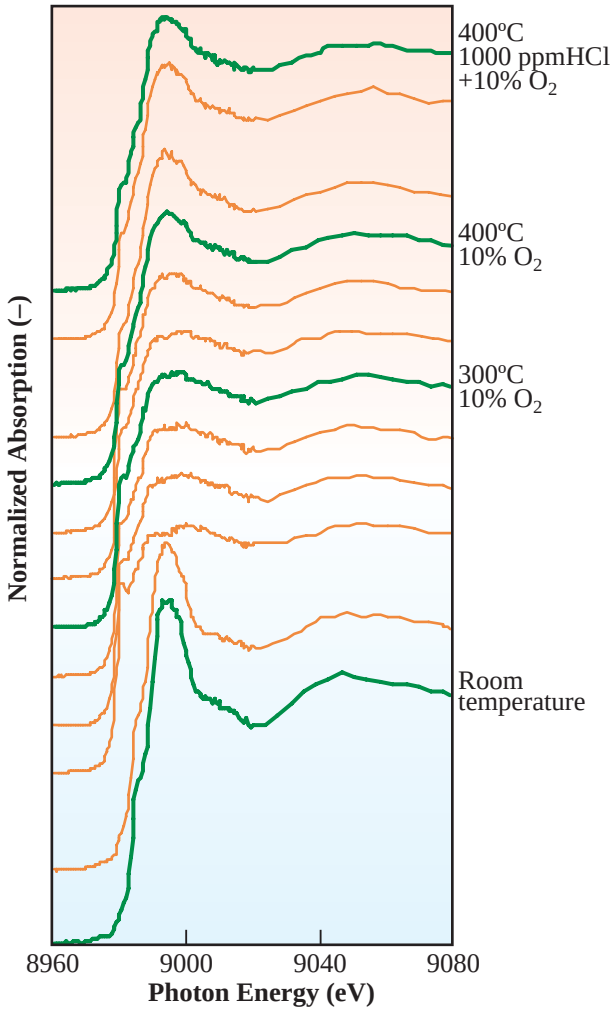

Fig. 3. Change in the chemical form of copper in real fly ash during heating.

Masaki Takaoka

Department of Urban & Environmental Engineering, Kyoto University

E-mail: takaoka@epsehost.env.kyoto-u.ac.jp

References

[1] L. Stieglitz and H. Vogg: Chemosphere **15** (1986) 1373.
[2] *M. Takaoka, T. Yamamoto, A. Shiono, N. Takeda, K. Oshita, T. Matsumoto and T. Tanaka: Chemosphere **59** (2005) 1497.*
[3] C. Lamberti *et al.*: Angew. Chem. Int. Ed. **41** (2002) 2341.
[4] J.G.P. Born *et al.*: Environ. Sci. Technol. **27** (1993) 1849.

Individual Micrometer-size Aerosol Particle Analysis with On-site Combination of Electron Microscope and Synchrotron X-ray Microscope

Aerosol particles, absorbing atmospheric toxic elements during flight, adversely affect human health upon reaching the lower respiratory tract. Global environmental factors, including climate, are also vulnerable to the simultaneous mass transfer of atmospheric elements, which also disturbs the global radiative energy transfer (albedo). Recent desertification and air pollution accompanying Asian industrialization are deteriorating the situation.

A scanning electron microscope with an energy-dispersive X-ray spectrometer (SEM-EDX) has been commonly used for the topographic image observation of materials down to the nanometer scale. A secondary electron image provides a detailed 3D-like surface morphology, while information on elemental composition is obtained by detecting the characteristic X-rays from B to U with a detection limit of *ca*. 0.5 wt.% for most elements, together with the sub-micrometer area image observation. SEM-EDX is (i) sensitive to light elements, (ii) capable of performing qualitative and quantitative analyses within a few minutes for most samples, and (iii) inapplicable under atmospheric pressure, but an ultrahigh vacuum is not necessary. On the other hand, a low excitation efficiency induced by an electron beam for heavy elements, as well as bremsstrahlung that leads to strong continuous X-ray backgrounds, has been a concern when detecting trace and microamounts of elements.

A synchrotron radiation X-ray fluorescence (SR-XRF) spectromicroscope, the minimum detection limit of which is less than one femtogram, is another elemental analysis instrument used in detecting the characteristic X-rays. SR-XRF is (i) appropriate for detecting trace and microamounts of elements, (ii) a tunable beam size down to a sub-micrometer scale for local measurement, and (iii) applicable under atmospheric pressure. However, one critical problem of SR-XRF application to individual aerosol particles despite its higher sensitivity than SEM-EDX is that optical microscopes, often used for beam position alignment in SR-XRF, are inappropriate for micrometer-size sample observation due to the limited resolution and very small depth of focus. It has been a problem that the exclusiveness of SEM measurement due to the vacuum seal requirement obliges SR-XRF and SEM to be performed separately.

In the present research, we succeeded in simultaneously performing SR-XRF and SEM-EDX measurements for a micrometer-size single Kosa aerosol particle without changing the sample position, by introducing a synchrotron radiation beam into a SEM chamber [1-3]. Sensitive multielement determination by SR-XRF and detailed surface topography observation by SEM, both crucial for the investigation of the state of an individual particle, have been simultaneously applied to individual particles in the SEM chamber by aligning the X-ray and electron beam positions.

A low-vacuum SEM (JEOL JSM-5600LVS) mounted with a silicon drift detector (SDD), Röntec

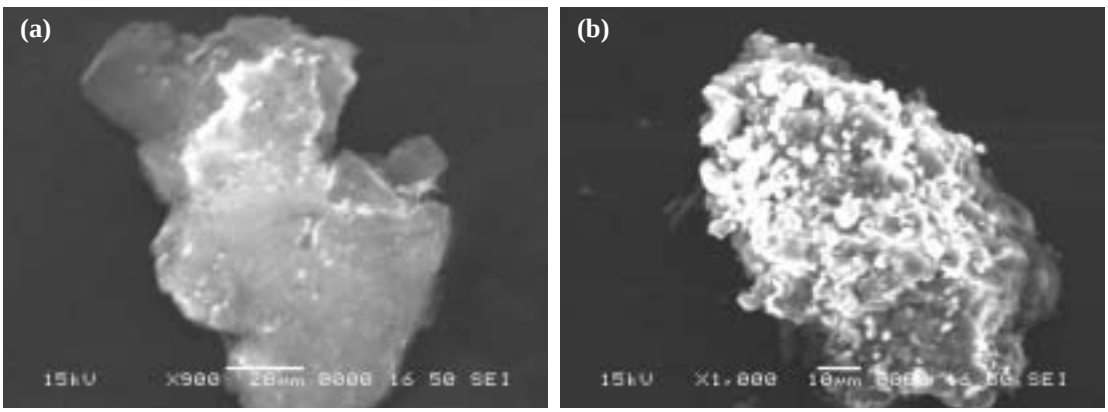

Fig. 1. Secondary electron images of single Kosa aerosol particles sampled in **(a)** Shenyang, China, in March 2004, and **(b)** Harbin, China, in September 2003.

Xflash 2000, was installed at beamline **BL37XU**. This SEM was equipped with a beryllium window (10 μm in thickness and 20 mm in diameter) to introduce a monochromatic synchrotron radiation microbeam inside the SEM chamber. The position of SEM was adjustable both vertically (by a pulse motor) and horizontally in such a manner that the synchrotron radiation beam and the electron beam can cross on the SEM sample stage.

The SEM images of two representative Kosa aerosol particles (*ca.* 50 μm in diameter) are shown in Fig. 1; one sampled at a building rooftop in Shenyang in March 2004, when severe Kosa aerosol outbreak was recorded, and the other sampled at a rooftop of a building in Harbin University of Science and Technology in September 2003, when Kosa was moderate (Shenyang and Harbin are major industrial cities located in northeastern China). Standard Kosa samples, CJ-1 and CJ-2, National Institute for Environmental Studies, Tsukuba, Japan, were also measured as typical Kosa particles before being contaminated.

The results have proved that the sensitivity of detecting constituent elements of individual Kosa aerosol particles is higher using this combination, as shown in Fig. 2, than solely using conventional SEM-EDX. It should be noted that elements from Mg to Fe, including major constituents of both soil and atmospheric pollutants, in a single particle were satisfactorily measured. We observed that the individual aerosol particles were contaminated with atmospheric sulfur and chlorine, by successfully detecting the deviation in elemental composition from the standard Kosa samples. Detailed SEM images were utilized in conjunction with the elemental analysis result, and it was implied that atmospheric sulfur primarily adheres to calcium intrinsic to Kosa aerosol and that the surface roughens as a consequence of the chemical reaction between the two elements ($CaSO_4$). The coexistence of sulfur and calcium was verified for tens of other aerosol particles by elemental distribution analysis.

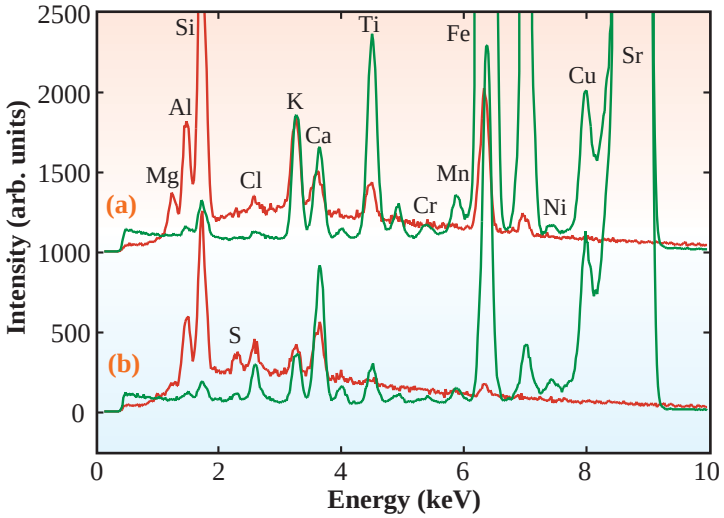

Fig. 2. SEM-EDX (red) and SR-XRF (green) spectra of **(a)** Shenyang and **(b)** Harbin particles, which are identical to those shown in Fig. 1.

Yoichi Tanaka, Teruo Tanabe and Jun Kawai*

Department of Materials Science and Engineering, Kyoto University

*E-mail:jun.kawai@materials.mbox.media.kyoto-u.ac.jp

References

[1] *M. Toyoda, K. Kaibuchi, M. Nagasono, Y. Terada, T. Tanabe, S. Hayakawa and J. Kawai: Spectrochim. Acta B* ***59*** *(2004) 1311.*

[2] *T. Tanabe, Y. Tanaka, D. Tanaka, Y. Taniguchi, M. Toyoda, J. Kawai, H. Ishii, C. Riu, Y. Yilixiati, S. Hayakawa, Y. Kitajima and Y. Terada: Bunseki Kagaku* ***53*** *(2004) 1411 (in Japanese).*

[3] *Y. Tanaka, Y. Taniguchi, D. Tanaka, M. Toyoda, H. Ishii, T. Tanabe, Y. Terada, S. Hayakawa and J. Kawai: Anal. Sci.* ***21*** *(2005) 839.*

INDUSTRIAL APPLICATIONS

Seven carefully selected experiments that were successfully accomplished in the Industrial Applications field in 2003B and 2004A are presented.

The very interesting and useful experiments described in this section were performed using the following five different beamlines: one experiment was accomplished using the XAFS beamline BL01B1, three experiments were carried out using the Engineering Science Research beamline, BL19B2, and three experiments were performed using the Medical and Imaging I beamline BL20B2, the White Beam X-ray Diffraction beamline BL28B2, and the R&D(1) beamline BL47XU. respectively.

The result of the first experiment clearly showed that the Ge atom in the crystal and amorphous phases of $Ge_2Sb_2Te_5$ alloy for the rewritable digital versatile disc is located at an octahedral (crystal) or a tetrahedral (amorphous) symmetry position (BL01B1).

In the second experiment, the electronic properties of the Pt nanoparticle surface was analyzed using the structural model obtained by *in situ* XAFS and *in situ* X-ray diffraction techniques (BL19B2). The third experiment concerned the study of the stress depth profile of ceramic layers of a cutting tool (BL19B2).

The fourth experiment was on white X-ray topography used to determine 3D dislocation structures in silicon (BL28B2), and in the fifth experiment, X-ray topography of a SiC single crystal produced by "Repeated A-Face" growth process was carried out (BL20B2).

The sixth experiment was a mechanism analysis of the curing reaction for polymer-modified cement (BL19B2), and the last experiment was on *in situ* high-resolution X-ray tomography of fracture in aluminum foam (BL47XU).

It can be declared with confidence that the outstanding articles presented in this section provide good models for material researchers and analytical scientists.

Tokuhiko Okamoto

XAFS Study of Local Structural Changes in Ge-Sb-Te during Optical Recording below the Diffraction Limit

Continuing progress in multimedia has lead to the need for ever increasing storage density requirements with fast data recording/access. One of the most promising solutions to these stiff requirements is phase-change optical data storage. The latest industrial implementation of optical data storage is the re-writable digital versatile disc (DVD), a medium that allow storage up to 4.7 Gb of information on a single-layer disk. The recording (phase change) medium of a DVD is either $Ge_2Sb_2Te_5$ (DVD-RAM) or a quaternary Ag-In-Sb-Te (DVD-RW) alloy.

The phenomenology of optical recording is very simple. CW-laser light crystallizes the recording layer while an intense laser pulse melts the material that is subsequently quenched into the amorphous state. The recorded bits are thus amorphous marks against a crystalline background.

Although the idea of phase-change recording has been around for almost 40 years and DVDs have been commercially available for over a decade, it has only been recently that the nanoscale structure of the recording material and its modification upon the amorphous-crystalline phase transition started to emerge.

Earlier X-ray diffraction studies suggested that – although the stable structure of $Ge_2Sb_2Te_5$ (GST) is hexagonal – thin GST layers crystallize into the rocksalt structure with a rather large isotropic temperature factor [1]. Whilst this was a very important finding it left several very important questions unanswered.

We have carried out X-ray absorption fine structure (XAFS) measurements of crystallized and laser-amorphized GST layers at beamline **BL01B1** and – which is important – our measurements were performed on real-device structures. For the crystalline state we found that Ge and Sb atoms were not located on the ideal rocksalt sites (in the center of the Te face-centered cubic (fcc) sublattice but were somewhat displaced from the center, i.e., similar to the GeTe structure, a distorted rocksalt, or rhombohedral structure. An immediate consequence of this is that GST in its metastable crystalline state possesses a net dipole moment, i.e., is a ferroelectric [2,3].

It was found that the "amorphization" of GST produced a structure with bonds *shorter and stronger* than in the crystalline phase as evidenced by comparison of Fourier-transformed extended X-ray absorption fine structure (FT EXAFS) spectra (Fig. 1) for the two phases. The results of a detailed data analysis are summarized in Table 1. Such a change is highly unusual for covalently bonded solids and suggests that the "amorphization" of GST is not a simple disordering of the structure but involve much more drastic changes [2].

To get more insight into the structural transformation we have also performed X-ray absorption near-edge structure (XANES) measurements and simulations. The best agreement between the experiment and simulations was obtained when Ge atom was placed into a tetrahedral symmetry position within the Te face-centered cubic (fcc) sublattice [2].

The structure of the crystalline and amorphous phases of GST are schematically illustrated in Fig. 2, which shows fragments of the structure with a Ge

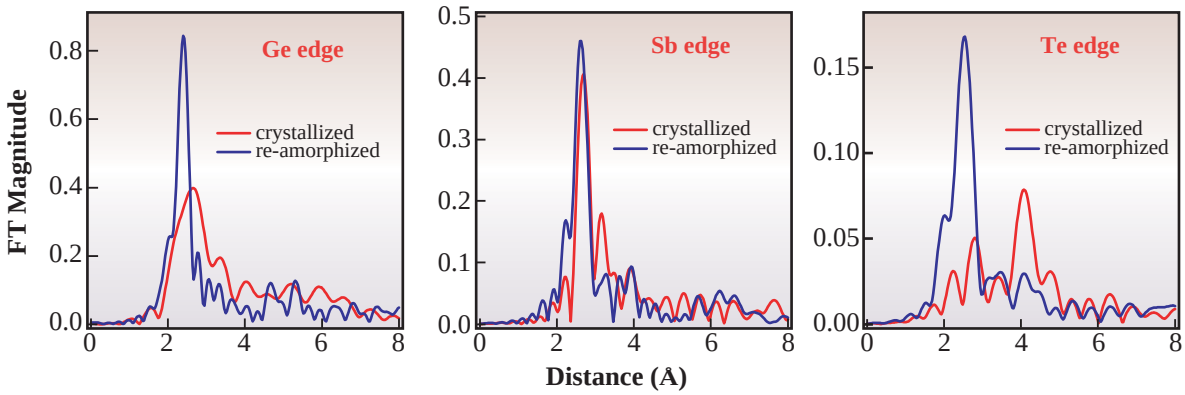

Fig. 1. FT-EXAFS spectra of crystalline and amorphous areas measured at Ge, Sb, and Te *K*-edges (after [2]).

atom located either in a octahedral (crystalline) or tetrahedral (amorphous) symmetry positions. As a double check of the amorphous structure, one can estimate the Ge-Te bond length assuming the Ge atoms are in tetrahedral symmetry positions. Based on the lattice parameter obtained by X-ray diffraction, this bond lengths is expected to be 2.61 Å, a value identical to the experimentally measured result (Table 1).

The phase-transition thus primarily consists in an umbrella flip of Ge atoms between the octahedral and tetrahedral symmetry positions without major structural rearrangement. It is the fact that the Te sublattice is preserved while only the Ge atoms switch position that accounts for the ultra-fast recording/erasing rates and the overall media stability [2,3].

It is interesting that the same materials, namely GST and Ag-In-Sb-Te alloy (AIST), are also the best-performing materials in the optical discs of new generation, the so-called super resolution near-field structure (Super-RENS) optical discs currently developed by our Center [4]. At present, bits with a characteristic size of less than 100 nm with a carrier-to-noise ratio (CNR) over 40 dB can be recorded with an inexpensive standard "red" diode laser. A significant difference between the DVD and Super-RENS structures is that in the latter the GST layer is crystalline in both recorded and non-recorded areas. Intensive investigations of the underlying mechanisms behind super-RENS recording and read-out are currently underway [5].

Table 1. Bond lengths and mean-square relative displacements (MSRD) obtained for crystalline and amorphous $Ge_2Sb_2Te_5$.

Bond	Bond length (Å) / MSRD ($Å^{-2}$)	
	Crystal	Amorphous
Te-Ge	2.83 ± 0.01 / 0.02	2.61 ± 0.01 / 0.008
Te-Sb	2.91 ± 0.01 / 0.02	2.85 ± 0.01 / 0.008
Te-Te (2^{nd})	4.26 ± 0.01 / 0.01	

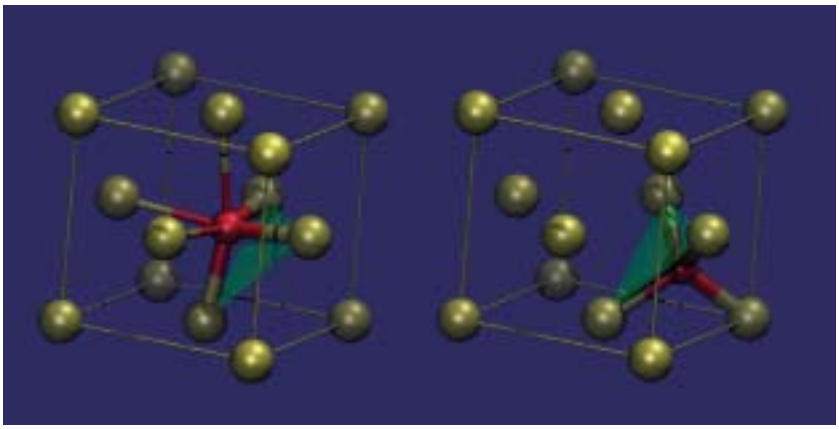

Fig. 2. Fragments of crystalline and amorphous structures. During the transition Ge atom switches between octahedral and tetrahedral symmetry positions (after [2]).

A.V. Kolobov*, P. Fons and J. Tominaga

Center for Applied Near-Field Optics Research, National Institute of Advanced Industrial Science and Technology

*E-mail: a.kolobov@aist.go.jp

References

[1] N. Yamada and T. Matsunaga: J. Appl. Phys. **88** (2000) 7020.
[2] *A.V. Kolobov, P. Fons, A.I. Frenkel, A.L. Ankudinov, J. Tominaga, T. Uruga: Nature Mater. **3** (2004) 703.*
[3] A.V. Kolobov *et al.*: Jpn. J. Appl. Phys. (Special issue - Proc. Int. Symp. Optical Memories) - in press.
[4] J. Tominaga *et al.*: Appl. Phys. Lett. **73** (1998) 2078.
[5] J. Tominaga *et al.*: Nanotechnology **15** (2004) 411.

Structural and Electronic Properties of Platinum Nanoparticle Surface in an Aqueous System Probed by *In Situ* X-ray Absorption Spectroscopy

There is a strong demand for new mobile batteries for powering mobile electronics, such as laptop computers, mobile phones, and personal digital assistants (PDAs), in the upcoming ubiquitous networking society, because the energy capacity of the currently widely used Li-ion batteries is insufficient to power the state-of-the-art electronics for long period of use. The micro-direct methanol fuel cells (DMFCs), that generate electricity by an electrochemical reaction between methanol and oxygen, are considered to be a potential successor to Li-ion batteries as its energy capacity is potentially more than ten times larger than that of Li-ion batteries. One of the main technological issues in developing DMFCs is the improvement of the efficiency of cathode catalysts. Currently, platinum nanoparticles are the best cathode catalysts for use in DMFCs. Their performance, however, is unsatisfactory for real wide spread commercial use.

The detailed mechanism of the cathode reaction in DMFCs, i.e., the oxygen reduction reaction (ORR) on platinum, at the atomic or molecular scale, has been a long-period problem in electrochemistry and is still controversial. Since this is directly related to the catalytic activity of platinum in the ORR, the elucidation of the ORR mechanism is important for developing new catalysts. As the first step toward a full understanding of the ORR mechanism, we investigated the structural and electronic properties of platinum nanoparticles in an aqueous system by X-ray absorption spectroscopy. [1]

In situ XAFS measurements were performed in an anodic oxidation process in an aqueous system in a wide potential range. Carbon supported platinum nanoparticles (*ca.* 3 nm, 50 wt%-Pt loading) were spread onto a carbon electrode. This electrode was placed in an originally designed electrochemical cell with 0.5 mol dm^{-3} H_2SO_4 electrolytes, and the potential of the electrode was controlled by an electrochemical analyzer. XAFS measurements were made in the transmission mode at beamlines **BL16B2** and **BL19B2**.

The results of *in situ* XAFS studies clearly showed the surface reconstruction and the formation of surface oxygen species in the ORR region (from 0.8 V to 1.2 V *vs.* reversible hydrogen electrode, RHE). As shown in Fig. 1, above 0.8 V *vs.* RHE, the amplitude of Fourier transforms that occur due to the interaction with the nearest neighbor Pt atoms significantly decreases, indicating that the surface is roughened by oxidation in this potential range. Simultaneously, the peak associated with Pt-O bonds appears and the amplitude increases upon increasing the potential.

Figure 2 shows the potential dependence of the interatomic distance and the coordination number

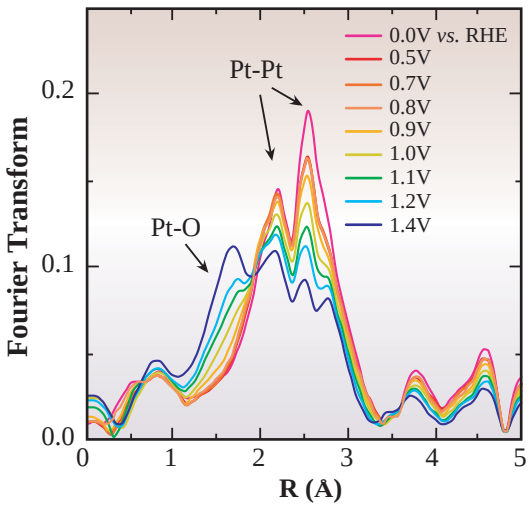

Fig. 1. Potential dependence of k^1-weighted Fourier transforms of Pt L_3 EXAFS.

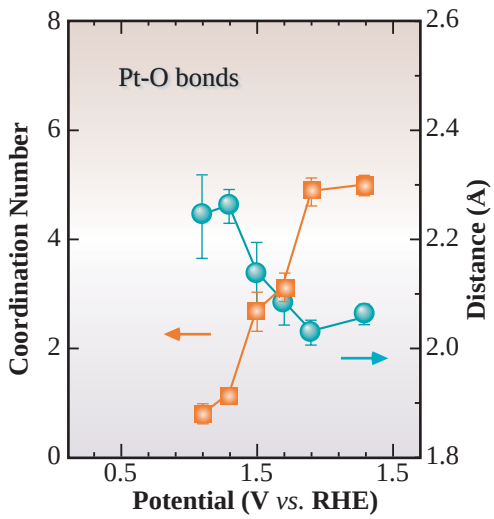

Fig. 2. Potential dependence of interatomic distance and coordination number.

(CN) for the surface Pt-O bonds. At 0.8 V, the Pt-O bond length is almost 2.3 Å and it gradually decreases and becomes 2.0 Å at 1.0 V. These oxygen-containing species can be assigned as waterlike Pt-OHH species and Pt-OH species at on-top sites, on the basis of comparison with theoretical studies [2-4]. Above 1.0 V, since the CN approaches three, which corresponds to the fully occupied hollow-site Pt-O bonds, the OH species gradually change to atomic oxygen at hollow sites and release protons. Above 1.2 V, the CN exceeds three. This indicates that some oxygen atoms go inside the surface and form amorphous oxides.

Considering the results described above, the surface structure of platinum in an aqueous system near the ORR potential regions are summarized and shown in Fig. 3. First, at 0.8 V, waterlike species begin to adsorb weakly on the surface. Then they change into Pt-OH species at on-top sites. Near 1.1 V, the OH species move to the hollow sites, and change to atomic oxygen. Finally, above 1.2 V, the amorphous oxides are formed on the surface.

Regarding the electronic properties of platinum nanoparticles, we can estimate the number of vacancies in the platinum 5*d* orbitals from the results of the analysis of the XANES spectra at L_3 and L_2 absorption edges. As shown in Fig. 4, the number of the vacancies is clearly correlated with the electrochemical reaction on the platinum surface. In the potential range from 0.8 V to 1.2 V, the number of vacancies slightly increases, indicating that charge transfer from platinum occurs to surface oxygen-containing species, and these adsorbates strongly adsorb on the platinum surface.

Since these surface OH species or atomic oxygen species block the adsorption of oxygen molecules, they may reduce the catalytic activity of platinum for ORR. The removal of such surface OH species would play a crucial role in improving the performance of catalysts.

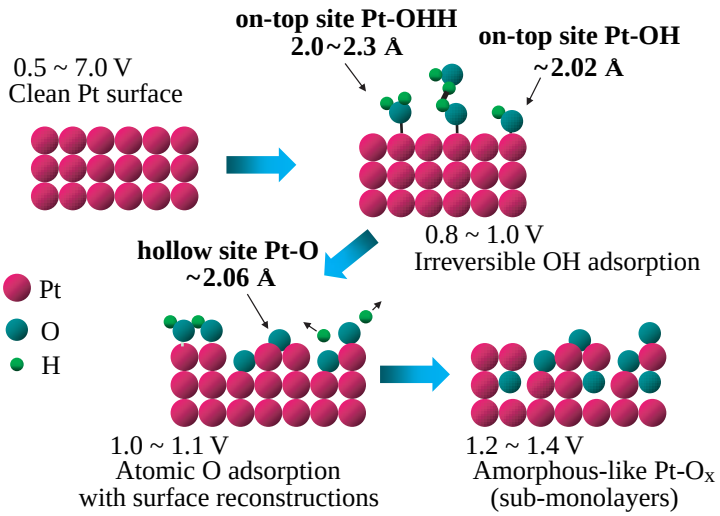

Fig. 3. The structural models for platinum surface near the ORR region.

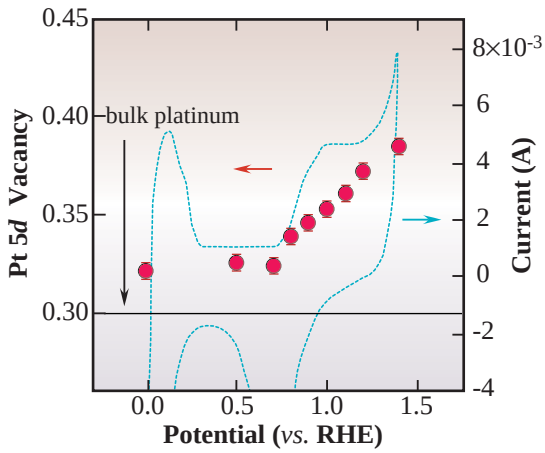

Fig. 4. Potential dependence of the number of vacancies in Pt 5*d* orbital. The dashed line shows the cyclic voltammetry for platinum nanoparticles supported on carbon in the same electrolyte.

Hideto Imai* and Koichi Izumi

Fundamental and Environmental Research Laboratories, NEC Corporation

*E-mail: h-imai@ce.jp.nec.com

References

[1] *H. Imai, K. Izumi and Y. Kubo - in preparation.*
[2] T. Jacob and W. A. Goddard: J. Am. Chem. Soc. **136** (2004) 9360.
[3] M. T. Koper *et. al.*: J. Phys. Chem. B **106** (2002) 686.
[4] T. Li and P. B. Balbuena: J. Phys. Chem. B **105** (2001) 9943.

Effect of Interfacial Layers on Stress Depth Profile of Ceramic Layers for Cutting Tools

Cemented carbide inserts with coatings of ceramic such as Al_2O_3, TiN and TiCN are widely used as cutting tools. In recent years, the speed of the cutting operation has been increased to improve the efficiency of the machining process. The high-speed operation results in high temperatures at the cutting edge and therefore causes large creep deformation of the cemented carbide substrate. The deformation enhances delamination of the coated film, which shortens the life of the tool. To prevent such delamination, it is known that reducing of the residual stress near the interface between the film and the substrate is effective [1,2].

The main component of residual stress in the CVD-deposited ceramic films is the thermal stress caused by the difference in the thermal expansion coefficient (TEC) between the film and the substrate. Figure 1 shows an example of a TiCN layer coated by a conventional CVD method. There is an interfacial layer (not visible in the SEM micrograph) between TiCN and WC. The typical material used for the interfacial layer is TiN, which has large TEC of 9.4×10^{-6} in comparison with the WC substrate. In this study a new interfacial layer of TiC was adopted as it has a lower TEC of 7.4×10^{-6}. The small TEC mismatch in the TiC interfacial layer system was expected to result in a low residual stress near the interface.

The stress depth distribution, however, cannot be revealed by a conventional residual stress measurement using a laboratory X-ray diffractometer. Therefore, a new measurement technique, which can yield a precise stress depth profile, is needed to elucidate the stress near the interface. We adopted a constant-penetration-depth method as it is less sensitive to preferred orientation, which is frequently observed in the case of thin film. This method is a combination of iso-inclination and side-inclination methods of the ordinary 2θ-$\sin^2\psi$ technique, wherein different ψ angles can be set without changing the X-ray penetration depth [3].

Stress depth profiles of the two TiCN layers schematically shown in Fig. 1 were measured using a multi-axis diffractometer at beamline **BL19B2**. A Soller slit and a sample spinner were employed to improve the 2θ resolution and to increase the number of crystallites that contribute to the diffraction, respectively. The energy of the incident X-ray was 11 keV. The TiCN (331) plane was used for the measurement.

Figure 2 shows the effect of controlling the X-ray irradiation area on the stress depth profile. The data acquired from a constant-irradiation area (fixed at 9 mmϕ) showed much lower scattering than that from a variable-irradiation area (varied from 4 to 10 mmϕ). This is attributed to a stress distribution in the TiCN layer towards the in-plane direction.

The obtained stress depth profiles are shown in Fig. 3(a). The sample with the TiC interfacial layer appeared to exhibit higher stress over the entire depth

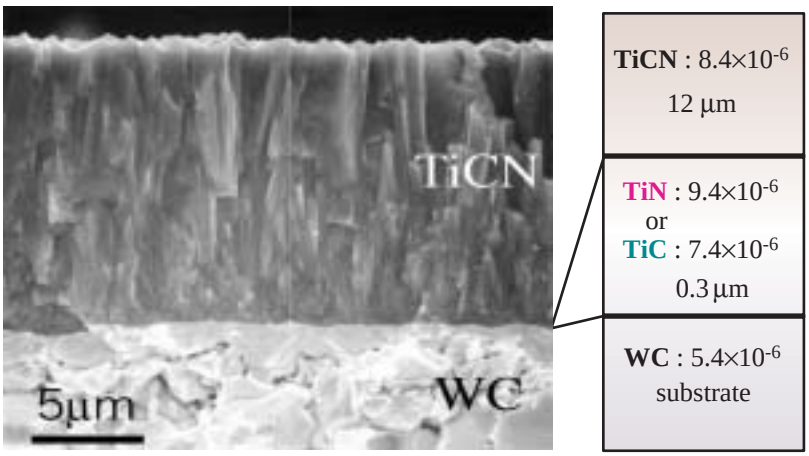

Fig. 1. Cross-section SEM image (left) and thermal expansion coefficient and thickness of each layer (right).

range. However, this was due to the peculiar axes of the plot, i.e., X-ray penetration depth on the horizontal axis and weighted average stress from the surface to the penetration depth on the vertical axis. Figure 3(b) shows the depth profiles with commonly used axes. The conversion was based on the fitting curves shown in Fig. 3(a).

The stress near the interface of the TiC layer is clearly lower than that of the TiN layer in Fig. 3(b). Chemical composition analysis using an Auger electron spectroscope and electron probe microanalyser showed no fluctuation through the entire film thickness for both TiCN layers. Hence the difference in the stress near the interface is ascribed to the TEC difference between the TiC and TiN interfacial layers.

In conclusion, a small mismatch in TEC at the interface is considered to be the major cause of the low stress near the interface. Hence the manipulation of TEC can be applied to control residual stress in cutting tools. The constant-penetration-depth method with a constant-irradiation area was effective for measuring the stress depth distribution.

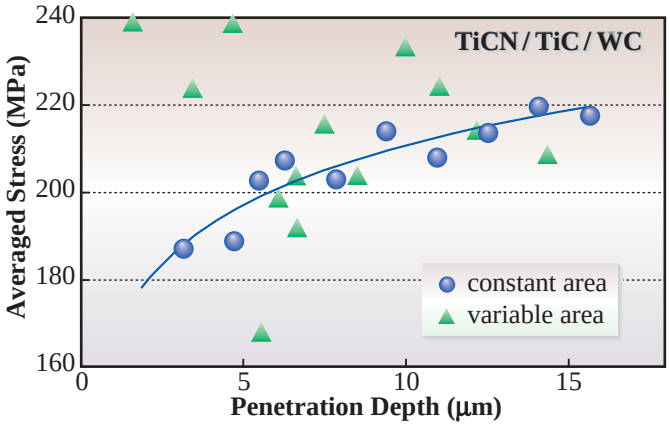

Fig. 2. Stress depth profiles of constant-irradiation area and variable-irradiation area. The sample and the diffraction plane are identical for both measurements.

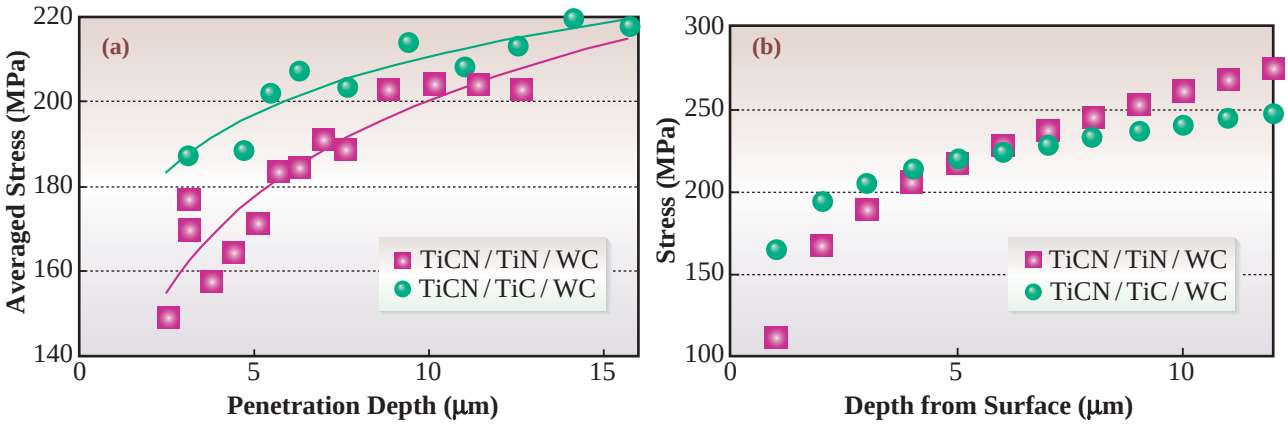

Fig. 3. **(a)** Experimental stress depth profiles of TiCN layers deposited on different interfacial layers. **(b)** Calculated depth profiles from fitting curves shown in **(a)**. Axes are converted from penetration depth to depth from surface and from averaged stress to stress at the depth, respectively.

Shin Tsuchiya

Mitsubishi Materials Corp.

E-mail: tsuchiya@mmc.co.jp

References

[1] Y. Fu *et al.*: Thin Solid Films **424** (2003) 107.
[2] H. Tönshoff *et al.*: Surface and Coatings Technology **142-144** (2001) 1100.
[3] *S. Tsuchiya, T. Oshika, F. Tsushima and A. Nishiyama: Trans. Mater. Res. Soc. Jpn.* ***29*** *(2004) 425.*

White X-ray Topography Combined with a Topo-tomographic Technique for Determining Three-dimensional Dislocation Structures in Silicon

A three-dimensional characterization of lattice imperfections in single crystals has often been required in X-ray topography studies. The topo-tomography technique, which was devised by Ludwig *et al.* [1] to analyze the configuration of individual dislocations, is extremely sophisticated. However, due to a lack of information regarding the image contrast, this technique is insufficient for determining the nature of individual dislocations, such as Burgers vectors and glide planes. Recently, we demonstrated that a combination of white X-ray topography and the topo-tomographic technique is a useful tool for the determination of the three-dimensional structure of the individual dislocations in silicon, i.e., the direction of the dislocation line, its Burgers vector and the glide plane [2]. The advantage of this method lies in its ability to acquire information regarding the configuration of the dislocations from the variation in their features observed in a specific Laue spot by the tomographic technique, in addition to information regarding the image contrast of the dislocations observed in several Laue spots by conventional white X-ray topography.

The production of large-scale integrated circuits in the future will require large-diameter Czochralski silicon crystals. Research and development of the crystal growth technology without Dash necking is required because the weight of a crystal with a diameter of 400 mm exceeds 400 kg. It is well known that dislocations are generated when the seed comes into contact with the melt, whereas the mechanism of the elimination of dislocations during the Dash necking process is still unclear [3].

In order to elucidate this mechanism, the determination of the three-dimensional structure of dislocations in the neck of a silicon crystal of 2-inch diameter, which was grown in the laboratory, was carried out at beamline **BL28B2** [4]. Figure 1 shows the experimental setup. The sample crystal was fixed, by positioning its growth axis [001] nearly parallel to the ω-axis, on the sample holder of the subsidiary goniometer that was mounted on the swivel stage of the main diffractometer.

On the basis of an *in situ* observation of the transmission Laue patterns, the orientation of the sample was adjusted such that the (100) plane was perpendicular to the incident X-ray beam, and the [010] orientation was horizontal. This angular position

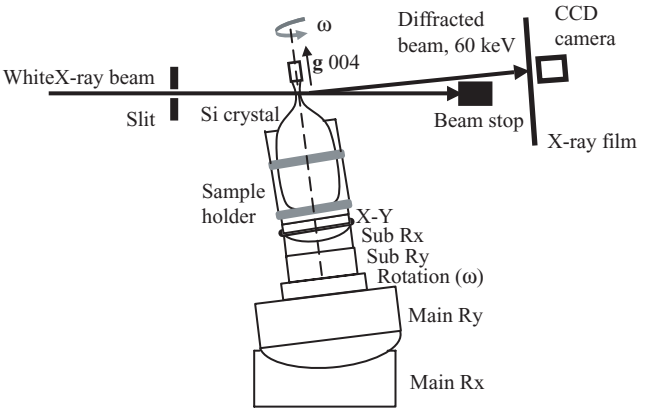

Fig. 1. Schematic illustration of the experimental arrangement. The subsidiary goniometer comprises a sample holder, and *x-y*, *Rx*, *Ry* and ω-rotation stages. Only the *Rx* and *Ry* swivel stages of the main diffractometer are drawn.

was designated as ω = 0º. Therefore, when ω = 45, 90 and 135º, the plane perpendicular to the incident X-ray beam corresponded to (110), (010) and $(\bar{1}10)$, respectively. The sample was inclined by 4.36º (Bragg angle), using the *Rx* stage of the main diffractometer, such that the 004 Laue spot could be formed by 60 keV X-rays. Finally, the growth axis [001] of the sample crystal was precisely adjusted so as to be parallel to the ω-axis. After the adjustment was completed, the 004 Laue spot was recorded, by rotating the ω-axis at intervals of 3º, onto the hard disk of a personal computer connected to a cooled CCD camera. In addition, several sets of Laue patterns were recorded on the X-ray films at ω-intervals of 45º.

The first step in the dislocation-structure analysis was to maintain a check on the variation in the features of individual dislocations owing to the ω-rotation, by reproducing their CCD images, in order to clarify the configuration of each dislocation and identify its images in the 004 spot obtained at ω = 0, 45, 90, and 135º. The second step was to determine their Burgers vectors from the variation in the contrast of their images in several Laue spots that were recorded on the X-ray film at each ω-angle. The final step was to fix glide planes on the basis of both the configuration of the dislocations clarified in the first step and the Burgers vectors determined in the second step.

The ω-dependence of the enlarged images in the

004 spot obtained from the neck region of the sample crystal is shown in Fig. 2(a). Dislocation half-loops as well as tangled dislocations are observed in these images. Figure 2(b) shows the enlarged images of the $\bar{1}\bar{1}1$, 111, $\bar{1}11$ and $1\bar{1}1$ spots. Five representative dislocations, designated as A, B, C, D, and E, were analyzed, and the results are summarized in Table 1 and Fig. 3. The present observation revealed that dislocation half-loops, which were generated from tangled dislocations formed near the interface of the seed and the grown crystal, were expanded on the {111} glide planes. The elimination of dislocations due to Dash necking was caused by the termination of the expansion of the dislocation half-loops inside the crystal and by pinning the dislocations on the crystal surface.

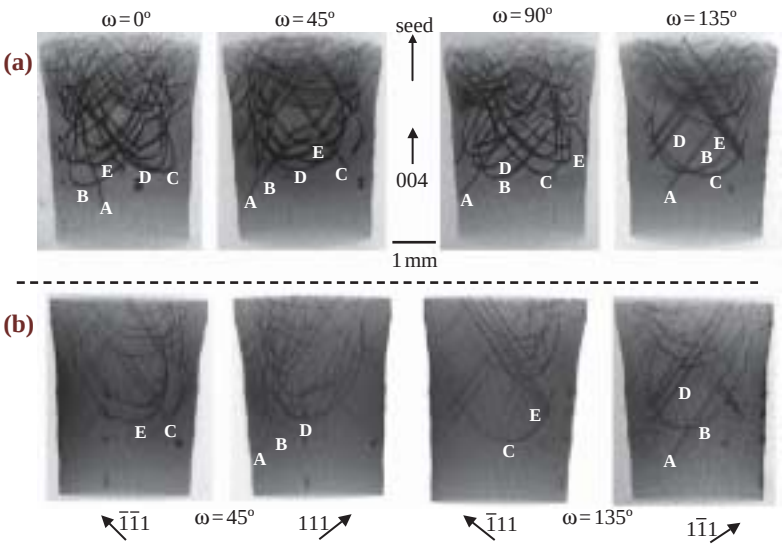

Fig. 2. **(a)** A series of enlarged images in the 004 spot obtained at ω = 0, 45, 90 and 135°. **(b)** Enlarged images of the $\bar{1}\bar{1}1$ and 111 spots obtained at ω = 45° and those of the $\bar{1}11$ and $1\bar{1}1$ spots obtained at ω = 135°.

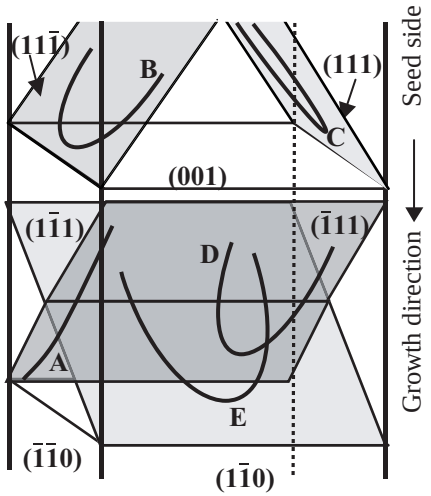

Fig. 3. Schematic illustration of dislocations designated as A, B, C, D and E. Dislocations A and D do not lie on the same ($\bar{1}$11) plane. Such a representation is adopted so as to avoid unnecessary complications.

Table 1. Identification of observed dislocations.

Dislocation image	shape	Laue spot invisible or weak		Burgers vector	Glide plane
A	straight	$\bar{1}\,\bar{1}\,1$	$\bar{1}\,1\,1$	**a**/2[1 0 1]	($\bar{1}$ 1 1)
B	curved	$\bar{1}\,\bar{1}\,1$	$\bar{1}\,1\,1$	**a**/2[1 0 1]	(1 1 $\bar{1}$)
C	curved	1 1 1	1 $\bar{1}$ 1	**a**/2[1 0 $\bar{1}$]	(1 1 1)
D	curved	$\bar{1}\,\bar{1}\,1$	$\bar{1}\,1\,1$	**a**/2[1 0 1]	($\bar{1}$ 1 1)
E	curved	1 1 1	1 $\bar{1}$ 1	**a**/2[1 0 $\bar{1}$]	(1 $\bar{1}$ 1)

Seiji Kawado[a,*], Satoshi Iida[b] and Yoshinori Chikaura[c]

(a) X-Ray Research Laboratory, Rigaku Corporation
(b) Faculty of Science, Toyama University
(c) Graduate School of Engineering, Kyushu Institute of Technology

*E-mail: kawado@rigaku.co.jp

References

[1] W. Ludwig *et al.*: J. Appl. Cryst. **34** (2001) 602.
[2] S. Kawado *et al.*: J. Synchrotron Rad. **11** (2004) 304.
[3] Y. Wang and K. Kakimoto: J. Crystal Growth **247** (2003) 1.
[4] *S. Kawado, T. Taishi, S. Iida, Y. Suzuki, Y. Chikaura and K. Kajiwara: J. Phys. D: Appl. Phys.* ***38*** *(2005) A17.*

Observations of RAF - SiC Single Crystals by Synchrotron X-ray Topography

Silicon carbide (SiC) is one of the promising semiconductor materials for next generation ultralow-loss and high-power electrical devices. However, SiC crystals still have a large number of crystal defects. One type of defect is macroscopic, such as micropipes and small-angle boundaries, and another type is elementary dislocations and stacking faults which are microscopic defects. It has already been reported that the former may adversely affect the electrical characteristics of SiC devices. Recently, the latter defects have also been suggested to be similarly harmful [1]. These defects have so far prevented the realization of high-efficiency, reliable electronic devices with SiC. An improvement of crystal quality is found to be indispensable for the realization of practical SiC devices.

We reported a method [2], the RAF (repeated a-face) growth process, designed to reduce the number of crystal defects in SiC single crystals. The aim of this research is to evaluate the crystal quality of RAF-SiC substrates by synchrotron X-ray topography. The identification of the types of crystal defects is important for the realization of practical SiC devices. X-ray topography is known to be the most effective nondestructive technique for large-area evaluation of defects in single crystals.

We used two in-house-fabricated 4H-SiC (0001) wafers as specimens. One is an ultrahigh-grade substrate, 4H-SiC (0001), 8 degrees off-axis, 2 inches in diameter, manufactured by the RAF process. The other is a conventional-grade substrate, 4H-SiC (0001), on-axis, 1.2 inches in diameter.

The synchrotron X-ray topography experiments were conducted at the second experimental hutch at beamline **BL20B2** [3,4]. In the experimental hutch, we can employ the horizontal-wide and monochromatic X-ray beam because of the distance from the bending magnet light source to the experimental hutch is as long as 200 m. Furthermore, the beamline is highly suitable for the X-ray topography experiment because the spatial distribution of the X-ray intensity is homogeneous. We performed topographic observations by means of the surface-sensitive method, which is the Berg-Barrett arrangement with a small glancing angle of 1 degree. The energy of the X-ray was tuned to 11.94 and 9.86 keV for the RAF substrate and for the conventional substrate, respectively, in order to obtain topographs using asymmetric reflection of $11\bar{2}8$ while maintaining the glancing angle of 1 degree. The X-ray penetration depths from the sample surface are estimated to be about 4 μm, and 2 μm, respectively. The topographs were recorded on nuclear plates at a high resolution.

The two topographs of SiC substrates, obtained by continuous scan of glancing angle, are shown in Fig. 1. Figure 1(a) shows that the crystal quality of the RAF

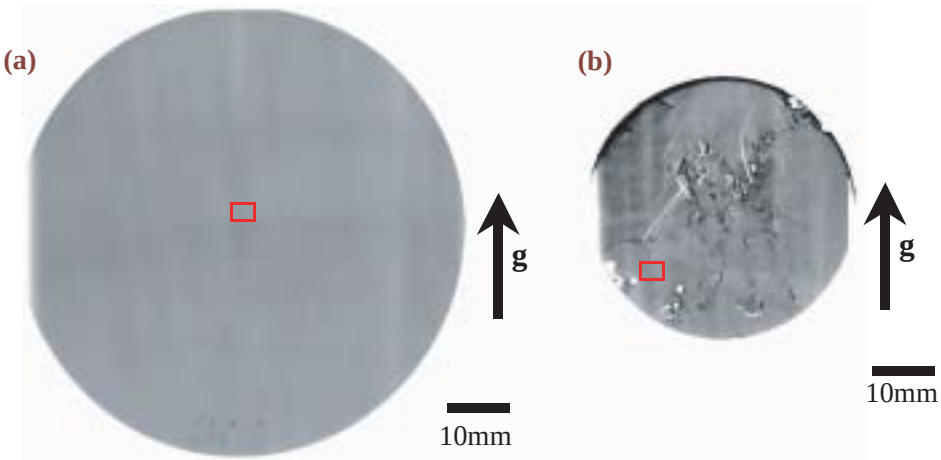

Fig. 1. X-ray topographs of the RAF SiC substrate **(a)** and the conventional substrate **(b)**, taken with the asymmetric reflection. The arrow indicates the diffraction vector **g** [2].

substrate is very homogeneous. Very few macroscopic or microscopic defects are seen in the enlarged image of the topograph (Fig. 2(a)). On the other hand, as shown in Fig. 1(b), the conventional substrate has many macroscopic defects, such as micropipes and small-angle boundaries. Many microscopic defects can also be seen in Fig. 2(b). In this enlarged topograph, two different kinds of dislocations are observable: screw dislocations and basal plane dislocations. The dots correspond to the screw dislocations running almost parallel to the c-axis, i.e., perpendicular to the sample surface. The basal plane dislocations, the dislocation lines of which lie in the basal plane, have the white or black arch-shaped features, and form dislocation networks. In Fig. 2(b), more basal plane dislocations are observed, although the observation depth for the RAF substrate is shallower than that for the conventional substrate. Clearly, the crystal quality of the RAF substrate is much better than that of the conventional substrate.

In summary, synchrotron X-ray topography has revealed that the RAF method can yield ultrahigh-quality SiC single crystals. The macroscopic defects can be eliminated completely and the microscopic defects can be reduced considerably. Consequently, these substrates will promote the development of high-power SiC devices and the reduction of energy losses of the resulting electrical systems.

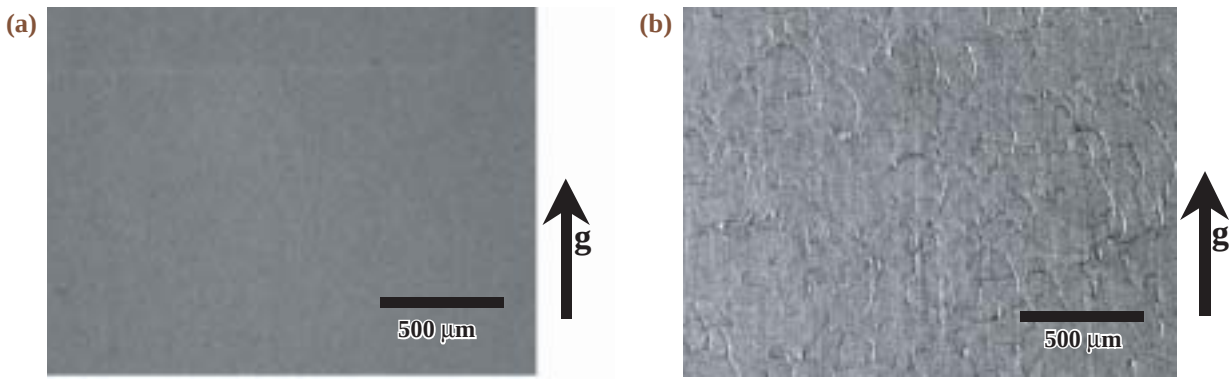

Fig. 2. The enlarged images of the regions indicated in Fig. 1. The arrow indicates the diffraction vector **g** [2].

Satoshi Yamaguchi*, Daisuke Nakamura and Yoshiharu Hirose

Toyota Central R&D Laboratories, Inc.

*E-mail: e1238@mosk.tytlabs.co.jp

References

[1] P.G. Neudeck *et al.*: Solid State Electronics **42** (1998) 2157.
[2] *D. Nakamura, I. Gunjishima, S. Yamaguchi, T. Ito, A. Okamoto, H. Kondo, S. Onda and K. Takatori: Nature **430** (2004) 1009.*
[3] Y. Chikaura *et al.*: J. Phys. D: Appl. Phys. **34** (2001) A158.
[4] S. Kawado *et al.*: SPring-8 Research Frontiers **1999/2000** (2001) 89.

Mechanism of Curing Reaction for Polymer-modified Cement Waterproofing Membrane

Recently, with the demands for material properties becoming more complex and severe for waterproofing applications, polymer-modified cement materials which consist of a polymer emulsion and cement materials, have been widely developed for building materials fields for roofs, balconies and underground outer walls, for example. Figure 1 shows photographs of polymer-modified cement materials. After mixing polymer emulsion and cement powder, the viscous polymer-modified cement paste was applied to a thickness of 1-2 mm onto the concrete, followed by drying and curing. By this process, a polymer-modified cement-waterproofing membrane was obtained. This organic/inorganic composite product possesses the characteristics of both toughness from the cement materials and flexibility and adhesiveness from the polymer emulsion. Therefore, the material properties can be controlled by changing the polymer/cement mixing ratio. Furthermore, in order to satisfy the demand for high-performance materials, not only the material properties but also workability, such as shortening of the construction period, is increasingly required.

The formation process of the polymer-modified cement membrane at ambient temperature involves simultaneous evaporation of water within the polymer emulsion and curing of the cement. The curing process is the hydration reaction of alumina cement, which is already known as the reaction formula [1,2]

$$CA + H \rightarrow C_3AH_6 ,$$

where C = CaO, A = Al_2O_3 and H = H_2O. To successfully obtain the polymer-modified cement material it is important that the hydrate crystal of cement is generated by the hydration reaction during the curing process with the existence of the polymer emulsion. In this study, the mechanism of the curing reaction of the polymer-modified cement paste was investigated by X-ray diffraction (beam size of 0.3 mm (V) × 3 mm (H), wavelength 1 Å, X-ray exposure time 900 s) at beamline **BL19B2** using the Debye-Scherrer camera.

In order to obtain good mechanical properties, excellent thermal resistance and high chemical resistance, alumina cement was used as the cement material. The sample was alumina cement and polymer emulsion mixed in the polymer/cement ratio

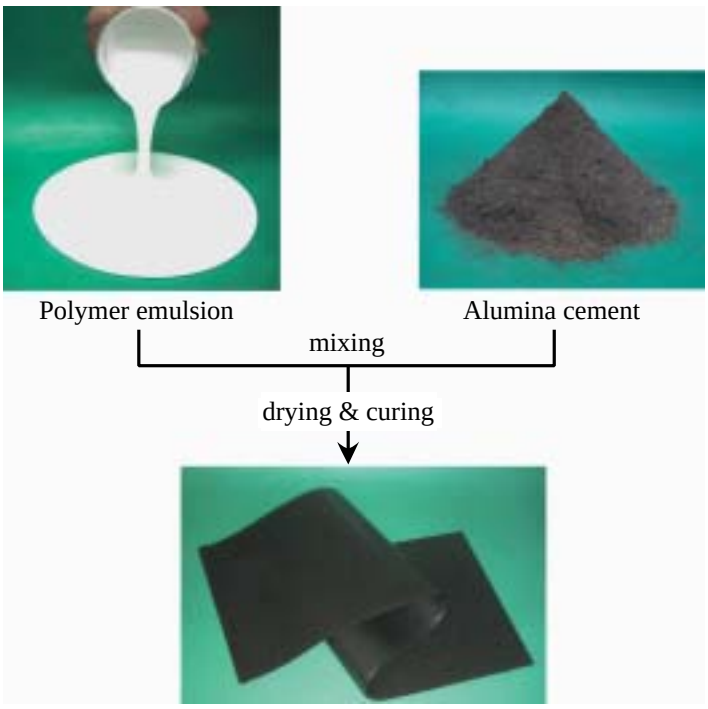

Fig. 1. Photographs of polymer-modified cement materials.

of 100%. After mixing, the sample was wrapped with Mylar film in order to prevent drying. Figure 2 shows the X-ray diffraction profiles of the polymer-modified cement membrane before and after curing at ambient temperature. The diffraction peaks of calcium aluminate (CA) almost disappeared after curing. On the other hand, the peaks of hydrate crystals of alumina cement, such as C_2AH_8 and C_3AH_6, could be observed at diffraction angles 2θ=5.3 and 11°, respectively. After curing, a tough and flexible polymer-modified cement membrane was obtained in spite of preventing water evaporation. This polymer-modified alumina cement paste underwent a hydration reaction during the formation of the membrane. This implies that the water within the polymer emulsion participates in the hydration reaction of the cement during the curing process.

Figure 3 shows the temporal changes of the conversion to hydrate crystals of alumina cement. With curing time, the amount of CA (■) decreased, and the amount of the alumina hydrate (C_2AH_8 (●) and C_3AH_6 (○) increased. This means that the hydration reaction of CA occurred during the forming process of the polymer-modified cement membrane. The hydration reaction to form C_2AH_8 from CA began at around 300 min and was almost completed at 700 min. Thereafter, the amount of C_2AH_8 hydrate exceeded 100% once and then decreased gradually, and the amount of C_3AH_6 hydrate increased. The C_2AH_8 hydrate is in the form of unstable hexagonal crystals. This implies that the crystal transition from C_2AH_8 to C_3AH_6 occurred to form the more stable phase.

Accordingly, stable hydrate crystals of C_3AH_6 were obtained by the hydration reaction of calcium aluminate through the crystal transition of the unstable C_2AH_8 even with the coexistence of the polymer emulsion. That is, it is thought that the alumina cement was cured via the consumption of the water within the polymer emulsion, and the polymer-modified cement materials formed a thick film.

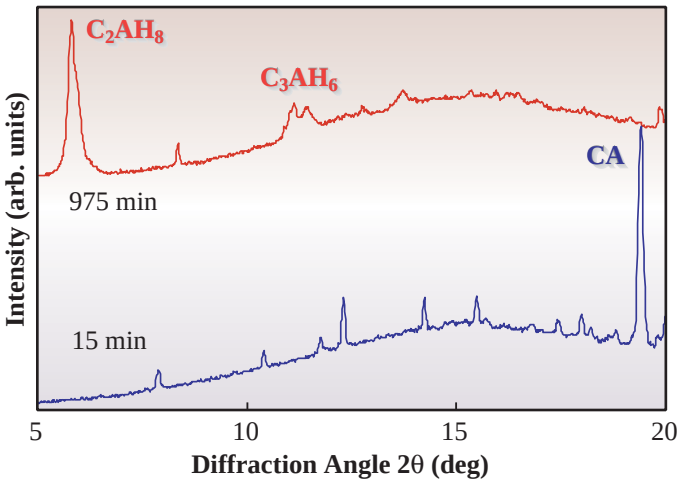

Fig. 2. X-ray diffraction profiles of polymer-modified cement membrane before and after curing.

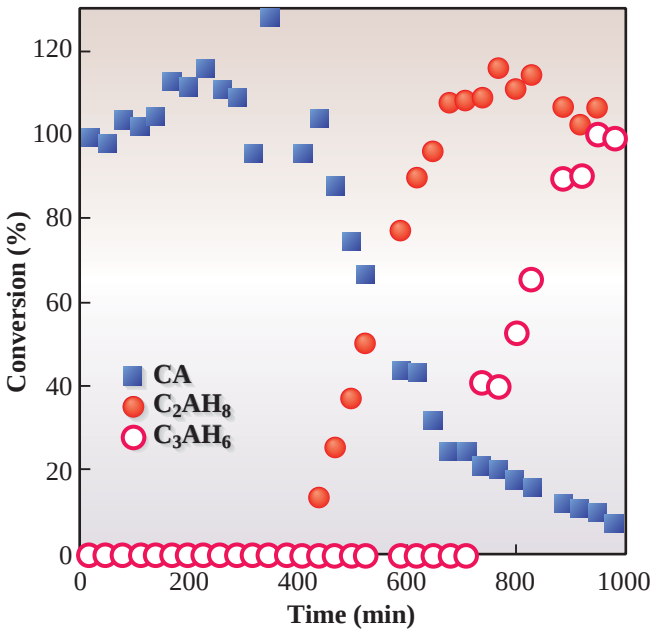

Fig. 3. Relationship between the conversion of hydrate crystals and the curing time.

Masaru Kotera[a,*], Ikuyo Matsuda[b] and Keiko Miyashita[b]

(a) SPring-8 / JASRI
(b) Ozeki Chemical Co., Ltd.

*E-mail: mkotera@spring8.or.jp

References

[1] S. Koide and K. Mishima: Ceramics Jpn. **4** (1969) 36.
[2] P. Barnes *et al.*: J. Synchrotron Rad. **7** (2000) 167.

In Situ High-Resolution X-ray Tomography of Fracture Micromechanisms in Aluminium Foam

Aluminium foam is an attractive engineering material that offers potential-energy-absorption capacity during deformation, which is useful for efficient crash-energy management. Figure 1 shows the typical cell structure of aluminium foam. The typical cell size is a few mm, which is unusually coarse for practical structural materials, while the cell wall is sometimes less than 50 μm thick. Such a unique combination of "macro" (i.e., coarse cell structure) and "micro" (i.e., membrane) features makes a mechanistic approach difficult. In particular, the thin cell wall amplifies the effects of the internal microstructure due to the small membrane thickness/microstructural dimension ratio. However, despite the fact that cell materials exhibit microstructural features far more inhomogeneous than these of their dense equivalent, quite a few reports are available in the literature, of the qualitative observation of the 2D microstructural features. X-ray tomography has been used at low-resolution levels which are more than one to two orders of magnitude coarser than the microstructures due to the coarse cell structures.

In this study, high-resolution phase contrast imaging technique achieved at SPring-8 is applied. A combination of several state-of-the-art characterization techniques then enables 3D quantitative image analyses of the microstructures together with the interpretation of deformation and fracture behaviors. The application techniques include the liquid metal wetting technique to visualize microstructural features well below the resolution level, local-area tomography by which large specimens can be visualized at high magnification, and a microstructural gauging technique by which 3D local strain is mapped by tracking microstructural features.

Fig. 1. Tomographic image of typical aluminium foam.

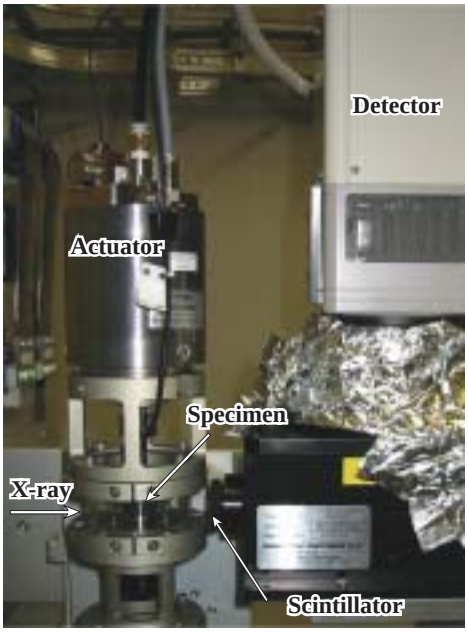

Fig. 2. The test rig specially designed for tomographic *in situ* observations in the experimental hutch.

High-resolution X-ray tomography was performed at beamlines **BL20B2** and **BL47XU**. Monochromatic X-ray beams having a photon energy of 20 keV from double-crystal monochromators were used. Cooled 1000×1018-element or 4000×2624-element CCD detectors were positioned 50 mm behind samples, thereby making the imaging systems sensitive to phase modulation. Isotropic voxels with a 0.5 μm edge at maximum were achieved in the reconstructed slices. *In situ* compression tests were performed using the material test rig shown in Fig. 2, which was specially designed for the CT at SPring-8.

Owing to the superlative optical setup, the microstructural features, such as micropores, intermetallic particles and solute atom segregation, could be clearly visualized. Since the images of virtual slices are as distinct and offer similar detail as a high-magnification optical microscope image, 3D quantitative image analysis (such as center of gravity, volume, surface area, etc.) was readily performed using the Marching Cube algorithm. The 3D distribution of micropores within a rendered cell wall is shown in

Fig. 3. A large number of micropores is observed in the volume. A point to note is that the coarse micropores tend to lie on periodic lines, suggesting a characteristic solidification pattern during its production process, probably due to the lack of sufficient nuclei for solidification. A characteristic crystallographic structure was also revealed by the liquid metal wetting technique, indicating that single-crystal membranes of a few hundred micrometers in width are patched up two-dimensionally to form each cell wall.

Sequential observations of static deformation behaviors have revealed the contribution of each microstructural feature to the overall fracture. Centroid locations for each micropore were tracked as a function of applied strain in the sequential tomographic scans, thereby allowing us to estimate the local strain distribution in the cell materials, as shown in Fig. 4. As such, high-density mapping with micrometer-level resolution has been realized by the procedure as was previously demonstrated by the present authors [1,2]. Locally inhomogeneous strain distribution was found, due particularly to the existence of underlying coarse micropores, which can be readily observed in the rendered 3D images.

In summary, it has been clarified that the microstructures are highly inhomogeneous in the aluminium foam compared to solid materials. Some of the microstructural features are unlikely to have any influence on fracture, while some of them provide premature fracture initiation sites. The results clearly provide a microstructural design concept to enhance the energy absorption capacity.

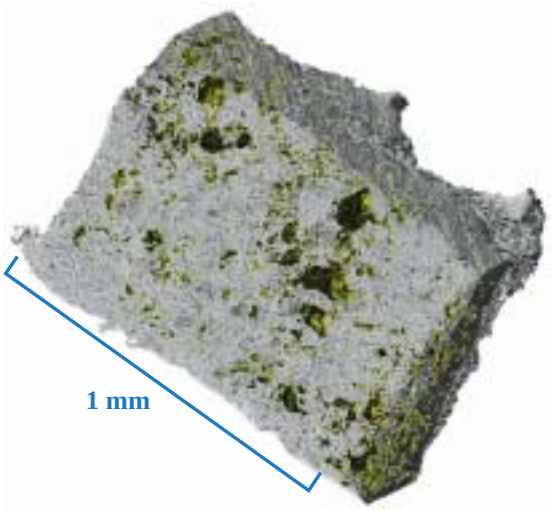

Fig. 3. A 3D rendered perspective view, representing micropore distribution superposed on the surface contour of a cell wall. Aligned coarse micropores indicate the solidification pattern of the cell wall.

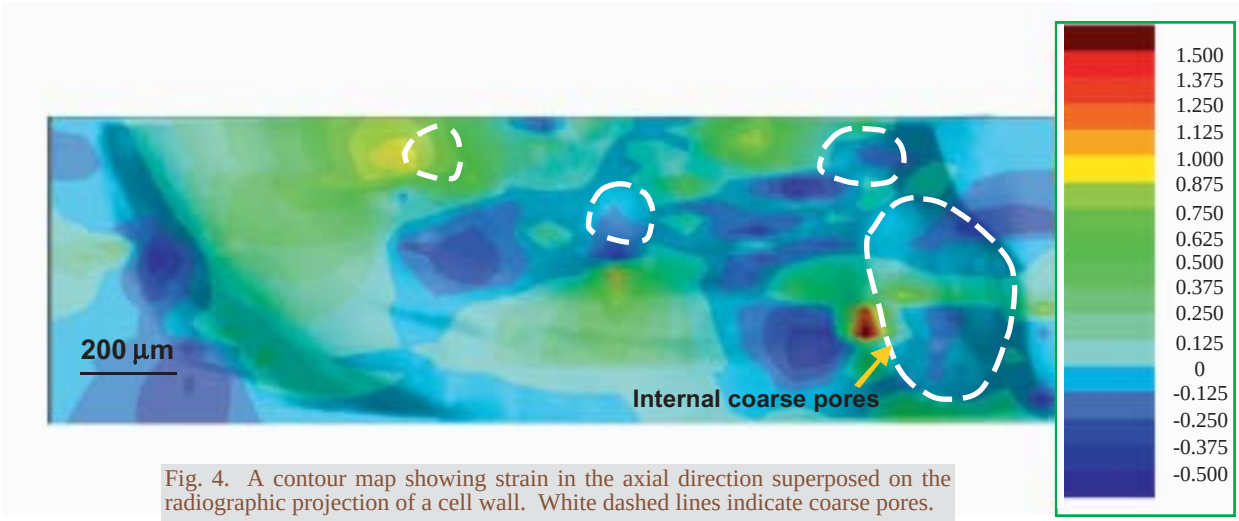

Fig. 4. A contour map showing strain in the axial direction superposed on the radiographic projection of a cell wall. White dashed lines indicate coarse pores.

Hiroyuki Toda [a,*], Tomomi Ohgaki[a] and Kentaro Uesugi [b]

(a) Dept. of Production Systems Engineering, Toyohashi University of Technology
(b) SPring-8 / JASRI

*E-mail: toda@tutpse.tut.ac.jp

References

[1] H.Toda *et al.*: Phil. Mag. A **83** (2003) 2429.
[2] *H. Toda, I. Sinclair, J.-Y. Buffiere, E. Maire, K.H. Khor, P. Gregson and T. Kobayashi: Acta Mater.* ***52*** *(2004) 1305.*

Instrumentation & Methodology

The development of new science is strongly related to the development of new experimental techniques or new instrumentations. High quality synchrotron radiation from SPring-8 has opened many new scientific fields. In this section, some of new instrumentation and methodology developed at SPring-8 are introduced.

The development of high quality diamond is required to provide high quality beams without sacrificing the high performance of the synchrotron radiation. Large synthetic IIa diamonds show a high quality with nearly intrinsic rocking curve widths. On the other hand, the evaluation of beryllium windows that limit the unique coherence of beams continues and a physical-vapor-deposited foil gave highly uniform beams compared with other conventional beryllium foils. These developments will open the door for the utilization of more highly coherent SASE FEL beams.

A novel hard X-ray micro-interferometer of the wavefront-division type has been developed using optics for an imaging microscope. The image of polystylene microparticles was clearly observed with a spatial resolution of 160 nm. Further improvement is expected with the development of optical elements.

Arbitrarily polarized X-ray beams were provided by a rotating four-quadrant phase-retarder system and polarization-dependent six-beam pinhole topographs were taken. The experimental topograph images agreed well with the simulated ones derived from the n-beam dynamical diffraction theory. A Sc/Cr multilayer was developed and applied as a phase plate in the soft X-ray region. It showed good performance as a polarizer and potential for use in a quarter-wave plate.

Masaharu Nomura

Characterization of Synthetic IIa Diamonds for Third and Fourth Generation X-ray Sources

Diamond has been expected as a good candidate for optical elements in synchrotron radiation science because of their superior thermal and optical properties, i.e., a low linear thermal expansion coefficient, a high thermal conductivity, and a low X-ray absorption. However, the use of diamonds is limited than has been expected. Most high-heat-load monochromators are still using silicon crystals rather than diamonds, because the available quality and size of diamonds are believed to be insufficient.

The needs for perfect diamonds may be more serious for forthcoming self-amplified spontaneous emission free-electron-laser (SASE FEL) sources, such as SCSS at SPring-8 [1], which will deliver FEL pulses with a huge peak power of several gigawatts. Although the average power is easily manageable, the peak energy dose to the optical elements will be close to the melt limit for most materials, e.g., the melt limit of silicon is estimated to be 0.4 eV/atom [2] and the peak energy dose is calculated to be 0.1 eV/atom for 6 keV FEL beams at SCSS. Only low-Z materials, such as Li, Be, B, and C, can be used due to their smaller photoionization cross sections. Considering the preservation of the high spatial coherence of the FEL beams, perfect diamond crystals should be a unique solution.

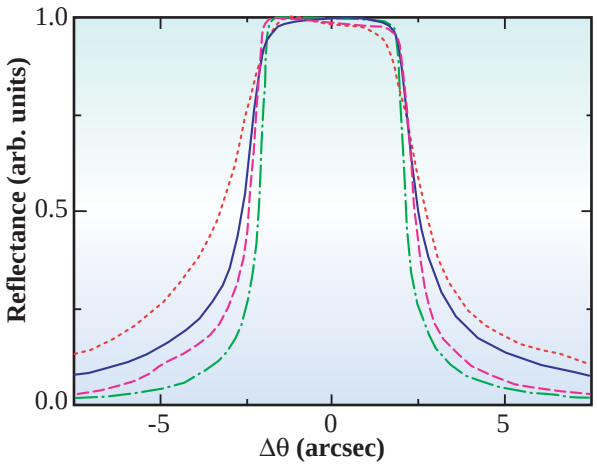

Fig. 1. Rocking curves of the 111 reflection in the reflection geometry for samples 1 (dotted line) and 2 (solid line) measured on the entire surface, sample 2 with a beam size of 0.5×0.5 mm^2 (broken line), and the theoretical curve calculated using the DuMond diagram (dot-dashed line).

We characterized (111) synthetic IIa diamonds at the 1-km beamline **BL29XU** [3]. These crystals were synthesized by Sumitomo Electric Industries Ltd. under high pressure and high temperature conditions [4]. The as-cleaved surface had a sufficiently large area (more than 7×4 mm^2) for the monochromators.

Figure 1 shows the rocking curves of the 111 reflection in the reflection geometry of two samples, i.e., samples 1 and 2. Both the rocking curves measured on the entire surface showed narrow widths comparable to the theory, indicating a high crystalline perfection. The rocking curve of sample 2 almost agreed with the theoretical curve for a smaller beam size (0.5×0.5 mm^2). However, the width of the rocking curve depended slightly on the type of sample. When we compared quasi-plane wave topographs, sample 1 was found to include more defects, especially stacking faults, than sample 2 (Fig. 2). The width of the rocking curve seems to be related to the defect density.

To confirm such a relationship, we performed reciprocal space mapping. The 111 reciprocal space point of sample 1 did not spread uniformly, but was characterized by two strong streaks (Fig. 3(a)), which broadened the rocking curve. From a geometrical consideration, we found that the streak denoted as S1 is directed towards the projection of [1-11] and S2 is the projection of [11-1]. The findings that S1 was not observed and S2 showed an interference effect for sample 2 (Fig. 3(b)) indicate that the <111> streaks originated from {111} stacking faults and not from the rough surface formed by cleavage.

We then investigated the crystal of high quality, sample 2, using the quasi-plane wave topograph (Fig. 2(b)). Two or three sets of stacking faults, many outcrops of dislocations (black spots), several surface scratches (black lines), and several dark streaks were observed. Such contrast was the origin of the broadening of the rocking curve. The dark streaks that extended from the lower part near the seed crystal were not isolated defects, such as dislocations, but were considered as strain bands. We detected small amounts of Fe and Co by scanning fluorescent X-ray analysis. These impurities included in the early stage of crystal growth were considered as the origin of the dark streaks.

In conclusion, synthetic type IIa diamonds of sufficient quality and dimensions for the high-heat-load monochromators at the third generation facilities are now available, when one selects crystals with a lower stacking fault density and uses a nearly defect-free area. Further reduction in defect density is desired for the future use of diamonds under fully spatial coherent radiation from SASE FEL.

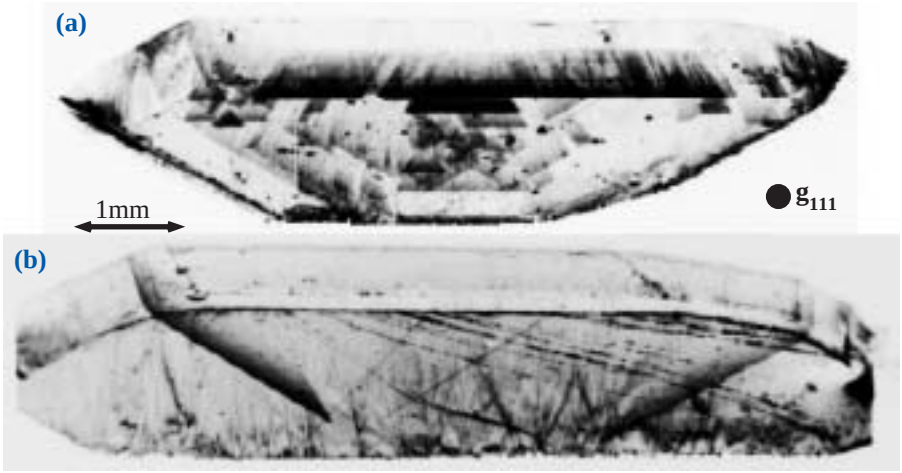

Fig. 2. Reflection topographs with the 111 reflection of samples 1 **(a)** and 2 **(b)** measured at the lower tail of the rocking curve.

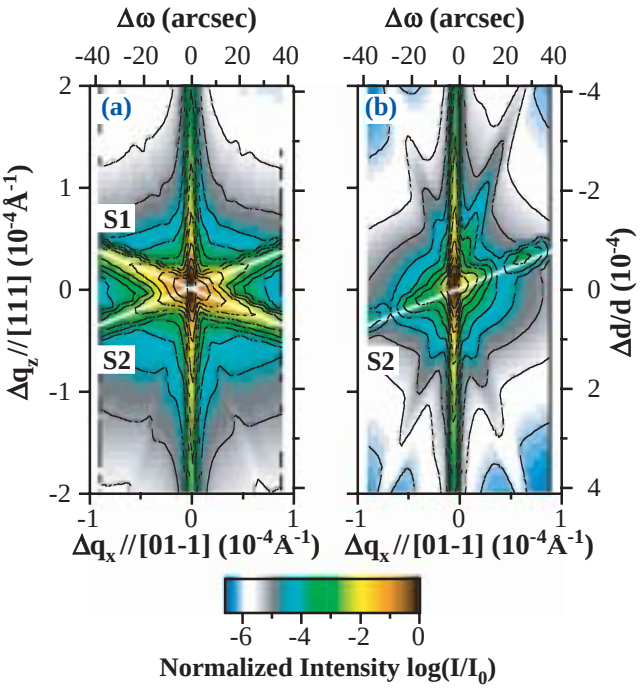

Fig. 3. Reciprocal space maps of samples 1 **(a)** and 2 **(b)** within the [111]-[01-1] plane around the 111 reciprocal space point.

Kenji Tamasaku

SPring-8 / RIKEN

E-mail: tamasaku@spring8.or.jp

References

[1] T. Shintake *et al.*: AIP Conference Proc. **705** (2003) 117.
[2] J. Arthur *et al.*: Linac Coherent Light Source (LCLS) Conceptual Design Reportt SLAC-R-593 (Stanford: SLAC).
[3] *K. Tamasaku, T. Ueda, D. Miwa and T. Ishikawa: J. Phys. D: Appl. Phys.* ***38*** *(2005) A61.*
[4] N. Toda *et al.*: Proc. SPIE **3151** (1997) 329.

Characterization of Beryllium Windows using Coherent X-rays

Beryllium foils are widely used as extracting windows at the end of hard X-ray beamlines, detector windows, and entrance windows of a vacuum chamber for some X-ray applications, because of their high X-rays transmittance and ultrahigh vacuum compatibility. However, an increase in non-uniformity, speckles at transmission images, and serious deterioration of spatial coherence due to surface roughness and defects have been pointed out [1-3]. Using spatially coherent X-rays at the 1-km beamline, we found that speckles (bright X-ray spots) are due to Fresnel diffraction from surface pits and presumably from internal voids in beryllium foils that are fabricated by conventional foiling processes [4]. Our objectives in this work are to characterize several types of beryllium in foiling and obtain a high quality beryllium foil for coherent X-ray applications.

Several commercially available beryllium foils were examined. A powder foil (sample #1) was produced by hot isostatically pressing of beryllium powders. An ingot foil (sample #2) was produced by hot rolling of the beryllium ingot, which was cast from a vacuum-melted and refined flake. A physical-vapor-deposited (PVD) beryllium foil (sample #3) was also characterized. The surface roughness was set to be less than 0.1 μm rms by polishing. The thickness ranged from about 100 to 250 μm.

We carried out the experiments at the 1-km beamline **BL29XU** with spatial coherence area (FWHM) of 0.14 mm in the horizontal direction and 5.9 mm in the vertical direction for 0.1-nm X-rays. The geometrical spatial resolutions (FWHM) at a sample-to-detector distance of 1 m are 0.68 μm in the horizontal direction and 17 nm in the vertical direction. We performed high spatial resolution experiments using the coherent beams at the beamline. We guided the 0.1-nm X-rays through the long transport channel to the 1-km end station. We used a Kapton window at the end of the 1-km beamline. A Hamamatsu zooming tube C5333 with a spatial resolution of 0.3 μm was used to obtain transmission X-ray images. We observed the images of the sample placed 90 mm (near image) or 1400 mm (far image) away from the detector.

Figure 1 shows the X-ray images of three samples under near- and far-image conditions. We found bright X-ray spots in samples #1 and #2 due to Fresnel diffraction from deficiencies. We picked up typical X-ray spots from far images as shown by blue circles in the images and compared with the results of

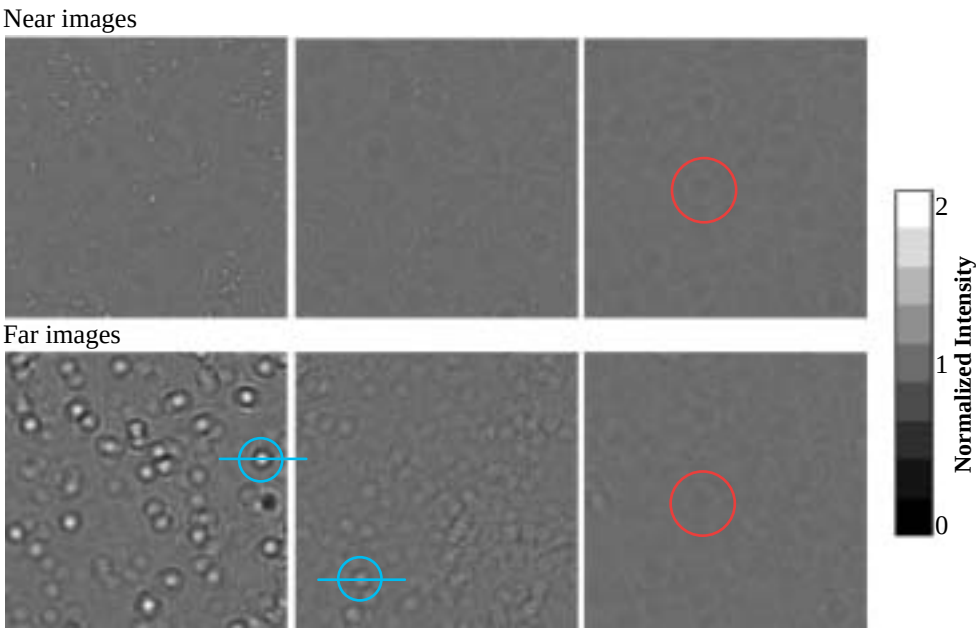

Fig. 1. X-ray images of sample #1 (left), sample #2 (center), and sample #3 (right). Upper panels: near images (distance 90 mm); lower panels: far images (1400 mm). The area is 300×300 μm^2. Dark spots such as indicated by red circles come from a Kapton window 3 m upstream of the detector, because they do not show distance dependence.

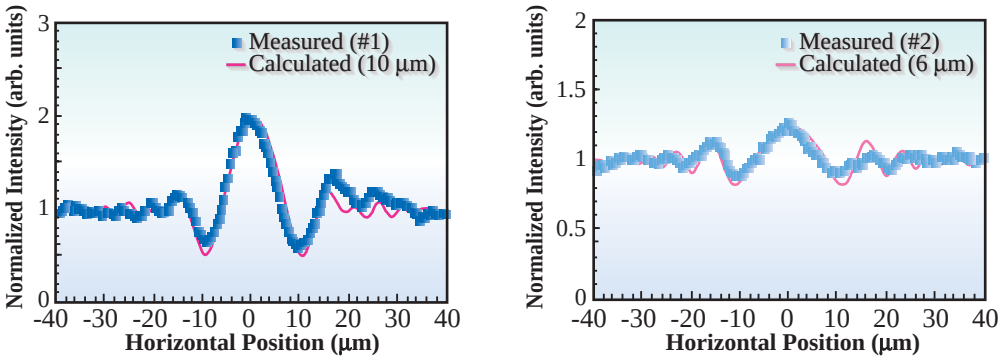

Fig. 2. Comparison of measured intensities at typical X-ray spots indicated by blue circles in Fig. 1 with calculation of Fresnel diffraction from spherical voids of 10 μm diameter for sample #1 and of 6 μm diameter for sample #2.

Fresnel diffraction calculation by assuming spherical voids in the beryllium. The measured intensity distributions are well reproduced by calculation, assuming several to ten microns of voids as shown in Fig. 2.

We counted X-ray spots as a function of beryllium thickness to clarify that defects are not only surface pits but also internal voids. We used wedged beryllium foils and changed the thickness from 0.2 mm to 1 mm. Figure 3 shows X-ray spot densities as a function of beryllium thickness. The distance between beryllium and the zooming tube was set to be 200 mm to obtain near images. The densities are proportional to the thickness for both samples #1 and #2. The thickness dependence of defect density suggests strongly that the defects are inside the beryllium foils. We estimated the defect densities of 5×10^3 mm^{-3} for sample #1 and 6×10^3 mm^{-3} for sample #2.

Compared with samples #1 and #2, the PVD foil (#3) yields highly uniform beams after the transmission of the window, as shown in Fig. 1. The PVD process eliminates the internal voids in principle and the PVD foil is considered to be the best material for coherent X-ray applications.

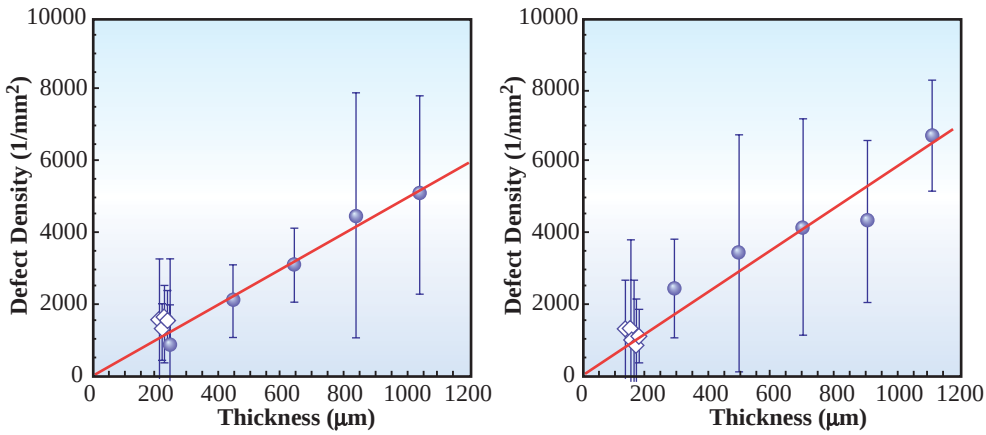

Fig. 3. X-ray spot densities as a function of beryllium thickness. Left: sample #1, right: sample #2.

Shunji Goto

SPring-8 / JASRI

E-mail: sgoto@spring8.or.jp

References

[1] A. Snigirev *et al.*: Nucl. Instrum. Meth. A **370** (1996) 634.
[2] Y. Wang *et al.*: J. Synchrotron Rad. **7** (2000) 209.
[3] I.K. Robinson *et al.*: Physica B **336** (2003) 56.
[4] *S. Goto, M. Yabashi, K. Tamasaku, S. Takahashi and T. Ishikawa: AIP Conference Proc.* ***705*** *(2004) 400.*

High Spatial Resolution Phase Measurement by Micro-interferometry using a Hard X-ray Imaging Microscope

Owing to the highly brilliant undulator radiation in third generation synchrotron radiation facilities, a much higher coherence than ever is available even in the hard X-ray region, and thus, many kinds of X-ray optics requiring coherence can be developed. They are scanning microscopy, diffraction microscopy, holography, interferometry and so on. Among them, the X-ray interferometry is one of the most powerful methods for directly retrieving the phase information of samples. The high coherence available in the facilities has made X-ray interferometry possible, not only of the amplitude-division type [1,2] but also of the wavefront-division type [3]. We proposed and demonstrated a novel hard X-ray micro-interferometer of the wavefront-division type using an optical system of an imaging microscope for high spatial resolution phase measurement [4]. In this report, we present some results indicating the feasibility of this micro-interferometer.

The optical system is shown in Fig. 1. Both object and reference waves are necessary to form a wavefront-division type interferometer. Two zone plates (ZP-A and ZP-B) are arranged closely in the same plane perpendicular to the beam axis. One zone plate (ZP-A) forms a reference wave, while the other zone plate (ZP-B) functions as a magnifying lens. If the two zone plates are illuminated coherently, the corresponding two secondary point sources (S_A and S_B) are produced at their back focal positions. Two spherical waves diverging from these two point sources overlap each other and interference fringes can be formed in an image plane. To prevent the –1st-order diffractive waves from being mixed in the interference region, ZP-A was designed to have a half-moon shape. We call this optical element consisting of two zone plates the "twin zone plate." Its detailed parameters are shown in Fig. 2. It was fabricated by NTT Advanced Technology Corporation [5]. It should be mentioned that the proposed interferometer is analogous to Young's interferometer, and therefore, a high fringe visibility can be expected.

We constructed the hard X-ray micro-interferometer at the Hyogo beamline **BL24XU** (Fig. 1). The photon energy of the fundamental harmonic peak of an undulator was tuned to be 9 keV (λ = 0.138 nm). The spatial coherence region in the vertical direction, which is determined by the vertical source size and the distance from the source, is about 200 μm in the plane of the twin zone plate. From Figs. 1 and 2, the illuminated region is 175 μm, therefore, this region is included in the spatial coherence region. The temporal coherence length, $\lambda^2/2\Delta\lambda$, is about 0.5 μm. Since the maximum optical path difference between the two waves is 34 nm, it is much shorter than the temporal coherence length. Therefore, the coherence condition is completely satisfied. An X-ray zooming tube was employed to observe interference patterns. To convert the interference pattern into the phase-shift distribution, the fringe scanning method was applied. A 125-μm-thick Kapton film was used as a phase plate and arranged in the path of reference waves, as shown in Fig. 1. The phase of the reference wave was varied by rotating the phase plate appropriately.

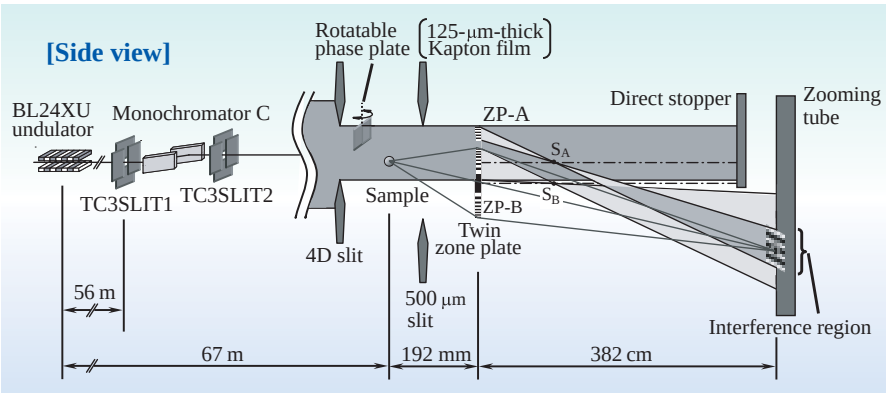

Fig. 1. Schematic illustration of the hard X-ray micro-interferometer. The photon energy used was 9 keV. The optical magnification was ×20. The rotatable phase plate arranged in the path of reference waves was used for the fringe scanning method.

For a pure phase sample, we first used a 75-μm-thick Kapton film with a transmission of 96.3%. The obtained fringe interval was evaluated to be 10 μm, which was equal to the expected value. Furthermore, a visibility of as high as 60% was also achieved. The sample images obtained are shown in Fig. 3: (a) the absorption-contrast image, (b) the interference pattern, and (c) the phase-shift-distribution image retrieved using the fringe scanning method.

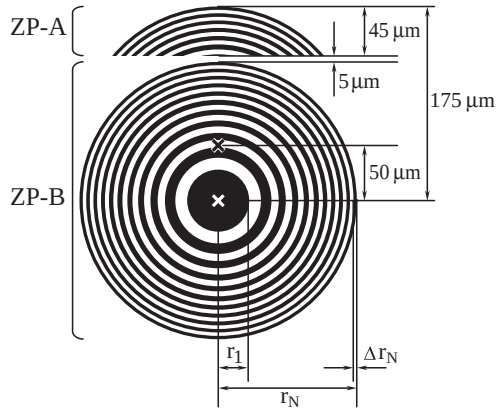

Fig. 2. Design of a twin zone plate made of tantalum. The parameters are as follows: the radius of the innermost zone r_1 of 5 μm, outer diameter $2r_N$ of 250 μm, outermost zone width Δr_N of 100 nm, tantalum thickness of 1 μm, focal length at 9 keV of 181.5 mm and ideal diffraction efficiency at 9 keV of 15.7%.

In Fig. 3(b), the fringe dislocations corresponding to the sample edge were clearly observed. The 75-μm-thick Kapton yields a phase shift of 12.9 rad by calculation. This value agreed well with the resultant distribution in Fig. 3(c).

Next, for another pure phase sample, polystyrene microparticles with a diameter of 7 μm and a transmission of 99.8% were used. The sample images obtained are shown in Fig. 4. Even though the fringe dislocations could hardly be recognized in Fig. 4(b), the sample images were clearly observed using the fringe scanning method, as shown in Fig. 4(c). The spatial resolution of this system was about 160 nm, which was estimated by analyzing the edge response of the phase-retrieved image of a copper #2000 mesh.

From these results, it can be concluded that our new optical system has successfully realized the micro-interferometry in the hard X-ray region. We are now improving the sensitivity of the system to the phase shift. Increasing the signal-to-noise ratio and expanding the interval of the fringe pattern will realize it. Furthermore, by combining our micro-interferometer with a tomographic technique, the three-dimensional refractive index distribution in biological specimens, micropolymers, and optoelectronic devices can be measured without any destruction.

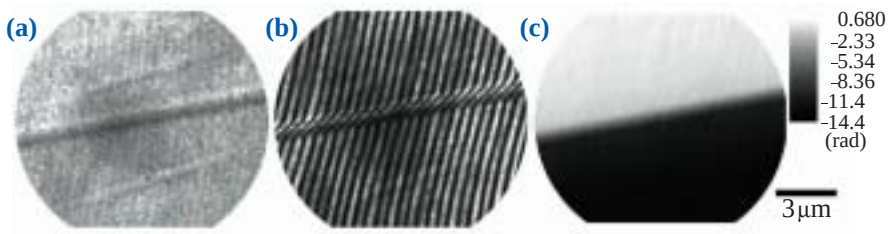

Fig. 3. X-ray micrographs of 75-μm-thick Kapton film: **(a)** Absorption-contrast image. Only the sample edge is slightly observed. **(b)** Interference pattern. The fringe dislocations at the sample edge are clearly observed. **(c)** Retrieved phase-shift image. The sample is observed clearly and the absolute phase shift is evaluated to be 12.0 rad.

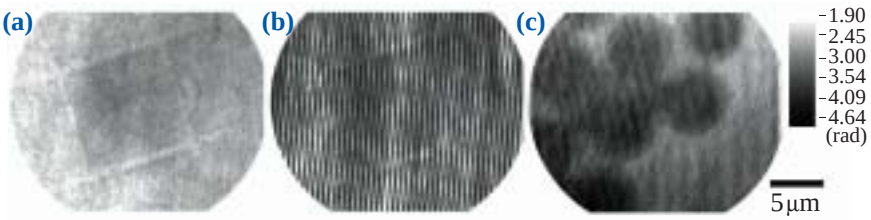

Fig. 4. X-ray micrographs of polystyrene microparticles: **(a)** Absorption-contrast image. The sample is hardly observed. **(b)** Interference pattern. **(c)** Retrieved phase-shift image. The sample is observed clearly and the absolute phase shift is evaluated to be 1.1 rad.

Takahisa Koyama* and Yasushi Kagoshima

Graduate School of Material Science,
University of Hyogo

*E-mail: koyama@sci.u-hyogo.ac.jp

References

[1] U. Bonse *et al.*: Appl. Phys. Lett. **7** (1965) 99.
[2] A. Momose *et al.*: Nature Med. **2** (1996) 473.
[3] Y. Suzuki: Jpn. J. Appl. Phys. **41** (2002) L1019.
[4] *T. Koyama, Y. Kagoshima, I. Wada, A. Saikubo, K. Shimose, K. Hayashi, Y. Tsusaka and J. Matsui: Jpn. J. Appl. Phys.* ***43*** *(2004) L421.*
[5] A. Ozawa *et al.*: Microelectron Eng. **35** (1997) 525.

Verification of a New X-ray *n*-Beam Dynamical Theory using an Arbitrary-polarization-generating X-ray Phase-retarder System

While an ordinal diffraction case in which the incident X-ray beam and only one reflected X-ray beam are strong in the crystal is called the two-beam case, cases in which more than one Bragg-reflected X-ray beams are strong are called *n*-beam cases when *n* beams are strong.

The present author has, for the first time, derived a Takagi-Taupin-type X-ray *n*-beam dynamical theory [1,2] which can deal with X-ray *n*-beam wave fields in a distorted crystal without neglecting the polarization effect. The new theory has a simple form that can be written by one partial differential equation supposing that suffixes are taken in 2*n* ways.

On the other hand, the present author and co-authors have developed a rotating four-quadrant phase-retarder system to generate arbitrarily polarized X-rays from the horizontally polarized synchrotron radiation based on the four-quadrant phase-retarder system [3]. Because the behavior of X-ray *n*-beam wave fields excited in a crystal is expected to strongly depend on the polarization state of the incident X-rays, the apparatus for generating arbitrarily polarized X-rays will have an effective role in experimentally verifying the new *n*-beam dynamical diffraction theory.

Figure 1 shows the rotating four-quadrant phase-retarder system for generating arbitrarily polarized X-rays. Four diamond crystals with a total thickness of about 8 mm were set on small tangential-bar goniometers in a χ-circle goniometer with an angular interval of 90 deg. The angular deviations of diamond crystals from the Bragg conditions of 1 1 1 reflection in an asymmetric Laue geometry and the rotation angle

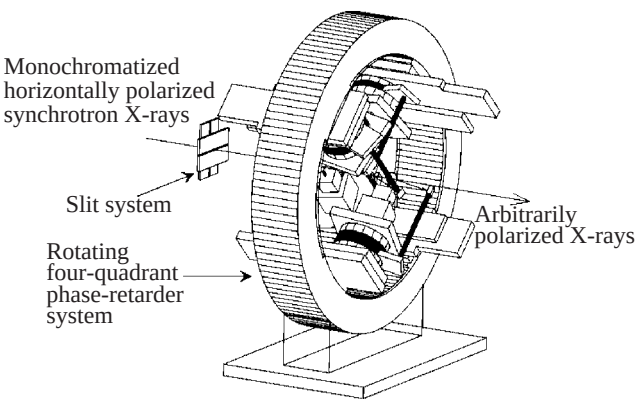

Fig. 1. Rotating four-quadrant phase-retarder system.

of the χ-circle were controlled properly to generate the objective polarization states of X-rays (18.245 keV; the Bragg angle of 0 8 8 reflection is almost 45 deg and free from the glitch of diamond crystals used for phase retarders). Figure 2 shows a schematic drawing around the sample FZ silicon crystal of 9.6 mm thickness arranged to take six-beam 'pinhole topographs' [2,4] with the incidence of X-rays whose polarization state was controlled. After the orientation of the sample silicon crystal was adjusted by monitoring forward-diffracted, 4 4 0-reflected and 4 8 4-reflected X-rays to satisfy the six-beam condition, the dimensions of X-ray beams were limited to a width of 25 μm and a height of 25 μm. Six-beam topograph images were simultaneously recorded on an imaging plate with a pixel size of 50 μm square placed about 27 mm behind the sample crystal. The *Experimental* topograph images of 0 0 0-, 4 4 0-, 4 8 4- and 0 8 8-reflected X-rays with an incidence of *left*-circular polarization are shown in the left column of Fig. 3 together with the corresponding computer-*Simulated* topographs based on the new theory in the right column. Also with the incidence of other polarization states, experimental and simulated results agreed well, while their evident differences were found to be strongly dependent on the polarization states of the incident X-rays. Thus, the applicability of the new *n*-beam X-ray dynamical theory and the efficiency of the rotating four-quadrant phase-retarder system were simultaneously confirmed.

Incidentally, there is a big problem in the crystal structure analysis, that is, the phase values of crystal structure factors cannot be obtained with ordinal (two-beam) X-ray diffraction experiments (phase problem). It has been known from many years ago (1930s) that the phase information of crystal structure factors can be extracted from X-ray intensity profiles in the vicinity of the *n*-beam condition. This is a dynamical diffraction effect. However, most of the crystals whose structures have to be solved exhibit marked distortion, thus the conventional *n*-beam (limited to three-beam) dynamical theory cannot be directly applied to such crystals. In almost all cases of crystal structure analysis, the kinematical diffraction theory has been applied.

The final purpose of the present study is to construct an *n*-beam dynamical theory applicable to

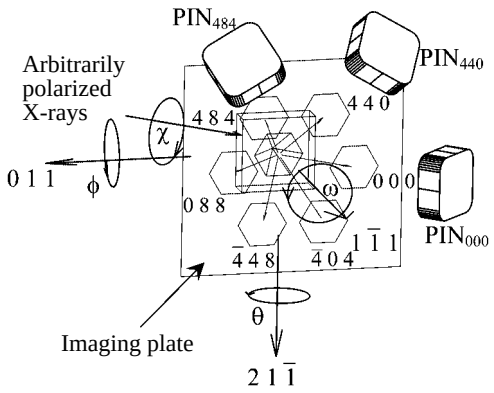

Fig. 2. Schematic drawing around the 111-oriented FZ silicon sample crystal [2].

solving the phase problem of large molecular crystals. In 1970s-1980s, Kato constructed the statistical dynamical theory based on Takagi-Taupin equations, which deals with lattice displacements in a distorted crystal statistically and describes X-ray wave fields in mosaic crystals. Therefore, a new *n*-beam dynamical theory that describes X-ray wave fields in mosaic crystals and extracts the phase information will be constructed using Kato's statistical procedure for lattice displacements based on the theory derived by the present author [1,2].

Kouhei Okitsu

Nano-Engineering Research Center,
The University of Tokyo

E-mail: okitsu@soyak.t.u-tokyo.ac.jp

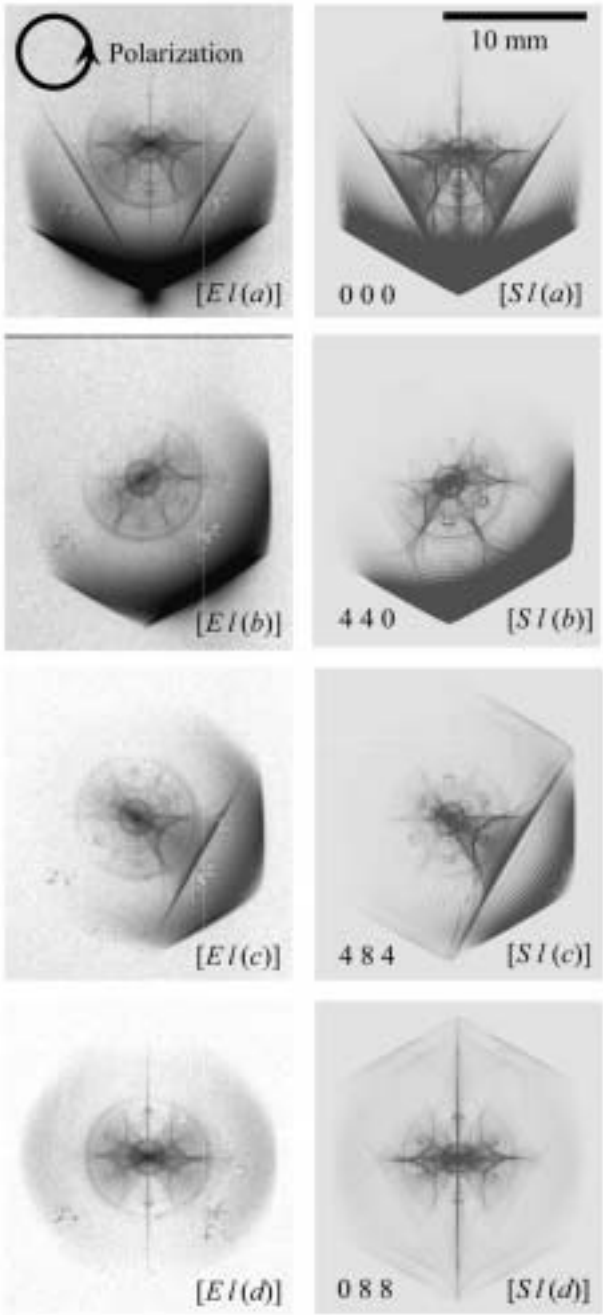

Fig. 3. Left and right column figures show *Experimental* and computer-*Simulated* pinhole topographs with the incidence of *left*-screwed circular polarization. (*a*), (*b*), (*c*) and (*d*) correspond to 0 0 0-, 4 4 0-, 4 8 4- and 0 8 8-reflected X-ray images, respectively [2].

References

[1] K. Okitsu: Acta Cryst. A **59** (2003) 235.
[2] *K. Okitsu: Adv. X-ray Chem. Ana. Jpn.* ***36*** *(2005) 95 (in Japanese).*
[3] K. Okitsu *et al.*: Acta Cryst. A **58** (2002) 146.
[4] *K. Okitsu, Y. Imai, Y. Ueji and Y. Yoda: Acta Cryst. A* ***59*** *(2003) 311.*

Development of Quarter-wave Plates and Full Polarization Measurement near 400 eV

In the soft X-ray region, many types of undulators were made to provide synchrotron radiation (SR) of various polarization states. Polarization measurement is required to obtain the actual polarization state of these light sources. The polarization state can be measured using a phase shifter and a polarizer. Furthermore, polarization elements can change the polarization state of light, for example, from linear polarization to circular polarization. Expensive undulators specialized for a specific polarization state would not be required to obtain the desired polarization state. In this report, we present the developments of a phase shifter near 400 eV and show the results of full polarization measurement using the phase shifter.

The phase shifter has two important parameters, namely, phase retardation (Δ) and polarizance (P_Z). Δ is the phase difference between p- and s- components retarded by transmitting the phase shifter (Fig. 1). With $\Delta = \pm 90°$, the circularly polarized component of the incident light is changed into a linearly polarized component. A phase shifter with $\Delta = \pm 90°$ is called the quarter-wave plate. The non-polarized component is not affected by the Δ of the phase shifter. The circularly polarized component is distinguished from the non-polarized component using a phase shifter.

P_Z expresses a polarizer ability and is defined as $(T_S - T_P)/(T_S+T_P)$, where T_P and T_S are the transmittances of p- and s-components. Both the circularly polarized component and non-polarized component are changed into linearly polarized component by this property. An element with a large absolute P_Z value works as a polarizer rather than a phase shifter. P_Z is required to be close to zero for a usable phase shifter. An ideal phase shifter with $\Delta = 90°$ and $P_Z = 0$ can transform circularly polarized light to linearly polarized light and vice versa. It enables the measurement of the P_C of highly circularly polarized light with a high accuracy.

In the soft X-ray region, transmitting-type multilayers are used as phase shifters [1]. Sc/Cr multilayers have a large phase retardation near 400 eV. A freestanding Sc/Cr multilayer was designed as a quarter-wave plate by considering the practical interface roughness of $\sigma = 0.35$ nm from the previous work [2]. The incident angle of the multilayer was optimized to 60°, where the multilayer of $\sigma = 0.35$ nm had the largest phase retardation. The designed parameters were the periodic length d = 3.15 nm, the number of periods N = 300, and the ratio of Cr layer thickness Γ (= d_{Cr} / d) = 0.47. Figure 2 shows a photograph of Sc/Cr multilayer samples [3].

The evaluation of the Sc/Cr multilayers was performed at beamline **BL27SU** using a versatile apparatus for polarimetry and ellipsometry [2]. The light source of the beamline is a figure-8 undulator and emits linearly polarized light. The absorption edge of the multilayer was 398.2 eV, which was shifted by -0.5 eV from the Sc 2p absorption edge of bulk state, 398.7 eV. The photon energy was selected to be 398.1 eV, because the phase retardation is the largest at the energy of the absorption edge and degrades rapidly at a higher energy.

A rotating analyzer method (RAM) was performed in the versatile apparatus for polarimetry and ellipsometry. The experimental setup of RAM is shown in Fig. 1. A Sc/Cr polarizer was used as an analyzer and rotated with a detector around the incident beam axis. The outputs of the detector against the azimuth of the analyzer follow the Malus law, which has a cosine squared form. The amplitude of the variation of the outputs indicates the degree of linear polarization (P_L) and the phase indicates the azimuth of the major axis of polarization ellipse (δ).

To obtain Δ and P_Z, RAM was performed on the incident light (Fig. 1 without the phase

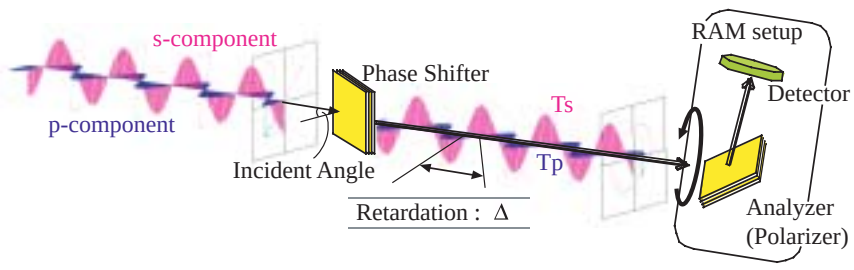

Fig. 1. Schematic view of experimental setup. The polarization state is measured using a phase shifter and a polarizer. The phase shifter changes the phase between the s- and p- components by its phase retardation. The RAM setup contains a polarizer and a detector and is rotated around the incident beam axis.

shifter) and the light transmitted through the phase shifter (Fig. 1 with the phase shifter). The P_L and δ of the incident and transmitted light were obtained. The differences in P_L and δ between the incident and transmitted light were changed according to the Δ and P_Z of the phase shifter and the degree of circular polarization (P_C) of the incident light. These Δ and P_Z were derived from the results of RAM at two different azimuths of the phase shifter [4]. Figure 3 shows the measured Δ and P_Z as a function of the incident angle from the normal. The maximum and minimum of Δ values exceeded ±90°. At the incident angle of 59.77°, Δ was 90°, and P_Z was nearest to zero. The phase shifter can therefore be used as a quarter-wave plate at this incident angle. P_Z was -0.19, and the transmittance of the p-component was 0.4% at the angle. With this quarter-wave plate, we can obtain circularly polarized light from linearly polarized light of δ = 34.2°.

Next, the Sc/Cr multilayer quarter-wave plate was used for the full polarization measurements of the highly circularly polarized light from the undulators [5]. The experiment was carried out at **BL25SU**. The beamline has twin helical undulators as light sources. The measured P_C values of the right- and left-hand circularly polarized light at the photon energy were 0.96±0.03 and -0.97±0.03, respectively. The twin undulators produced symmetrically circularly polarized light, because the right- and left-handed circularly polarized light have the same absolute P_C values. The P_L values of such light were also measured as 0.10±0.01 and 0.08±0.01, respectively. The degree of polarization ($V = \sqrt{P_C^2 + P_L^2}$) was derived from P_C and P_L as 0.97. The light source was designed to generate circularly polarized light having $|P_C|$ as high as 0.9998. P_L was not sufficient high to explain the degradation of P_C by the transformation of circularly polarized light into linearly polarized light. The investigation of the causes of non-polarization is required to obtain a higher P_C.

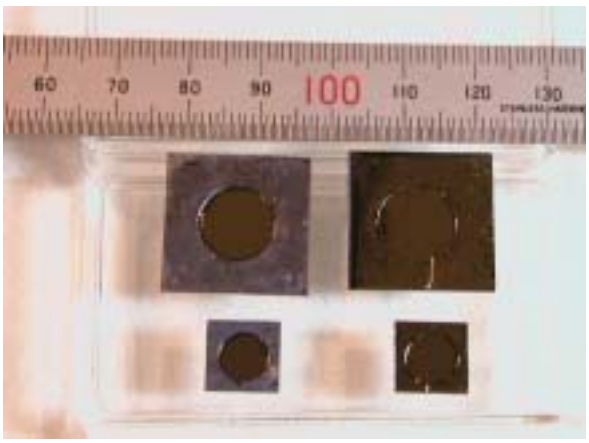

Fig. 2. Transmitting-type Sc/Cr multilayers fabricated by X-ray Co., Ltd. [3]. The front and back surfaces of the phase shifters are shown. The central part transmits light where there is no substrate.

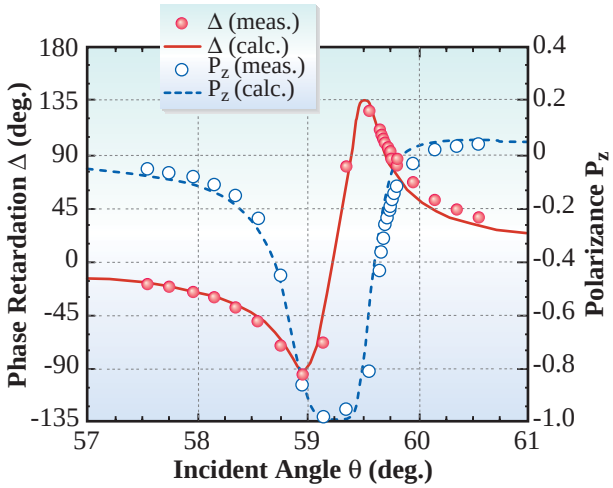

Fig. 3. Measured Δ and P_Z of Sc/Cr multilayer at 398.1 eV as a function of incident angle from normal. The circles indicate the measured data and the lines indicate the result of fitting with the parameters of photon energy = 398.1 eV, optical indices for Cr = 0.995254 – 0.001006i and for Sc = 1.003401 – 0.000286i, d = 3.05 nm, N = 300, Γ = 0.47, σ = 0.4 nm, and beam divergence = 0.2°.

Toko Hirono* and Hiroaki Kimura

SPring-8 / JASRI

*E-mail : hirono@spring8.or.jp

References

[1] See for example: F. Schäfers *et al.*: Nucl. Instrum. Meth. A **467-468** (2001) 349.
[2] H. Kimura *et al.*: Proc. 8th Int. SRI AIP **CP705** (2004) 537.
[3] N.N. Salashchenko *et al.*: in preparation.
[4] *H. Kimura, T. Hirono, Y. Tamenori, Y. Saitoh, N.N. Salashchenko and T. Ishikawa: J. Electr. Spectr.* ***144-147*** *(2005) 1079.*
[5] *T. Hirono, H. Kimura, T. Muro, Y. Saitoh and T. Ishikawa: J. Electr. Spectr.* ***144-147*** *(2005) 1097.*

Nuclear Physics

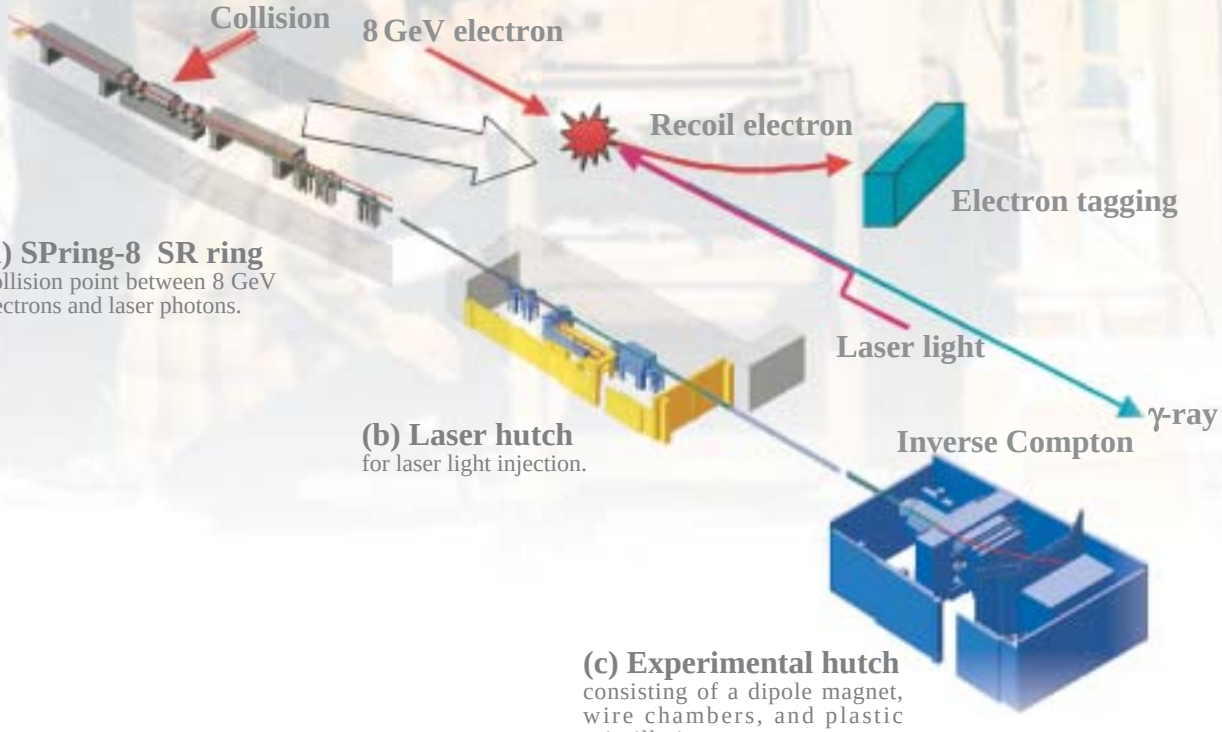

(a) SPring-8 SR ring
Collision point between 8 GeV electrons and laser photons.

(b) Laser hutch
for laser light injection.

(c) Experimental hutch
consisting of a dipole magnet, wire chambers, and plastic scintillation counters.

ϕ-Meson Photoproduction Near the Threshold

The ultimate building blocks of subatomic particles (hadrons) are quarks and gluons. Quantum chromodynamics (QCD) describes how hadrons are formed from quarks and gluons. Gluons serve as the glue between quarks (q) and anti-quarks ($\bar{q}$) to form a hadron. A particle made of three quarks is called a baryon. A particle made of a quark and an anti-quark is called a meson. There are six flavors to distinguish different types of quarks, i.e. up, down, strange, charm, beauty and top. An example of a baryon is a proton which is made of two up quarks and a down quark.

Most hadrons are made of three quarks qqq or a quark anti-quark pair $q\,\bar{q}$. However QCD does not rule out the existence of baryons made of more than three quarks, mesons made of more than two quarks and particles made of only gluons (glueball). An example of such exotic hadrons is a penta-quark particle, Θ^+, found by the LEPS collaboration at beamline **BL33LEP** and in other experiments [1].

Other than penta-quark states, there has been much effort in the search for the glueball state for many years. There are some candidates for the glueball state although no clear experimental confirmation has been made. In 1997, Nakano and Toki suggested that diffractive ϕ-meson photoproduction near threshold may be sensitive to the possible existence of a glueball with spin-parity $J^P=0^+$ [2]. In diffractive photoproduction, ϕ-mesons are predominantly produced by a conversion from a photon (vector meson dominance). Therefore, the incident photon beam can be viewed as a virtual ϕ-meson beam. Interactions of ϕ-mesons with the target protons can be intensively studied in this reaction. Note that the quark configuration of a ϕ-meson is almost purely a strange quark and an anti-strange quark. Thus, exchanges of quarks are highly suppressed in this reaction because no net strange quark is contained in protons (OZI rule). The reaction is expected to be dominated by exchanges of multi-gluons. In the other low-energy hadronic reactions, the contribution from quark exchanges is usually large enough to hide multi-gluon exchange processes. Thus, ϕ-meson photoproduction is an ideal reaction for studying the multi-gluon exchange processes.

Historically, the ϕ-meson photoproduction reaction has been measured mainly at high photon energies. The slow increase of cross section with the total energy was successfully interpreted by a dominant contribution from the Pomeron exchange process. The Pomeron exchange process is explained in terms of a multi-gluon exchange in QCD. The contribution from the Pomeron exchange process is predicted to be almost constant near the threshold. In this regard, the presence of the 0^+ glueball exchange process may lead to a non-monotonic behavior of the energy dependence of the cross section in the near-threshold region.

The concept of the Pomeron was originally introduced in the high-energy limit. There is no justification that the same picture can be applied to the low-energy process. Consequently, the low-energy ϕ-meson photoproduction reaction can also provide information on how the Pomeron exchange process behaves at low energies.

We obtained data using a liquid hydrogen target with linearly polarized photons at beamline BL33LEP. ϕ-Meson photoproduction was identified through K^+K^- decay mode. Details of the experiment and data analysis are described in Ref. [3]. Figure 1 shows the energy dependence of the differential cross section at the forwardmost production angle, $d\sigma/dt_{t=-|t|min}$ [3,4]. The energy dependence of $d\sigma/dt_{t=-|t|min}$ shows a non-monotonic behavior, i.e., a peak structure appears at around photon energy E_γ = 2 GeV. The data was compared with a model which includes the Pomeron exchange and π, η-meson exchange processes without the 0^+ glueball exchange process [5] (dashed curve). The model does not describe the data points in this energy region.

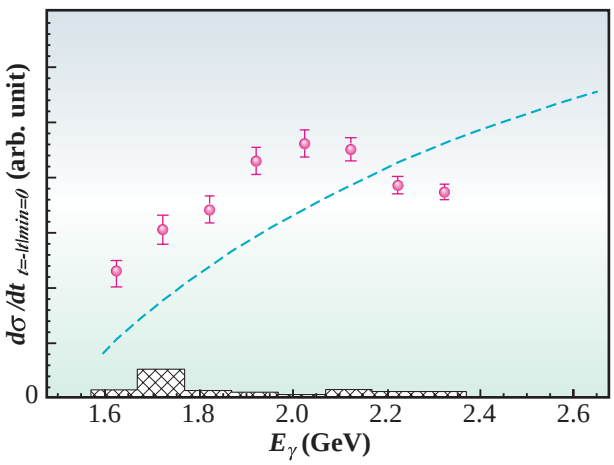

Fig. 1. Differential cross section at $t = -|t|_{min}$. The hatched histogram indicates systematic errors. The prediction based on the Pomeron exchange process and π, η-meson exchange process in ref. [5] is shown by the dashed curve.

To understand the cause of the peaking structure in the cross section, ϕ-meson decay angular distributions were measured at forward angles ($-0.2 < t+|t|_{min} < 0$ GeV^2) in two different energy ranges: $1.973 < E_\gamma < 2.173$ GeV (near the cross section peak) and $2.173 < E_\gamma < 2.373$ GeV (above the cross section peak). The ϕ-meson decay angular distributions, $W(\cos\theta, \phi, \Phi)$, have rich information on the underlying production mechanism. The angles θ, ϕ and Φ stand for the K^+ polar angle, the K^+ azimuthal angle and the azimuthal angle of the photon polarization vector.

Figure 2 (left panel) shows the angular distribution $W(\cos\theta)$. In both energy ranges, $W(\cos\theta)$ follows 3/4 $\sin^2\theta$, which indicates the dominance of a spin conserving process, such as the Pomeron exchange process, π, η-meson exchange and 0^+ glueball exchange. Figure 2 (right panel) shows the $W(\phi-\Phi)$ distribution. In both energy ranges, the ϕ-meson exhibits preferential decay in parallel to the direction of photon polarization. This implies that the contribution of the unnatural parity exchange (π, η-meson exchange) is not dominant. The relative contribution between natural parity exchange and unnatural parity (π, η-meson) exchange is nearly the same for the two energy bins. Taking into account that the contribution from the Pomeron exchange is expected to be almost constant in this energy range, the peaking structure of the cross section cannot be explained by only unnatural-parity exchange processes. A possible explanation of this effect might be related to the 0^+ glueball exchange. However, a fit suggested in ref. [2] failed to reproduce the peaking structure with the proposed set of parameters. Further measurement in a wider energy range using different targets, as well as theoretical studies, would help to better understand the underlying mechanism of the peaking structure.

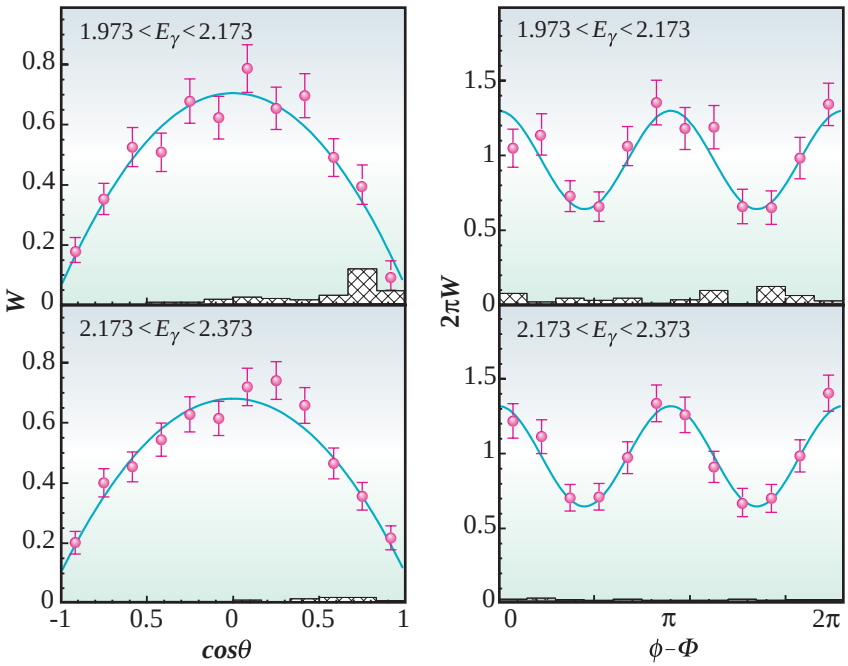

Fig. 2. ϕ-meson decay angular distributions in two beam energy ranges. The hatched histograms indicate systematic errors. Solid curves show fits to the distributions.

T. Mibe[a,*], W.C. Chang[b] and T. Nakano[c]

(a) Department of Physics, Ohio University, USA
(b) Institute of Physics, Academia Sinica, Taiwan
(c) Research Center for Nuclear Physics, Osaka University

*E-mail: mibe@jlab.org

References

[1] T. Nakano: SPring-8 Research Frontiers (2003) 130; T. Nakano *et al.* [LEPS collaboration]: Phys. Rev. Lett. **91** (2003) 012002.
[2] T. Nakano and H. Toki: Proc. International Workshop on Exciting Physics and New Accelerator Facilities, SPring-8, Hyogo (World Scientific) (1997) 48.
[3] *T. Mibe: Doctor thesis, Osaka university (2004); T. Mibe, W.C. Chang, T. Nakano, D.S. Ahn, J.K. Ahn, H. Akimune, Y. Asano, S. Daté, H. Ejiri, H. Fujimura, M. Fujiwara, K. Hicks, T. Hotta, K. Imai, T. Ishikawa, T. Iwata, H. Kawai, Z.Y. Kim, K. Kino, H. Kohri, N. Kumagai, S. Makino, T. Matsuda, T. Matsumura, N. Matsuoka, K. Miwa, M. Miyabe, Y. Miyachi, M. Morita, N. Muramatsu, M. Niiyama, M. Nomachi, Y. Ohashi, T. Ooba, H. Ohkuma, D.S. Oshuev, C. Rangacharyulu, A. Sakaguchi, T. Sasaki, P.M. Shagin, Y. Shiino, H. Shimizu, Y. Sugaya, M. Sumihama, A.I. Titov, Y. Toi, H. Toyokawa, A. Wakai, C.W. Wang, S.C. Wang, K. Yonehara, T. Yorita, M. Yoshimura, M. Yosoi, R.G.T. Zegers [LEPS collaboration]: arXiv:nucl-ex/0506015.*
[4] J. Ballam *et al.*: Phys. Rev. D **7** (1973) 3150; H.J. Besch *et al.*: Nucl. Phys. B **144** (1982) 22; D.P. Barber *et al.*: Zeit. Phys. C **12** (1982) 1; J. Barth *et al.*: Eur. Phys. J. A **17** (2003) 269.
[5] A.I. Titov and T.-S.H. Lee: Phys. Rev. C **67** (2003) 065205.

Is the Property of Mesons Modified in the Nuclear Medium?
– ϕ Meson Photoproduction from Nuclei –

The concept of mass modification is generally applied for many fields in physics. The effective mass of electrons in material science is widely discussed, for example, when calculating the conductivity. In nuclear physics, the concept of the effective mass is sometimes used to describe the effect of the average potential. In these cases, we believe that the bare mass does not change and the concept of "effective mass" is treated as a conventional method of taking into account the potential effect from the medium. A similar concept is applicable to treating mesons in hadron physics.

The modification of vector mesons in nuclear matter is an interesting subject since its origin stems from the chiral symmetry violation or recovery in a nuclear medium. Theoretically, a broadening of the width and/or a decrease of the mass has been predicted for the ϕ meson with a pure $s\bar{s}$ component in the nuclear medium [1,2], although no clear evidence for the mass shift of the ϕ meson has been reported.

The total ϕ-nucleon cross section $\sigma_{\phi N}$ in free space determined from the ϕ photoproduction on the proton is very small, 7.7-8.7 mb [3]. If $\sigma_{\phi N}$ in the nuclear medium is the same as that in free space, the ϕ photoproduction cross section from nucleons in a nucleus (incoherent process) σ_A should be approximately proportional to the mass number of the target nuclei A since the ϕ meson produced in the nucleus almost goes out the nucleus because the mean free path is much longer than the nuclear size. If $\sigma_{\phi N}$ becomes larger in the nuclear medium, some fraction of photoproduced ϕ mesons would interact with nucleons in the nucleus and disappear via inelastic reactions such as $\phi p \rightarrow K^+\Lambda$ and $\phi n \rightarrow K^-\Sigma^+$. In this case, the A-dependence considerably deviates from $\sigma_A \propto A^1$, as illustrated in Fig. 1. Therefore, we can study the properties of the ϕ meson in the nuclear medium by measuring the ϕ photoproduction cross sections from nuclei.

The ϕ photoproduction cross sections from Li, C, Al, and Cu nuclei were measured at beamline **BL33LEP**. High energy photons were obtained by backward Compton scattering in the 8 GeV storage ring. The produced ϕ mesons with a decay mode to K^+ and K^- meson pairs were detected at forward angles using a magnetic spectrometer. Figure 2 shows the invariant mass spectrum reconstructed by the momentum information of K^+ and K^- mesons for the $\gamma Cu \rightarrow K^+K^-X$ reaction. A peak corresponding to ϕ mesons was clearly observed, and similar peaks were also observed in the runs with other targets. The measured mass and width of the ϕ meson for each target nucleus are consistent with the free ϕ meson mass of 1.02 GeV.

Among the ϕ meson events produced, we identified ϕ mesons produced not from individual nucleons in a nucleus (incoherent process) but from the nucleus as a whole (coherent process). The A-dependence of the ϕ photoproduction cross section of the incoherent process gives the relation $\sigma_A \propto A^{0.72\pm0.07}$ shown in Fig. 3 after subtracting the contribution of coherently produced ϕ mesons as background.

To determine $\sigma_{\phi N}$ from the obtained A-dependence, an optical model of a Glauber-type multiple scattering theory for incoherent production is applied [4]. The value of $\sigma_{\phi N}$ is estimated to be 35^{+17}_{-11} mb, which is much larger than $\sigma_{\phi N}$ in free space. This suggests that the properties of ϕ mesons might change in the nuclear medium.

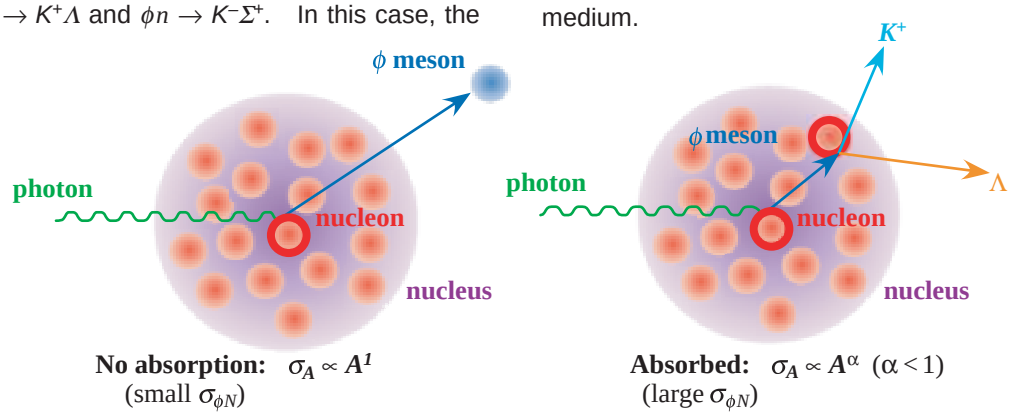

Fig. 1. Left: when ϕ mesons are produced in a nucleus and go out, the A-dependence is proportional to A. Right: If there is a considerable deviation of the ϕ-N interaction cross section in the nuclear medium, the cross section becomes large.

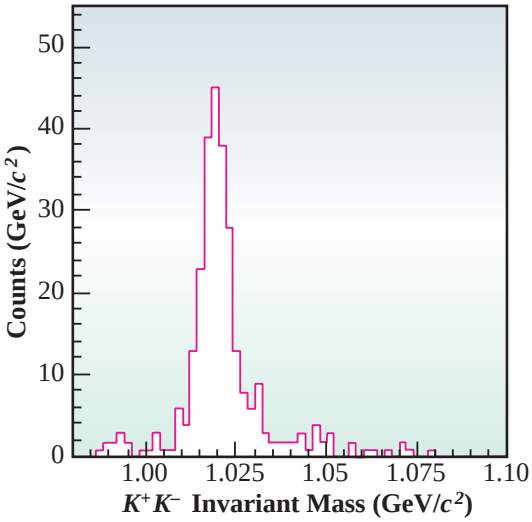

Fig. 2. K^+K^- invariant mass spectrum for $\gamma Cu \rightarrow K^+K^-X$ reaction.

On the basis of the self-energy calculation for ϕ mesons in the nuclear medium, Cabrera *et al*. presented the *A*-dependence in terms of the variable $P_{out} = \sigma_A / A\sigma_N$ which represents the probability of a photoproduced ϕ meson going out a nucleus [5], where σ_N denotes the ϕ photoproduction cross section from a nucleon. Figure 4 compares the P_{out} obtained in the experiment and the theoretical predictions given by Cabrera *et al*. as a function of *A*. The obtained P_{out} are smaller than the theoretical predictions. This discrepancy implies that the ϕ-nucleon interaction is stronger than that estimated theoretically due to the modification of the ϕ properties in the nuclear medium.

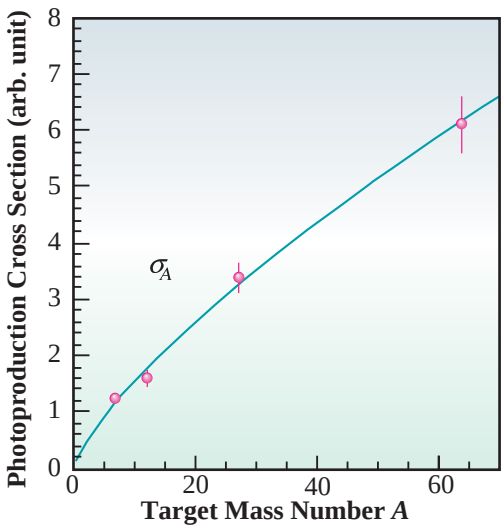

Fig. 3. *A*-dependence of ϕ photoproduction cross section of the incoherent process. The data points are fitted as a function of $A^{0.72}$.

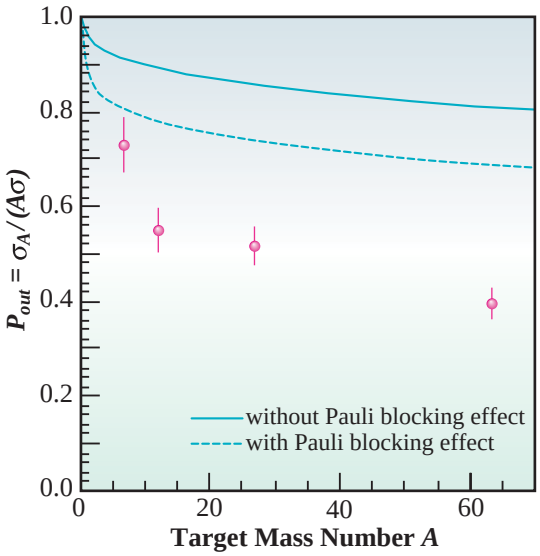

Fig. 4. Probability P_{out}. The solid and dashed curves show the theoretical calculations given by Cabrera *et al*. [5] without and with the Pauli-blocking effect, respectively.

Takatsugu Ishikawa [a,*] and Mamoru Fujiwara [b,c]

(a) Laboratory of Nuclear Science, Tohoku University
(b) Research Center for Nuclear Physics, Osaka University
(c) Advanced Photon Research Center, Japan Atomic Energy Research Institute

*E-mail: ishikawa@lns.tohoku.ac.jp

References

[1] T. Hatsuda, S.H. Lee: Phys. Rev. C **46** (1992) 34.
[2] E. Oset *et al.*: Phys. Lett. B **508** (2001) 237.
[3] H.-J. Behrend *et al.*: Phys. Lett. B **56** (1975) 408.
[4] K.S. Kölbig and B. Margolis: Nucl. Phys. B **6** (1968) 85.
[5] D. Cabrera *et al.*: Nucl. Phys. A **733** (2004) 130.
[6] *T. Ishikawa, D.S. Ahn, J.K. Ahn, H. Akimune, W.C. Chang, S. Daté, H. Fujimura, M. Fujiwara, K. Hicks, T. Hotta, K. Imai, H. Kawai, K. Kino, H. Kohri, T. Matsumura, T. Mibe, K. Miwa, M. Miyabe, M. Morita, T. Murakami, N. Muramatsu, H. Nakamura, M. Nakamura, T. Nakano, M. Niiyama, M. Nomachi, Y. Ohashi, T. Ooba, D.S. Oshuev, C. Rangacharyulu, A. Sakaguchi, Y. Shiino, Y. Sakemi, H. Shimizu, Y. Sugaya, M. Sumihama, Y. Toi, H. Toyokawa, C.W. Wang, T. Yorita, M. Yosoi and R.G.T. Zegers: Phys. Lett. B **608** (2005) 215.*

Accelerators & Beamlines

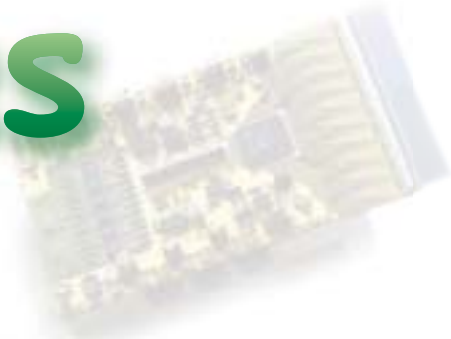

Frontiers

Beam Performance

Beam Performance and Upgrades of the Storage Ring

Top-up Operation

The top-up operation at the SPring-8 was started in May 2004. In this operation mode, the beam is injected every one minute or every five minutes to maintain the stored current at a maximum of 100 mA. The stored current in the top-up mode is kept constant with a deviation less than 0.1%. Thus the top-up operation yielded considerable profit for users, for example, increment of average radiation intensity, stabilizations of the intensity and the constant heat load on experimental equipments, and so on [1].

In order to make the top-up operation available to user experiments, we had to overcome cruxes in beam injection with an open photon beam shutter. The most serious problem is injected beam loss since an open photon beam shutter permits the bremsstrahlung from lost electrons to be transported into the experimental hall. Furthermore, there is the fear of the demagnetization of insertion devices (IDs) due to the lost electron bombardment during beam injection with a closed gap. Through the study of the injected beam loss process, we found that the injected electrons with large horizontal amplitude are not captured in the storage ring [2]. For the purpose of disposing of troublesome lost particles in the beam tail, a collimation system for the injected electron beam was installed at the beam transport line from the booster synchrotron to the storage ring (SSBT). The collimation system consists of two pairs of collimators (SL1A_ss and SL1B_ss), which were placed on a dispersion-free section in the SSBT. Because of the negligible dispersion, the collimators can only be used for betatron collimation. In order to limit x and x' in the betatron phase space, the horizontal phase difference between SL1A_ss and SL1B_ss were designed to be $\pi/2$. For both collimators, two stainless-steel plates 21.2 mm thick were prepared as left- and right-side blades. An optical transition radiation (OTR) on the surface of the blade was observed using a CCD camera. Figure 1 shows that beam tails on the blades were observed. To determine the relation between injection efficiency and the collimator gaps, the efficiencies with various gaps were measured [3]. Figure 2 shows the effect of the collimator on the efficiency of injection to the storage ring. Even under the condition that all ID gaps are close to the minimum, a high injection efficiency of over 80% is achieved with the use of the collimator when the half-gap width is set to 1 σ (standard deviation) of the injected beam distribution.

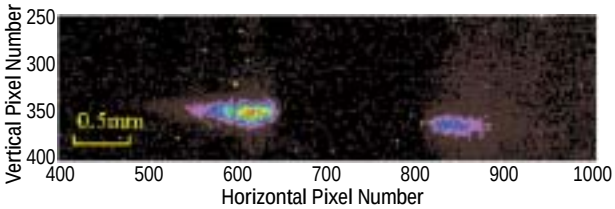

Fig. 1. Relative intensity distribution of OTR at the surface of SL1A_ss. Red and black points indicate the highest and the lowest intensities, respectively. Scale is 8.1 μm/pixel.

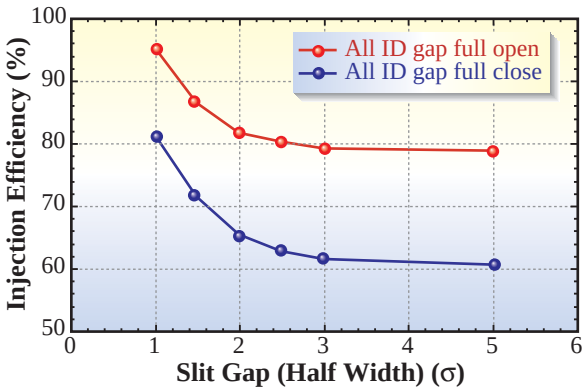

Fig. 2. Dependence of injection efficiency on slit gap of SSBT collimator. The gap width of the collimator is measured from the beam size of the injected beam.

For the top-up operation, it is also important that beam injection dose not excite orbit variation of the stored beam in order not to disturb user experiments. If the injection bump orbit is not completely closed, the stored beam suffers an error kick while passing through the bump orbit. We found that the excitation occurred due to the non-similarity fields of bump magnets and the non-linear field of sextupole magnets within the bump orbit, and that this non-similarity of bump magnet fields originates from the eddy current generated in the metallic end plates of bump magnets. The excitation of the stored beam orbit variation by the non-linearity of the bump

magnet field was hence avoided by replacing the bump magnets with new ones having non-metallic end plates [4]. In order to suppress the stored beam oscillation excited by a sextupole non-linear field, we have developed novel optics for the storage ring [5]. We also measured the vertical oscillation excitation of the stored beam by beam injection to the storage ring. We found that the amplitude of the vertical oscillation is proportional to the waveform of the bump magnet field. Hence we correct the vertical oscillation of the stored beam orbit by tilting two of four the bump magnets. After the main portion of the stored beam orbit oscillation excited by the beam injection was improved by the above countermeasures, the corrector bump magnets were installed to reduce the residual oscillations in both horizontal and vertical directions. The improvements of the stored beam orbit oscillation excited by beam injection in the horizontal direction is shown in Fig. 3. These oscillations excited by the injection bump are measured using turn-by-turn beam position monitors. The horizontal and vertical oscillation amplitudes of the stored beam induced by the injection bump are reduced to one-third and two-thirds of the beams, respectively. At present, the excited oscillation of the stored beam gives negligible disturbance to users.

To deliver beams to user experiments with the top-up operation, a new interlock logic was necessary; the amount of lost electrons during injections to the storage ring in the top-up operation must be controlled. The integration of lost electrons at the time of injection during one week should not exceed the value permitted for the top-up operation. An interlock system was installed to deal with the top-up operation requirements. The amounts of loss are calculated from the difference between injected charges and the increment of the stored current of the storage ring. The injected charges are measured with integrated current transformers (ICT) combined with beam charge monitors (BCM) installed in the most downstream part of the SSBT. The stored current of the storage ring is measured with direct current current transformers (DCCT). Data taken with these devices are sent to a programmable logic controller (PLC), and logics inside the PLC judge the condition and issue an interlock signal when necessary.

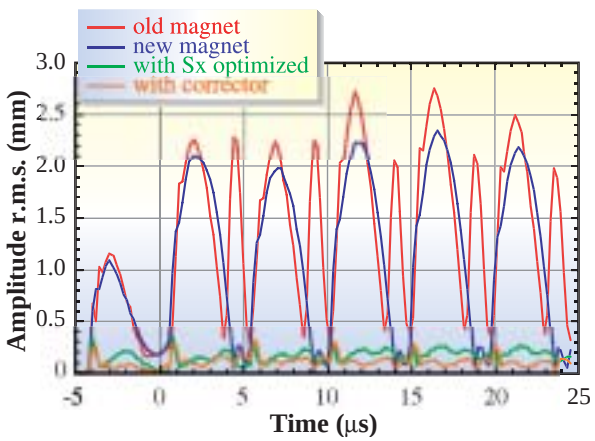

Fig. 3. Improvement of stored beam oscillation excited by injection bump in horizontal direction. The origin of the abscissa in the figure corresponds to the peak of the bump waveform.

In non-top-up operation, a slow drift of the electron beam orbit, the magnitude of which is approximately 10 μm per week, is observed even though the orbit correction is performed with about 250 normal steering magnets (NSTs) before and after beam refilling. Since top-up operation is continuous over a long period, about two or three weeks, suppression of the slow orbit drift is quite important for user experiments. To solve this problem, a greater number of special steering magnets with high setting resolution (HRSTs) are required. To this end, we conceived an idea to make NST function as HRST merely by improving the power supply system of NST. We succeeded in the modification of the power supply system to achieve the current setting resolution of 21 bit by introducing double remote IO units [6]. By the beam test for checking the basic performance, we carried out the improvement of the periodic orbit correction system based on the modification of the NST power supply system to provide another 48 HRSTs for the correction system. By this change, the number of HRSTs in each plane was increased from 24 to 48. Figure 4 shows the orbit stability during the top-up operation over 1 week after the improvement of the periodic orbit correction system. The long-term stability of the orbit is dramatically improved by both this improvement and top-up operation compared with the stability in the case of non-top-up operation.

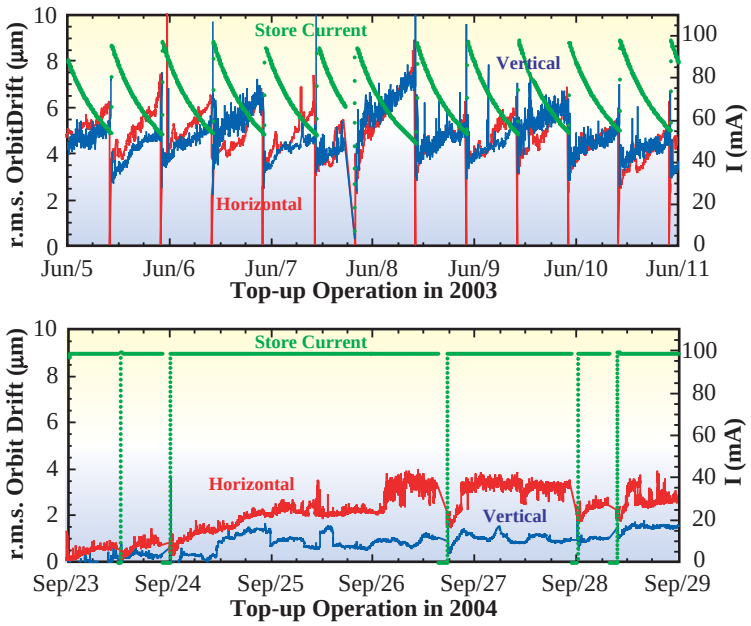

Fig. 4. Long-term stability of electron beam orbit over one week. The upper and lower graphs show the long-term stability during non-top-up and top-up operations, respectively.

Bunch-by-bunch feedback

A bunch-by-bunch feedback [7] system is developed to suppress the horizontal and vertical beam instabilities that arise during low chromaticity operation for the top-up operation of the ring or for future high bunch current operation. The feedback has been in operation in the user mode from the beginning of 2004 without any trouble or any additional tuning during the current year. The measured feedback damping time is less than 1 ms, which is one order faster than that of radiation damping, 8 ms. The noise in the beam position propagates through the feedback to the kicker and excites the beam motion. To reduce this residual motion to less than one-tenth of the beam size, 1 μm, the feedback is made by a low noise system using a newly developed high-resolution beam position monitor of single pass resolution 5 μm and 12-bit ADCs with a new concept analog demultiplexer. Any degradation of the beam quality is observed and reported by users. The reconfigurable hardware logic, field programmable gate array (FPGA), is employed for digital signal processing and its one-order-higher processing power than DSPs or CPUs make our system simple, fast and cost effective. Also, with the newly developed FIR filter algorithm for feedback signal production in combination with this FPGA processing power, the system is versatile and flexible and easy to apply to other storage rings. A new board with ADCs, DAC and a single FPGA that processes both FIR filters, and a multiplexer is being developing to reduce the number of tuning parameters for easy tuning, control and maintenance (Fig. 5).

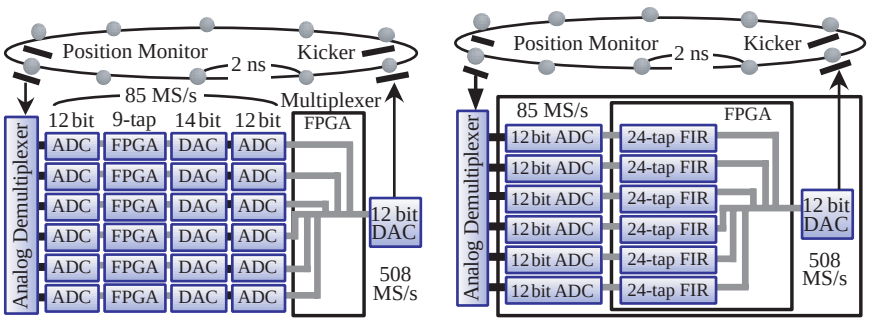

Fig. 5. Current system (left) and new system under development (right).

Accelerator Diagnostics Beamlines

Diagnostics of the electron beam for storage ring tuning towards the realization of ideal top-up operation have been performed at the diagnosis beamline I (BL38B2) using visible and X-ray synchrotron radiation (SR). Information on the bunch impurity and the beam current of each bunch is important for the top-up operation in several-bunch modes. The evolution of bunch impurity during the top-up operation has been measured using the gated photon-counting system with fast light shutters in the visible light region. An example of the variation of the bunch impurity, which is the ratio of the number of electrons in the bucket adjacent to the target bucket on the trailing time side to that in the target bucket, during one week of top-up operation is shown in Fig. 6. The increase of the impurity to the level of 2×10^{-9} was observed during one week, which is a sufficiently small level for user experiments.

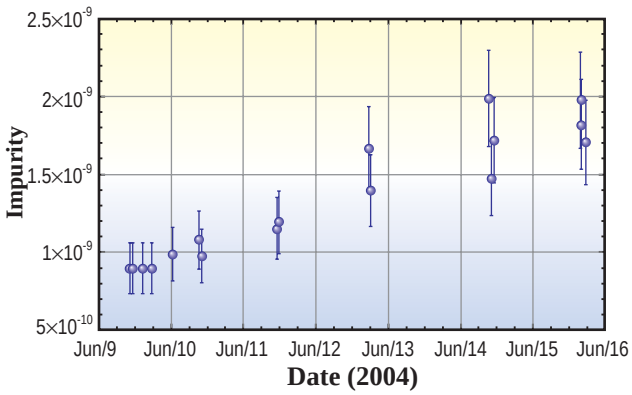

Fig. 6. Observed variation of bunch impurity during top-up operation.

The transient behaviors of the effective beam profile after beam injections have been measured by the X-ray beam imager (XBI) based on a Fresnel zone plate and an X-ray zooming tube. The time variation of effective horizontal and vertical beam sizes normalized to the values of the damped beam, which were measured in the top-up operation, are shown in Fig. 7.

Construction of the accelerator diagnosis beamline II (BL05SS) is in progress. The beamline has a straight section for IDs. An ID with flexibility for exchanging magnet arrays has been designed to provide a variety of SR for various kinds of

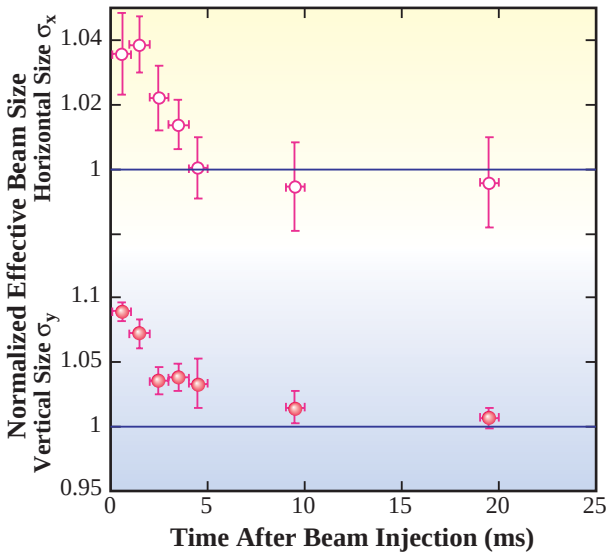

Fig. 7. Time dependence after beam injections of horizontal and vertical effective beam sizes in top-up operation obs erved by XBI. The integration time is 1 ms. The beam sizes are normalized to values of the damped beam which were measured between injections.

experiments. It has a C-shaped magnet support structure of an out-vacuum type. The magnet support structure can be moved off the electron beam axis to the maintenance position by sliding it on guide rails (Fig. 8), so that magnet arrays can be exchanged easily. The slide system will be installed in a pit and embedded below floor level. A magnet array of multi-pole wiggler (MPW) type has been designed to produce high-power SR for the purpose of studying radiation damage to accelerator components and developing of high-heat-load components such as photon absorbers. The period length and the period number are 76 mm and 51, respectively. At the minimum magnet gap of 20 mm, the deflection parameter K is 5.8, and the total power and peak power density are 10 kW and 200 kW/mrad^2, respectively, for the beam current of 100 mA. The ID and the ID vacuum chamber will be installed in summer of 2005.

A compact photon absorber for the front-end has been developed, which withstands high heat load of the SR from the MPW. To make the absorber compact, two absorber blocks made of Glid-Cop with different tilt angles of the surface have been arranged in tandem in the vacuum chamber. The front absorber intercepts the upper and lower parts of SR, and the rear one absorbs the central part of SR. The photon absorber will be installed in the front-end also in the summer of 2005.

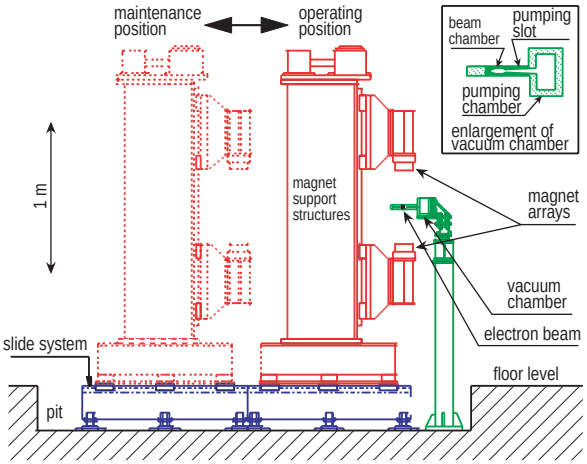

Fig. 8. Schematic of ID of accelerator diagnosis beamline II.

Other Topics

Damage of the injection chamber by aborted electron beam

The stored electrons in the storage ring should be aborted using the safety interlock. RF power supply would be turned off because the stored electrons should be aborted as soon as possible. The radius of electron orbits decreases and the electrons finally vanish on the chamber wall. The storage ring was operated with low-emittance optics between autumn 2002 and autumn 2003. In this case, most aborted electrons hit the thin stainless-steel wall (0.7 mm thickness of SUS316L) of the injection vacuum chamber. During the passage through the chamber material, electron energy is converted to heat by growth of the electromagnetic shower: the cascade reactions of bremsstrahlung, electron positron pair creation, multiple scattering and the ionization of electrons and positrons. The small electron beam size corresponds to the highly localized high-heat-load on the chamber. In October 2003, the thin wall of the injection chamber was broken due to such large heat load and vacuum leakage occurred as a result of the deformation and the cracking of the chamber wall due to the residual stress. Figure 9 shows the damaged thin wall of the vacuum chamber and etched cross sections of the damaged part. On the surface of the thin wall, some straight lines are seen, cause by the oxidization of stainless-steel due to the high-heat-load of electron beam passage. On the cross section, there are several features that are evidence of heat load: holes due to the meltdown, and resolidified solids after meltdown or semi-meltdown. These observations indicate that the aborted electrons hit the thin wall several times.

The damaged vacuum chamber was replaced by a spare one. Since October 2003, the normal-emittance optics has been employed for user time operation. A new injection chamber with an electron beam damper made of aluminum has been designed and is under construction. It will be installed in the summer of 2005, and the ring optics will be changed to a low-emittance optics.

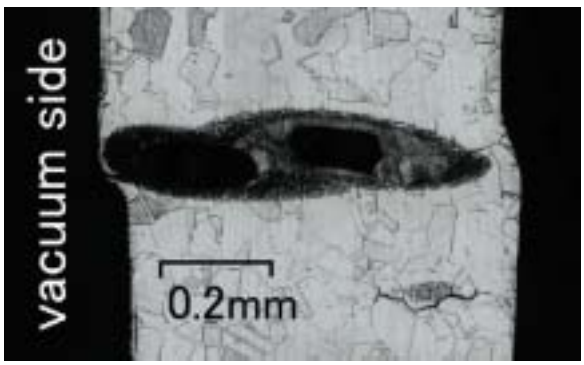

Fig. 9. Details of cross-section of stainless-steel chamber wall at the broken part.

HLS System [8]

In order to measure very slow ground movement over a wide area, a 50-meter-long hydrostatic leveling system (HLS) has been set up in the storage ring tunnel above a vehicle underpass. The system has 6 sensors at intervals of 5 or 10 m. The long-term movement from January to November of 2004 is shown in Fig. 10. It is clear that the level of the tunnel floor changes seasonally. The floor begins to rise from the lowest position in March and reaches the highest position in September. The level difference is 0.25 mm. The rate of change is 2 μm/day in June and July. The underpass is a π-shape structure 8-meters wide and 6-meters high viewed from the passage. The shape of this structure is considered to depend on the temperature gradient between the passage side and the inner tunnel or underground. The deformation occurs because of the expansion of sidewalls and bending of the floor.

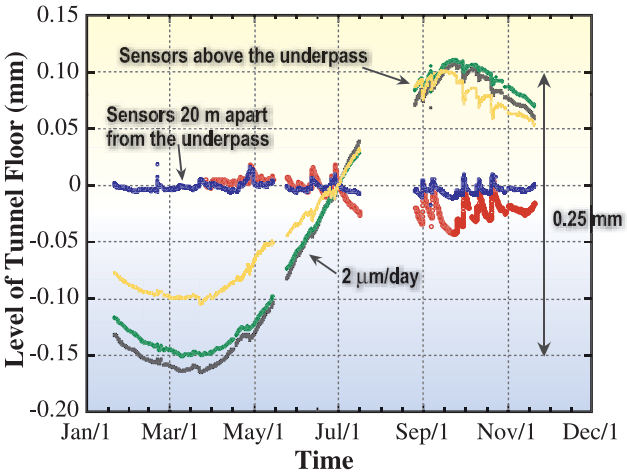

Fig. 10. Long-term movement of the tunnel floor above the vehicle underpass. The level changes by 0.25 mm from late March to September 2004. The rate of change is 2 μm/day.

Developments and Upgrades of Linac

Improvements towards top-up operation [9]

The SPring-8 linac has been improved since 1998 in order to provide beams with the stable energy and current; the energy stability has since been enhanced to 0.01% rms [10]. Temperature fluctuations in the klystron gallery, however, have not been negligible since 2002 when electric power saving of the linac began. We reduced the RF repetition rate from 60 Hz to 10 Hz for electric power saving in 2002 and accordingly observed remarkable room temperature drift in winter when the outdoor air temperature was low. These temperature variations caused the RF phase variations, as we experienced before 1998. The beam energies during acceleration from a buncher system to the end accordingly varied slightly, resulting in a distortion of the beam trajectory. We therefore investigated this room temperature issue to stabilize the trajectory fluctuations. The final beam energy, however, was stabilized by an energy compression system (ECS). The long-term energy stability was measured using BPM and OTR monitors. Figure 11 presents the beam energy variations before and after the ECS during a period of two days. The plotted energies before show the accidental reduction; the compensated energies, however, maintained the stability of 0.14% (p-p) throughout the measurement. Thus the ECS is effective in maintaining both shot-by-shot and long period beam energy stability.

The Linac is equipped with a bending magnet which switches a beam from the transport line for the New SUBARU storage ring to one for the booster synchrotron. In order to perform simultaneous top-up operation of the two rings, the previous block-type bending magnet was replaced with a fast-response bending magnet which could be momentary excited at short intervals. The new bending magnet must repeatedly turned on and off at short intervals to inject the beams frequently into both the synchrotrons. In order to achieve fast response and a small residual field, a 50A400 silicon steel plate 0.5 mm thick was chosen for the lamination-type yoke of the new magnet. The measured residual field was about 10 gauss, one-third of the previous field. A fast-response power supply was also fabricated for the new bending magnet. This power supply can excite the new magnet at 0.9 T with the rise/fall time of 200 ms.

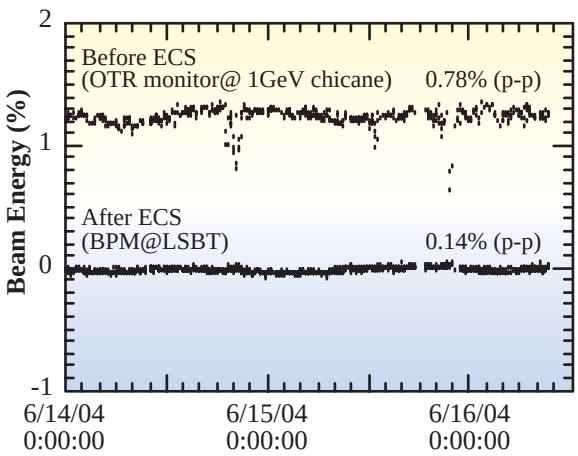

Fig. 11. Variations of the beam energy before and after ECS.

Study of high gradient acceleration

It is quite important to investigate high gradient acceleration for the development of RF guns, because an RF gun must stably maintain a high gradient of more than 100 MV/m in its RF cavity to reduce the beam emittance. The linac group has collaborated with KEK to study high-gradient acceleration with S-band accelerating structures.

It has been reported that a high-pressure ultrapure water rinsing (HPR) technique is very effective in improving the field gradients for accelerating structures. We have investigated the effectiveness of the HPR process to flush contamination in a traveling-wave accelerating structure. Results of the investigation at KEK revealed that the HPR treatment considerably accelerated the RF conditioning process of the accelerating structure and raised the possible maximum accelerating gradient [11].

In order to know what kind of phenomena has been promoted by RF conditioning and to understand the basic mechanism of RF discharge, we have diagnosed the RF breakdown by fast spectrographic analysis of atomic lines and quadrupole mass spectroscopic analysis [12]. Our results show that the HPR process may not completely flush carbon compounds and may cause water molecules to be injected into copper surfaces. We consequently proposed an alternative treatment, that is, a chemical etching method of dissolving contamination on copper surfaces such as dust and copper oxides [13].

We determined the optimum etching thickness by etching test pieces. The optimum value obtained, at which the surface roughness did not increase, was 0.3 mm. One RF gun cavity, which was RF-conditioned before, was processed by chemical etching with controlled etching time so as not to exceed the optimum etching thickness. The treated cavity was RF-conditioned at an RF gun test bench. Figure 12 presents results of RF conditioning of the cavity. Before the treatment the cavity could hold a maximum gradient of only 76 MV/m on a cathode after 3.3×10^7 shots of RF conditioning. The etching treatment, however, considerably accelerated the RF conditioning process and increased the gradient to 183 MV/m after 1.9×10^7 RF shots. The maximum gradient finally reached 187 MV/m. The measured quantum efficiency of the copper cathode reached 8.6×10^{-3} %.

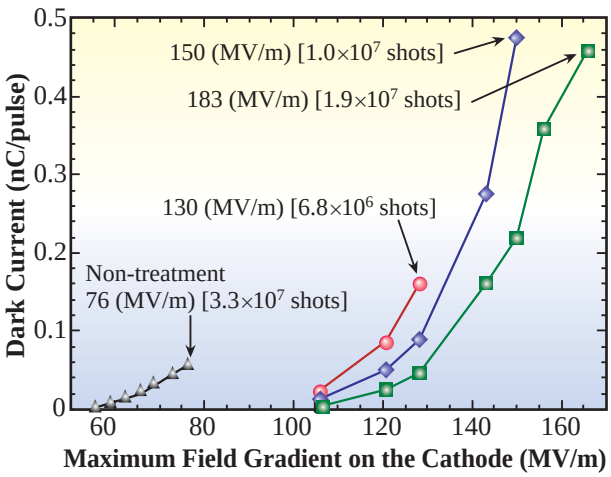

Fig. 12. Effect of RF conditioning of an RF gun cavity are expressed as variations of the dark current and the attained gradients on the cathode. The dark current at the gradient of 183 MV/m is not plotted because it was unstable.

References

[1] H. Tanaka *et al.*: EPAC 2004, Lucerne, Switzerland, p. 222.
[2] M. Takao *et al.*: EPAC 2004, Lucerne, Switzerland, p. 417.
[3] K. Fukami *et al.*: Proc. of APAC 2004, Gyeongju, Korea.
[4] T. Ohshima *et al.*: EPAC 2004, Lucerne, Switzerland, p. 414.
[5] H. Tanaka *et al.*: EPAC 2004, Lucerne, Switzerland, p. 1330.
[6] H. Takebe *et al.*: http://acc-web.spring8.or.jp/~takebe/mag/powersupply-E.html.
[7] T. Nakamura *et al.*: EPAC 2004, Lucerne, Switzerland, p. 2646.
[8] C. Zhang *et al.*: IWAA2002, SPring-8, Japan, (2002) 297.
[9] S. Suzuki *et al.*: EPAC2004, Lucerne, Switzerland, p.1327.
[10] H. Hanaki *et al.*: Proc. of APAC 2004, Gyeongju, Korea.
[11] Y. Igarashi *et al.*: Proc. of APAC 2004, Gyeongju, Korea.
[12] H. Tomizawa *et al.*: Applied Surface Sci. **235** (2004) 214.
[13] H. Tomizawa *et al.*: Proc. 29th Linear Accelerator Meeting in Japan, Funabashi (2004) 147 (in Japanese).

Haruo Ohkuma, Hiroto Yonehara,
Hirofumi Hanaki and Noritaka Kumagai
SPring-8 / JASRI

Insertion Devices

Development of Cryoundulators

Introduction

Short period undulators are an attractive light source for synchrotron radiation facilities. Since a short periodicity increases the number of undulator periods in a limited space of straight sections, higher brilliance can be obtained for undulator radiation. Also, short undulator periodicity enables the emission of high energy photons and opens the way for X-ray beamline operation in medium size facilities [1,2].

As the undulator periodic length decreases, the dimensions of the magnet pieces become smaller, and consequently, the undulator should be operated at small magnetic gaps in order to obtain sufficient magnetic fields. From this aspect, in-vacuum undulators, which accommodate permanent magnet arrays inside a vacuum chamber, are indispensable for the realization of short period undulators [3,4]. One example of an in-vacuum short-period undulator is the 11-mm-period undulator developed by collaboration between SPring-8 and NSLS. This undulator has been successfully operated at the gap of 3.3 mm for years in the NSLS storage ring [2]. However, this device has a blank region in its radiation spectrum which neither fundamental nor higher harmonics can cover, which is a drawback for some user experiments. The practical limit to the minimum undulator gap is determined by the effect to the electron beam. If the gap is too small, there is not only a reduction in beam lifetime, but also the possibility of demagnetization of the undulator magnets.

To solve these problems and realize shorter undulator period, high performance magnets are required. One prospective technology is superconducting magnets, which have been widely used as wigglers. Unlike wigglers, superconducting undulators operated at small gaps should endure a larger amount of heat load due to resistive wall effects of electron beams and synchrotron radiation from upstream bending magnets. However, superconducting devices are normally operated at around the temperature of liquid helium and the cooling capacity is limited to a few watts. Therefore careful consideration should be paid to this thermal budget problem, otherwise the device will be easily quenched [5].

At SPring-8, we are developing a new device for improving the undulator magnetic field performance, which we call the cryoundulator, using permanent magnets at the temperature of liquid nitrogen or higher, where a cryocooler of a few hundreds watts is easily achievable with the current technology [6,7].

Characteristics of permanent magnets at cryogenic temperatures

The permanent magnets used in the SPring-8 undulators are NdFeB magnets having the highest magnetic field performance among permanent magnet materials. Although there is a variety of NdFeB magnets, a magnet with sufficiently high coercivity (iHc) should be chosen for the in-vacuum undulator to ensure good field stability against demagnetization due to electron beam irradiation [8]. In general, NdFeB magnets with high iHc show small remanent field (Br). Therefore, the in-vacuum undulators do not take advantage of the highest magnetic field of NdFeB magnets. However, under the circumference of cryogenic temperatures, both iHc and Br increase with decreasing temperature, and high Br NdFeB magnets come to have sufficiently high iHc for the undulator magnet. This is the basic concept of the cryoundulator.

Figure 1 shows the measured Br and iHc of two NdFeB magnets as a function of temperature. 35EH is the magnet currently used in the SPring-8 in-vacuum undulators and 50BH is a typical high Br magnet. Both magnets show the highest magnetic field (Br) at temperatures around 140~150 K, and their iHc increases inversely proportional to the temperature. From Fig.1 (b), it is inferred that iHc of 50BH at 150 K (~3000 kA/m) exceeds the room temperature iHc of 35EH (~2000 kA/m). This means that the high Br magnet (50BH) at low temperature is more stable than the room temperature magnet (35EH) used for current

in-vacuum undulators [9]. This high Br magnet (50BH) is one of the candidate materials for the cryoundulator. Compared with conventional in-vacuum undulators, the expected magnetic field of the cryoundulator is superior by about 30% with better demagnetization characteristics.

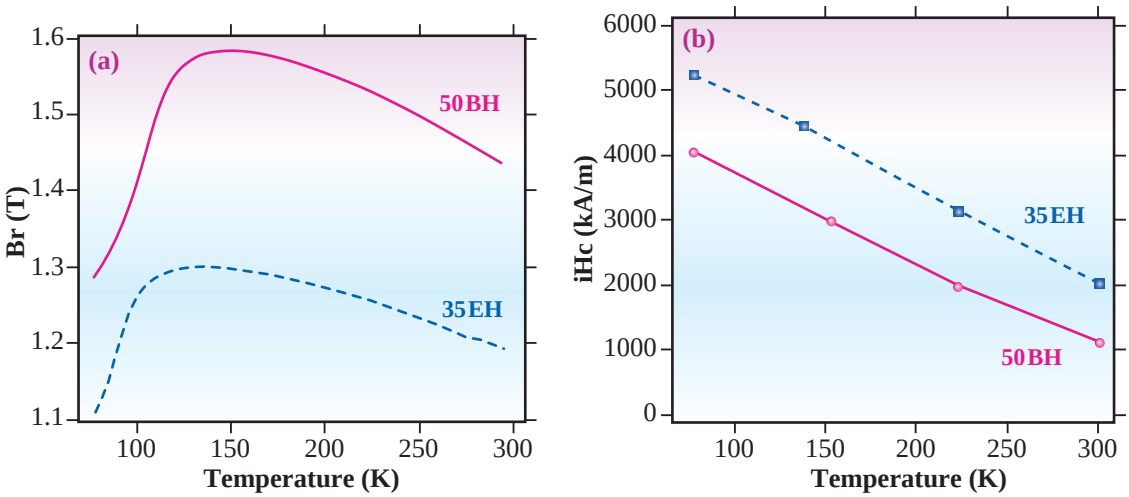

Fig. 1. Measured remanent fields Br **(a)** and coercivity iHc **(b)** of NdFeB magnets at cryogenic temperatures. 35EH is the magnet used in the SPring-8 in-vacuum undulators and 50 BH is a typical high Br magnet. 35EH and 50 BH are commercial products of NEOMAX Co., Ltd.

Prototype undulator

The construction of the cryoundulator requires only slight modification of the conventional in-vacuum undulators, since the magnet arrays are already placed under good thermal isolation with vacuum. A design example of the cryoundulator is shown in Fig. 2, where thermal insulation is enforced at the magnet supports and the undulator magnets are cooled by cryocoolers. A compact Gifford McMahon type cyocooler can provide sufficient cooling capacity of a few hundreds watts around the temperature of liquid nitrogen. The expected heat load of a 1.5-m-long undulator, for example, is about 130 W at the gap of 3 mm, assuming operation in SPring-8 in the 203 bunch mode.

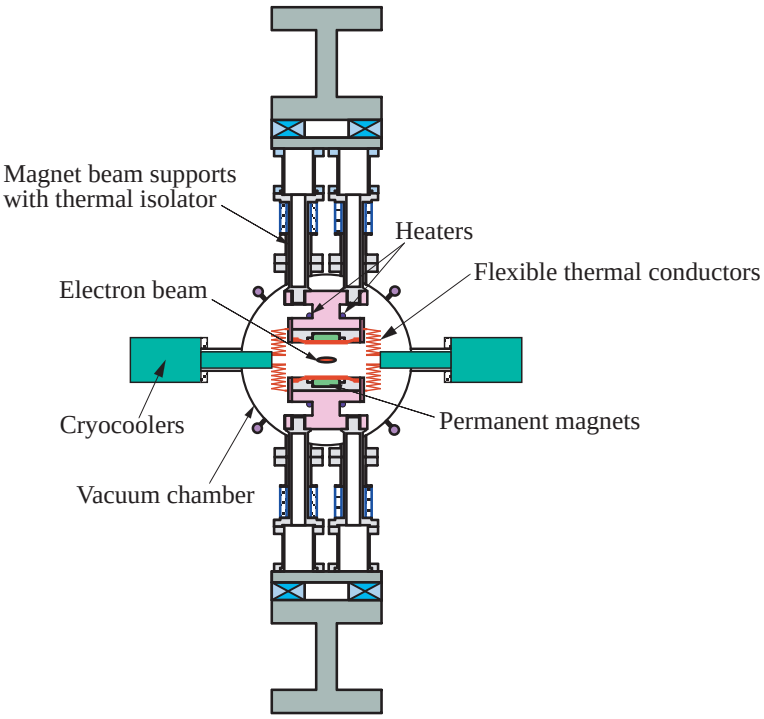

Fig. 2. Design example of the cryoundulator.

Figure 3 is a prototype cryoundulator under development at SPring-8, whose period is 15 mm. Using heaters, the temperature of the magnets is controlled to be the optimum temperature, at which the highest magnetic field can be obtained. Preliminary results of the magnetic field measurements show that the magnetic field errors do not depend on the temperature. This means that once the undulator field is aligned at room temperature, realignment at low temperatures is not necessary, which simplifies the procedure of undulator construction. Detailed field measurements are currently being carried out on this prototype undulator.

The cryoundulators will play an important role as a synchrotron radiation source, particularly in medium size facilities. They are also attractive for SASE-FEL facilities, since they lower the electron beam energy necessary for X-ray FEL operation, resulting in the reduction of the facility size [10]. Unlike superconducting devices, there is no worry concerning the quenching and thermal budget problem. Therefore, stable operation can be expected for the cryoundulators.

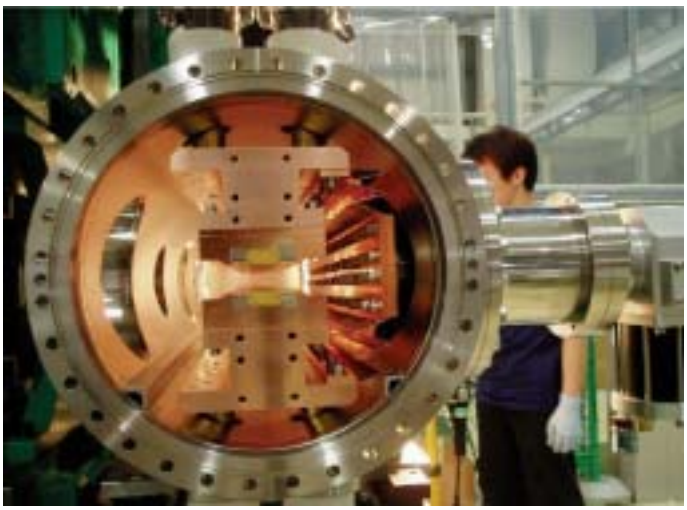

Fig. 3. Prototype of the cryoundulator developed at SPring-8. The undulator period is 15 mm and 50BH NdFeB magnets are used.

Toru Hara

SPring-8 / RIKEN

E-mail: toru@spring8.or.jp

References

[1] T. Schmidt *et al.*: Nucl. Instrum. Meth. A **467-468** (2001) 126.
[2] P.M. Stefan *et al.*: J. Synchrotron Rad. **5** (1998) 417.
[3] S. Yamamoto *et al.*: Review of Scientific Instruments **63** (1992) 400.
[4] H. Kitamura: J. Synchrotron Rad. **5** (1998) 184.
[5] E. Wallén: "Thermal budget of a cold bore superconducting insertion devices," Proc. of Workshop on Superconducting Undulators and Wigglers, June 30-July 1, 2003, Grenoble, France.
[6] *T. Hara, T. Tanaka, H. Kitamura, T. Bizen, X. Maréchal, T. Seike, T. Kohda and T. Matuura: Phys. Rev. ST. AB.* ***7*** *(2004) 050702.*
[7] H. Kitamura *et al.*: Proc. EPAC04 (2004) 59.
[8] T. Bizen *et al.*: AIP Conf. Proc. **705** (2004) 167.
[9] T. Bizen *et al.*: Proc. EPAC04 (2004) 2089.
[10] T. Shintake *et al.*: Nucl. Instrum. Meth A **507** (2003) 382.

Detectors

Introduction

The scientific results from the synchrotron radiation facility depend on the radiation source, optics such as monochromator and mirror, detectors, and data acquisition system adopted. From the beginning of the SPring-8 project, the importance of detectors was realized and detectors were properly included in the research and development program. Detectors are adopted on the basis of specific parameters such as their size, dimensionality, detection efficiency, energy range, energy resolution, spatial resolution, dynamic range, countability, and real-time measurement capacity, and as well as on the basis of their detection technique of either photon counting or integrating type, for each research program. Many detectors exist in the X-ray region, but none of them are universal applicable and detector development has to be performed for different kinds of synchrotron radiation experiments. An important point of their development is that the program has to be carried out in close collaboration with the user groups.

At SPring-8, there have been several development programs including an imaging plate, a CCD readout two-dimensional detector and a high-spatial-resolution CCD-coupled imaging system. In this issue of SPring-8 Research Frontiers, recent developments will be touched upon. The articles concern the One-dimensional Microstrip Germanium Detector for Compton scattering experiment, a Pixel Detector and Microstrip Detector for diffraction, scattering and time-resolved XAFS experiments, and a Flat Panel Detector for imaging. Previously, SPring-8 Research Frontiers 2003, the YAP imager was rreported and in the near future a Two-dimensional Microgap Detector will be described.

Tatzuo Ueki
SPring-8 / JASRI

One-dimensional Microstrip Germanium Detector

Upon being absorbed in semiconductors such as silicon or germanium, X-ray photons are converted into energetic electrons through mechanisms such as the photoelectric effect and Compton scattering process. Energetic electrons lose their energies by ionizing and exciting the local lattices of the absorbing semiconductors. When a sufficiently high electric field is established across the semiconductor with a parallel-plate electrode configuration, the electrons and holes that are generated through the ionization process can be separately collected on the anode and cathode, respectively. One could determine the X-ray energy by measuring the total charge collected on either electrode, since the total amount of charge is proportional to the X-ray energy absorbed in the semiconductor. If an electrode is segmented into strips in a certain direction, one could obtain information on the X-ray photons in terms of not only their energies but also their arrival locations, thus realizing position-resolved X-ray spectroscopy.

The one-dimensional microstrip germanium detector is the one that embodies the concept explained above (see Fig. 1) [1]. The X-ray absorption medium is a planar crystal of high-purity germanium (55.5 mm × 50.5 mm × 6 mm), which is cooled down to liquid nitrogen temperature in a cryostat in order to reduce the thermal noise. On the front surface of the crystal, 128 microstrips are photochemically formed with a length and pitch of 5 mm and 350 μm, respectively, as a segmented cathode, while a single electrode is formed on the back surface as an anode. These microstrips are connected to four external application-specific ICs, each functioning as a 32-channel charge sensitive preamplifier-shaper circuit. The anode is connected to an independent charge-sensitive amplifier system to measure the total charge created by an X-ray photon over the entire volume of the crystal. When the total charge detected on the anode exceeds the predetermined threshold, there is a trigger issued to sequentially readout the positive charges detected on the microstrips.

With the one-dimensional microstrip germanium detector system, one could perform position-resolved

X-ray spectroscopy with a position resolution, an energy resolution, and a dead time of 350 μm, ~5% at 100 keV, and 110 μs, respectively. Since the detector is insensitive to external magnetic fields, one could adopt it for experiments that need to employ high magnetic fields. The detector system has been developed for high-resolution Compton scattering experiments conducted at the High Energy Inelastic Scattering Beamline (**BL08W**), and has been yielding directional Compton spectra fifty times faster than traditional single-body germanium detectors.

Fig. 1. One-dimensional Microstrip Germanium Detector.

Masayo Suzuki

SPring-8 / JASRI

E-mail: msyszk@spring8.or.jp

References

[1] M. Suzuki, H. Toyokawa, K. Hirota, M. Itou, M. Mizumaki, Y. Sakurai, N. Hiraoka and N. Sakai: Nucl. Instrum. Meth. A **510** (2003) 63.

Pixel Detector and Microstrip Detector

Position-sensitive detectors are powerful devices for use in synchrotron radiation experiments. Imaging plates are representative of them, and CCD-based detectors have become a major tool for protein crystallography recently. These detectors, however, record X-ray intensity by integrating the energy deposited by X-ray photons. Conventional Si, Ge, and NaI detectors are, therefore, still essential instruments, when fluorescence background has to be rejected by energy discrimination. In this respect, pixel and microstrip detectors are regarded as a new generation of X-ray detectors, since they possess not only position sensitivity but also energy resolving power.

The SPring-8 detector team has been developing such a pixel detector in collaboration with the *Paul Scherrer Institut* (PSI) in Switzerland [1-3], which operates a 2.4 GeV third generation synchrotron radiation source called the *Swiss Light Source* (SLS). The developed pixel detectors consist of a number of detector modules. SPring-8 introduced a *Single-Module Detector* (SMD) in September 2002 (Fig. 1), which has a silicon sensor of 300 μm in thickness with an active area of 79.4 mm × 34 mm, and 366 × 157 pixels with a pixel size of 217 μm × 217 μm,

Fig. 1. A single-module pixel detector with 366 × 157 pixels.

associated with 8 × 2 readout electronics chips. The chip has 44 × 78 pixels, each having a charge-sensitive preamp, a shaper, a single-level discriminator, and a 15-bit pseudorandom counter. An individual pixel is thus capable of being operated in a single photon counting mode. The counters can be read out digitally with a frequency of 10 MHz. These conditions result in the maximum frame rate to 30 Hz with the readout time of 6.7 ms.

The SMD has been examined at beamlines **BL38B2**, **BL44B2** and **BL46XU** of SPring-8 so far. The former two beamlines are for protein crystallography, and the last one is for instrumental R&D. Although the SMD is a prototype with about 5% dead pixels due to the DMILL process, it realizes a sufficiently high performance to allow the methodological study of its fields of applications. For protein crystallography, the major advantages of the SMD are that the readout time is much faster than that of a CCD-based detector, and that a mechanical shutter is unnecessary for definition of the exposure time. In materials science, on the other hand, its major advantage is its ability to discriminate among low-energy X-rays below a certain threshold.

The SLS detector group is currently developing an advanced pixel detector which has 60 × 97 pixels with a pixel size of 172 μm × 172 μm and 20-bit binary counters by improving the readout chips with a 0.25 μm CMOS process. The readout chips were delivered to SLS in December 2004, and no dead pixels were found in four chips selected at random. The goal of the SPring-8 and SLS collaboration is to fabricate a 6M-pixel detector for the protein crystallography beamline of the SLS and to produce a general-purpose 1M-pixel detector for SPring-8.

A microstrip detector module was also introduced from the PSI to SPring-8 in February 2004 (Fig. 2), which is a one-dimensional detector consisting of a silicon sensor with 1280 strips and 10 readout chips [2]. The strip length, the pitch, and the thickness are 8 mm, 50 μm, and 300 μm, respectively. The design concept of this readout chip is, in principle, the same as the one for the pixel detector described above, except that the counter has 18 bits. The readout time is 250 μm. Such a fast readout time allows time-resolved measurements. This single module microstrip detector has been examined at the BL46XU by carrying out powder diffraction measurements.

Now SPring-8 is introducing additional microstrip detector modules to realize time-resolved studies at a powder diffraction beamline and a dispersive XAFS beamline.

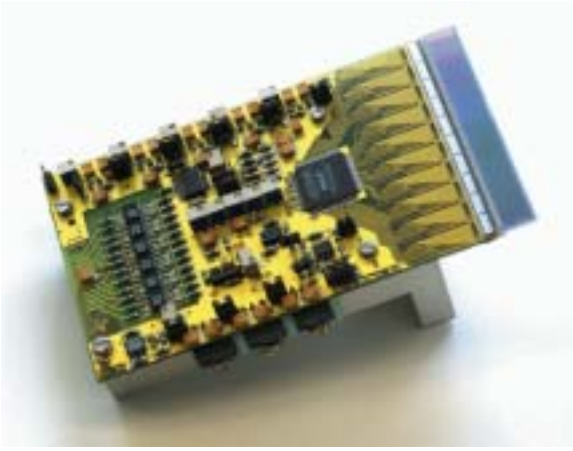

Fig. 2. A single-module microstrip detector with 1280 strips.

Hidenori Toyokawa* and Masayo Suzuki

SPring-8 / JASRI

*E-mail: toyokawa@spring8.or.jp

References

[1] E.F. Eikenberry *et al.*: Nucl. Instrum. Meth. A **501** (2003) 260.
[2] B. Schmitt *et al.*: Nucl. Instrum. Meth. A **518** (2004) 436.
[3] Ch. Brönnimann, Ch. Bühler, E.F. Eikenberry, R. Horisberger, G. Hülsen, B. Schmitt, C. Schulze-Briese, M. Suzuki, T. Tomizaki, H. Toyokawa, A. Wagner: Synchrotron Rad. News **17** (2004) 23.

Flat Panel Detector

A flat panel detector (FPD, C7942-CA, Hamamatsu Photonics K.K.) was installed and used for large field X-ray imaging including X-ray diffractions (Fig. 1). The FPD consists of a scintillator (needle-like CsI crystals) and a complementary metal-oxide semiconductor (CMOS) photodiode array. Its characteristics are described in Table 1.

The advantages of the FPD over other image detectors are its compactness and low cost. Its weight is about 3 kg and its thickness is about 3 cm, and, therefore, it can be positioned anywhere in an experimental setup quite easily. Its cost is at least one order of magnitude lower than that of a CCD-based detector for protein crystallography with a similar number of pixels.

The performance of the FPD was tested [1]. The tests determined the conversion gain, noise, spatial resolution, and linearity. The preliminary results are also described in the previous report. A small angle X-ray diffraction pattern of a dried tendon of chicken, a diffraction pattern of a lysozyme crystal and refraction-enhanced X-ray image of rat were reported. The experimental results showed that the FPD was already suitable for application to synchrotron radiation experiments, however, some corrections were necessary for quantitative analysis.

Table 1. Characteristics of C7942-CA.

Number of pixels	2240×2368
Pixel size (μm)	50
Readout time	0.44 (eight channel)
Dark current (e^- $pixel^{-1}$ s^{-1})	5900
Readout noise (R.M.S., e^-)	1100
AD converter (bits)	12
Maximum charge (e^- $pixel^{-1}$)	2.2×10^6
Electrons per ADU	500
Electrons per X-ray photon	165 @ 12.4 keV
Resolution (LP mm^{-1})	8
Phosphor	CsI:Tl
Operating temperature	Room temperature
Size (mm)	200×198×28
Weight (kg)	3.2

The FPD is used at beamline **BL20B2** for optical alignment of large size beams, topography and refraction enhanced imaging, at **BL28B2** for topography, and at **BL13XU** for X-ray diffraction.

Fig. 1. Photograph of flat-panel detector. The frame drawn in black is the detection area, which has an area of 112 mm × 117 mm.

Kentaro Uesugi

SPring-8 / JASRI

E-mail: ueken@spring8.or.jp

References

[1] N. Yagi, M. Yamamoto, K. Uesugi and K. Inoue: J. Synchrotron Rad. **11** (2004) 347.

New Apparatus & Upgrades

High-Resolution Micro-CT System using 10-Megapixel-CCD X-ray Detector

A micro-CT (computed tomography) system, shown in Fig. 1, was developed using a 10-megapixel CCD camera for 3D biomedical imaging [1]. The detector consists of a beryllium window for X-ray incidence, a fluorescent screen, an optical mirror, high-numerical-aperture lenses and the CCD camera. X-rays are converted into a visible image on the screen with a thickness of 10 μm. The screen and mirror are built in behind the beryllium window. The mirror deflects the luminescent light by 90° to the lens system that focuses the light onto the camera. The X-ray field of view is 24 mm wide × 16 mm high (4024 × 2648 pixels); each pixel measures 6 × 6 μm^2.

A rabbit auricle specimen implanted with a carcinoma was fixed in formalin and sealed in the specimen case in the micro-CT system (Fig. 1) after a barium sulfate solution was injected into blood vessels as a contrast agent. Projection images were recorded from 1800 views during 180-degree rotation. Three-dimensional images of the specimen, shown in Fig. 2 were obtained by tomographic reconstruction, and small blood vessels induced by the tumor were visualized. The avascular area at the center is dead tumor tissue. In contrast, the number of blood vessels increased markedly around the avascular area, where tumor cells were vital and the tumor's growth rate was rapid.

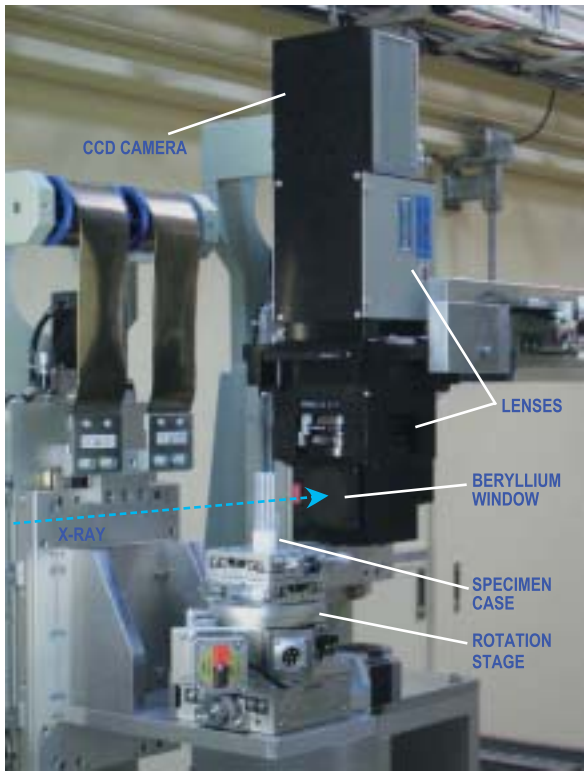

Fig. 1. Micro-CT system with 10 megapixels.

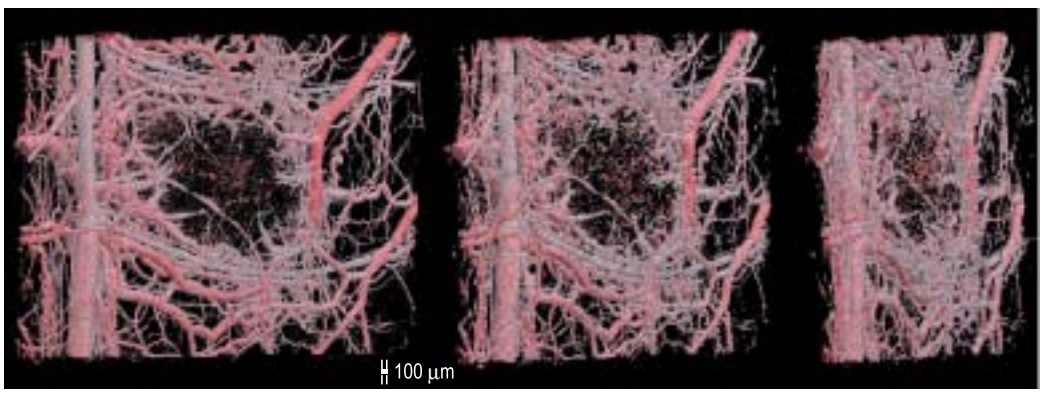

Fig. 2. Three-dimensional images of a tumor surrounded by the network of blood vessels induced by the tumor. The images are shown at viewing angles of 0 (front view), 30, and 60 degrees, from left to right.

Keiji Umetani

SPring-8 / JASRI

E-mail: umetani@spring8.or.jp

References

[1] *K. Umetani, K. Uesugi, N. Yagi, M. Kobatake, A. Yamamoto, T. Yamashita, S. Imai, and Y. Kajihara: to be published in Nucl. Instrum. Meth.*

Extending the Limits of Inelastic X-ray Scattering: 12 Analyzers and 1 meV Resolution

Inelastic X-ray scattering is a technique that pushes the limits of what is possible with even a third generation synchrotron radiation facility: ~meV bandwidths and small inelastic cross sections mean that nearly all experiments are severely flux limited. There is strong impetus to improve the SPring-8 instrument, both to maximize the use of the available flux and to improve the resolution. In fact, better resolution is generally accompanied by a reduction of flux on the sample, and so drives the push to become more efficient. We embarked on an ambitious plan to improve the performance of the **BL35XU** spectrometer [1]: tripling the number of analyzers and improving the resolution to 1 meV. This involved modifying nearly all the optical components of the beamline downstream of the high-heat-load monochromator.

Our first step was reduction of the heat-load onto the backscattering crystal. The ~100 mW monochromatic X-ray beam is enough to cause local heating and lattice distortions at the level of parts in 10^8, degrading the resolution. While this problem was partially solved by using a grazing incidence geometry to distribute the power on the backscattering crystal [2], additional power load reduction was needed to attain 1 meV resolution. In the original beamline design [1], Fig. 1(a), a pair of Si (111) crystals was used *downstream* of the backscattering monochromator to shift the beam vertically and provide space at the sample position. We moved these crystals *upstream* of the backscattering monochromator, Fig. 1(b). The Si(111) crystals used previously were replaced with Si(220) crystals. These crystals, cut asymmetrically, accept the full angular divergence of the beam from the high-heat-load monochromator but reduce the bandwidth of the beam from ~3.5 eV at 25.7 keV after the Si(111) crystals to ~2.1 eV, a crucial reduction in terms of heat load.

The upgrade from 4 to 12 analyzer crystals involved replacing the analyzer stages, slit system and detector on the 10 m arm of the spectrometer, as well as tripling the number of temperature control channels. While no major conceptual changes were needed, a lot of new equipment had to be installed and debugged. The general setup is shown in Fig. 2.

The new crystal mounts and slits were carefully designed to minimize the center-to-center spacing of the analyzers, as this improves the quality of data from both liquids and solids. A 120 mm center-to-center spacing was chosen for the 100-mm-diameter analyzers in the 10-m chamber. Likewise, the slit system required some care, with, finally, a venetian-blind-style system (see Fig. 2) allowing maximum angular acceptance with little dead space.

A new 12-channel detector system was also installed near the sample location with detector elements both above and below the path of the beam from the sample. The detector elements are CZT and operated at room temperature. They perform very well, with good pulse height response (3 to 4 keV FWHM, without a low-energy tail), essentially 100% stopping power, and low dark-count rates, ~ 5×10^{-4} Hz in our energy range of interest, 16-26 keV.

Present spectrometer performance is summarized in Table 1, for one of our better analyzer crystals. It is worth emphasizing that the unique two-dimensional analyzer array of this instrument makes it possible to efficiently measure both longitudinal phonons *and* transverse phonons using, respectively, horizontal and vertical lines of analyzers along high symmetry directions.

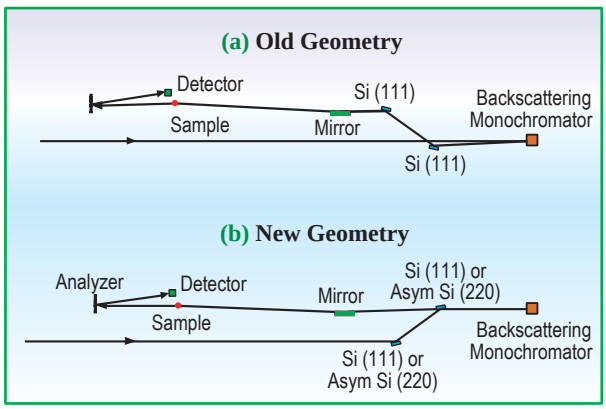

Fig. 1. Re-arrangement of the optics to allow 1 meV energy resolution.

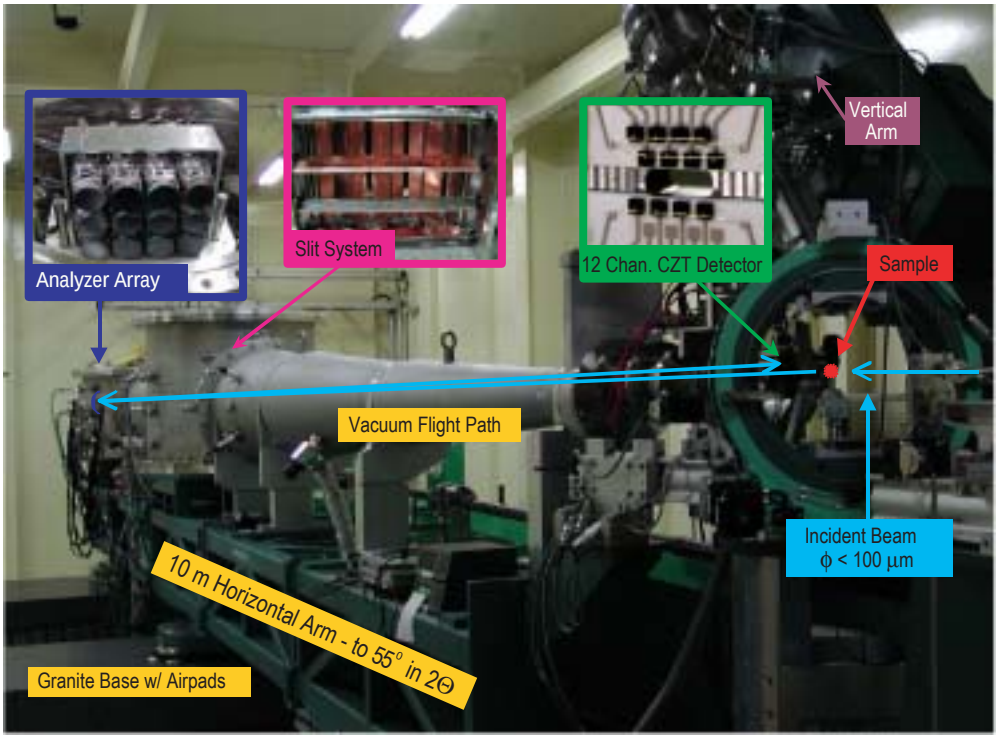

Fig. 2. Photograph of the 10 m arm from a viewpoint just upstream of the sample location. Insets show various pieces of equipment, as labeled. Please note the scale changes: the analyzer array has 12 circular analyzers visible, each 10 cm in diameter, while the detector chips are only 2.5 × 2.5 mm^2.

Table I. Summary of spectrometer performance with one of the better analyzer crystals. Spot size ~70 × 90 μm^2. FWHM at the sample.

Si Order (nnn)	Energy (keV)	Single Reflection Bandwidth (meV)	Flux at Sample (GHz)	Resolution FWHM (meV)
8	15.816	4.1	30	5.9
9	17.794	1.8	10	2.9
11	21.747	0.8	4	1.5
13	25.702	0.35	0.7	0.95

Alfred Q. R. Baron*, John P. Sutter and Satoshi Tsutsui

SPring-8 / JASRI

*E-mail: baron@spring8.or.jp

References

[1] A.Q.R. Baron *et al.*: J. Phys. Chem. Solids **61** (2000) 461.
[2] *A.Q.R. Baron, Y. Tanaka and S. Tsutsui, SPring-8 Research Frontiers 2001/2002, p. 104; A.Q.R. Baron et al.: in preparation.*

New Surface Microscopy – Spectroscopic Photo-emission Electron Microscopy and Low Energy Electron Microscopy (SPELEEM) with Synchrotron Radiation

A new type of surface electron microscope (SPELEEM) that uses synchrotron radiation light (SR-SPELEEM) [1] was installed at SPring-8 and has been offered for public use since this year (2004) [2]. This instrument includes a low energy electron microscope (LEEM) and a photoemission electron microscope (PEEM) with an energy filter. This microscope has recently received much attention in the surface science, nanoscience and nanotechnology because it can produce dynamic images of the surface dynamics at a video rate and a wide variety of technical information. For example, it provides high-resolution (better than 10 nm) LEEM images at surface regions, LEED patterns (surface structure analysis possible at 200-300 nmϕ), high-resolution (better than 10 nm) magnetic domain images of single crystals when using an electron spin source, high-resolution (20-50 nm) X-ray photoelectron spectroscopy (XPS) images, high-resolution (50 nm) X-ray absorption near edge spectroscopy (XANES) images and high-resolution (50-100 nm) magnetic domain images of any material with MCD and MLD. In particular, the high-spatial-resolution (20-50 nmϕ) chemical bonding information at surfaces and the magnetic domain images are almost impossible to obtain with other types of instruments. This SPELEEM is now tentatively installed at the public soft X-ray beamline of **BL27SU**, as shown in Fig. 1. Already, several interesting results have been obtained on the studies of chemical bonding in oxidation of Fe surfaces, Co/Si(111) and In/Si(111) surfaces, and magnetic domains in NiO. This type of instrument was, for the first time, installed at ELETTRA (Trieste, Italy) a few years ago, and three other SR facilities (BESSY II, Germany; SLS, Switzerland and DLS, Great Britain) have installed or started to install the same or a similar type of SPELEEM. The SPELEEM will be installed at beamline **BL17SU** from summer 2005,

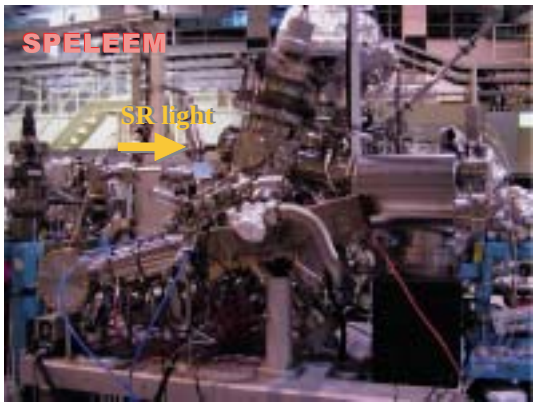

Fig. 1. SPELEEM installed at BL27SU.

which will enable users to address various kinds of issues under much more stable conditions.

Here we describe several examples of results obtained with SPELEEM using BL27SU. Figure 2 shows that "nano-XANES" observation is possible by integrating image intensities in fixed areas of nanosize, while scanning photon energy across target absorption edges. Figure 2(a) shows XANES spectra of a Co-deposited Si(111)7×7 surface [2]. After annealing at *ca.* 600 ºC, the surface exhibited the formation of Co silicide islands, which were surrounded by flat regions, as shown in Fig. 2(b). The red and blue curves in Fig. 2(a) are $L_{2,3}$ XANES

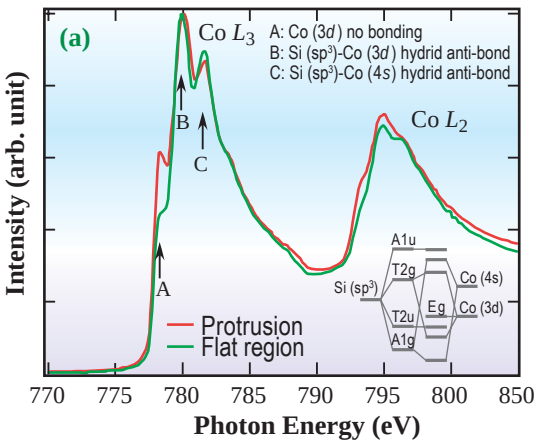

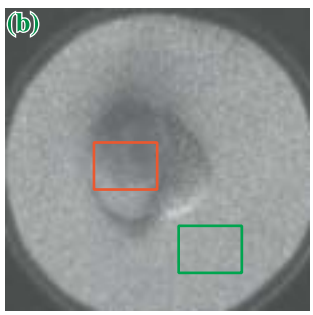

XPEEM (FOV 30 μm, *hν* 780 eV)

Fig. 2. **(a)** Micro-XANES of $CoSi_2$ and the surrounding flat regions. The inset shows the energy diagram of Si-Co hybridization. **(b)** XPEEM image of Co/Si(111) surface. The protrusion corresponds to $CoSi_2$.

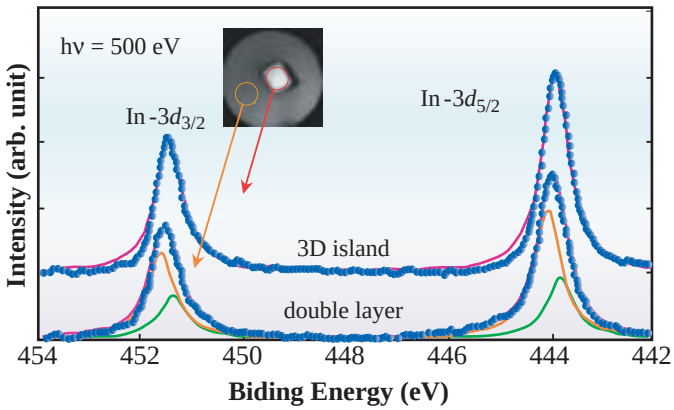

Fig. 3. XPS spectra from double layer and 3D island. Accumulation time for each spectrum was 300 s.

spectra of the island and flat regions, respectively. Three structures are clearly resolved in the L_3 absorption edge. These are assigned to transitions from Co $2p_{2/3}$ to nonbonding, bonding Si(sp^3)-Co(3*d*), and bonding Si(sp^3)-Co(4*s*) states. Interestingly, it is noted that the nonbonding structure is more pronounced in the island region than in the flat region, suggesting a weaker Si-Co hybridization in the chemisorbed flat region.

As an example of "nano-XPS," $3d_{3/2}$ and $3d_{5/2}$ core spectra are measured in the In 3D island and In double-layer regions on a Si(111) surface, as denoted by circles in the inset of Fig. 3. To obtain the surface in which 3D islands and the double In layer coexist, we evaporated In onto the Si(111)7×7 surface at approximately 500 ºC and cooled it to room temperature during the evaporation. The spectrum obtained from the double layer is decomposed into two components, which may be considered to be as to originating from surface and interface atoms with charge transfers in opposite directions to each other.

As a new development, we are now improving the spatial resolution of PEEM by correcting the spherical aberration by the "moving focus method (MOF)" proposed by Ikuta [3,4]. This project, supported by MEXT, is now being carried out by Koshikawa's group [5]. Sub-ten-nm-resolution XPS images are expected. The PEEM images that were tentatively obtained with a Hg lamp in a laboratory at Osaka Electro-Communication University is shown in Fig. 4. This method will be applied to SR-SPELEEM in the near future in order to improve the resolution.

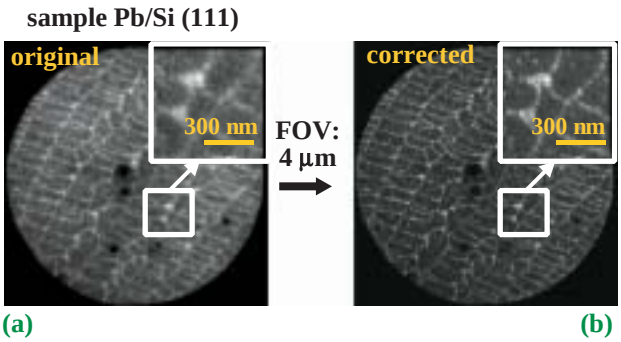

Fig. 4. **(a)** Original PEEM image, **(b)** PEEM image with aberration corrected by "MOF."

Takanori Koshikawa[a,*], Keisuke Kobayashi[b] and Fangzhun Guo[b]

(a) Fundamental Electronics Research Institute, Osaka Electro-Commun. University
(b) SPring-8 / JASRI

*E-mail: kosikawa@isc.osakac.ac.jp

References

[1] Th. Schmit et al.: Surf. Rev. Letters **5** (1998) 1287.
[2] *F.Z. Guo, T. Wakita, H. Shimizu, T. Matsushita, T. Yasue, T. Koshikawa, E. Bauer and K. Kobayashi: J. Phys.: Condens. Matter.* ***17*** *(2005) 1363.*
[3] T. Ikuta: Appl. Opt. **24** (1985) 204.
[4] T. Ikuta: J. Electron Microsc. **38** (1989) 415.
[5] *T. Koshikawa, H. Shimizu, R. Amakawa, T. Ikuta, T. Yasue and E. Bauer: J. Phys.: Condens. Matter.* ***17*** *(2005) 1371.*

Development of Monochromator Stabilization System

The stability of a photon beam is a serious problem in the case of third generation light sources. A beam position stability in the order of microns is required to transport a small beam to a sample position, at a distance of more than 50 m from the source point. In SPring-8, due to the efforts to improve the performance of the storage ring, the fluctuation of the electron beam orbit was reduced to few μm per day. However, instabilities in the photon beam intensity and in the position at the sample location were observed.

One of these instabilities is caused by the double-crystal monochromators (DCM). The DCM is equipment used to tune the X-ray energy via the Bragg reflection of the two monochromator crystals with a parallel arrangement. If there is an instability in the parallel arrangement, the energy, position, and intensity of the exit beam become unstable. Moreover, since many users set a slit width of less than 100 μm × 100 μm for a sample, the beam position fluctuation causes a further instability in beam intensity. To stabilize the exit beam from the DCM, we introduced the monochromator stabilization system (MOSTAB). This was originally designed as a system that maintains a constant beam intensity [1], and has been widely used at synchrotron radiation facilities.

We developed a MOSTAB with mode selectivity for stabilizing the beam position or intensity in SPring-8 [2,3]. Since the beam position and intensity from the DCM correlate with each other, both are similarly stabilized by single feedback control. The MOSTAB is shown in Fig. 1. The beam position or intensity is measured using a beam position monitor (BPM) [4] or an ionization chamber, and is fed to a control electronics

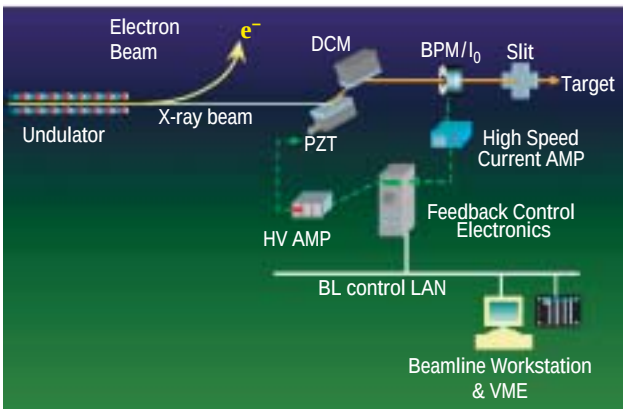

Fig. 1. Schematic diagram of MOSTAB. In this diagram, the feedback electronics is controlled by a workstation-based software. In addition, we have developed a PC-based control software as an alternative.

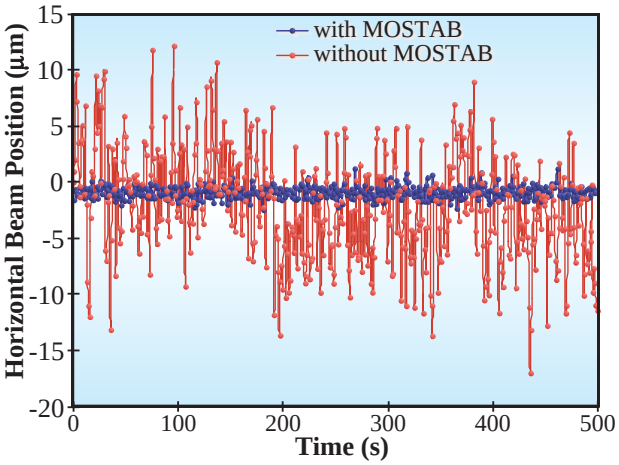

Fig. 2. Beam position stabilization using MOSTAB and BPM at beamline BL46XU experimental hutch. The standard deviation of the beam position was reduced from 4.9 μm to 0.5 μm. The beam energy provided by the Si(111) DCM was 24 keV.

system with an embedded a digital signal processor. It calculates the feedback voltage that is applied to a high-voltage amplifier for driving a piezo translator (PZT). Then the angle of the first crystal of the DCM is tuned by the PZT. A workstation-based control software automatically provides proper feedback parameters to the system at any energy setting of the DCM [5]. The software also enables or disables the MOSTAB on the basis of the status of the beamline and storage ring. All the hard X-ray beamlines in SPring-8 have identical SPring-8 standard monochromator and control systems; hence, it is easy to install the MOSTAB. Presently, 13 beamlines utilize the MOSTAB. Figure 2 shows the result of beam position stabilization with the MOSTAB at R&D beamline BL46XU.

Togo Kudo

SPring-8 / JASRI

E-mail: kudo@spring8.or.jp

References

[1] A. Krolzig *et al.*: Nucl. Instrum. Meth. **219** (1984) 430.
[2] Y. Nishino *et al.*: Proc. of SPIE **5195** (2003) 94.
[3] *T. Kudo, Y. Nishino, M. Suzuki, H. Tanida, Y. Furukawa, T. Hirono and T. Ishikawa: J. Jpn. Soc. Synchrotron. Rad. Res.* ***16*** *(2003) 173.*
[4] R. Alkire *et al.*: J. Synchrotron Rad. **7** (2000) 61.
[5] Y. Furukawa: BioXHIT Workshop on Automated X-ray Provision, ESRF, Grenoble, France (2004).

Facility Status

Machine Operation

The operation statistics since the facility was opened to users are shown in Fig. 1. Before summer the shutdown in 2004, the SPring-8 storage ring was operated on four- or five-week period for one operation cycle. After the summer shutdown, the long-term operation cycle was started. The total operation time of the accelerator complex was 5759.2 hours, of which 79.7% (4590.9 hours) was made available to the users. In 2004, there was no injection time because top-up injection was being introduced. The down time due to failure accounted for 1.4% (82.4 hours) of the operation time; in October 2004, a great loss of user time was incurred due to an approaching typhoon, consequently, user time of 28.6 hours was canceled for the suspension of machine operation. The remaining 18.9% (1085.9 hours) was dedicated to (i) machine and beamline study, (ii) machine and beamline tuning, and (iii) the commissioning of new photon beamlines. The high availability (ratio of the net user time to planning user time) of 98.% was achieved.

The operation modes of three different filling patterns were provided for the user time: 36.6% in the multi-bunch mode operation; 43.8% in the several-bunch mode such as the 203-bunch mode (203 equally spaced bunches) and 29 equally spaced 11-bunch trains; and the 19.6% in the hybrid filling mode such as a 1/12-partially filled multi-bunch with 10-isolated bunches. For the hybrid filling mode, 1 or 1.5 mA is stored in each isolated bunch. An isolated bunch purity of better than 10^{-9} is routinely maintained in the top-up operation.

Table I presents a summary of the useful beam parameters of the storage ring. The ring optics were returned to the former HHLV optics from October 2003. In September 2005, the low-emittance optics will be re-introduced to user time with a top-up operation by breaking the achromatic condition.

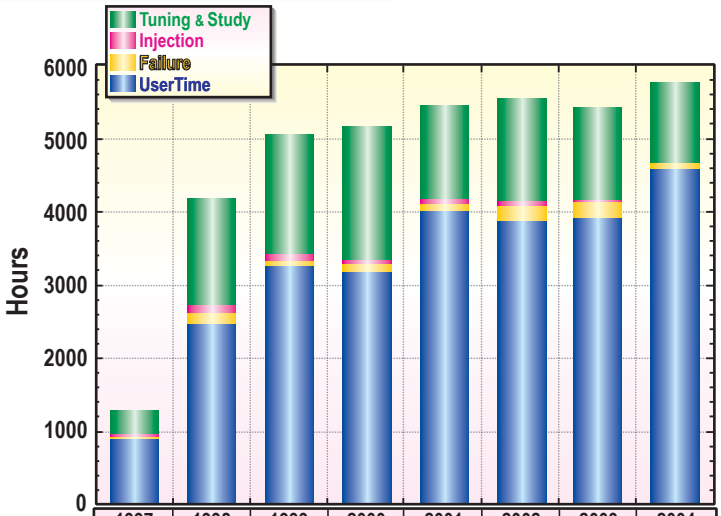

	1997	1998	1999	2000	2001	2002	2003	2004
Accelerator Operation Time	1286	4189.6	5051.6	5167.5	5456.1	5542.9	5419.5	5759.2
Storage Ring Operation Time	1270.6	4135.4	4863.9	4972.9	5340.6	5484.1	5328.5	5736.7
Tuning & Study (Accel. & BL)	304	1457.6	1624.2	1815	1276.5	1394.9	1245.8	1085.9
Injection	50	110	95.2	70.4	59.3	60.8	39.2	0
Failure	26	110	57.2	88.7	87.1	190.5	208.5	82.4
User Time	906	2512	3275	3193.4	4033.2	3896.7	3926	4590.9
Planning Time	984	2712	3432	3352	4176	4152	4176	4680
Availability (%)	97.2	96.7	98.2	97.4	98	95.3	95	98.1

Fig. 1. Operation statistics since the facility became available to users.

	HHLV Optics	Low Emittance Optics
Tunes (ν_x / ν_y)	40.15 / 18.35	40.15 / 18.35
Current[mA]: single bunch	13	10
multi bunch	100 (120 *1)	100
Bunch length (FWHM) [psec]	32	34
Horizontal emittance [nm·rad]	6.3 *2 / 6.6 *3	3.1 *2
Vertical emittance [pm·rad]	16.9 *3	8.7 *3 / 3.9 *4
Coupling [%]	0.26 *3	0.28 *3 / 0.13 *4
Beam size [μm]: (σ_x / σ_y) *5		
Long ID section	381 / 13.4	283 / 11.4
ID section	397 / 8.5	289 / 7.2
BM section	149 / 21.0	103 / 15.2
Beam Divergence [μrad]: ($\sigma_{x'}$ / $\sigma_{y'}$) *5		
Long ID section	16.1 / 1.2	11.9 / 0.81
ID section	15.9 / 1.9	11.7 / 1.3
BM section	57.4 / 0.78	53.8 / 0.68
Operational Chromaticities: (ξ_x / ξ_y)	+7 / +6 (+2 / +2) *6	+8 / +8
Lifetime [hr]: 100 mA (multi bunch)	~ 150	~ 97
1 mA (single bunch)	~ 24	~ 9
Dispersion distortion [mm]: horizontal (rms)	4	9.3
vertical (rms)	1.1 *7	1.1 *7
Orbit stability (tune harmonics) [μm]:		
horizontal (rms)	–	1.3
vertical (rms)	–	0.35

*1 Maximum stored beam current at machine study.
*2 Measured by a pulse bump and scraper, *3 two dimensional interferometer, and *4 two photon correlation.
*5 Assuming that 0.26% coupling for "HHLV" and 0.2% coupling for "Low Emittance Optics"
*6 With bunch-by-bunch feedback. *7 With correction by 24 skew Q's.

Table I. Beam parameters of SPring-8 storage ring

BEAMLINES

SPring-8 beamlines are categorized into the following groups.

(1) Public Beamlines
(2) Contract Beamlines
(3) JAERI / RIKEN Beamlines
(4) Accelerator Beam Diagnosis

The public beamlines were constructed by JAERI and RIKEN on government grants and are available for public use. Among them, three beamlines have been used for R&D. Since the 2005A period, the status of the three R&D beamlines has been changed to public beamlines on the recommendation of the R&D Beamline Review Committee, although one of the three (BL46XU) temporarily retained its R&D function. At present, 25 public beamlines (22 X-ray beamlines, two soft X-ray beamlines and one infrared beamline) are operational and available for public use.

The contract beamlines are, on the other hand, installed, owned, operated and maintained by universities, companies and other organizations for exclusive use by contractors. Twenty percent of beamtime is, in principal, offered to public use by contract. Hyogo Prefecture took the lead in contract beamline construction, followed by Industrial Consortium, National Synchrotron Radiation Research Center (NSRRC, Taiwan), Institute for Protein Research (Osaka Univ.), Research Center for Nuclear Physics (RCNP, Osaka Univ.), National Institute for Materials Science, and Pharmaceutical Consortium, in that order. NSRRC was the first to construct foreign contract beamlines (BL12B2 and BL12XU) at SPring-8. Currently, these nine contract beamlines are all in operation.

The JAERI/RIKEN beamlines are those constructed by JAERI and RIKEN for the exclusive use to promote their own research activities, although 20% of beamtime is reserved for public use. JAERI has already been constructed four beamlines. Experimental stations of BL22XU and BL23SU are located at RI Laboratory and dedicated to research utilizing radioactive isotopes and actinide materials. RIKEN has constructed six beamlines. As of April 2005, one beamline (BL17SU) has been in the commissioning phase. BL19LXU is the sole long undulator beamline and can provides the highest brilliance of all beamlines. BL26B1 and BL26B2 are beamlines used for high throughput protein crystallography in the line with the human genome project. BL29XU has two experimental stations, one located in the experimental hall, and the other at the end of the 1 km beamline.

Dedicated to studying the characteristics of the electron beam accumulated in the storage ring, the accelerator beam diagnosis beamlines are currently under the exclusive use of the JASRI accelerator group.

All 62 beamlines that SPring-8 can accommodate (34 insertion devices, 4 long undulators, 23 bending magnets and 1 infrared) are shown on the Beamline Map (Fig. 2). Including the two accelerator beam diagnosis beamlines, there are 47 beamlines, which is about 75% of full capacity (Table II).

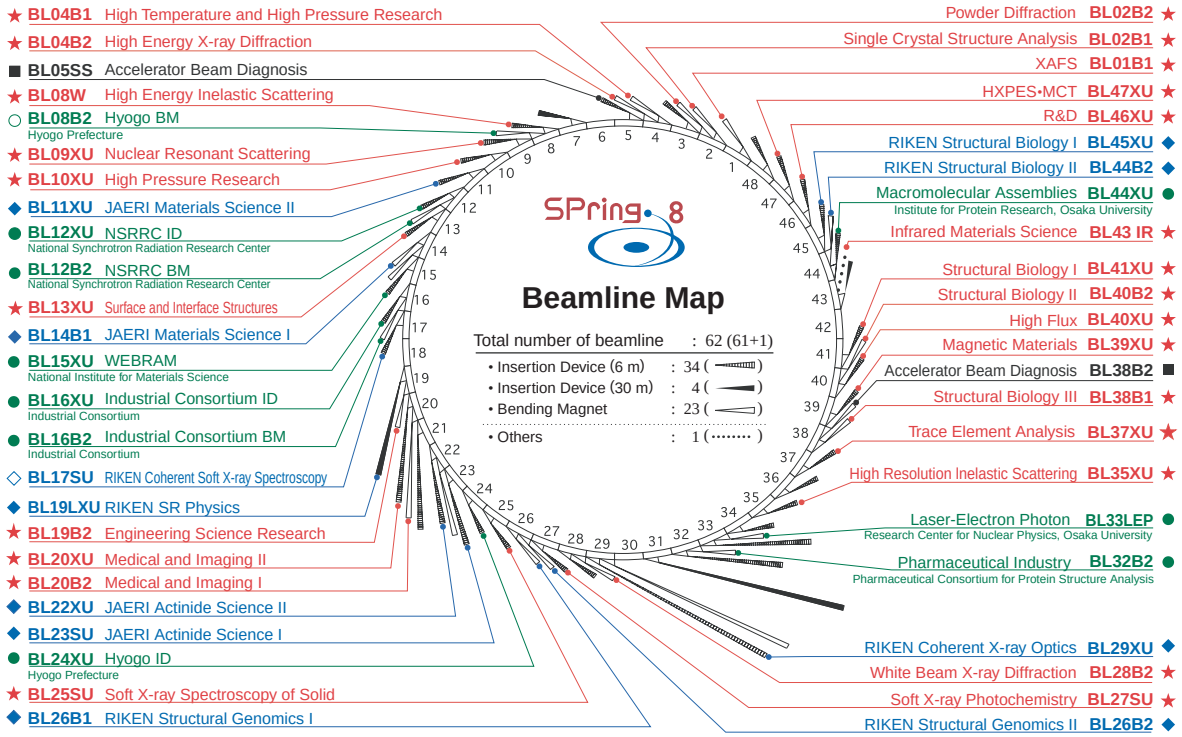

Fig. 2. Beamline Map.

Table II. List of beamlines

BL #	Beamline Name	(Public Use)	Areas of Research
★ Public Beamlines			
BL01B1	XAFS	(Oct. 1997)	XAFS in wide energy region (3.8 to 113 keV). XAFS of dilute systems and thin films.
BL02B1	Single Crystal Structure Analysis	(Oct. 1997)	Structure physics using single crystal analysis. Precise structure analysis of photo-excited state.
BL02B2	Powder Diffraction	(Sep. 1999)	Accurate structure analysis of crystalline materials using powder diffraction data by Rietveld refinements and MEM (maximum entropy method).
BL04B1	High Temperature and High Pressure Research	(Oct. 1997)	Mineral physics at high temperature and high pressure. Energy-dispersive X-ray diffraction and X-ray radiography using the large-volume press.
BL04B2	High Energy X-ray Diffraction	(Sep. 1999)	Structural analysis of glass, liquid, and amorphous materials. X-ray diffraction under ultra high-pressure. Precise single crystal structure analysis
BL08W	High Energy Inelastic Scattering	(Oct. 1997)	Magnetic Compton scattering. High-resolution Compton scattering. High-energy Bragg scattering. High-energy fluorescent X-ray analysis.
BL09XU	Nuclear Resonant Scattering	(Oct. 1997)	Time domain Mössbauer spectroscopy. Lattice dynamics study using nuclear resonant scattering.
BL10XU	High Pressure Research	(Oct. 1997)	Structure physics and earth science under ultra high pressure using DAC.
BL13XU	Surface and Interface Structures	(Sep. 2001)	Atomic-scale structure analysis of an ultra-thin film, nanostructure and surface, using in-air measurements (room temperature to 500 ºC) and in-vacuum measurements (20 to 1300 K).
BL19B2	Engineering Science Research	(Nov. 2001)	Industrial application using XAFS in wide energy region, residual stress measurement, structural analysis of thin film, surface and interface, powder diffraction, and X-ray imaging.
BL20XU	Medical and Imaging II	(Sep. 2001)	Medical application: Microangiography, refraction-enhanced imaging. / Micro-imaging: Scanning microscopy, imaging microscopy, microtomography, X-ray holography and X-ray optics. / Ultra-small angle scattering.
BL20B2	Medical and Imaging I	(Sep. 1999)	Medical application: Microradiography, microtomography and refraction-enhanced imaging. / Micro-imaging: R&D of optical elements for novel imaging techniques.
BL25SU	Soft X-ray Spectroscopy of Solid	(Apr. 1998)	High resolution photoemission spectroscopy. Photoelectron diffraction and holography. Magnetic circular dichroism (MCD). Photoelectron emission microscope (PEEM).
BL27SU	Soft X-ray Photochemistry	(May 1998)	Industrial research of functional material. Atomic and molecular spectroscopy by high resolution electron spectroscopy. Surface analysis and solid state physics.
BL28B2	White Beam X-ray Diffraction	(Sep. 1999)	White X-ray diffraction. Time-resolved energy-dispersive XAFS (DXAFS).
BL35XU	High Resolution Inelastic Scattering	(Sep. 2001)	Material dynamics on ~ meV energy scales using inelastic X-ray scattering (IXS) and nuclear resonant scattering (NRS).
BL37XU	Trace Element Analysis	(Nov. 2002)	X-ray microbeam spectrochemical analysis. Ultra trace element analysis. High energy X-ray fluorescence analysis.
BL38B1	Structural Biology III	(Oct. 2000)	XAFS. R&D of optics and detector. Macromolecular crystallography.
BL39XU	Magnetic Materials	(Oct. 1997)	X-ray magnetic circular dichroism (XMCD) spectroscopy. Element-specific magnetometry. X-ray emission spectroscopy and its magnetic circular dichroism. Resonant or non-resonant magnetic scattering.
BL40XU	High Flux	(Apr. 2000)	Time-resolved diffraction and scattering experiments. X-ray speckle. X-ray fluorescence trace analysis.
BL40B2	Structural Biology II	(Sep. 1999)	Macromolecular crystallography. Small angle X-ray (solution) scattering.
BL41XU	Structural Biology I	(Oct. 1997)	Biological macromolecular crystallography.
BL43IR	Infrared Materials Science	(Apr. 2000)	Infrared microspectroscopy. Magneto-optical spectroscopy. Infrared surface science. Absorption and reflection spectroscopy. Time-resolved experiments with pulsed laser and SR (pump and probe).
BL46XU	R&D	(Nov. 2000)	Insertion devices R&D. Resonant and non-resonant magnetic scattering structural analysis.
BL47XU	HXPES・MCT	(Oct. 1997)	R&D of microtomography and microbeam technique. High energy photoemission spectroscopy.

BL #	Beamline Name	(First Beam)	Areas of Research
● Contract Beamlines			
BL12XU	NSRRC ID (NSRRC)	(Dec. 2001)	High resolution non-resonant or resonant inelastic X-ray scattering. High resolution near-edge X-ray Raman scattering. Phase transitions under high-pressure, low and high temperatures. High-resolution X-ray absorption and emission spectroscopy. X-ray physics and optics.
BL12B2	NSRRC BM (NSRRC)	(Oct. 2000)	X-ray absorption spectroscopy. Powder X-ray diffraction. High resolution X-ray scattering. Protein crystallography.
BL15XU	WEBRAM (National Institute for Materials Science)	(Jan. 2000)	High resolution X-ray photoemission microscopy. High energy excitation X-ray photoelectron spectroscopy. High resolution X-ray emission spectroscopy. Highly precise X-ray powder diffraction and ultra-small angle scattering.
BL16XU	Industrial Consortium ID (Industrial Consortium)	(Oct. 1998)	Characterization of thin films for ULSI and magnetic devices, catalysts, functional materials, and structural materials by X-ray diffraction, fluorescence X-ray analysis, X-ray magnetic circular dichroism, and imaging with X-ray microbeam.
BL16B2	Industrial Consortium BM (Industrial Consortium)	(Oct. 1998)	Characterization of industrial materials, such as metal and oxide films, semiconductor crystals by XAFS, topography and other methods.
BL24XU	Hyogo (Hyogo Prefecture)	(May 1998)	Structure analysis of small bio-crystals for industry. Surface/interface analysis for industry by fluorescent X-ray analysis, strain measurements and grazing incidence X-ray diffraction. Microbeam formation studies for materials and life sciences.
BL32B2	Pharmaceutical Industry (Pharmaceutical Consortium)	(Apr. 2002)	Protein structure analysis for structure-based drug design: Design and optimization of new leading compounds based on pharmacodynamic action mechanism elucidated at the molecular level which obtained from a detailed interaction analysis of receptor-drug complexes.
BL33LEP	Laser-Electron Photon (Osaka University)	(Jun. 1999)	Meson photoproduction from nucleon and nucleus. Photoexcitation of hyperons, nucleon resonances, and other exotic states. Photonuclear reactions. Beam diagnoses. Test and calibration of detectors with GeV photon beam.
BL44XU	Macromolecular Assemblies (Osaka University)	(May 1999)	Crystal structure analysis of biological macromolecular assemblies (e.g. membrane complexes, protein complexes, protein-nucleic acid complexes, and viruses).
◆ JAERI Beamlines			
BL11XU	JAERI Materials Science II	(Oct. 1998)	Nuclear resonant scattering. Surface and interface structure with MBE. Inelastic scattering. XAFS.
BL14B1	JAERI Materials Science I	(Dec. 1997)	Materials science at high pressure. Structure physics.
BL22XU	JAERI Actinide Science II	(May 2002)	Materials science at high pressure. Resonant X-ray scattering (activity at RI laboratory).
BL23SU	JAERI Actinide Science I	(Feb. 1998)	Surface chemistry with supersonic molecular beam. Biophysical spectroscopy. Photoelectron spectroscopy (activity at RI laboratory). Magnetic circular dichroism (activity at RI laboratory).
◆ RIKEN Beamlines			
BL17SU	RIKEN Coherent Soft X-ray Spectroscopy	(Sep. 2003)	Spectroscopy of multiply charged ions. Angle-resolved photoemission spectroscopy (ARPES). Soft X-ray emission spectroscopy.
BL19LXU	RIKEN SR Physics	(Oct. 2000)	Any research field requiring the highly brilliant X-ray beam.
BL26B1/B2	RIKEN Structural Genomics I & II	(Apr. 2002)	Structural genomics research based on single crystal X-ray diffraction.
BL29XU	RIKEN Coherent X-ray Optics	(Dec. 1998)	X-ray optics, especially coherent X-ray optics.
BL44B2	RIKEN Structural Biology II	(Feb. 1998)	Macromolecular crystallography.
BL45XU	RIKEN Structural Biology I	(Jul. 1997)	Macromolecular crystallography. Time-resolved structures of non-crystalline biological materials using small-angle scattering and diffraction technique.
■ Accelerator Beam Diagnosis			
BL05SS	Accelerator Beam Diagnosis	(Mar. 2004)	Accelerator beam diagnostics. R&D of accelerator components.
BL38B2	Accelerator Beam Diagnosis	(Sep. 1999)	Accelerator beam diagnostics. R&D of accelerator components. Production of MeV γ-ray photons.

User Operation

Statistics

SPring-8 invites research proposals twice a year, and submitted proposals are reviewed by the SPring-8 Proposal Review Committee (PRC). In General Proposal, the PRC approved 406 out of 648 proposals for 2003B and 387 out of 529 for 2004A. In Priority Field Proposal, 215 proposals were adopted from among 290 proposals for 2003B and 208 from among 243 for 2004A. A total of approximately 4,000 hours of beamtime was allocated to successful applicants from 2003B through 2004A.

SPring-8 user operation results for the period from 1997B to 2004A are shown in Table III. This table shows the user beamtime available to users and the numbers of users and experiments conducted at both public and contract beamlines, which are also illustrated in Fig. 3. The results in the table and the figure include the numbers of experiments using reserved beamtime and of priority research proposals.

Research Term	User Time (hours)	Public BL		Contract BL	
		Experiments	Users	Experiments	Users
1997B: 1997.10 - 1998.03	1,286	94	681		
1998A: 1998.04 - 1998.10	1,702	234	1,252	7	
1999A: 1998.11 - 1999.06	2,585	274	1,542	33	467
1999B: 1999.09 - 1999.12	1,371	242	1,631	65	427
2000A: 2000.02 - 2000.06	2,106	365	2,486	100	794
2000B: 2000.10 - 2001.01	1,558	382	2,370	88	620
2001A: 2001.02 - 2001.06	2,381	473	2,915	102	766
2001B: 2001.09 - 2002.02	1,893	486	3,277	114	977
2002A: 2002.02 - 2002.07	2,093	543	3,246	110	1,043
2002B: 2002.09 - 2003.02	1,893	538	3,508	143	1,046
2003A :2003.02 - 2003.07	2,244	632	3,777	172	1,347
2003B: 2003.09 - 2004.02	1,844	548	3,428	154	1,264
2004A: 2004.02 - 2004.07	2,095	568	3,756	163	1,269
TOTAL	25,027	5,379	33,869	1,243	10,020

Table III. SPring-8 user operation results.

In 2003B and 2004A, SPring-8 provided users with 1,844 and 2,095 hours of beamtime in four and five operation cycles, respectively. In 2003B, 3,428 individuals used the public beamlines in 548 separate experiments, while 1,264 individuals used the contract beamlines in 154 experiments. In 2004A, 3,756 individuals used the public beamlines in 568 separate experiments, while 1,269 individuals used the contract beamlines in 163 experiments. From October 1997, when SPring-8 was opened to the public, through to 2004A, a total of 43,889 public and contract beamline users conducted 6,622 experiments.

Figures 4 and 5 indicate the numbers of selected proposals according to the affiliations of applicants and the research fields from 1997B to 2004A. As can be seen from the charts, proposals submitted by researchers affiliated with universities accounted for approximately 70% and those from other organizations made up the rest almost equally. The percentage of approved proposals from overseas was 4.7% for 2003B and 4.9% for 2004A. The ratio of proposals on Life Science, Diffraction & Scattering and others has been 1:1:1 since the inauguration of SPring-8. The ratio of proposals on XAFS, Spectroscopy, and Method & Instrumentation, all falling under “others,” has also been 1:1:1.

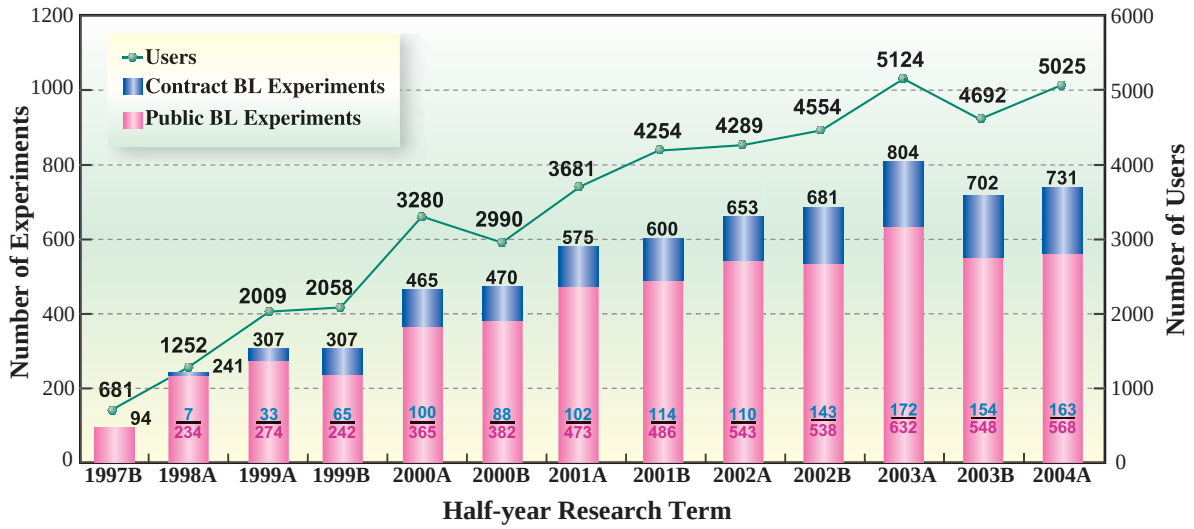

Fig. 3. Number of users and experiments conducted.

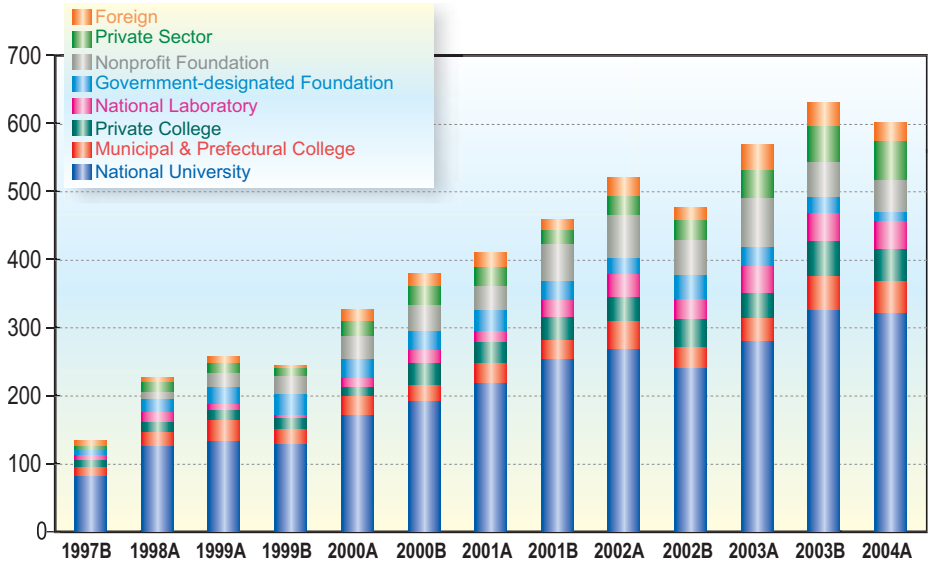

Fig. 4. Number of selected proposals by affiliation of applicants (public beamlines).

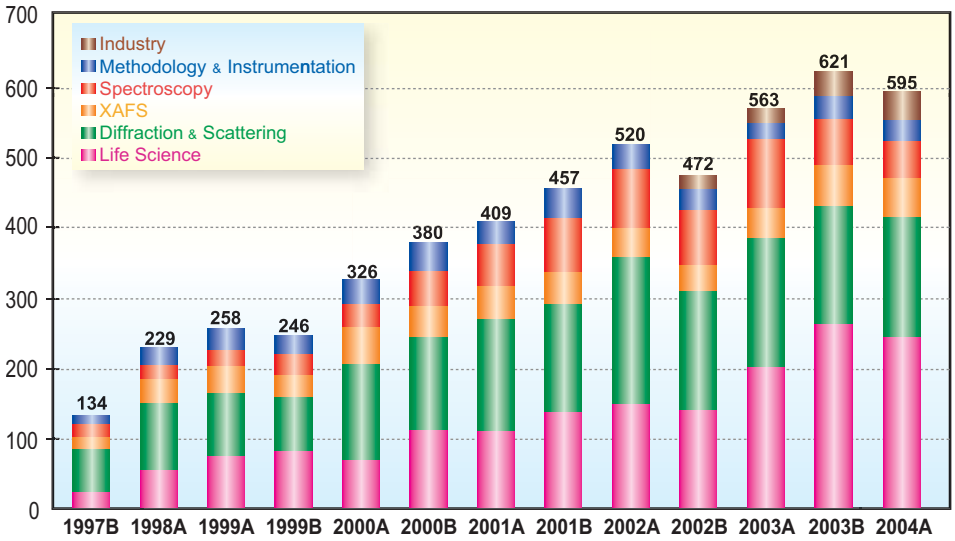

Fig. 5. Number of selected proposals by research fields (public beamlines).

Priority Research Proposal

Until FY2002, there were only **General** and **Long-term Proposals** and proposals using beamtime reserved for JASRI. In FY2003, a new scheme for the management of public beamlines was established, based on the report on SPring-8 by the governmental review committee. The report called on SPring-8 to further promote the use of public beamlines to produce more research results. The important point of the report was to launch the Priority Research Program. The scheme is shown in Table IV. As can be seen from the table, beamtime not exceeding 50% is allocated to Priority Research Proposals and proposals using beamtime reserved for JASRI, so that more than 50% of the total user beamtime is guaranteed for general and long-term proposals. The scheme for Priority Research Program is intended to make the best use of SPring-8 and to produce more research results. The Priority Research Proposals are tentatively categorized into the following three groups:

- Priority Field Proposal,
- Power User Proposal and
- Strategy Proposal.

Details of each proposal are provided below.

Priority Field Proposal

JASRI designates research fields which are expected to produce excellent research results or fields of strategic significance as priority fields. The Priority Field Proposal is further categorized into three subgroups: Nanotechnology Support, Protein 500 and Industrial Use. This proposal is reviewed before General Proposal by the review committee designated for each priority field. The outline of each priority research field is as follows:

Nanotechnology Support

This research field concerns the support of developments in nanotechnology, using 12 beamlines at SPring-8. Nanotechnology Support at SPring-8 was started in 2002 under the Nanotechnology Researchers Network Project (Nanonet Project) of MEXT (Ministry of Education, Culture, Sports, Science and Technology) and was merged into the Priority Research Program in FY2003. In 2003B and 2004A, a total of 104 proposals were selected from 186 submitted proposals. The Nanonet Project is valid until FY2006.

Protein 500

Similar to Nanotechnology Support, Protein 500 at SPring-8 started shortly after MEXT launched the Protein 3000 Project in 2002 as a post-human genom program to analyze 3,000 kinds of protein structures and became part of the Priority Field Program in FY2003. Under the Project, three of SPring-8 structural biology beamlines are assigned to analyze 500 kinds of protein structures, and 30% of their beamtime is allocated every year. In 2003B and 2004A, a total of 276 proposals were selected. The Protein 500 Project is valid until FY2006.

Industrial Use

As part of industrial use, the Trial Use Program originally ran from 2001B to 2002A, for the purpose of attracting new users to SPring-8, mainly from industries. It was restarted as one of the Priority Field Proposals in 2003A. In 2003B, 23 Trial Use proposals were selected from among 38 proposals. In 2004A, 20 Trial Use proposals were selected from among 33 proposals.

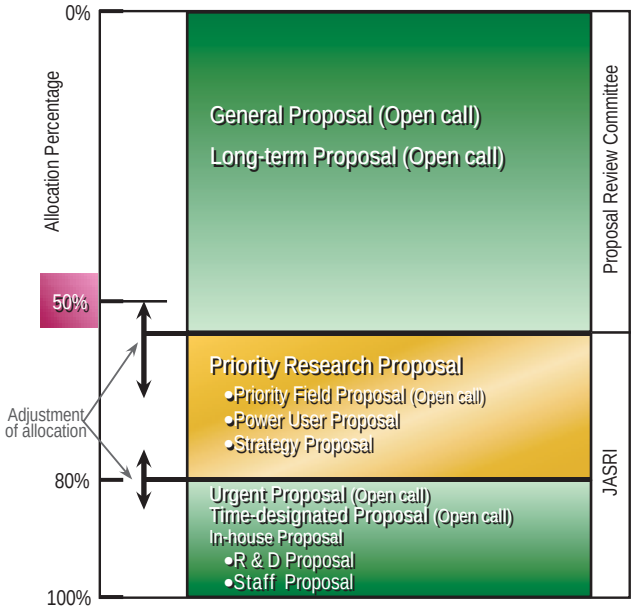

Table IV. Beamtime allocation scheme for public beamlines.

Power User Proposal

This category refers to proposals by user groups who have full knowledge of beamline instrumentation and are also highly likely to produce outstanding research results in the future. Such user groups are designated as Power Users (PUs) by JASRI and are expected to provide support to general users. In return for their support, up to 20% of beamtime of relevant beamlines can be used by PUs. Five groups were designated as PUs in May, 2003. Nine research subjects have been investigated, including the running subjects from 2003B and 2004A.

Strategy Proposal

Strategy Proposals are expected to contribute to the promotion of research at SPring-8, including the development of new technologies necessary for the operation of the facility. JASRI will conduct such research by alone or jointly with other organizations. The following two strategic research subjects were designated in May 2004.

- Basic Development of Nano-Particle Composite Materials
- Development of a New Powder Diffraction Technique for Medicinal Compounds

Long-term Proposal

Separately from General Proposals, SPring-8 has created a system for the long-term use of beamlines, where beam access is guaranteed for up to three years. This system aims to further promote research that is expected to produce outstanding results in science and technology, to pave the way for new research areas and research methodology and to help significantly improve the technology for industry by making the best use of SPring-8 characteristics. In 2003B, two of three proposals were selected; in 2004A, one of three proposals was selected. Seven proposals were being carried out at the end of 2004A.

Industrial Research

As well as the promotion of research activities in basic science, the contribution to the reinforcement of the technological base in industry has been one of the main pillars of the SPring-8 Project. The coordination system introduced in FY2000 to support industrial use mainly through consultation is a case in point. Equally important is the Trial Use Program. This program is aimed at revitalizing local industries and creating and promoting new industries. Public beamline BL19B2, the Engineering Science Research Beamline, built to promote SR use by industries, is the main beamline used in the Trial Use Program. There are three contract beamlines, which were constructed by Industrial Consortium and Pharmaceutical Consortium, for use by the consortium members. In addition to the above, workshops and training courses are also provided. These courses are intended for a variety of research fields and SR instrumentation and were attended by a total of 1,150 industrial users from FY2000 through FY2002.

Proprietary Research

Users conducting proprietary research are charged beamtime fees. Proprietary research is essential when users have commercially confidential information in their experiment or sample and do not wish to disclose their research results. In 2003B, 15 proprietary experiments were performed at public beamlines and 27 at contract beamlines (26 at BL32B2 and 1 at BL16XU); in 2004A, 10 experiments were conducted at public beamlines and 26 experiments at contract beamlines (24 at BL32B2 and 2 at BL24XU). During the period from 1999B, when the system was introduced, to 2004A, a total of 220 proprietary experiments were carried out at both public and contract beamlines. The Pharmaceutical Consortium spent about 79% of their beamtime on proprietary research at their contract beamline BL32B2, in 2004A.

Research Results

SPring-8 users are not charged for non-proprietary research as long as they submit an experiment report within sixty days after their experiments. When their results are disclosed in scientific journals or any other form of publication, the project leaders are required to inform and register it to JASRI. As of September 30, 2004, the number of refereed publications (journals, proceedings and dissertations) is 1,706 (1,313 for public use, 158 for contract beamlines and 287 for JAERI and RIKEN beamlines; the results obtained using two or more beamlines are counted for each beamline.)

Budget and Manpower

SPring-8 consisting of accelerators, beamlines and facilities for users, was constructed by the JAERI/RIKEN Project Team during the period from 1991 through 1997 at a total cost of about 110 billion yen. In 1994, JASRI was designated, under the Law Regarding Promotion of Common Use of the Synchrotron Radiation Facility (SPring-8), as the Organization for the Promotion of Synchrotron Radiation Research responsible for managing SPring-8. As a result, the SPring-8 research complex comprises JAERI Kansai Research Establishment, RIKEN Harima Institute and JASRI. JASRI has been entrusted by JAERI and RIKEN with the operation, maintenance, improvement, upgrading, R&D and safety management of SPring-8, as well as the technical support for new beamline construction after the construction of the main

facilities and buildings at SPring-8 was completed and public use started in 1997.

About 87% of the total budget of JASRI comes from the Government through JAERI and RIKEN and is appropriated for the above-mentioned missions of JASRI. The remaining 13% comes directly from the Government in the form of grants for user support. Figure 6 illustrates the budget at SPring-8. It shows that the total budget for JASRI for FY2004 was 10 billion 556 million yen and the total budgets for JAERI and RIKEN were 888 million yen and 2 billion 587 million yen, respectively. As can be seen from the figure, the budgets for JAERI and RIKEN have been reduced since FY2001 because the construction such as of utility facilities is approaching completion. Meanwhile, construction of beamlines has been halted due to lack of budget.

In FY2004, the total number of JASRI staff members was 488. The total number of SPring-8 staff members amounts to 1,099 when staff at JAERI Kansai Research Establishment and RIKEN Harima Institute is combined with the JASRI staff. The breakdown of the staff according to the types and fields of employment is shown in Fig. 7.

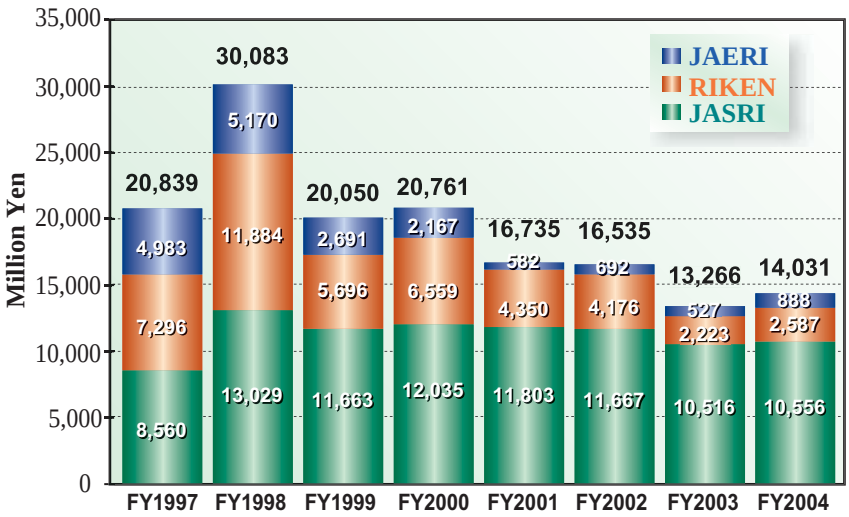

Fig. 6. Budget at SPring-8: JASRI, JAERI and RIKEN.

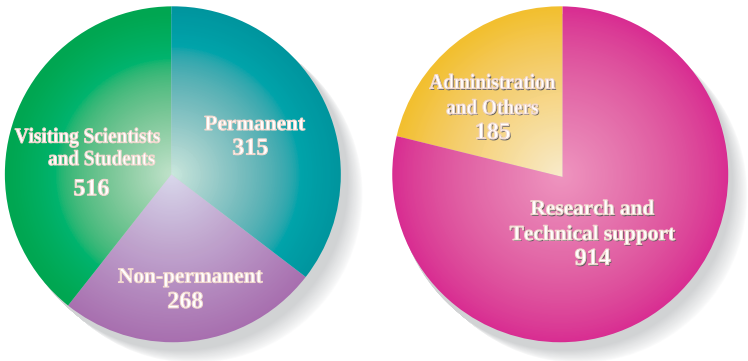

	by Type			by Field		Total
	Permanent	Non-permanent	Visiting Scientists and Students	Research and Technical Support	Administration and Others	
JASRI	219	130	139	349	139	**488**
JAERI	34	20	9	54	9	**63**
RIKEN	62	118	368	511	37	**548**
	315	**268**	**516**	**914**	**185**	**1,099**

Fig. 7. Manpower at SPring-8: JASRI, JAERI and RIKEN (FY2004).

Organization

As mentioned earlier in the Budget and Manpower, the SPring-8 research complex comprises JASRI, JAERI Kansai Research Establishment and RIKEN Harima Institute, all of which are on site. While JAERI and RIKEN conduct their own research at SPring-8, JASRI is entrusted by the two with the operation, maintenance, improvement, upgrading, R&D and safety management of SPring-8. Since SPring-8 is a facility open to the public, user support is also an important task of JASRI. The organization that JASRI has formed to accomplish these missions is shown in Fig. 8. The organizations of JAERI and RIKEN are shown in Fig. 9 and Fig. 10, respectively.

SPring-8 Organization

April, 2005.

Japan Synchrotron Radiation Research Institute (JASRI)

Director General A. Kira
Senior Exec. Director H. Ohno
Managing Exec. Director M. Yamada, M. Nagata, M. Hattori
Administrative Consultant O. Shimomura

Research Sector

- **Accelerator Div.** — N. Kumagai
  - Operation & Beam Dynamics — H. Ohkuma
  - Linear Accelerator — H. Hanaki
  - Circular Accelerator — H. Yonehara
  - Control — R. Tanaka
- **Beamline Div.** — T. Ishikawa
  - Insertion Device & Front End — H. Kitamura
  - Optics & Transport Channel — S. Goto
  - Control — R. Tanaka
  - Instrumentation Development — Y. Asano
  - Technical Support — T. Ishikawa
- **Research & Utilization Div.** — H. Suematsu
  - Materials Structure I — M. Takata
  - Materials Structure II — J. Mizuki
  - Materials Structure III — N. Yagi
  - Spectroscopy I — H. Suematsu
  - Spectroscopy II — T. Kinoshita
  - Structural Biology — M. Yamamoto
  - Imaging — Y. Suzuki
- **Industrial Application Div.** — S. Komiya
  - User Support — S. Komiya

Administration Sector

- **Facility Management Div.** — N. Kumagai
- **General Affairs Div.** — Y. Senge
- **Research Coordination Div.** — O. Shimomura
- **User Administration Div.** — T. Matoba
- **Public Relations Office** — M. Hara
- **Planning Office** — M. Moriyama

Safety

- **SPring-8 Safety Office** — J. Tada

Figure 8

April, 2005.

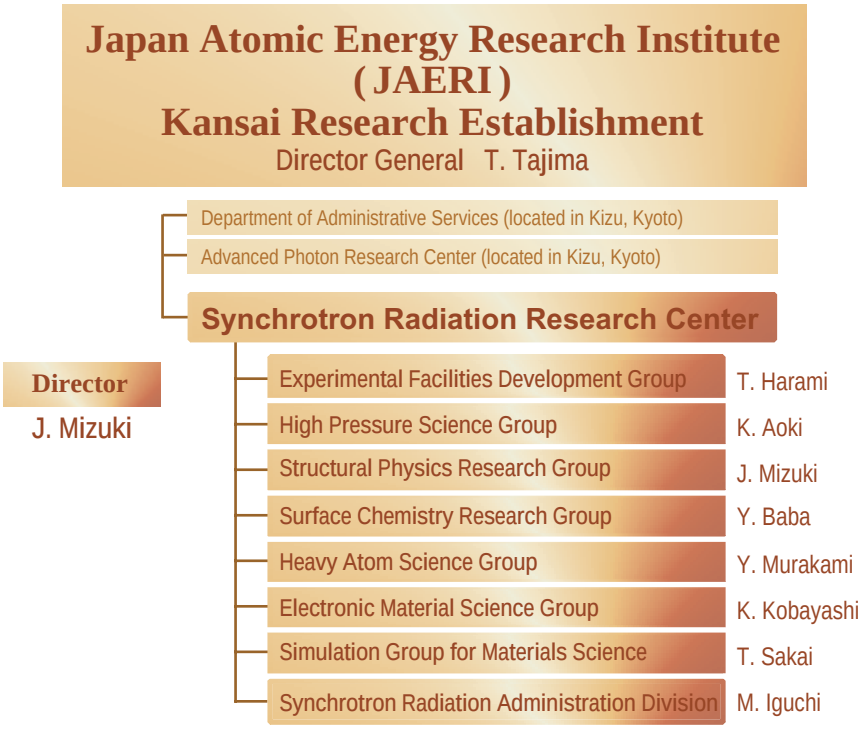

Figure 9

Figure 10

International Conferences and Workshops

International Conferences and Workshops sponsored by SPring-8 (JASRI, JAERI, RIKEN) held in 2004 is listed below.

Third CCLRC-JASRI Symposium
January 14 - 15

Asia Pacific Workshop on Neutrinos in Nuclear Physics 2004 (APN04)
July 12 - 14

International Workshop PENTAQUARK04
July 20 - 23

Glycolipid & Sphingolipid Biology Gordon Research Conference
July 25 - 30

3rd Annual Meeting of Structural-Biological Whole Cell Project of *Thermus thermophilus* HB8
July 30 - August 1

Satellite Workshop of BSR2004: SAXS in the 21st Century
September 5 - 7

Satellite Workshop of BSR2004: Structural Biology with Angstrom X-ray Lasers
September 7

8th International Conference on Biology and Synchrotron Radiation (BSR2004)
September 7 - 11

9th SPring-8, ESRF, APS Workshop
November 8 - 10

2nd PICS Workshop on High Energy Spectroscopies in d and f Electron Systems and
RIKEN Workshop on Quantum Materials Research Group
November 14 - 16

3rd International Workshop on Radiation Safety of Synchrotron Radiation Sources (Radsynch'04)
November 17 - 19

Users' Meeting

The Users Meeting sponsored by SPring-8/JASRI held in 2004 is listed below.

8th SPring-8 Symposium
October 18 - 19

Editor
Seishi Kikuta
SPring-8 / JASRI

Editing & Layout
Marcia M. Obuti-Daté
SPring-8 / JASRI

Printing
ROKKO Publishing & Sale Co.

J A S R I
Library and Information
Users Administration Division

1-1-1 Kouto, Sayo-cho, Sayo-gun
Hyogo 679-5198 • JAPAN
Tel. +81-(0)791 58-2797 Fax. +81-(0)791 58-1869

frontiers@spring8.or.jp
http://www.spring8.or.jp/

July 2005

SPring-8

Japan Synchrotron Radiation Research Institute
1-1-1 Kouto, Sayo-cho, Sayo-gun, Hyogo 679-5198 JAPAN
http://www.spring8.or.jp